In the name of God, the most Gracious, the most Merciful

UNIVERSITY OF SOUTHAMPTON

FACULTY OF ENGINEERING AND THE ENVIRONMENT

ROTOR EDDY CURRENT POWER LOSSES IN HIGH SPEED PERMANENT MAGNET SYNCHRONOUS GENERATORS

by

Arfakhshand Ali Qazalbash

Thesis for the degree of Doctor of Philosophy

April 2014

UNIVERSITY OF SOUTHAMPTON

ABSTRACT

FACULTY OF ENGINEERING AND ENVIRONMENT
ELECTRICAL ENGINEERING

Doctor of Philosophy

ROTOR EDDY CURRENT POWER LOSSES IN HIGH SPEED PERMANENT MAGNET SYNCHRONOUS GENERATORS

by Arfakhshand Ali Qazalbash

Rotor electromagnetic losses can be problematic in high speed permanent magnet synchronous machines, especially when the speed or the electrical loading are high and the slotting and winding configuration results in high magnitude asynchronous harmonics. Accurate estimation of these travelling flux harmonics in the initial design stage is essential, as small errors can result in significant errors in the estimated rotor losses, which could lead to misinformed design decisions.

This Thesis makes a number of contributions to the subject of rotor losses in PM machines. It firstly investigates the accuracy of the commonly used current sheet method for estimating losses for each harmonic. In this method, the losses are calculated using a multi-layer model of the machine in which each asynchronous harmonic in the rotor frame is represented by current sheet on the surface of the bore of a slotless stator. The harmonics are calculated using double Fourier transform of flux density data on the surface of the magnet obtained from a number of magnetostatic finite element (FE) solutions at different rotor position. The losses are also calculated using 2D transient FEA with rotor motion, with appropriate mesh refinement and time step determined based on a mesh and time step dependence study. The results show that the current sheet method accurately calculates the losses in ring magnets if the amplitudes of the harmonics are estimated accurately.

Secondly, the Thesis extends 3 analytical methods that have been reported in the literature by Zhu and Howe (1993), Gieras (2004) and Ẑarko et al (2006) to estimate the amplitude of the no-load asynchronous travelling flux density harmonics, the magnet flux tooth ripple harmonics, in the rotor frame. The accuracy of these methods is evaluated by comparison to those calculated using non-linear finite element analysis for variants of a particular machine. The results show that (Ẑarko et al, 2006) complex permeance method provides the closest estimate, when the level of saturation in the machine is negligible. However, if the saturation, of the tooth tip in particular is significant, then all methods underestimate the amplitudes of the harmonics. And accordingly, the estimated rotor losses are grossly underestimated by a factor of 1:3 in a machine with heavy tooth tip saturation.

Thirdly, the Thesis tackles the problem of losses in a loaded generator with sinusoidal currents. It is shown that the total losses in the machine are dependent on the power factor and the phase angle between the emf and current. The total loss cannot be simply calculated by adding the no-load loss due to magnet flux tooth ripple harmonics and the loss due to stator mmf asynchronous harmonics. This is due to the interaction between the stator mmf harmonics and the magnet flux tooth ripple harmonics, which need to be added vectorially. This is verified

by comparing the results calculated analytically (using the most accurate Ẑarko's method for calculating no-load harmonics), with those obtained from transient FEA in a machine with no significant saturation.

Fourthly, the Thesis investigates rotor losses in a generator with two slots per pole per phase connected to an uncontrolled diode rectifier, considering the two cases of constant current and constant voltage dc link. Two winding and rectifier configurations are considered: a 3-phase winding with a 3-phase, 6 pulse bridge rectifier and a double 3-phase winding with a 3-phase rectifier each, connected in series i.e., a 12 pulse rectifier. Both magnet flux tooth ripple and armature reaction stator mmf harmonics are considered in the calculation of rotor loss; the harmonics were added vectorially. It is shown that the machine with double 3-phase windings and 12 pulse rectifier has considerably lower rotor losses that the machine with one single 3-phase winding due to cancellation of high order harmonics.

Finally, limited studies are performed in the Thesis for the calculation of rotor losses in PMSGs with different slot opening, number of slots per pole and airgap (with magnet thickness adjusted to keep the airgap flux density and emf constant). It is shown that increasing the airgap and reducing slot opening reduced the losses The results plotted in a normalised form of loss per unit rotor surface area are versus the ratios of gap/slot pitch and slot opening divided by pole pitch. These curves are shown to give reasonable quick estimates of rotor losses in machines with different sizes. Also, rotor losses are calculated in three PMSGs with different numbers of slots per pole and winding / rectifier configurations. The results show that the popular 1.5 slots per pole concentrated winding configuration have considerably higher rotor losses due to the strong second harmonic than the other machines with lap windings.

The work in the Thesis was based on two-dimensional calculations, assuming ring magnets. Further work is needed to evaluate the 3D effect and magnet segmentation.

Table of Contents

List of Tables

List of Figures

Academic Thesis: Declaration of Authorship

I, Arfakhshand Ali Qazalbash, declare that the Thesis entitled "Rotor Eddy Current Power Loss in high speed Permanent Magnet Synchronous Generators" and the work presented in the Thesis are both my own, and have been generated by me as the result of my own original research. I confirm that:

- this work was done wholly or mainly while in candidature for a research degree at this University;
- where any part of this Thesis has previously been submitted for a degree or any other qualification at this University or any other institution, this has been clearly stated;
- where I have consulted the published work of others, this is always clearly attributed;
- where I have quoted from the work of others, the source is always given. With the exception of such quotations, this Thesis is entirely my own work;
- I have acknowledged all main sources of help;
- where the Thesis is based on work done by myself jointly with others, I have made clear exactly what was done by others and what I have contributed myself;
- parts of this work have been published in peer-reviewed conferences and journals (please see list of publications in the following page).

Signed: ……..

Date: …….

List of Publications

1. S.M. Sharkh, A.A. Qazalbash, N.T.Irenji, R.G. Wills, "*Effect of Slot Configuration and Airgap and Magnet Thicknesses on Rotor Electromagnetic Loss in Surface PM Synchronous Machines", ICEMS 11*, pp.1-6, 2011.

2. A.A. Qazalbash, S.M. Sharkh, N.T.Irenji, R.G. Wills, M.A.Abusara, "*Rotor Eddy Current Power Loss in Permanent Magnet Synchronous Generators Feeding Uncontrolled Rectifier Loads"* accepted in *IEEE Transaction on Magnetics*, and is currently available on *IEEE-Xplore*.

3. A.A. Qazalbash, S.M. Sharkh, N.T.Irenji, R.G. Wills, M.A.Abusara, "*Calculation of No-Load Rotor Eddy Current Power Loss in PM Synchronous Machines"* accepted in *IEEE Transaction on Magnetics*, and is currently available on *IEEE-Xplore*.

4. A.A. Qazalbash, S.M. Sharkh, N.T.Irenji, R.G. Wills, M.A.Abusara, "*Rotor Eddy Current Power Loss in High Speed Permanent Magnet Machines"* submitted to *IEEE Transaction on Energy Conversion*, on Oct, 14th 2013.

5. A.A. Qazalbash, S.M. Sharkh, "*Comparison of Rotor Eddy Current Power Loss in PM Generators Connected to Un-Controlled Rectifier Loads"*, submitted to *IEEE ICEM 14 conference*.

Acknowledgements

Firstly, all praise to Almighty Allah, Who gave me courage, patience and consistency in all these years to complete my studies and I pray to Him for His help and refuge, in upcoming years.

I would like to express my sincere gratitude to my supervisor Dr. Suleiman M Sharkh for his help, guidance, support, encouragement and patience throughout the research. I am in particular thankful to him for his constructive suggestions in preparation of the Thesis and assistance throughout the process of writing.

I would like to thank all members of the department who have provided help during the project. I would like to thank and wish the best to my office mates, particularly to Shayan Motamedi Fakhr, Georgios I. Orfanoudakis, Dr. Adam P.Lewis, Vorapath Kokaew and Mutaz Ryalat for useful discussions and nice company in the office.

I also wish to express my gratitude's to Dr. Neamat Irenji Taghizadeh, Dr. Kamel Boughrara and Dr. Damir Ẑarko, Dr. M. Abusara and Dr. Richard Wills for their useful suggestions.

I am thankful to Dr. Sujitha Jayasoma at Control Techniques Dynamics (CTD) for facilitating me during my Thesis write up. A very special thanks go to Marcus O' Flaherty at CTD, who took his time out from his busy schedule to proof read this Thesis.

I am most grateful to, my father Nawazish Ali, my mother Shahnaz Parveen, my brother Saqlain Haider and sisters and their families. I really don't know how to express my love and gratitude for what they have done for me before and during these years. They encouraged me to start this PhD and helped me finish it by caring and supporting me at any time.

I would like to express my deep gratitude to my wife and my son Moiz-E-Haider for their patience, encouragement, and support through this study while been away from me.

To my Parents,

Mr. Nawazish Ali Qazalbash
&
Mrs. Shahnaz Parveen Qazalbash,

And to our families,

List of Symbols

Chapter 2

θ	Rotor position
ω	Angular frequency
n	Integer (1,2,3…)
P	Permeance coefficients
h	Permeance harmonic order
k	Temporal order
q	mmf spatial order
Q_s	Integer number of slots per pole
F_{qk}	Amplitude of stator mmf harmonic
N_{ph}	Number of turns per phase
p	Machine pole pairs
K_{wq}	Winding distribution factor
I_k	rms value of stator winding current
K_{dq}	Winding distribution factor
K_{pq}	Winding pitch factor
K_{sq}	Winding skew factor
m	Number of slots per pole per phase
β'	Slot pitch angle

δ'	Ratio of short-chorded to full-chorded coil pitch
α'	Stator slot skew angle in radians
δ'''	Position of the phase belt
ξ	Arbitrary time-phase angle
T	Rotor pole-pitch

Chapter 3

δ''	Skin depth
μ	Permeability of the material
σ	Conductivity of the material
N	Number of data points
b_0	Slot-opening
ω_r	Angular rotor speed
R_3	Stator bore radius
$\hat{J}_{qk}$	Amplitude of current sheet with temporal order k and spatial order q
J_{qk}	Line current density
q	Harmonic spatial order
k	Harmonic temporal order
p	Pair of poles in machine
ω	Angular frequency
f	Frequency
A	Vector potential
r	Radius
θ	Rotor position
t	Instant in time
B_r	Radial component of airgap flux density

B_θ	Tangential component of airgap flux density
H_θ	Tangential component of magnetic field intensity
V'	Volume of the electrically conducting region
E	Electric field intensity
H	Magnetic field intensity
S	Surface area
P_m	Power loss in the magnet
P_h	Power loss in the rotor hub
P_t	Total power loss

Chapter 4

$\vec{B}$	Airgap flux density
$\vec{H}$	Magnetic field intensity
$\vec{M}$	Magnetization vector
μ_0	Permeability of free space
μ_r	Relative permeability of the material
φ	Scalar field
h_m	Magnet thickness
$\vec{a}_r$	Radial component of magnetization
$\vec{a}_\theta$	Tangential component of magnetization
α_p	Pole arc to pole pitch ratio
p	Pair of machine poles
n	Integer i.e., number of harmonics (1,2,3…)
H_r	Radial component of field intensity
H_θ	Tangential component of field intensity

Υ	Separation constant
R_1	Rotor hub radius
R_2	Magnet outer radius
R_3	Stator bore radius
R_4	Stator outer radius
$\mathbf{B}_g$	Airgap flux density in slotless PM machine (general)
$\mathbf{B}_s$	Airgap flux density in slotless PM machine
λ	Relative permeance function (general)
B_{gr}	Radial component of airgap flux density in slotted PM machine
$B_{g\theta}$	Tangential component of airgap flux density in slotted PM machine
λ_{RP}	Relative permeance function developed by (Zhu and Howe, 1993)
Λ_0	Fundament term for fourier coefficient
Λ_n	Fourier coefficient
Q_s	Integer number of slots
k_c	Carter's coefficient
β	Determines the variation in the airgap flux density due to slotting
b_0	Slot opening
τ_t	Tooth pitch
γ	Slot-opening factor
g_e	Corrected airgap length
g'	Effective airgap length
g	Original airgap length

λ_{GR}	Relative permeance function developed by (Gieras, 2004)
s_{ok}	Slot opening factor
τ_s	Slot pitch factor
G'	Airgap length
b_0'	Slot-opening
λ_a, λ_b	Fourier series of relative permeance function
$\lambda_0, \lambda_{an}, \lambda_{bn}$	Fourier coefficients
λ_{CP}	Complex relative permeance function developed by (Ẑarko et al., 2006)
RP	Relative Permeance by (Zhu and Howe, 1993)
GR	Relative Permeance by (Gieras, 2004)
CR	Complex relative permeance function (Ẑarko et al., 2006)

Chapter 5

φ	Phase angle
V	Voltage
I	Current
E	Induced fundamental emf
δ	Angle between V and E
ψ	Load angle
X	Reactance of the PM machine
ϕ	Flux linkages
α	The angle between magnet flux tooth ripple and armature reaction stator mmf harmonic

Chapter 6

ψ	Angle between back emf E and Current I

N_c	Number of turns per coil
I_k	rms value of stator winding current
spp	Slot per pole phase
$\vec{f}_{a1}$	mmf due to windings in first slot of the PM machine
$\vec{f}_{a2}$	mmf due to windings in second slot of the PM machine displaced by 30 degrees

Chapter 7

λ_q	Wavelength of harmonic
B_q	Peak normal flux density
s	Slot-opening
g	Airgap length
λ	Slot-pitch

Chapter 1

Introduction

1.1 Overview

The focus of this Thesis is on the investigation of asynchronous flux harmonics and their corresponding rotor eddy current power loss in PMSGs rotating at high speed i.e., 90,000 rpm. Asynchronous harmonics are caused by permeance variations due to stator slotting, saliency, saturation and armature reaction stator mmfs. The eddy currents caused by these harmonics could result in overheating of the rotor. The overheating in the rotor can be problematic as, unlike the stator, the rotor is more difficult to cool. Cooling of the rotor is restricted by the small airgap and a lack of heat transfer through the sleeve materials. Overheating may cause demagnetisation of the permanent magnets, sleeve failure or bearing drying.

The problem of overheating due to rotor eddy current power loss gets aggravated in PM machines with saturation. Saturation mainly occurs in the stator tooth tips of the PM machine and causes a virtual increase in slot opening, resulting in an increase of the amplitudes of rotating harmonics, which in turn increase eddy current losses.

Higher rotor eddy current losses can also occur in PM generators connected to rectifier loads. In this case power electronics devices, such as diodes, which cause stator mmf harmonics and can lead to increased rotor power loss.

Accurate calculation of rotor eddy current losses in high-speed PM synchronous

machines can be critical. These machines are highly stressed mechanically and thermally and a relatively small change in rotor loss of say 100 W in a 100 kW machine can make a difference when determining the feasibility of an efficient design variant.

Finite element analysis (FEA) software packages capable of solving transient models including rotation and external circuits are now widely available. With such advanced computational tools, it is now possible to accurately calculate rotor losses taking into account realistic features such as saturation, magnet segmentation and end effects (if a 3D solver is used). However, these solvers require a very fine mesh and time step to get good accuracy, which means simulations can take a long time (Sharkh et al., 2011).

Rotor eddy current power loss can also be calculated using analytical methods. These methods can be quicker and are usually employed in the initial design calculation of PM machines. These methods also help provide an insight into the sources of rotor losses. Though simplifying assumptions are necessary in developing analytical methods; including negligence of end effects, non-linearity of the material and conducting paths between magnet poles through the rotor hub; they still provide the designer with more insight into the sources of losses, which could suggest design changes that could help reduce them. However, the accuracy of these analytical techniques needs further investigation.

1.2 Analytical Methods used to Calculate Amplitude of Asynchronous Harmonics

This section presents a review of analytical methods that have been developed for the calculation of the amplitude of flux harmonics in the airgap flux density of PM machines, caused by permeance variation due to stator slotting and armature reaction stator mmf.

1.2.1 **Magnet flux tooth ripple harmonics**

In many PM machines, rotor eddy current power loss due to magnet flux tooth ripple harmonics is generally assumed negligible compared to rotor losses caused by stator

mmf space and time harmonics. In addition, these losses are also difficult to model. (Atallah et al., 2000; Jiabin et al., 2010; Polinder and Hoeijmakers, 1999; Ishak et al., 2005; Toda et al., 2004; Nakano et al., 2006; Zhu et al., 2001a; Zhu et al., 2004; Fang, 1997), presented analytical techniques for calculating stator mmf harmonics and associated losses. The assumption is however valid only if rotor losses due to magnet flux tooth ripple harmonics can be sufficiently reduced, by increasing the airgap and reducing the slot opening (Sharkh et al., 2011). In practice, winding insertion requirements, set limits on the minimum slot opening, and maximum airgap and hence the achievable reduction in tooth ripple loss. In many high-speed machines the magnet flux tooth ripple component of rotor loss can be higher and therefore can't be ignored in the calculation of rotor eddy current power loss (Sharkh et al., 1999; Wu et al., 2011).

Methods derived by Gibbs (1947), Freeman (1962), Lawrenson et al (1966) and others, can be used to estimate magnet flux tooth ripple harmonics in large synchronous machines with solid steel pole faces. Gibbs (1947), claims that a curve showing the variation of current density in time for any point on the pole surface is identical in shape with the curve of flux density distribution in space provided that suitable units are chosen. Thus the time harmonics in the surface current density can be obtained from an analysis of the flux density curve along the pole-face.

Based on Gibbs' work, Freeman (1962) developed method of tooth ripple determination on the basis of conformal transformation. The method assumed infinite permeability for stator and rotor materials, flux not penetrating to the bottom of the slot, rotor and stator un-saturated and rotor and stator with infinite curvature radii. Therefore, with these assumptions, in the absence of teeth and slots airgap flux density distribution will be uniform. But in a real machine this is not the case, this fact along with the presence of the permanent magnet material with relative permeability near to unity, at top of a hub made of ferromagnetic materials, makes the application of the conformal mapping method to a PM machine inaccurate.

Lawrenson et al (1966) summarized the opinion of earlier authors on the significance of the rotor eddy current reaction effects. It is mentioned that, although the stator is laminated, eddy currents are produced in it due to airgap flux. This varies the

amplitude of airgap flux harmonics but the effect is been neglected by assuming zero conductivity for stator material.

In general, the above mentioned methods assume the flux to be homopolar i.e., flux due to one magnet pole either north or south. The assumption of homopolar flux is reasonable in sufficiently large machines as they have a large pole pitch to slot pitch ratio; this is not true for the small machines where the pole pitch to slot pitch is of lower ratio e.g., 3-6 and flux is strongly hetero-polar. In case of hetero-polar, the flux due to both north and south poles is taken into account. Using these methods for the machines under study in this Thesis may therefore not accurately estimate the amplitude of magnet flux tooth ripple harmonics.

Another approach which can be used to determine the amplitude of these harmonics is to calculate the airgap flux density waveform distribution using two analytical methods; viz. sub-domain and method permeance method. Both methods make the following common assumptions:

1. Stator and rotor materials are assumed to be infinitely permeable
2. Field equations are solved in a two-dimensional model, i.e., the end effects are neglected
3. The effect of stator tooth tip saturation on airgap flux density is neglected

In the sub-domain method, the PM machine is divided into different sub-domains, i.e., magnets, airgap and slots. The analytical solutions of Laplace's and Poisson's equations in each sub-domain are obtained by applying boundary conditions to the interfaces between each sub-domain. The method can accurately predict the airgap flux distribution in PM machines and accounts for the effect of pole transition over the slot, tooth tips and effect of neighbouring slots (Liu and Li, 2007; Dubas and Espanet, 2009; Zhu et al., 2010; Wu et al., 2011a, Wu et al., 2011b). The method has proved to have high accuracy in terms of calculating airgap flux density distribution in slotted PM machines. The subdomain method has been extended for the calculation of amplitude of airgap magnet flux harmonics in (Wu et al., 2012b). The simplifying assumptions mentioned earlier are also true in the development of this method, and

this may result in discrepancies between analytical and FEA methods for the calculation of amplitude of harmonics.

In the relative permeance method the airgap flux density distribution waveform is determined by calculating a permeance function, which caters for the variation in airgap flux due to stator slotting. This variation is higher than the average value under the teeth and lower that its average value under a slot. The function is then multiplied with the flux density of a hypothetical slotless PM machine. The variation in permeance was investigated by Carter (1900). This investigation resulted in the development of a conformal mapping technique that enables the calculation of an effective airgap from 'Carter's coefficient', k_c, which characterises the slot opening and airgap length. As this method assumes an infinite slot pitch, various corrections of Carter's coefficient have been introduced for accurate calculation of slotting effect in (Bedrich Heller and Hamata, 1977; Oberretl, 1972; Weber, 1928; Freeman, 1962). Bedrich Heller and Hamata, 1977, highlighted corrections by various authors. The Carter factor for slotted stator and rotor has been verified experimentally by Oberretl, 1972. His results showed agreement with the Carters coefficient for two sided slotting. Weber, 1928, introduced a simple relation by replacing the distribution of the magnetic induction B over the slot pitch. The relation takes into account the periodic distribution of B and finiteness of the slot pitch. Freeman, 1962 developed an improved method for tooth ripple determination based on conformal transformation taking into account effect of neighbouring slots on airgap flux density.

The airgap flux variation due to stator slotting in the airgap of PM machine is also catered for by developing 2D permeance function see (Zhu and Howe, 1993; Gieras, 2004; Dajaku and Gerling, 2010; Ẑarko et al., 2006) and others. This permeance function has been developed using different methods; conformal mapping is used by Zhu and Howe (1993) and Gieras (2004), whereas Dajaku and Gerling (2010), employed a reluctance network technique. The permeance functions generated using these methods can only be used to calculate the effect of slotting on the radial component of airgap flux density. A more accurate method i.e., Schwarz Christoffel transformation has been used by Ẑarko et al (2006) for the calculation of a permeance function that can calculate the effect of slotting on both radial and tangential components of airgap flux density.

In addition to previously mentioned assumptions the permeance methods also assumes simple slot geometry with an infinite slot depth to cater for the effect of slotting. All these assumptions may result in the effect of slotting on airgap flux density being estimated incorrectly.

Nonetheless, the method has been widely used for the calculation of cogging torque, induced back emf and iron losses, where the amplitude of rotating harmonics isn't of much concern;(Wu et al., 2012; Xinghua et al., 2003; Kumar and Bauer, 2008; Ẑarko et al., 2008).

Given that we have many methods available for the calculation of airgap flux density distribution, question is how accurate they are compared to FEA for calculating rotor eddy current power loss. In this regard the permeance methods by Zhu and Howe (1993), Gieras (2004) and Ẑarko et al (2006) for the calculation of airgap flux density distribution is further extended for the calculation of harmonic amplitude and their respective rotor power loss as will be discussed in chapter 4 of this Thesis.

1.2.2 **Stator MMF harmonics only**

The amplitude of armature reaction flux harmonics caused by winding distribution and temporal harmonics in the current can be calculated using winding factor equations, as discussed in (McPherson, 1981). Depending on the winding configuration i.e., full pitch, fractional pitch, or concentrated winding; the winding factor equations are modified accordingly to calculate the amplitude of armature reaction flux harmonics in (Zhu et al., 2004; Ede et al., 2007; Toda et al., 2004; Fang, 1997; Atallah et al., 2000) and others. The winding factor equation in (McPherson, 1981) neglects the effect of stator slot opening width, effect of stator tooth tip saturation and end effects on the amplitude of armature reaction flux harmonics. Though the slot opening width has been catered for in Zhu and Howe (1993), but in comparison to FEA, the discrepancy caused by neglecting stator slot opening width, effect of stator tooth tip saturation and end effects in the analytical rotor eddy current power loss calculation is another research question dealt in chapters 5 and 6 of this Thesis.

1.2.3 **Resultant harmonics**

Each PM machine has its own particular set of tooth ripple harmonics, due to the specific rotor flux density distribution; and a particular set of stator mmf harmonics due to the specific airgap geometry and winding arrangement. In order to combine the effects of both sources, the interaction between magnet flux tooth ripple harmonics and armature reaction stator mmf flux harmonics needs to be accounted for using phasor (vector) addition, taking into account the phase angle between each harmonic. In the literature the interaction between harmonics is rarely mentioned. Oberretl (1972) and Wu et al (2012a) discussed the importance of phasor addition and calculated the resultant harmonics due to interaction between the two sources of harmonics. A comparison is presented between analytical and FEA results for the calculation of amplitude of resultant harmonics in PM machines with negligible effect of reaction of eddy currents. The amplitude of resultant harmonics in PM machine do vary due to the reaction of eddy current field or magnetising and demagnetising effect due to current advance angle. The variation in resultant harmonics due to reaction of eddy current field and current advance angles has been accounted for in chapter 5 and 6, respectively.

1.3 Analytical Methods used for the Calculation of Rotor Eddy Current Power Loss due to Asynchronous Harmonics

This section presents the analytical methods for the calculation of rotor eddy current power loss in PM machines due to asynchronous flux harmonics caused by magnet flux tooth ripple, armature reaction stator mmf and resultant mmf. Generally, rotor eddy current power loss is calculated using a two dimensional current sheet method taking into account reaction of eddy currents. In this method each rotating flux harmonic in space and time is represented by a current sheet placed at the stator bore of a slotless stator, as discussed by Sharkh et al (1999), Stoll and Sykulski (1992), Zhu et al (2004) and others.

The rotor eddy current power loss in case of static solution (without eddy currents) cannot be readily calculated using current sheet method. Firstly, rotor power loss is

calculated using transient solution i.e., taking eddy currents into account and then this power loss is modified to calculate static rotor power loss. The methodology for calculating rotor eddy current power loss using static solution has been discussed in detail in chapter 3 of this Thesis.

1.3.1 **Rotor Eddy Current Power Loss due to Magnet Flux Tooth Ripple**

Rotor eddy current power losses in PM machines due to magnet flux tooth ripple harmonics have been reported on by various authors; see (Gibbs, 1947; Lawrenson et al., 1966; Oberretl, 1972; Rahman, 1974; Stoll and Sykulski, 1992) and others. The common features of these papers can be summarised as:

1. A rectilinear model of the machine is assumed;
2. It is assumed that the machine consists of three regions, i.e., stator, airgap, and rotor;
3. It is assumed that the tooth ripple flux density i.e., open circuit mmf is produced by a travelling current sheet placed in the stator surface;
4. It is assumed the airgap flux is homopolar;
5. The amplitude of the tooth ripple is determined by a conformal transformation technique;
6. Field equations are solved in two dimensions, i.e., end effects are neglected;
7. The stator conductivity is assumed to be zero;
8. The stator and rotor are assumed to be infinitely permeable;
9. The effect of saturation is neglected;

The major differences among the methods are the value used for the rotor material permeability. Lawrenson et al (1966) used the absolute value of relative permeability of the rotor material; Rahman (1974) and Stoll and Sykulski (1992) applied an incremental permeability; whereas Gibbs (1947) and Oberretl (1972) approximate the permeability of the pole material in terms of the tangential field intensity.

Freeman (1962) and Oberretl (1972) presented a concise expression for the total no-load power loss due to all harmonics, given as a function of the power loss due to the fundamental harmonic and the amplitudes of the higher order harmonics, and taking into account the reaction of eddy currents. A set of curves are given to extract the harmonic loss factor, in order to take into account the effect of all harmonics at no-load.

The above mentioned methods of calculating rotor eddy current power loss cannot be readily used to obtain good accuracy for the PMSGs under consideration in this Thesis for two main reasons:

1. The slot pitch / pole pitch ratio is typically smaller than that of a large conventional machine. The assumption of homopolar flux in the machines under study cannot be made and therefore the curves in Freeman (1962) and Oberretl (1972) cannot be used.

2. Since these methods don't account for permanent magnet regions therefore these methods cannot be used in case of PM machines.

The above limitations in the calculation of rotor eddy current power loss in PM machines has been overcome by Boules (1981), Irenji (1998), Zhu et al (2001c), Wu et al (2012b) and others. A five layer rectilinear model of PM machine which takes into account the sleeve and magnet layers is used by Boules (1981) and Irenji (1998) for the calculation of rotor eddy current power loss taking into account reaction of eddy currents. Boules (1981) assumes the magnet edges to be constant mmf pulses / sources. But because of inter-polar flux leakage, the working point of the magnets will not be constant throughout their volume, so that the mmf acting across the pole arc will vary over a pole arc. The simplifying assumption of constant mmf between the two faces of a pole can lead to errors in rotor loss calculation (Zhu and Howe, 1993).

Zhu et al (2001c), Wu et al (2012b) used a cylindrical model of a PM machine with ring and segmented magnet configurations for the calculation of rotor eddy current power loss. The method assumed eddy currents to be resistive limited in the magnet. The assumption may not be true for PM machines having ring magnets, where the

effect of reaction of eddy currents is significant (Atallah et al., 2000). A gap in the knowledge; for the calculation of rotor eddy current power loss using cylindrical model of PM machines with ring magnet configuration taking into account reaction of eddy current is addressed in chapters 3 and 4 of the Thesis.

1.3.2 **Rotor Eddy Current Power Loss due to Armature Reaction Stator mmf**

Rotor eddy current power loss due to armature reaction flux harmonics are considered to be the main source of power loss in a PM machines. Using an analytical current sheet method the rotor eddy current power loss due to different stator winding configurations can be calculated. See (Polinder and Hoeijmakers, 1997; Zhu et al., 2001c; Zhu et al., 2004; Ede et al., 2004; Toda et al., 2004; Fang, 1997) and others, who calculated rotor eddy current power loss due to armature reaction stator mmf harmonics. But the methods either neglected magnet flux tooth ripple loss and / or effect of reaction eddy currents on amplitude of harmonics.

In many PM machine models the losses are assumed to be resistive limited, in which case the techniques developed by Polinder and Hoeijmakers (1997), Ede et al (2004), Toda et al (2004) and others, would give reasonably accurate results, even for machines with segmented and insulated magnets. However, in high-speed machines with solid steel rotors, where the magnets' widths are larger than the wavelength of the main harmonics, the eddy currents are typically inductance limited; this is especially true for losses in the rotor steel, as shown in (Atallah et al., 2000). In these cases the reaction of the eddy currents need to be taken into account for rotor losses in high-speed PM machines; see (Sharkh et al., 1999; Zhu et al., 2004; Fang, 1997) for further details on loss calculation.

The calculation of rotor eddy current power loss due to armature reaction stator mmf harmonics in PMSG connected to a rectifier load has also been of interest in recent years, primarily because the losses in these machines can be higher; see (Vadher et al., 1986; Seok-Myeong Jang, 2006; Van der Veen et al., 1997; Nagarkatti et al., 1982). Apart from fundamental harmonic component losses due to the armature reaction stator mmf, other harmonics of different spatial and temporal orders can also induce eddy currents in the conducting structures on the rotor, which can result in overheating

of the magnets or the retaining sleeve. Rotor eddy current power losses in these machines have also been calculated; see (Seok-Myeong Jang, 2006) and (Yunkai et al., 2011). In (Seok-Myeong Jang, 2006), a combined FEA and analytical method similar to Irenji (1998) is used to calculate rotor eddy current power loss. Though the method is time consuming, but good accuracy in terms of rotor loss can be achieved. Yunkai et al (2011) employs the method developed in (Atallah et al., 2000) to investigate the effect of modular winding configurations on rotor eddy current power loss in PMSGs connected to a rectifier loads. The method assumes that eddy currents are resistive limited. A comparison in terms of rotor eddy current power loss results are presented to show agreement between analytical and FEA method for PMSGs running at low speed. The level of discrepancy between the two methods increases at high speed, where the problem is no longer resistive limited and the effects of reaction eddy currents may become significant.

1.3.3 **Rotor Eddy Current Power Loss due to Resultant mmf**

For both magnet and stator mmf sources are active, rotor eddy current power losses in PM machines depend upon the angle between the mmf and rotor fluxes, i.e., the angle between the current *I* and back emf *E*; see (Sharkh et al., 1999; Wu et al., 2012a; Oberretl, 1972). Tooth ripple and armature reaction flux harmonics of the same order interacts depending on this angle. Under certain conditions, namely when the advance angle between *E* and *I* is zero, eddy current power loss due to magnet flux tooth ripple harmonics and armature reaction flux harmonics can be calculated using superposition of the losses; see (Ishak et al., 2005; Toda et al., 2004; Zhu et al., 2001a; Fang, 1997); (Schofield et al., 1997); (Zhu et al., 2001c); (Zhu et al., 2004); (Boules, 1981); (Nuscheler, 2008). For all other current advance angles superposition of the losses leads to inaccurate results (Kaczmarek et al., 2007), (Wu et al., 2012a). The correct procedure is therefore to calculate the resultant harmonics by adding tooth ripple and armature reaction flux harmonics of the same order vectorially, and then calculate the losses caused by the resultant harmonics as will be discussed in chapter 5 and 6 of the Thesis.

Wu et al (2012a) calculated rotor eddy current power loss caused by resultant harmonics in PM machines. Both magnet configurations i.e., segmented and ring magnet has been catered for in the analytical calculation of losses with the assumption that eddy currents are resistive limited. For specific slot-pole combination in PM machines, the analytical results for the rotor loss calculation are comparable to those using FEA. The discrepancy between analytical method and FEA may occur for the calculation of rotor eddy current power loss in PM machines with inductive limited eddy currents in the magnet. The problem has been addressed in chapter 5 and 6 of the Thesis; rotor eddy current power loss is analytically calculated in PM machines with inductive limited eddy currents and results are compared with FEA.

1.4 Methods for Reducing Rotor Eddy Current Power Loss

The overheating problem in the rotor of PM machines can be overcome by reducing the flow path of eddy currents. This can be achieved by using the process of magnet segmentation. In this process the permanent magnets are cut into small pieces and glued onto the surface of the rotor. The effect of segmentation is advantageous in terms of reducing the flow path of eddy currents and hence losses, but the process itself is laborious and costly.

Partial magnet and rotor yoke segmentation has also been investigated to reduce rotor eddy current power loss by Wills and Kamper (2010b). For magnet segmentation, three cases are investigated i.e., full magnet segment (FMS), single sided partial magnet segmentation (SS-PMS) and double sided partial magnet segmentation (DS-PMS). The depth for magnet segmentation in SS-PMS and DS-PMS is determined from the penetration of eddy currents in the skin depth of the magnet. In comparison to FMS the result shows a 50 % more reduction in power loss for the case of SS-PMS and DS-PMS. It is shown that in the PM machine the rotor yoke eddy currents vanish in the 30% of the yoke from the stator facing side. Therefore partial segmentation of rotor yoke can also be advantageous in reducing rotor losses and could potentially be less laborious.

The effect of both axial and circumferential magnet segmentation in PM synchronous machines has been investigated using analytical and FEA methods (Kirtley et al.,

1998; Ede et al., 2007; Polinder and Hoeijmakers, 1999; Atallah et al., 2000) and others. Effect of one, two and three axial segmentation of permanent magnet has been investigated by Ede et al., 2007, in two PM machines having; four-phases, 8-slots, 10-poles and five phases, 10-slots, 12-poles, respectively. It has been shown that though axial segmentation of permanent magnet reduces rotor eddy current power loss, but using 2D analytical and transient FEA methods in case of higher number of magnet segments either circumferential or axial are inappropriate. It is suggested that 3D analysis is required. The methodology for the calculation of rotor eddy current power loss in 3D is then presented which provides faster and accurate solution in PM machines with higher number of axial magnet segments. Polinder and Hoeijmakers, 1999, developed an empirical method based on magnet loss resistance network for the calculation of rotor eddy current power loss in PM synchronous generator having circumferential magnet segmentation. This method may not give accurate results due to number of assumptions involved including; magnet width is assumed small enough so that the flux is constant on the surface of the magnet, negligence of tooth ripple loss and reaction of eddy currents. Atallah et al., 2000 developed analytical method to cater for the effect of circumferential magnet segmentation. A comparison study between FEA and analytical method is presented, which showed decrease in rotor eddy current power loss of 30 % (approx) in PM machines with circumferentially segmented magnets. But the developed analytical method is only applicable when rotor has at least one magnet segment per pole. From the literature; cicumferential magnet segmentation has proved to be more effective in terms of reducing rotor eddy current power loss in the magnets and can be modelled in 2D.

In this Thesis the ring magnet configuration is used in the PMSGs, under study. Though axial and circumferential magnet segmentation does indeed reduce losses, but the level of segmentation required to reduce no-load loss is high, which increases cost significantly. In the actual machines individual non-segmented poles are used, but the poles may touch each other or indeed conduct through the steel hub, and hence they are similar to ring magnets. The level of rotor loss is manageable by the cooling system and the rotor temperature rise is acceptable and hence the magnets are not segmented.

In chapter 7 of this Thesis FEA is used to show that for the PM machines under study, there is no significant difference between no-load rotor loss calculated assuming ring magnets and losses calculated in a machine with separated individual poles. This is due to the fact that the wavelength of the tooth ripple harmonics is much shorter than the magnet arc length. Hence segmentation was not taken into account in the analytical or FEM calculation, which enables direct comparison between the two methods as the analytical solution of the diffusion equation in ring non-segmented magnets is exact. For instance a comparison is presented in Table 1.1 for PMSG1 (shown in chapter 3 of this Thesis) with 0, 2 and 4 magnet segments. In comparison to 0-magnet segments, the results show decrease in rotor power loss by <10% and <17% in case of 2 and 4 magnet segments, respectively.

PMSG1 with 0-Magnet Segment	PMSG1 with 2-Magnet Segments	PMSG1 with 4-Magnet Segments
127	115	106

Table 1.1. Rotor eddy current power loss comparison in PMSG1 with 0, 2 and 4 magnet segments

Van der Veen et al (1997) has presented a method to reduce rotor eddy current power loss caused by armature reaction stator mmf harmonics in a 1400kW, 6000 rpm PM generator connected to a rectifier load by using the conducting sleeve and splitting the 3-phase winding into three sets of three-phase winding i.e., 30 degrees apart. The method, however, neglects magnet flux tooth ripple harmonics and assumes resistive limited case for eddy current power loss. The method has been further developed in chapter 6 of the Thesis in terms of taking into account both magnet flux tooth ripple and stator mmf harmonics for the calculation of rotor eddy current power loss taking into account reaction of eddy currents field effect on airgap flux harmonics.

Various studies have been presented in the literature for reducing rotor eddy current power loss in PM machines using different winding and slot-pole combinations; see (Bianchi et al., 2007; Bianchi and Fornasiero, 2009; El-Refaie, 2010) and others. General guidelines are defined for selecting suitable winding configuration for a PM machine with specific slot-pole combination for reduced rotor losses.

1.5 Computational Studies

Sharkh et al (1999) investigated the effect of different current advance angles on rotor eddy current power loss in PMSG. FEA static solutions were used to calculate the amplitude of the resultant harmonics. The rotor eddy current power loss due to each harmonic was calculated using a current sheet method, taking into account the reaction of eddy currents. The results presented show an increase in rotor eddy current power loss as the current advance angle varies from an inductive to capacitive load.

Al-Naemi and Moses (2006) investigated the effects of sleeve material on rotor eddy current power loss in FEA. A comparison table for different sleeve materials with different magnetic properties and conductivities was presented. The results of this investigation may guide designers in choosing a suitable sleeve material for their machine to reduce rotor power loss.

Nakano et al (2006) calculated the effect of different slot-pole combinations on rotor eddy current power loss in concentrated wound PM machines using finite element method (FEM) analysis. The machine studied were 6 slots-8 poles, 9 slots-8 poles, 12 slots-8 poles, 9slots-10 poles, 12slots-10 poles, respectively. It is shown that the distribution of eddy currents in the conducting regions of the rotor is a strong function of armature reaction stator mmf harmonics. The eddy current rotor power loss increases even due to low order spatial harmonic component if it's asynchronous with respect to the rotor. The variation in rotor eddy current power loss caused by the distribution of eddy currents in the magnet and rotor hub region is presented for different machines. It is shown that PM machine with 6-slots- 8 poles showed higher loss in the rotor hub region compared to permanent magnet due to armature reaction stator mmf harmonics, which caused higher distribution of eddy currents in the rotor hub region. On the other hand, 12slots-8 poles machine showed negligible rotor loss compared to other slot-pole combinations under study.

Drubel and Stoll (2001) compared analytical and FE methods for the calculation of tooth ripple losses in salient pole synchronous machines taking into account stator saturation. Four methods i.e., finite difference time step method, Gibbs' method, Oberretls' method and finite element method were used for the calculation of rotor

losses. It was shown that tooth ripple losses using Oberretls' method for the particular machine showed agreement with FEA in comparison to the other two methods. This is due to the fact that this method caters for two dimensional effect, but doesn't allow for saturation. On the other hand Gibbs' method is one dimensional and gives higher losses, but caters for saturation effect in PM machines.

Belli and Mekideche (2013) investigated the effect of magnet segmentation in PM machines. It has been observed that magnet segmentation is a strong function of frequency and simply segmenting the magnets may not help in reducing the magnet loss. The optimisation technique is developed in MATLAB which aims to find the best parameters in terms of magnet span, number of segments and angular space between two adjacent magnet blocks to reduce magnet loss.

Yamazaki and Fukushima (2011) also investigated the effect of magnet segmentation on rotor eddy current power loss using 3D FEM. It was shown that magnet segmentation only reduces the rotor losses in cases where the skin depth of the magnet is larger than the wavelength of higher order harmonics, i.e., the eddy currents are resistive limited. In cases where the skin depth of the magnet is smaller than the wavelength of higher order harmonics, i.e., the inductive limited case, the rotor losses increases rather than decrease even the magnets been segmented.

To reduce computational time in 3D FEA method, hybrid methods are currently been used as discussed by Saban and Lipo (2007) and Yamazaki and Watari (2005). In these methods the amplitude of the resultant current sheet due to tooth ripple and armature reaction stator mmf harmonics is calculated analytically in 2D. The current sheet is then applied in 3D FEA to cater for end effect in rotor loss calculation.

Generally, the computational studies performed in the literature tend to be for specific machines, or presented in terms of figures of merit to enable the comparison of the relative effect of different design changes on rotor loss. A systematic study of rotor losses is presented in chapter 7 of this Thesis for a number of generic machines with different number of slots, slot opening, winding configuration, and magnet and airgap thicknesses using both analytical and FEA methods for a reasonable sized PM generator. The results are presented in a normalised fashion showing losses per unit surface area of the rotor versus s/λ and g/λ, where s, g and λ denote slot-opening,

total gap between hub and stator bore, and slot pitch, respectively. A limited computational study is also performed to investigate the effect of magnet segmentation on rotor eddy current power loss in three PMSGs connected to rectifier loads. The results re-established the fact that random magnet segmentation doesn't always result in reducing rotor eddy current power loss in PM machines.

1.6 Objective of the Thesis

The main purpose of the research presented, is the investigation of asynchronous flux harmonics and their corresponding electromagnetic rotor eddy current power loss in high-speed PM synchronous generators (PMSGs) with ring magnet configurations under no-load and on-load conditions. The main objectives of the Thesis are as follows:

1. Develop FEA models of PMSGs with ring magnet configuration for the calculation of rotor eddy current power loss;

2. Extend and develop analytical techniques in cylindrical coordinates for the calculation of rotor eddy current power loss in PMSGs taking into account the effect of reaction of eddy currents on airgap flux harmonics;

3. Calculation of no-load magnet flux tooth ripple harmonics and their corresponding rotor electromagnetic losses in PMSG using analytical and static FEA methods, and compare the results for rotor losses with those using transient FEA method;

4. Calculation of armature reaction stator mmf harmonics and their corresponding rotor electromagnetic losses in PMSG feeding a purely resistive load, using analytical and static FEA methods and compare the rotor loss results with those using transient FEA method;

5. Analytical calculation of vector (phasor) addition between magnet flux tooth ripple and armature reaction stator mmf harmonics for the calculation of resultant harmonics. Calculate rotor eddy current power loss due to these resultant harmonics taking into account reaction of eddy currents and compare

the rotor loss results with those calculated using transient FEA;

6. Calculation of rotor electromagnetic losses in PMSGs connected to rectifier loads, taking into account both magnet flux tooth ripple and armature reaction stator mmf harmonics using both analytical and transient FEA methods. Also investigating effect of splitting three-phase winding on rotor eddy current power loss in these generators.

7. Develop a normalisation technique for quick calculation of rotor eddy current power loss in PMSG due to variation in machine design parameters;

1.7 Thesis Outline

According to the objectives, the main body of the Thesis is thematically divided into three parts:

The first part, comprising chapters 2-3, provides the basis of the Thesis in terms of calculating travelling flux harmonics, their speed and direction of rotation and corresponding losses. In chapter 2 the airgap flux harmonics in PM machines caused by various mechanism e.g., stator mmf time harmonics, stator mmf space harmonics, saturation and others are discussed in both stator and rotor reference frames. Chapter 3 provides a discussion of the general methodologies for calculating the amplitudes of travelling flux harmonics and their corresponding rotor eddy current power losses using analytical and computational methods.

The second part, consisting of chapters 4-6, compares the accuracy of analytical methods with FEA for the calculation of harmonics and their respective rotor eddy current power loss in PMSGs. In chapter 4 the accuracy of three permeance methods is compared with FEA for the calculation of no-load (magnet flux tooth ripple) harmonics and respective power loss. In chapter 5, analytical calculation of on-load rotor eddy current power loss and the effects of current advance angle on these losses are performed and the results are compared with FEA. In chapter 6, the rotor eddy current power losses are calculated in PMSGs connected to a rectifier loads. The effect of splitting three phase winding is investigated and results are compared with FEA.

In the third part i.e., chapter 7, FEA parametric study is performed to develop a normalisation technique for the quick calculation of rotor eddy current power losses in variant designs of PMSG. Also the effect of; stator slotting, airgap and magnet thicknesses, different winding, slot-pole combination, rectifier topologies and magnet segmentation on rotor eddy current power loss in PMSGs has been investigated.

Chapter 8 presents the conclusions of this study and outlines related future work. Finally, the appendices include supplementary material (MAPLE and MATLAB codes).

1.8 Original Contributions

The work presented in this Thesis resulted in the development of FEA models and analytical methodologies for calculating harmonic amplitudes and their corresponding rotor eddy current power losses in PM machines. All sources of harmonics were included with the exception of rotor induced eddy currents whose effect on harmonics is assumed to be negligible. Using FEA the effect of saturation is taken into account and the level of discrepancy between analytical and computational methods is highlighted. For the case of a generator feeding a rectifier load, the losses caused by mmf time harmonics due to quasi-square current waveforms are calculated for two different winding configurations. Finally, normalization technique is developed based on systematic computational study for rotor eddy current power loss in PMSGs.

The main contributions of this Thesis are summarised below:

1.8.1 **Extending Existing Three Analytical Permeance Methods for the Calculation of No-load Rotor Eddy Current Power Loss in PMSG (Chapter 4)**

Three permeance methods by Zhu et al (1993), Gieras (2004) and Ẑarko et al (2006) are used to calculate airgap flux distribution in PMSG. The methods are extended to calculate travelling flux harmonics in the rotor reference frame. The amplitude of each harmonic and its corresponding rotor eddy current power loss, taking into account reaction of eddy currents is calculated and compared with static and transient

FEA solutions. The effect of saturation on rotor eddy current power loss is also investigated.

1.8.2 Comparison between Analytical and FEA methods for Rotor Eddy Current Power Loss in High Speed PMSG Feeding a Sinusoidal Load (Chapter 5)

The on-load rotor eddy current power loss caused by resultant harmonics (calculated using vector addition between magnet and stator mmf harmonics), taking into account the reaction of eddy currents is calculated in PMSG with ring magnet configuration. The effect of current advance angle and saturation on rotor eddy current power loss is also investigated using both Analytical and FEA methods.

1.8.3 Comparison between Analytical and FEA methods for the Calculation of Rotor Eddy Current Power Loss in High Speed PMSG Feeding Uncontrolled Rectifier Loads (Inductive and Capacitive) (Chapter 6)

The rotor electromagnetic loss is calculated in a PMSG connected to an uncontrolled bridge rectifier. Two winding and rectifier topologies were considered: a 3-phase winding with a 3-phase bridge rectifier; and a double 3-phase winding, with a 3-phase rectifier in each winding and the two rectifiers connected in series. Both tooth ripple and armature reaction flux harmonics are considered in the calculation of rotor loss; the harmonics are added vectorially.

1.8.4 Development of Normalization Technique to Approximate Rotor Eddy Current Power Loss and Investigate Effect of Magnet Segmentation in PMSGs (Chapter 7)

A systematic study is performed to investigate the effect of slotting, i.e., number of slots, slot opening, and airgap and magnet thicknesses, on rotor electromagnetic losses in surface magnet synchronous generators. The results are presented in a normalised fashion showing losses per unit surface area of the rotor versus s / λ and g / λ. The validity of this approach is investigated by comparison of losses estimated from the

normalised data with those calculated using FEA. The effect of different winding and slot-pole combination and magnet segmentation on rotor eddy current power loss is also investigated in three PMSGs connected to rectifier loads.

1.9 Summary

This chapter discussed the importance of rotor eddy current power losses in high speed PM machines. The state of the art analytical and computational methods are presented along with their limitations in the calculation of harmonic amplitudes and corresponding rotor eddy current power loss.

The importance of magnet flux tooth ripple harmonics has been highlighted. These harmonics play an important role in the calculation of rotor eddy current power loss and hence cannot be ignored in all PM machines. It has been highlighted that for accurate calculation of rotor eddy current power loss, vector addition between magnet flux tooth ripple and armature reaction stator mmf harmonics must be performed.

The accuracy of analytical solutions may be compromised by invalidation of their simplifying assumptions, it is therefore important to compare the results with FEA. The importance of the reaction of eddy current effects is highlighted in PM machines with ring magnets. The reaction of eddy currents varies the amplitude of harmonics due to all sources except rotor induced eddy currents.

Computational methods can be a good alternative to compensate for discrepancies in analytical solutions, but these methods are expensive and their solution time is still high, especially for 3D models.

1.10 Conclusions

From the literature it can be concluded that there are still gaps in the knowledge in the following areas which needs to be addressed:

1. The accuracy of analytical methods for the calculation of no-load airgap flux density distribution in PM machines needs to be compared with static FEA and

transient FEA methods in terms of calculating amplitude of harmonics and corresponding rotor eddy current power loss.

2. Magnet flux tooth ripple harmonics are generally ignored in the calculation of rotor eddy current power loss. They need to be taken into account using the vector addition between magnet flux tooth ripple and stator mmf harmonics.

3. Rotor eddy current power loss in PM machine at different current advance angles (i.e., the angle back emf *E* and current *I*), doesn't increase or decrease proportional to the ratio of the voltage or the angle between fundamental *E* and current *I*. It depends on the angle between each magnet flux tooth ripple and stator mmf harmonic, which needs to be catered for using vector addition.

4. Rotor eddy current power loss in PMSGs connected to rectifier loads is generally attributed to armature reaction stator mmf harmonic; this may not be true for all PM generators and may cause discrepancy in rotor eddy current power loss calculation unless magnet flux tooth ripple loss is taken into account.

5. Most of the computational studies performed in literature for the calculation of rotor eddy current power loss are either machine specific or results are in terms of figures of merit. These computational techniques are quiet time consuming therefore a method is required which can provide quick estimation of rotor eddy current power loss in a range of PM machines.

Chapter 2

Harmonics in PM Synchronous Machines

2.1 Introduction

This chapter presents an overview of synchronous and asynchronous rotating flux harmonics in PM synchronous machines, as a basis for discussion in the later chapters. These harmonics are the consequence of a non-sinusoidal temporal or spatial mmf variation and / or a peripherally non-sinusoidal permeance variation, for instance due to slotting. Their manifestation in the airgap flux is due to the fact that the airgap flux is the product of the mmf and permeance distribution (Bedrich Heller and Hamata, 1977; Zhu and Howe, 1993; Robinson, 1962). Asynchronous harmonics cause eddy currents to flow in the conducting materials of the rotor, i.e., the permanent magnets, sleeve (if conductive) and rotor hub. The understanding of these harmonics and their sources provides an insight into methods that can be used to reduce rotor power loss and hence reducing associated overheating problems. These harmonics can be summarized using one equation as: (stator mmf + rotor mmf) x (stator permeance + rotor permeance). The discussion in this chapter only

considers few combinations of these harmonics, and ignores the effect of three-dimensional (3D) features i.e., end effects of the PM machine.

2.2 Harmonics seen by the Stator

Harmonics in the airgap of a 3-phase symmetric PM machines seen by the stator i.e., in the stator reference frame are caused by any of the following sources (Irenji, 1998):

a. Rotor mmf
b. Rotor Saliency
c. Stator Slotting
d. Stator mmf Space Distribution
e. Stator mmf Time Variation
f. Saturation
g. Induced Eddy Currents

2.2.1 **Harmonics due to Rotor mmf**

The peripheral airgap flux distribution due to permanent magnets on the rotor is generally non-sinusoidal, but it is still periodic with spatial period of a double pole pitch as shown in Figure 2.1. Assuming the magnets are equally radial or parallel magnetized and the gap between the magnets is negligible, the flux distribution will have either odd or even harmonics depending on machine symmetry.

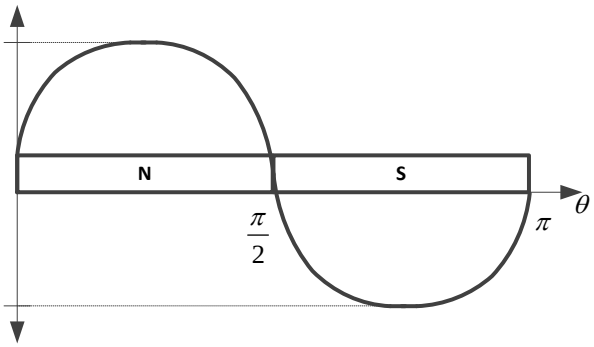

Figure 2.1. Magnet flux variation due to permanent magnets, only, i.e., rotor mmf in PMSG

For the machine having odd symmetry and the rotor rotating at synchronous speed ω in the counter clockwise (CCW) direction, the spatial angle θ in the stator reference frame is $\theta - \omega t$. Rotor position $\theta = 0$ is assumed to be the pole centreline. The harmonics due to rotor mmf that will be seen by the stator are given by:

$$F_{rs}(t,\theta) = F_1\cos(\theta-\omega t) + F_3\cos 3(\theta-\omega t) + F_5\cos 5(\theta-\omega t) + F_7\cos 7(\theta-\omega t) + \ldots \\ F_{2n+1}\cos(2n+1)(\theta-\omega t) + \ldots \quad (2.1)$$

In equation (2.1), $F_{n=1,2,3\ldots}$ represents the amplitude of the n^{th} harmonic, at an angle θ and at time *t*. The amplitude of each harmonic depends on the magnet and airgap geometry and is inversely proportional to its order. The direction of rotation of these harmonics depends on the flux distribution. For instance, in a flux distribution in equation (2.1), the 3rd, 7th and 11th … harmonics rotate in the same direction to the fundamental. . The speed of all harmonic with respect to the stator is the synchronous speed and the stator experiences each harmonic at a frequency proportional to its order.

2.2.2 **Harmonics due to Rotor Saliency**

Harmonics will also be experienced by the stator if there is any rotor saliency. Saliency is a variation in the permeance along a given path through the rotor due to a variation in the amount of magnetic material along that path as shown in Figure 2.2. Saliency can occur if the rotor has a faceted hub instead of a circular cross section hub, or if there are recesses for accommodating magnets (Dajaku and Gerling, 2010).

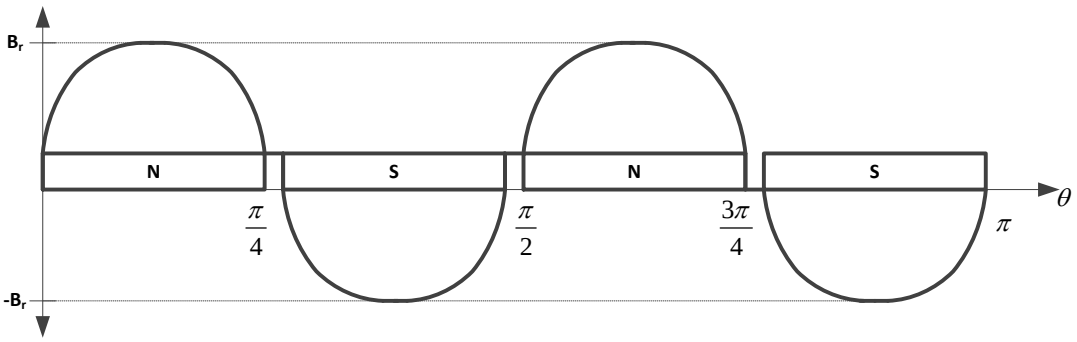

Figure 2.2. Rotor saliency due to airgap between magnet poles

Rotor permeance is a periodic function of rotor periphery, with a period of one pole-pitch, or twice or more the periodicity of the rotor mmf. The permeance function (due to rotor saliency) for the h^{th} spatial harmonic in the stator reference frame can be represented as a Fourier series of the form (Irenji, 1998):

$$P_h = P_{0h} + P_{2h}\cos 2(\theta-\omega t) + P_{4h}\cos 4(\theta-\omega t) + \ldots \quad (2.2)$$

In equation (2.2), $P_{0h}, P_{2h}, P_{4h}, \ldots$ are coefficients which can take different values for

each value of *h.* Multiplying equation (2.2) with equation (2.1) as shown in program *HRS.*mw in Appendix 1, results in a description of the flux produced due to interaction between rotor saliency and rotor mmf. After some algebraic and trigonometric manipulation, the resultant harmonics can be written in the form of $B_{ab}\cos(a\theta - b\omega t)$ as given in Table 2.1. The first figure in each pair is the spatial order, *a*, and the second element is the temporal order, *b*, for the harmonics experienced by the stator.

mmf spatial order, *q*	Permeance harmonic orders, *h*				
	0	2	4	6	8
1	(1,1)	(1,1), (3,3)	(3,3), (5,5)	(5,5), (7,7)	(7,7), (9,9)
3	(3,3)	(1,1), (5,5)	(1,1), (7,7)	(3,3), (9,9)	(5,5), (11,11)
5	(5,5)	(3,3), (7,7)	(1,1), (9,9)	(1,1), (11,11)	(3,3), (13,13)
7	(7,7)	(5,5), (9,9)	(3,3), (11,11)	(1,1), (13,13)	(1,1), (15,15)
11	(11,11)	(9,9), (13,13)	(7,7), (15,15)	(5,5), (17,17)	(3,3), (19,19)
13	(13,13)	(11,11), (13,13)	(9,9), (17,17)	(7,7), (19,19)	(5,5), (21,21)
17	(17,17)	(15,15), (19,19)	(13,13), (21,21)	(11,11), (23,23)	(9,9), (25,25)
19	(19,19)	(17,17), (21,21)	(15,15), (23,23)	(13,13), (25,25)	(11,11), (27,27)

Table 2.1. Spatial and temporal orders of harmonics produced by the interaction of rotor saliency permeance harmonics and the rotor mmf in the form of $B_{ab}\cos(a\theta - b\omega t)$. In each pair the first element is *a* and the second element is *b*; and *q* is the mmf spatial order

2.2.3 **Harmonics due to Stator Slotting**

Permeance variation due to stator slotting in a PM machine also causes harmonics in the airgap flux distribution B_r as shown in Figure 2.3. These harmonics rotate both in space and time on the surface of the rotor.

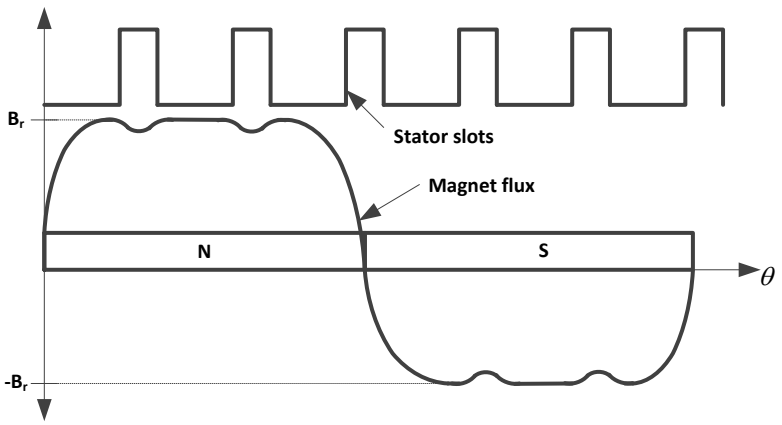

Figure 2.3. Permeance variation in the rotor mmf due to stator slotting

It is assumed here that the airgap mmf is due to magnet flux only as given in equation (2.1). Accurate estimation of these harmonics has been of interest to many authors, for example (Freeman, 1962; Gibbs, 1947; Lawrenson et al., 1966) and others.

For an integer number of slots per pole, Q_s, the Fourier series of the permeance function (due to stator slotting) for the h^{th} spatial harmonic in the stator reference frame can be written as:

$$P_h = P_{0h} + P_{2nh}\cos 2Q_s\theta + P_{4nh}\cos 4Q_s\theta + ... \tag{2.3}$$

In equation (2.3), θ is peripheral angle. In a PM machine with number of poles, p, variable θ is replaced by $p\theta$. To cater for the effect of slotting the permeance in equation (2.3) is multiplied with the rotor flux harmonics in equation (2.1) as shown in program *HSS*.mw in Appendix 1, to give:

$$\begin{aligned} F(t,\theta) = {} & P_{0h}\left(F_1\cos(\theta-\omega t) + F_3\cos 3(\theta-\omega t) + F_5\cos 5(\theta-\omega t) + ...\right) \\ & + P_{2nh}\cos 2n\theta\left(F_1\cos(\theta-\omega t) + F_3\cos 3(\theta-\omega t) + F_5\cos 5(\theta-\omega t) + ...\right) + ... \end{aligned} \tag{2.4}$$

The result of equation (2.4) can be written as a summation of terms of the form $B_a\cos(a\theta - q\omega t)$. For a machine with three slots per pole the parameter a, which is a function of q and h is shown in the Table 2.2. The temporal order is equal to the mmf order q.

mmf order, q	Permeance harmonic orders, h					
	0	6	12	18	24	30
1	1	-5, 7	-11, 13	-17, 19	-23, 25	-29, 31
3	3	-3, 9	-9, 15	-15, 21	-21, 27	-27, 33
5	-5	-1, 11	-7, 17	-13, 23	-19, 29	-25, 35
7	7	1, 13	-5, 19	-11, 25	-17, 31	-23, 37
11	-11	5, 17	-1, 23	-7, 29	-13, 35	19, 41
13	13	7, 19	1, 25	-5, 31	-11, 37	-17, 43
17	-17	11, 23	5, 29	-1, 35	-7, 41	-13, 47
19	19	13, 25	7, 31	1, 37	-5, 43	-11, 49

Table 2.2. Spatial orders of harmonics produced by the interaction of stator saliency and rotor mmf, for a machine with 3 slots per pole. Fundamental wavelength is a double pole-pitch. Negative sign indicates CW rotating harmonics

It is interesting to see from Table 2.2 that some mmf spatial harmonics of a high order, e.g., 11, interact with a high permeance harmonic order, e.g., 12, to produce a

harmonic with a fundamental space order of 1. Other mmf spatial harmonics of a high order interact with permeance harmonics to produce a resultant with a lower spatial order; for example q = 13 and h = 6 produces a harmonic of order 7.

2.2.4 **Harmonics due to Stator mmf Space Distribution**

The spatial distribution of three-phase windings in the stator slots will also cause rotating flux harmonics on the surface of the rotor. Commonly, full pitch, fractional pitch, and concentrated winding distributions are used in PM machines. For a symmetrical three phase and two pole stator winding, the non-sinusoidal mmf spatial distribution can be written in the form of a Fourier series as:

$$\begin{aligned} F_{ss}(t,\theta) &= F_1\cos(\omega t-\theta)+F_5\cos(\omega t+5\theta)+F_7\cos(\omega t-7\theta)+... \\ &\quad +F_{6n\mp1}\left(\omega t\pm(6n\mp1)\theta\right)+... \end{aligned} \tag{2.5}$$

In equation (2.5), n is an integer. The airgap mmf is assumed to be due to the stator mmf only and of fundamental time order. The mmf harmonics with even order are absent in the stator reference frame, due to the symmetrical spatial distribution of the stator windings. The harmonics of the order 3 and its multiples do not produce a resultant mmf for a three phase winding distribution, with each phase 120^0 apart, as their fields cancel out. The leakage fields may produce triplen harmonics but they are neglected.

Stator mmf spatial distribution harmonics in the stator reference frame are sinusoidal in space and time with a spatial order of $(6n\mp1)$. For a PM machine, all harmonics rotate with the speed of -1/ (6n-1) or +1/ (6n+1) times the synchronous speed. These harmonics are experienced by the stator at an angular frequency ω, and will produce flux harmonics with amplitude proportional to stator mmf for an ideal case of uniform permeance. The interaction between stator mmf space distribution harmonics in equation (2.5) and the stator slotting permeance function in equation (2.3) as shown in program *HMS*.mw in Appendix 1, can be written as:

$$\begin{aligned} F(t,\theta) = {} & P_{0h}\left(F_1\cos(\omega t-\theta)+F_5\cos(\omega t+5\theta)+F_7\cos(\omega t-7\theta)+...\right) \\ & P_{2nh}\cos 2n\theta\left(F_1\cos(\omega t-\theta)+F_5\cos(\omega t+5\theta)+F_7\cos(\omega t-7\theta)+...\right) \\ & P_{4nh}\cos 4n\theta\left(F_1\cos(\omega t-\theta)+F_5\cos(\omega t+5\theta)+F_7\cos(\omega t-7\theta)+...\right)+... \end{aligned} \quad (2.6)$$

This can be given as a summation of single cosine term, i.e., $B_a\cos(\omega t+a\theta)$. Table 2.3 shows the spatial order *a* and direction of rotation for some harmonics in a PM machine with three slots per pole.

mmf spatial order, *q*	Permeance harmonics orders, *h*						
	0	6	12	18	24	30	36
1	1	-5, 7	-11, 13	-17, 19	-23, 25	-29, 31	-35, 37
5	-5	-11, 1	-17, 7	-23, 13	-29, 19	-35, 25	-41, 31
7	7	1, 13	-5, 19	-11, 25	-17, 31	-23, 37	-29, 43
11	-11	-17, -5	-23, 1	-29, 7	-35, 13	-41, 19	-47, 25
13	13	7, 19	1, 25	-5, 31	-11, 37	-17, 43	-23, 49
17	-17	-23, -11	-29, -5	-35, 1	-41, 7	-47, 13	-53, 19
19	19	13, 25	7, 31	1, 37	-5, 43	-11, 49	-17, 55

Table 2.3. Spatial orders of harmonics produced by the interaction between permeance due to stator slot and the stator mmf space harmonics, for a machine with 3 slots per pole. Negative sign indicates CW rotating harmonics

The amplitudes of the harmonics in Table 2.3 can be calculated using winding distribution equations as derived in (McPherson, 1981):

$$F_{qk} = \frac{3}{2}\frac{4}{\pi}\frac{N_{ph}}{p}\frac{1}{q}K_{wq}\sqrt{2}I_k \quad (2.7)$$

In equation (2.7), *p* is the number of machine poles, *q* is the harmonic order, K_{wq} is the winding distribution factor and I_k is the root mean square (rms) value of stator current. The winding distribution factor K_{wq} is defined as the ratio of flux linked by a given winding distribution to the flux that would have been linked by a single layer, full pitch, non-skewed integral slot winding with the same number of turns and with single slot per pole per phase (Bakshi and Bakshi, 2009). The winding factor K_{wq} can be broken down as:

$$K_{wq} = K_{dq}K_{pq}K_{sq} \quad (2.8)$$

In equation (2.8), K_{dq}, K_{pq}, and K_{sq} are the distribution, pitch and skew factors of the harmonic order *q*. The distribution factor K_{dq} is defined as the ratio of the resultant electro-motive force (emf) when coils are distributed to the resultant emf when coils are concentrated. It is always less than one.

$$K_{dq} = \frac{E_a(\text{distributed coils})}{E_a(\text{concentrated coils})}$$

$$K_{dq} = \frac{\sin\left(\frac{m\beta' pq}{2}\right)}{m\sin\left(\frac{\beta' pq}{2}\right)} \tag{2.9}$$

In equation (2.9), m and β' are the number of slots per pole per phase and slot pitch angle, respectively.

The pitch factor or coil span factor K_{pq} is defined as the ratio of the resultant emf when coils are short pitched to the resultant emf when coils are full pitched. It is also always less than one.

$$K_{pq} = \frac{E_a(\text{short pitched coils})}{E_a(\text{fully pitched coils})}$$

$$K_{pq} = \sin\left(q\delta'\frac{\pi}{2}\right) \tag{2.10}$$

In equation (2.10), δ' is the ratio of short-chorded to full-chorded coil pitch.

The skew factor K_{sq} caters for the angularly twisted winding in the PM machine, which results in an angular spread and reduced emf as given by:

$$K_{sq} = \frac{E_a(\text{skewed coils})}{E_a(\text{un-skewed coils})}$$

$$K_{sq} = \frac{\sin\left(\frac{q\alpha'}{2}\right)}{\frac{q\alpha'}{2}} \tag{2.11}$$

In equation (2.11), α' is the stator slot skew angle in radians.

2.2.5 **Harmonics due to Stator mmf Time Variation**

Time harmonics may be introduced by static converters used to drive the machine or by the rectifier bridge in cases when the machine is connected as a generator. In these cases the stator mmf may contain 1st, 5th, 7th ..… time harmonics. The sources could also contain 3rd harmonics (triplen harmonics), but 3rd (triplen) harmonics cancels out when calculating net flux. For the fundamental spatial component, the stator mmf can be written as a Fourier series of temporal components, given by:

$$F_{st}(t,\theta) = F_1 \cos(\omega t - \theta) + F_5 \cos(5\omega t + \theta) + F_7 \cos(7\omega t - \theta) + \ldots \quad (2.12)$$

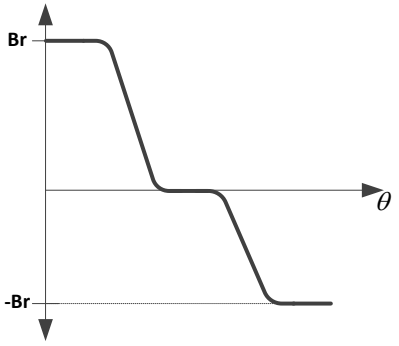

Figure 2.4. Magnet flux density variation due to stator mmf only

Due to winding symmetry, even temporal harmonics also cannot exist in this series. Harmonics due to stator mmf time variation rotate at a higher speed than the synchronous speed. The 7th, 13th, 19th… harmonic orders rotate in the same direction as the fundamental wave, whereas the 5th, 11th, 17th … harmonic orders rotate in the opposite direction to the fundamental.

Generally, harmonics due to both the spatial distribution of windings and time harmonics in the stator current exist alongside one another, and need to be analysed simultaneously (Langsddorf, 1955). This can be catered for using the general equation derived by Langsddorf (1955), which can be written as:

$$F_{st}(t,\theta) = \sum_{q=1}^{\infty}\sum_{k=1}^{\infty} F_{qk}\left(R\cdot\sin\left(P-(q+k)\frac{2\pi}{3}\right)+S\cdot\sin\left(Q-(q-k)\frac{2\pi}{3}\right)\right) \quad (2.13)$$

In equation (2.13), *P,Q,R* and *S* are given as:

$$P = k(\omega t - \xi) - q(\theta - \delta''') \quad (2.14)$$

$$Q = k\left(\omega t - \xi\right) + q\left(\theta - \delta'''\right) \tag{2.15}$$

$$R = \frac{\sin\left(q+k\right)\pi}{\sin\left(q+k\right)\frac{\pi}{3}} \tag{2.16}$$

$$S = \frac{\sin\left(q-k\right)\pi}{\sin\left(q-k\right)\frac{\pi}{3}} \tag{2.17}$$

The amplitude of these harmonics, with space order of q and time order of k, F_{qk} can be calculated using equation (2.7). In equations (2.14) and (2.15), δ''' defines the position of the phase belt of the phase 1 winding with respect to the arbitrary specified axis, and ξ is an arbitrary time-phase angle. It is apparent from equations (2.14) and (2.15) that the speed and direction of each harmonic depends on its space order q and time order k. In following Table 2.4, where all speeds are expressed as multiples of synchronous speed, denoted by +1. A similar Table can be found in (Langsddorf, 1955).

Spatial order, q	Temporal order, k						
	1	5	7	11	13	17	19
1	+1	-5	+7	-11	+13	-17	+19
5	-1/5	+5/5	-7/5	+11/5	-13/5	+17/5	-19/5
7	+1/7	-5/7	+7/7	-11/7	+13/7	-17/7	+19/7
11	-1/11	+5/11	-7/11	+11/11	-13/11	+17/11	-19/11
13	+1/13	-5/13	+7/13	-11/13	+13/13	-17/13	+19/13

Table 2.4. Speed and directions of rotation of components of stator mmf of three phase winding

A positive sign indicates harmonics that rotate in the same direction as the fundamental, whereas negative signs denote backward rotating harmonics, each with a speed of k/q. The wavelengths of these harmonics depend on their space order, and are proportional to $1/q$ times the double pole pitch.

2.2.6 **Harmonics due to Saturation**

Saturation in a PM machine produces a reduction in the effective inductance due to the reduced permeability of saturated areas. These areas commonly include the stator teeth,

stator core and rotor hub. The direction and intensity of the saturation depend on the angle and magnitude of the magnetising field in the airgap. Since the airgap flux is repeated every pole pitch, saturation harmonics are odd harmonics and cause increase in the amplitude of airgap flux harmonics (Binns and Schmid, 1975).

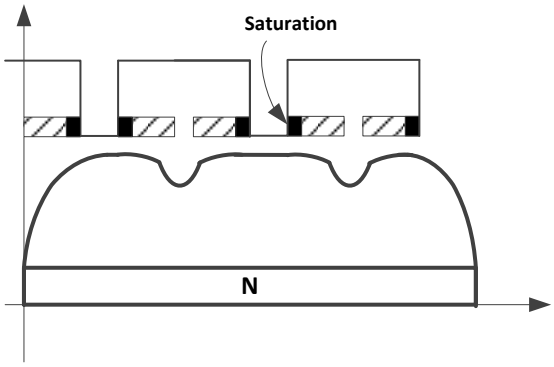

Figure 2.5. Virtual increase in stator slot opening due to saturation in the stator tooth tips

2.2.7 **Harmonics due to Induced Eddy Currents**

Asynchronous airgap flux harmonics will induce eddy currents in the conductive materials of the PM machine. In addition to the previously mentioned harmonics, the reaction of eddy currents field will themselves induce extra harmonics in the stator and rotor. The frequencies and space orders of the previous mentioned harmonics may coincide with those due to eddy currents. This interaction makes it difficult to distinguish between both harmonics in terms of their effect in PM machines (Binns and Schmid, 1975).

2.3 Harmonics seen by the Rotor

The method for calculating harmonics seen by the rotor is similar to that for those seen by the stator. But since the rotor moves at synchronous speed, the asynchronous rotating harmonics seen by the rotor are different to those seen by the stator. Harmonics in the airgap as seen in the rotor reference frame are caused by the same mechanisms as those in the stator reference frame.

2.3.1 **Harmonics due to Stator mmf Time Variation**

The variation of the three phase stator current in time causes flux waves that produce harmonics on the surface of the rotor. These mmf harmonics are experienced as fast, rotating waves by the rotor. Assuming the rotor is rotating at synchronous speed (in the steady state), then any point designated by θ in the stator reference frame is transformed to $\theta+\omega t$ in rotor frame. Therefore the stator time harmonics indicated in equation (2.12) are seen by the rotor as follows:

$$\begin{aligned} F_{sr}(t,\theta) = {} & F_1\cos\theta + F_2\cos(3\omega t+\theta) + F_4\cos(3\omega t-\theta) + \\ & F_5\cos(6\omega t+\theta) + F_7\cos(6\omega t-\theta) + F_8\cos(9\omega t+\theta) + \\ & \ldots + F_{3n\mp1}\cos(3n\omega t \mp \theta) + \ldots \end{aligned} \qquad (2.18)$$

Equation (2.18) shows the general form, including triplen harmonics. Harmonics of a spatial order of three and its multiples are absent due to the symmetry of the three phase currents in the windings, which are equally spaced by 120^0. The rotation of these harmonics depend on their time order. Harmonics of time order $k=3m-1$ (m =1,2,3..) rotates CW (with respect to rotor) with a speed of 3m times the synchronous speed while harmonics of time order $k=3m+1$ rotate CCW (with respect to rotor) with a speed of 3m times the synchronous speed.

2.3.2 **Harmonics due to Stator mmf Space distribution**

The spatial distribution of the three-phase windings also causes harmonics that produce flux waves on the surface of the rotor. These harmonics again do not include triplen harmonics due to the symmetric three phase winding distribution. The harmonics can be deduced in the rotor reference frame from equation (2.5), with θ in the stator reference frame transformed to $\theta+\omega t$ as:

$$\begin{aligned} F_{sr}(t,\theta) = {} & F_1\cos(\omega t+\theta) + F_5\cos(6\omega t+5\theta) + F_7\cos(6\omega t+7\theta) + \ldots \\ & F_{6n\mp1}\left(6n\omega t + (6n\mp1)\theta\right) + \ldots \end{aligned} \qquad (2.19)$$

From equation (2.19) it can be seen that the fundamental component is stationary with respect to the rotor, while all the harmonics are rotating waves. The speed of these

harmonics rotating at $\frac{\omega}{6n+1}$ and $-\frac{\omega}{6n+1}$ as seen by the rotor, can be written as:

$$\omega - \frac{\omega}{6n+1} = \frac{6n}{6n+1}\omega \tag{2.20}$$

and

$$\omega + \frac{\omega}{6n-1} = \frac{6n}{6n-1}\omega \tag{2.21}$$

The number of poles of these harmonics are $6n+1$ and $6n$-1, respectively and the time frequency of the field quantities induced in the rotor will be of order $6n\omega$. The wavelength of these harmonics at the rotor will be equal to $2T/(6n+1)$, where T is the rotor pole-pitch.

2.3.3 **Harmonics due to Rotor mmf**

The peripheral distribution of permanent magnet flux in the PM machine is non-sinusoidal but periodic. This produces only odd harmonics of flux density on the surface of the rotor. These harmonics rotate at the same speed as rotor and are stationary to the rotor. The spatial wavelength of these harmonics is inversely proportional to the harmonic order. The distribution of these harmonics is given as:

$$F_{rr}(r,\theta) = F_1\cos\theta + F_3\cos 3\theta + F_5\cos 5\theta + F_7\cos 7\theta + ... + F_{2n+1}\cos(2n+1)\theta \tag{2.22}$$

The harmonics in equation (2.22) don't produce rotor eddy currents but are presented here for generality.

2.3.4 **Harmonics due to Rotor Saliency**

The permeance function for the h^{th} spatial harmonic in the rotor reference frame can be represented as a Fourier series of the form:

$$P_h = P_{0h} + P_{2h}\cos 2\theta + P_{4h}\cos 4\theta + ... \tag{2.23}$$

The interaction between stator mmf spatial harmonics in equation (2.19) and rotor saliency in equation (2.23) can be catered for by multiplying these equations as shown

in program *HMSR*.mw in Appendix 1. The result can be written as a summation of cosine terms of the form $B_{ak}\cos(a\theta + k\omega t)$, for a machine with three stator slots per pole and one rotor saliency per pole. For some harmonics the spatial order *a* is given in Table 2.5 as:

Temporal order, *k*	Spatial order, *q*	Permeance harmonic orders, *h*						
		0	2	4	6	8	10	12
0	1	1	3, 1	5, 3	7, 5	9, 7	11, 9	13, 11
6	5	-5	-7, -3	-9, -1	-11, 1	-13, 3	-15, 5	-17, 7
	7	-7	-9, -5	-11, -3	-13, -1	-15,1	-17, 3	-19, 5
12	11	-11	-13, -9	-15, -7	-17, -5	-19,-3	-21, -1	-23, 1
	13	-13	-15, -11	-17, -9	-19, -7	-21,-5	-23, -3	-25, 1
18	17	-17	-19, -15	-21, -13	-23, -11	-25,-9	-27, -7	-29, -5
	19	-19	-21, -17	-23, -15	-25, -13	-27,-11	-29, -9	-31, -7

Table 2.5. Spatial order of harmonics produced by the interaction of rotor saliency and the stator mmf space harmonics, for a machine with 3 slots per pole. Negative sign indicates CW rotating harmonics

The interaction between stator mmf time harmonics in equation (2.18) and rotor saliency in equation (2.23) is similarly catered for by multiplying the two equations as shown in program *HMTR*.mw in Appendix 1.The result can be written as a summation of terms of the form $B_{ab}\cos(a\theta + b\omega t)$. Parameters *a* and *b* are given in Table 2.6 for harmonics with a stator temporal order *k* and permeance harmonic order *h*.

Temporal order, *k*	Permeance harmonic orders, *h*				
	0	2	4	6	8
1	(1,0)	(1,0), (3,0)	(3,0), (5,0)	(5,0), (7,0)	(7,0), (9,0)
2	(1,3)	(1,-3), (3,3)	(3,-3), (5,3)	(5,-3), (7,3)	(7,-3), (9,3)
4	(1,-3)	(1,3), (3,-3)	(3,3), (5,-3)	(5,3), (7,-3)	(7,3), (9,-3)
5	(1,6)	(1,-6), (3,6)	(3,-6), (5,6)	(5,-6), (7,6)	(7,-6), (9,6)
7	(1,-6)	(1,6), (3,-6)	(3,6), (5,-6)	(5,6), (7,-6)	(7,6), (9,-6)
8	(1,9)	(1,-9), (3,9)	(3,-9), (5,9)	(5,-9), (7,9)	(7,-9), (9,9)
10	(1,-9)	(1,9), (3,-9)	(3,9), (5,-9)	(5,9), (7,-9)	(7,9), (9,-9)
11	(1,12)	(1,-12), (3,12)	(3,-12), (5,12)	(5,-12), (7,12)	(7,-12), (9,12)
13	(1,12)	(1,12), (3,-12)	(3,12), (5,-12)	(5,12), (7,-12)	(7,12), (9,-12)

Table 2.6. Spatial and temporal orders of harmonics produced by the interaction of rotor saliency and the stator mmf time variation harmonics, for a machine with 3 slots per pole. Negative sign indicates CW rotating harmonics

2.3.5 **Harmonics due to Stator Slotting**

Stator slotting in a PM machine causes a variation in the rotor mmf as it passes over a tooth or a slot. The amount of flux increases from its average value under the tooth and decreases from its average value under the slot. Each point on the rotor, regardless of its position under either an N-pole or an S-pole, experiences this periodic variation, which is known as tooth ripple.

To calculate tooth ripple harmonics the airgap is assumed to be uniform, i.e., rotor saliency is ignored. The permeance function for the h^{th} spatial harmonic in equation (2.3) can then be written in the rotor reference frame by substituting θ with $\theta+\omega t$ as:

$$P_h = P_{0h} + P_{2nh}\cos 2n\left(\theta+\omega t\right) + P_{4nh}\cos 4n\left(\theta+\omega t\right)+... \tag{2.24}$$

Multiplying the rotor mmf in equation (2.22) with the permeance distribution in equation (2.24) as shown in program *HST*.mw in Appendix 1, results in:

$$\begin{aligned} F\left(t,\theta\right) = {} & P_{0h}\left(F_1\cos\theta + F_3\cos 3\theta + F_5\cos 5\theta +...\right) \\ & + P_{2nh}\cos 2n\left(\theta+\omega t\right)\left(F_1\cos\theta + F_3\cos 3\theta + F_5\cos 5\theta +...\right) \\ & + P_{4nh}\cos\left(\theta+\omega t\right)\left(F_1\cos\theta + F_3\cos 3\theta + F_5\cos 5\theta +...\right)+... \end{aligned} \tag{2.25}$$

Equation (2.25) can be written in the form of summation of single cosine terms, $B_{ab}\cos\left(a\theta+b\omega t\right)$ for machine with three slots per pole. For some harmonics the parameter *a* is given in Table 2.7.

Spatial order, *q*	Permeance harmonic orders, *b*						
	0	6	12	18	24	30	36
1	1	7, 5	13, 11	19, 17	25, 23	31, 29	37, 35
3	3	9, 3	15, 9	21, 15	27, 21	33, 27	39, 33
5	5	11, 1	17, 7	23, 13	29, 19	35, 25	41, 31
7	7	13, -1	19, 5	25, 11	31, 17	37, 23	43, 29
9	9	15, -3	21, 3	27, 9	33, 15	39, 21	45, 27
11	11	17, -5	23, 1	29, 7	35, 13	41, 19	47, 25
13	13	19, -7	25, -1	31, 5	37, 11	43, 17	49, 23

Table 2.7. Spatial order of harmonics produced by the interaction of stator saliency and the rotor mmf harmonics, for a machine with 3 slots per pole. Negative sign indicates CW rotating harmonics

Due to symmetry in the rotor mmf, the harmonics present in the tooth ripple have a spatial order that is always an odd number, with the fundamental wavelength equal to one double pole pitch.

2.3.6 **Harmonics due to Saturation**

As discussed in section (2.2.6), all harmonics flux waves due to saturation rotate at the same speed and in the same direction as the fundamental harmonic with respect to the stator. The harmonics due to saturation in the stator structure will be stationary in the rotor frame. But the saturation causes decrease in the magnetic circuit of PM machine resulting in increase of the amplitude of other harmonics.

2.3.7 **Harmonics due to Induced eddy currents**

As discussed in section (2.2.7), the harmonic fluxes associated with the combined mmfs of stator and rotor will induce eddy currents in the magnets. These eddy currents will produce mmf harmonics themselves that may vary the amplitude of the direct harmonics from stator and rotor sources.

2.4 Interaction between Harmonics

From an mmf point of view the harmonics in a PM machine are caused by two main sources, viz. rotor permanent magnets and three phase stator currents in the winding. The harmonics due to each mmf source cause rotor eddy current power loss. In the case of a PM machine operating such that the mmf is due to just one of these sources, the total rotor power loss can be calculated by the summation of the individual power losses due to each harmonic produced by that source.

In the case that the mmf in the PM machine is due to both rotor and stator mmfs, the harmonics induced will be the resultant of the interaction between harmonics from both sources. The common harmonics of both rotor mmf and armature reaction flux cannot be simply added algebraically. The two harmonics must be treated as vectors and the phase difference between each pair must be accounted for as discussed by Oberretl (1972) and Wu et al (2012a). Proof of this will be shown in chapter 5. In

certain PM machines the resultant harmonic may not be remarkably different from the armature reaction flux harmonic; this may be due to the small tooth ripple harmonic component.

One of the strong points of the analytical methods in this Thesis is that the resultant flux harmonics are calculated, which caters for the interaction between different harmonics from each mmf source, as will be discussed in chapters 5 and 6.

Chapter 3

Methodology for Calculating Rotor Eddy Current Power in PMSG

3.1 Introduction

Both analytical and FEA methods are used for the calculation of rotor eddy current power loss in PM machines in this chapter. The methodology is first described for the calculation of rotor eddy current power loss in PM machine using transient FEA solution in Maxwell 2D (Ansoft, 2006). Then the methodology is presented for the calculation of harmonic amplitudes using static FEA method. Following this, the procedure is described for the analytical calculation of rotor eddy current power loss due to asynchronous harmonics taking into account reaction of eddy currents in PM machine using cylindrical current sheet model.

Though the methodologies are general in nature, the focus in this chapter will be on three particular PM synchronous generator designs i.e., PMSG1, PMSG2 and PMSG3 shown in Figures 3.2, 3.3 and 3.4, respectively. The machines have arc-shaped ring magnets, 4-poles, maximum speed of 90000 revs/min and a slot opening of 3mm and 4mm, respectively. The stator in the machine is laminated, but the rotor is made of solid steel (necessary for sufficient strength). A non-conducting carbon fibre sleeve, the magnetic properties of which are assumed to be similar to those of air, is used to

hold the magnets. The generators' dimensions and properties of materials are shown in Table. 3.1, while Figure 3.1 shows the linear BH curve for the stator material.

Parameters	3-phase PMSGs
Number of poles, $2p$	4
Number of slots, Q_s	12 or 24 or 6
Number of winding layers	1 or 2
Number of turns per coil, N_c	1 or 2
Number of parallel paths	1
Coil pitch to pole pitch ratio	0.66 or 1
pole-arc to pole-pitch ratio, α_p	1
Core length, L	125 mm
Stator outer radius, R_4	53.5 mm
Stator bore radius, R_3	31 mm
Magnet outer radius, R_2	27.1 mm
Rotor hub radius, R_1	21.6 mm
Magnet thickness, h_m	5.5 mm
Stator back of core, R_{bc}	13.5 mm
Sleeve thickness, t_{sleeve}	2 mm
Tooth pitch, τ_t	16.23 mm or 8.11mm or 32.46mm
Airgap, g	1.9 mm
Tooth width, τ_w	6.5 mm or 3.25mm or 13mm
Slot opening, b_0	3 mm or 4mm
Tooth tip thickness, t_{tip}	1 mm
Rotor hub permeability , μ_r	750
Rotor hub conductivity, σ_r	6.7×10^6 S/m
Magnet conductivity, σ_m	0.77×10^6 S/m
Magnet material	NdFeB
Magnet Remanence, B_r	1.12T
Magnet Coercivity, H_c	781 kA/m
Stator core	Sura NO20, 0.2mm thick
Stator core permeability, μ_r	5000 (linear), BH curve (non-linear)
Stator core conductivity, σ_s	0

Table 3.1. Design specification of PMSG1PMSG2 and PMSG3. Dimensions are in mm, conductivity in S/m

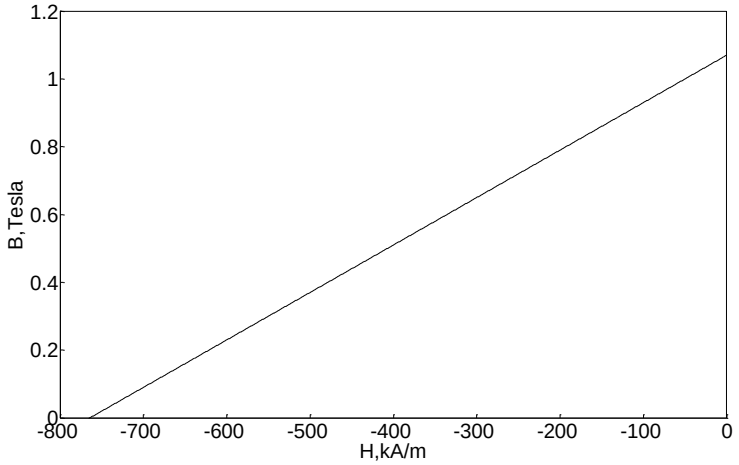

Figure 3.1. Magnet characteristic

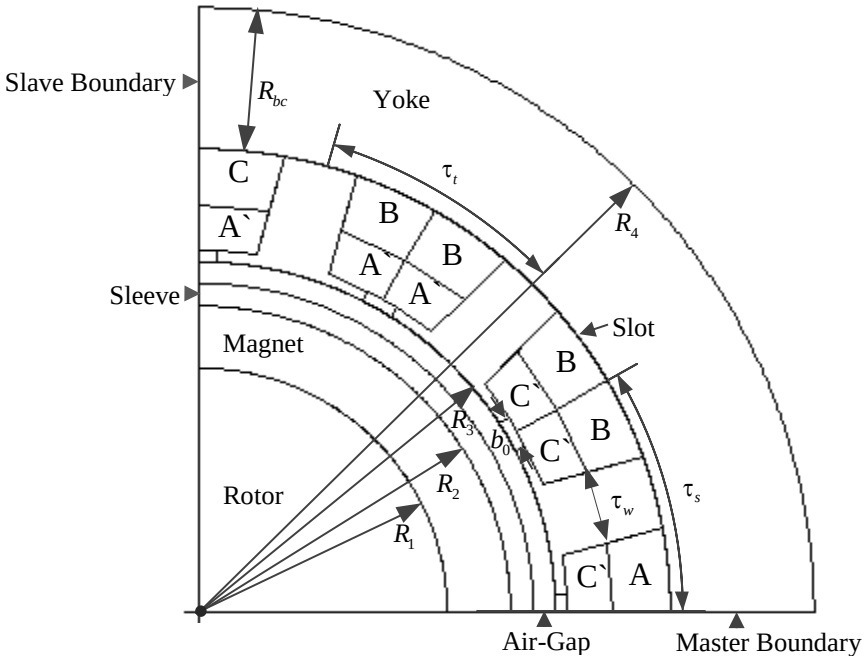

Figure 3.2. Quarter model of permanent magnet generator (PMSG1) under study

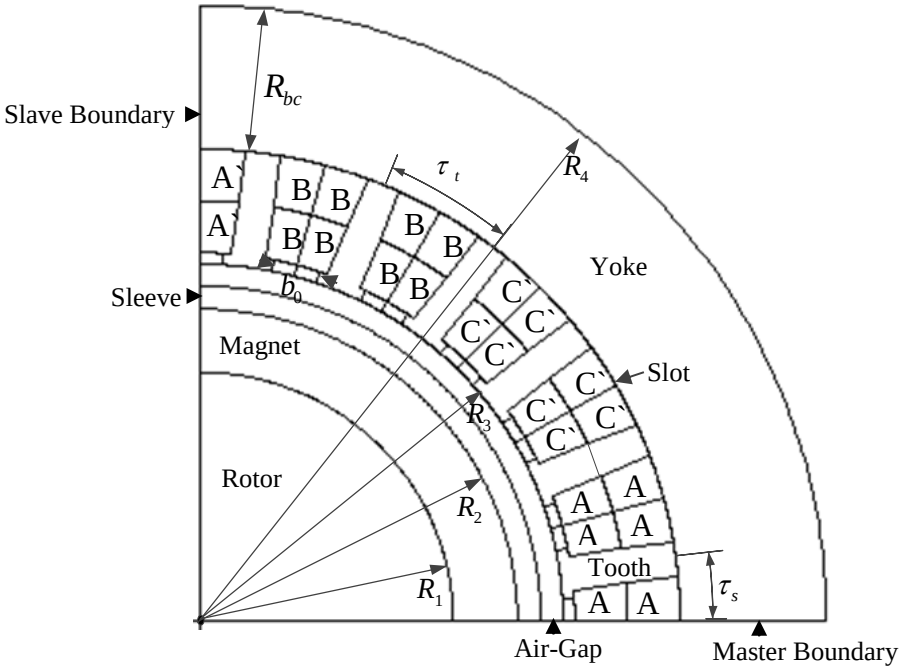

Figure 3.3. Quarter model of permanent magnet generator (PMSG2) under study

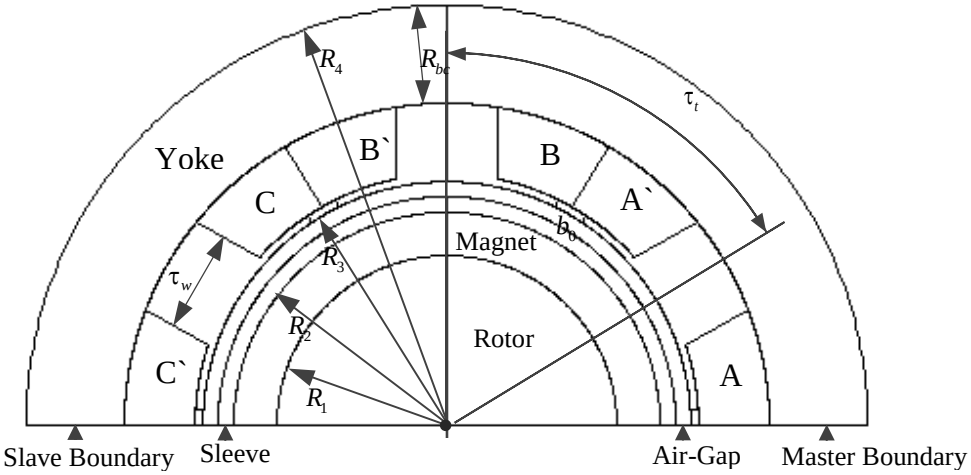

Figure 3.4. Half model of permanent magnet synchronous generator (PMSG3) under study

3.2 Transient FEA Method

Maxwell 2D is an FEA software package by ANSYS, that can be used as a tool in the design of electromagnetic devices. The software uses the finite element method to solve partial differential equations that may not be solved accurately using analytical methods. This section explains the pre-processing and post-processing stages in transient FEA solution for the calculation of rotor eddy current power loss in PM machine models with a moving rotor.

3.2.1 **Pre-processing**

In the pre-processing stage of transient FEA method following steps are performed:

3.2.1.1 Machine model

The geometry of the PMSGs shown in Figures 3.2, 3.3 and 3.4 are drawn in a 2D plane whose co-ordinates can be entered in Cylindrical or Cartesian systems such that whole geometry should fit in a defined region. The geometry is drawn as a set of polygonal regions such that the regions do not overlap. The sides of each region are composed of a number of segments. High numbers of segments result in a smoother geometry and hence more accurate results. The background region is excluded in the solution process.

Constraints can be used to edit two-dimensional PM machine models without redrawing. These are sets of user defined functions that describe the machine

geometry such that changing one parameter in the model results in the adjustment of all other parameters accordingly. For instance, if the magnet thickness is increased, the airgap length may be adjusted to keep the airgap flux density constant without changing the whole geometry.

Material characteristics are defined for the linear and non-linear magnetic components. An external circuit schematic is used to define the three phase stator current in the windings. In case of low saturation in the back of the core, the vector potential A on the external boundary of the stator core is set to zero, ensuring no flux leakage out of the stator surface. This is equivalent to making the normal component of airgap flux density B_n equal to zero on the outer stator boundary. Depending on the slot / pole combination, master and slave boundary conditions (BC) can be used to take advantage of the periodicity of the machine. For one quarter of PMSGs shown in Figures 3.2, 3.3 and half model of PMSG shown in Figure3.3, two planes can be defined: the master plane and the slave plane. For PMSGs in Figures 3.2 and 3.3, the H-field at every point on the slave surface is equal to minus the H-field at every point on the master surface. For PMSG3 in Figure 3.3 the H-field at every point on the slave surface is equal to positive the H-field at every point on the master surface.

3.2.1.2 Transient FEA Solution

Finite element discretisation forms the basis of the methods used in Maxwell 2D. Before the analysis, parameters need to be set for the convergence tolerance, output points, non-linear iteration type, mesh and time step.

3.2.1.2.1 Mesh

Mesh formation is an essential step in obtaining an accurate transient FEA solution for PM machine models. The mesh consists of a set of discretised elements and the accuracy of the solution depends on the size and shape of those elements. The calculation errors will be low if the size of the element is very small (fine mesh) and the shape of the triangles are close to equilateral. The requirement for a fine mesh

may not be possible or practical, in many cases, due to the complicated shape of the PM machine and computer memory limitation.

The resolution of the mesh in each region of the model is determined according to the skin depth δ'', which is calculated for each region as below:

$$\delta'' = \sqrt{\frac{2}{\sigma\omega\mu}} \tag{3.1}$$

In equation (3.1), ω represents the angular frequency of the harmonic, μ is the permeability of the region, and σ is its conductivity.

An example of a mesh in PMSG1 is shown in Figure 3.5. It is pertinent to mention that it has not been possible to achieve the required level of mesh resolution given by equation (3.1), especially in conducting layer of rotor. This may effect on the accuracy of the calculation of rotor eddy current power loss. The calculation of skin depth for conducting regions in PMSG1 including rotor hub, magnet, teeth and stator yoke is presented in Table. 3.2, for which the required parameters are listed in Table 3.1.

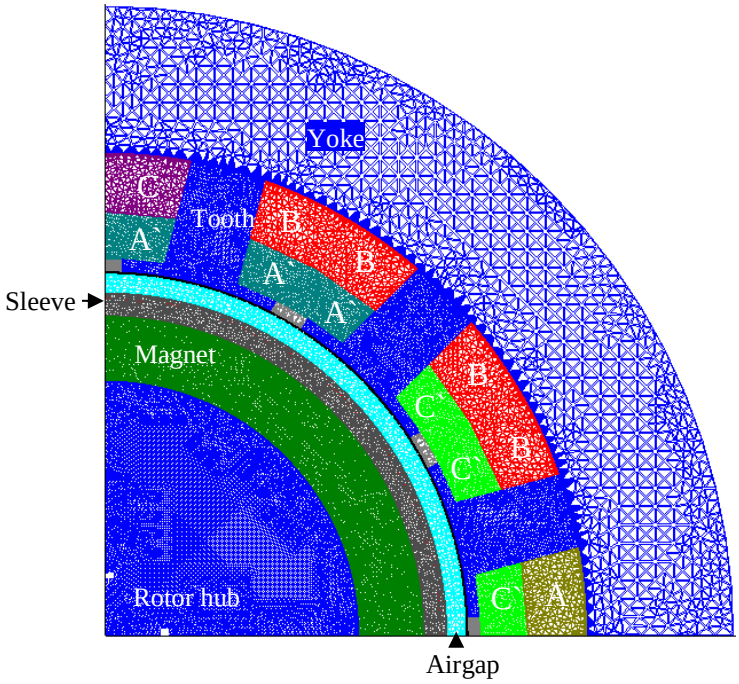

Figure 3.5 A typical mesh of PMSG1

Conducting Regions	Number of Elements	Number of Elements per skin depth @ 3000 Hz	Skin depth δ (m) @ Frequency *f*(Hz)			
			3000	15000	21000	33000
Rotor hub	8000	<1	1.29e-4	5.7e-5	4.8e-5	3.9e-5
Magnet	10000	<1	10e-3	4.5e-3	3.8e-3	3e-3
Stator yoke	8000	60	0.129	0.058	0.049	0.039
Teeth	5000	40	0.129	0.058	0.049	0.039

Table 3.2. Skin depth dependence on frequency

Table 3.2 shows decrease in the value of skin depth with increasing harmonic frequency in each conducting region. For accuracy, three elements per skin depth are required to capture eddy currents in each region. The required values of skin depth (according to equation 3.1) in the regions of interest (i.e., rotor hub and permanent magnet to capture eddy currents) are very small at high harmonic frequencies, requiring mesh resolutions that are not possible in these regions. Table 3.2 also shows the maximum achievable number of elements and number of elements per skin depth layers used in Maxwell 2D for the formation of mesh in PMSG1 is also shown in Tables 3.2. The discrepancy in calculated power loss due to number of mesh elements is shown in Figure 3.6. The result will be more accurate with higher number of elements. This is due to the fact; interpolation is used to calculate field quantities e.g. vector potential *A* between each element. The higher number mesh elements will result in accurate calculation of vector potential *A* between points.

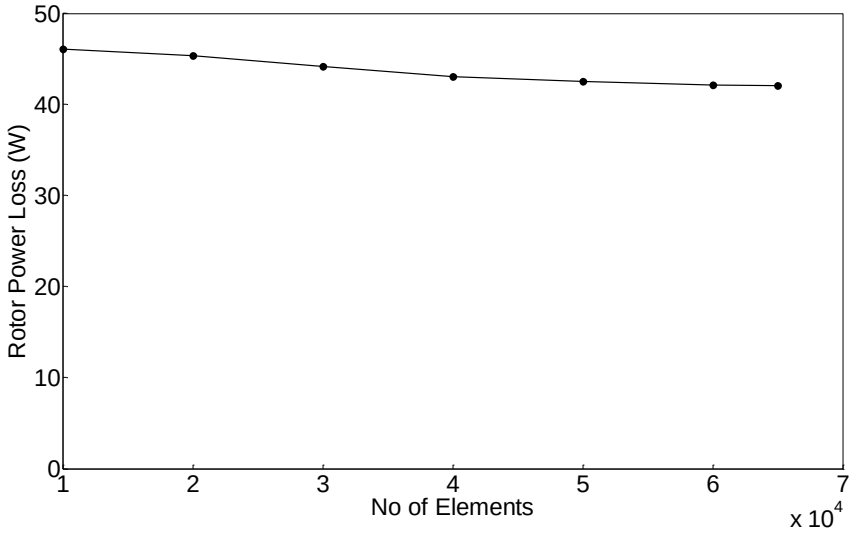

Figure 3.6. Effect of the number of elements on power loss in PMSG1. The time step was 6.84 × 10-7s

3.2.1.2.2 Time Step

The accuracy of a transient FEA solution is also affected by the time step Δt . The time step needs to be adjusted such that the distance travelled during each time step is significantly smaller than the wavelength of the highest significant space order harmonic. A reasonable approximation of time step for obtaining data points during the rotor rotation, covering a slot opening width can be obtained as:

$$\Delta t = \frac{b_0}{N \times R_3 \times \omega_r} \tag{3.2}$$

In equation (3.2), N, b_0 and ω_r are number of data points, slot-opening, and angular rotor speed, respectively. The importance of time step for the calculation of rotor eddy current power loss in PMSG1 is shown in Figure. 3.7. The result shows rotor loss increase with smaller time step. This may be due to the fact that at smaller time step, more harmonics are captured and respective rotor eddy current power loss due to each harmonic is calculated.

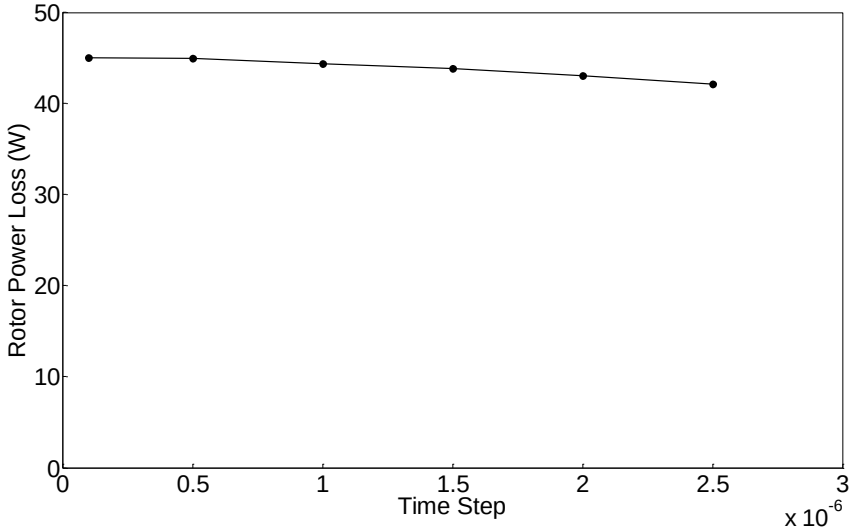

Figure 3.7. Effect of the time step on power loss in PMSG1. The number of elements was 59788

3.2.2 **Post Processing**

In the post-processing stage, transient analysis solutions can be displayed; the data is read and processed for further analysis. Field quantities including vector potential, field intensity, normal flux density and flux distribution can be displayed at points, along lines or as contour plots over a region. The data can be transferred for further

analysis into Excel or any other program desired. For instance, the normal flux density over the magnet surface can be calculated in the post processing stage, and the data saved in the '.dat' format which can easily be transferred into Excel for further analysis.

3.3 Transient FEA Solution: Rotor Eddy Current Power Loss

A typical rotor eddy current power loss solution from FEA transient analysis is presented in Figure 3.8. The time step for the analysis has been set to 6.84×10^{-7} s and about 60000 mesh elements (concentrated mainly in the steel rotor hub and magnets) have been used for a good compromise between speed and accuracy. The power loss is calculated by taking the average value of the steady state waveform in Figure 3.8.

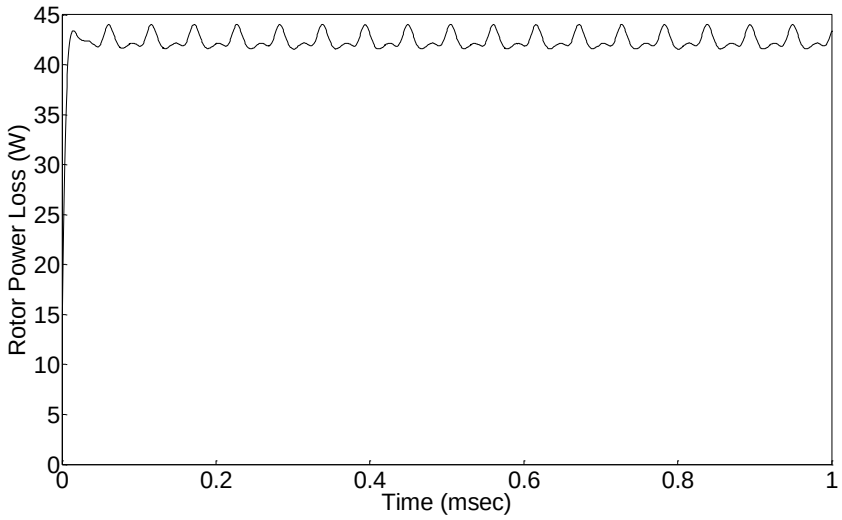

Figure 3.8. No-load power loss in PMSG1 calculated using transient FEA

3.4 Calculation of Asynchronous Harmonics using Magnetostatic FEA

The amplitude of rotating harmonics in the airgap of PMSGs can be determined using a static FEA method. The method takes in magnetic or electric fields and solves for the vector potential defined by a non-linear Poisson equation. Two main steps are performed to obtain harmonics: 1) data generation 2) two dimensional Fast Fourier Transform (FFT). In the data generation stage solutions are obtained using the Maxwell 2D FEA software; the subsequent two-dimensional FFT of the generated

data is performed using Matlab.

3.4.1 **Data Generation**

In the data generation stage the generated models are solved using static FEA analysis and post-processed to calculate both the normal component of airgap flux density on the surface of the magnet and the corresponding instantaneous mmf distribution within the slots. This is performed at each rotor position, with each position being represented by it's own machine model. In contrast to slotless stator PM machines, the flux distribution under an S-pole in a slotted PM machine may not necessarily be equal to the negative flux distribution under an N-pole, depending on the ratio of slots to poles. Only for an integer number of slots per pole will the flux density under the two adjacent poles be equal and opposite in the case of a slotted PM machine.

In the post processing stage, an arc is defined slightly above the surface of the magnet (r = 27.15 mm) covering one magnetic pole pitch at each rotor position, such that the data is always for the same points. The arc is defined based on number of sample points, arc angle and number of segments. 2D calculator is used to calculate two-dimensional normal component of airgap flux density 'B' on the surface of magnet. Figure 3.9 shows the B distribution in the airgap of PMSG1, highlighting the effect of number of arc segments. It should be noted that there should be reasonable amount of points on the arc in order to have accurate flux density distribution.

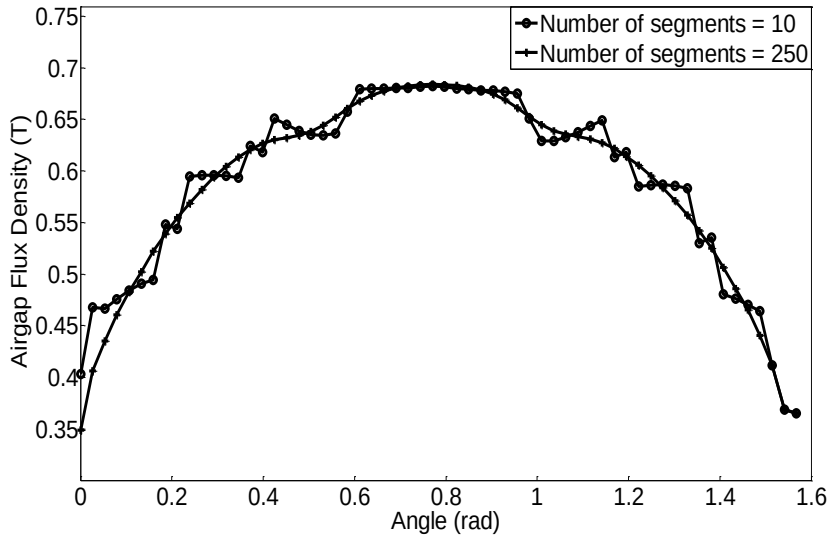

Figure 3.9. Effect of Number of Segments on Airgap Flux Density in PM machine

3.4.1.1 Airgap Flux Density due to Magnet Flux Only

Setting the three phase currents to zero allows the static FEA solution to be used to calculate the airgap flux distribution due to permanent magnets only, on the surface of the rotor. The flux density is calculated across the surface of the magnet at each rotor position, for a total of 30 rotor positions covering one slot-pitch. Due to the symmetry of the machine, with the same tooth-slot shape all around the stator bore, only positions covering one slot pitch are required. All field quantities then repeat themselves after each slot-pitch.

3.4.1.2 Airgap Flux Density due to Armature Reaction Stator Flux Only

The static FEA solution can also be used to calculate the airgap flux distribution data due to the armature reaction stator mmf. This is achieved by defining the magnet regions as a material that has permeability equal to the recoil permeability of the magnets and conductivity equal to zero. This isolates the effect of stator mmf flux harmonics from magnet flux tooth ripple harmonics.

Depending on the design requirement, the three-phase winding distribution may vary between machines. For instance, PMSG1 has three slots per pole, double layer and chorded winding with ratio of 2/3, PMSG2 has six slots per pole, double layer and full pitch winding distribution and PMSG3 has 1.5 slots per pole with concentrated winding. In FEA these winding arrangements must be considered and applied in the relevant section. The fact that the current density is defined in each slot region in a way that the fundamental component of the stator flux density rotates in synchronism with the rotor is catered for in Maxwell 2D FEA software. This is achieved by assigning current distribution values in the slot at different rotor position using *Current3*.m program in Appendix 2.

The airgap flux due to armature reaction stator mmf is strongly dependent on slot pole combination. This means it is not always enough to rotate the rotor by one slot pitch to fully capture the airgap flux density at all points. The angle of rotation should then be such that the flux quantities repeat themselves thereafter. A demonstration of this

is given by PMSG1, in which case winding distribution is shown at rotor position 0^0 electrical in Figure 3.10.

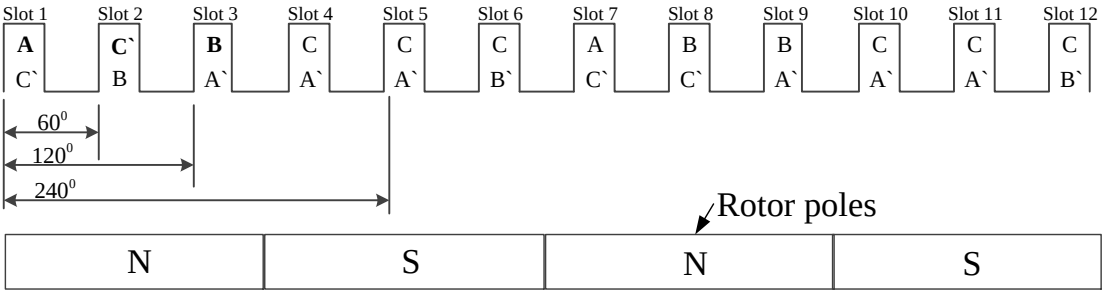

Figure 3.10. A typical 3 phase double layer, chorded winding with ratio of 2/3 at 0^0 rotor position

The general case for a stator current representing the k^{th} harmonic can be given as:

$$\begin{aligned} I_{a_0} &= I_m \cos k\omega t, \\ I_{b_0} &= I_m \cos k\left(\omega t - 120\right), \\ I_{c_0} &= I_m \cos k\left(\omega t - 240\right). \end{aligned} \tag{3.3}$$

As PMSG1 has one slot per pole per phase, the minimum change in rotor position after which field quantities will repeat will be 60 electrical degrees. For an odd *k*, after 60 electrical degrees the three phase currents in the windings can be given by:

$$\begin{aligned} I_{a_{60}} &= I_m \cos k\left(\omega t + 60\right) = -I_{b_0}, \\ I_{b_{60}} &= I_m \cos k\left(\omega t + 60 - 120\right) = -I_{c_0}, \\ I_{c_{60}} &= I_m \cos k\left(\omega t - 240 + 60\right) = -I_{a_0}. \end{aligned} \tag{3.4}$$

Figure 3.11 shows the winding distribution after 60 electrical degrees of rotor movement. It can be seen that the situations for each phase AC'BC'BA'…at $\omega t = 60^0$ are the same as at $\omega t = 0^0$ but with a 60^0 delay.

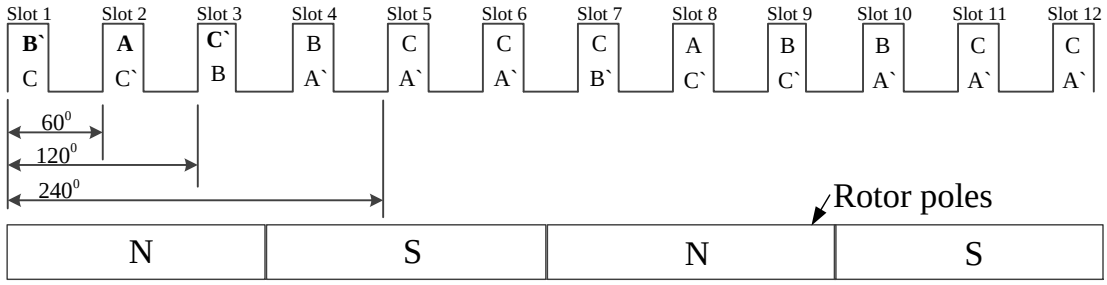

Figure 3.11. A typical 3 phase double layer, chorded winding with ratio of 2/3 at 60^0 of rotor movement

Following Figures 3.12 and 3.13, shows the winding configuration models for PMSG2. As the number of slots per pole per phase is now two the minimum change in rotor angle that reproduces an identical system is 60^0 covering two slot pitches. It can be seen that the sequence of phases AAAAC'C'C'C'BBBB at $\omega t = 60^0$ is the same as at $\omega t = 0^0$ but with a 60^0 delay. If the load current contains any even harmonics the stator must be rotated a full double pole-pitch or 360^0 electrical degrees.

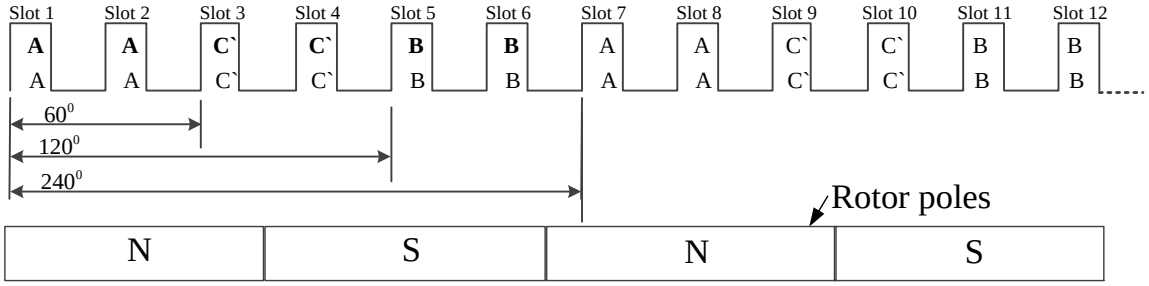

Figure 3.12. A typical 3 phase double layer full pitch winding at 0^0 rotor position

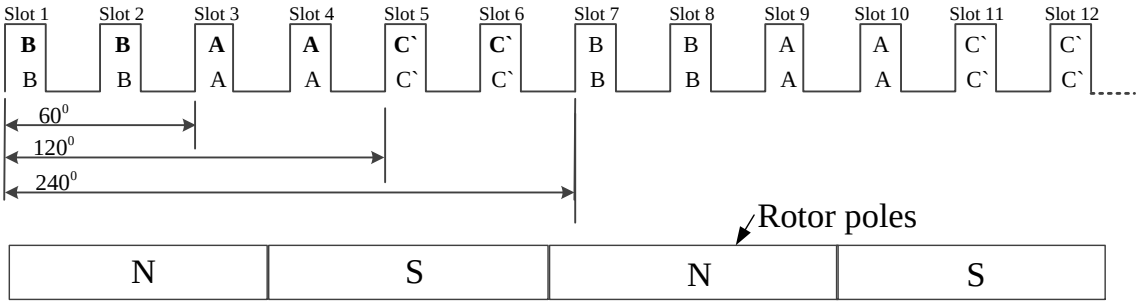

Figure 3.13. A typical 3 phase double layer full pitch winding at 60^0 rotor position

3.4.1.3 Airgap Flux Density due to Resultant Flux

The data for airgap flux due to the resultant flux caused by the interaction between magnet flux and armature reaction stator mmf can be calculated using a static FEA solution. This is achieved by defining the magnets same as defined for the calculation of magnet flux tooth ripple harmonics in section 3.4.2, and the current density in the stator slots is specified in the same way as in section 3.4.3. The stator flux density axis remains at 90 degrees to the rotor pole centre, i.e., the stator current and emf are

in phase. The number of degrees of rotor rotation over which airgap flux density is calculated is determined from the number of slots per pole per phase and whether the stator current contains even or odd harmonics.

3.5 Two Dimensional Fast Fourier Transform (FFT)

The data sets for airgap flux density distribution due to magnet flux, stator flux and resultant flux, are analysed using two dimensional FFT for the calculation of harmonic amplitudes. The analysis is performed using two Matlab programs developed by Irenji (1998). The first program *FFT1*.m shown in Appendix 2, reads in a set of Excel files containing data for the normal component of airgap flux density, calculated at each rotor position. The second program *FFT2*.m shown in Appendix 2 performs the two dimensional FFT to evaluate the amplitude of each harmonic; the results are saved in an Excel file in the form of a matrix.

As an example, using two-dimensional FFT the magnet flux tooth ripple harmonics in PMSG1 are presented in Table 3.3. The first row and first column of the matrix represent the temporal order '*k'* and spatial order *'q'* of each harmonic, respectively. The first column corresponds to the spatial spectrum of stationary flux density with respect to the rotor. The second column indicates the spatial spectrum of the fundamental CW rotating component. Higher time orders of CW rotating harmonics are indicated by column index counted from the second column as the first harmonic towards the middle column. The latter columns of the matrix represent CCW rotating harmonics, counting from the fundamental time order in the last column to higher orders toward the middle column. Time orders of CCW rotating harmonics are indicated by column index as counted from the last column towards the middle.

Spatial order *h*	Temporal order *k*								
	0	6	12	18	30	30	18	12	6
1	0.805503^{-}	0.000306^{-}	3.49E-05^{-}	3.21E-05^{-}	2.23E-05^{-}	2.26E-05^{+}	3.28E-05^{+}	4.24E-05^{+}	0.0001^{+}
3	0.192242^{-}	0.001069^{-}	2.32E-05^{-}	2.19E-05^{-}	1.58E-05^{-}	1.53E-05^{+}	2.27E-05^{+}	2.93E-05^{+}	5.4E-05^{+}
5	0.105301^{-}	0.006309^{-}	8.65E-05^{-}	5.35E-05^{-}	4.98E-05^{-}	4.95E-05^{+}	5.49E-05^{+}	6.03E-05^{+}	3.3E-05^{+}
7	0.071791^{-}	0.004625^{-}	0.000207^{-}	2.46E-05^{-}	2.58E-05^{-}	2.57E-05^{+}	2.01E-05^{+}	1.76E-05^{+}	4.2E-05^{+}
9	0.054358^{-}	0.000784^{-}	0.000474^{-}	1.05E-05^{-}	5.72E-06^{-}	5.15E-06^{+}	9.82E-06^{+}	1.73E-05^{+}	9.2E-06^{+}
11	0.043625^{-}	0.000262^{-}	0.002562^{-}	3.88E-05^{-}	3.75E-05^{-}	3.72E-05^{+}	4.28E-05^{+}	4.74E-05^{+}	2.6E-05^{+}
13	0.036249^{-}	0.000115^{-}	0.00133^{-}	5.56E-05^{-}	1.56E-05^{-}	1.52E-05^{+}	1.09E-05^{+}	6.39E-06^{+}	2.6E-05^{+}
15	0.030839^{-}	6.19E-05^{-}	0.000219^{-}	0.000111^{-}	1.83E-06^{-}	1.82E-06^{+}	5.85E-06^{+}	8.89E-06^{+}	1.0E-05^{+}
17	0.026668^{-}	3.93E-05^{-}	7.06E-05^{-}	0.00067^{-}	1.43E-05^{-}	1.56E-05^{+}	1.92E-05^{+}	2.54E-05^{+}	1.08E-05^{+}
19	0.023309^{-}	3.25E-05^{-}	2.43E-05^{-}	0.00027^{-}	9.34E-06^{-}	3.76E-06^{+}	2.85E-06^{+}	4.78E-06^{+}	1.17E-05^{+}

Table 3.3. Amplitudes of CCW and CW rotating magnet flux harmonics denoted by subscript + and -, respectively.

3.6 Analytical: Current Sheet Model

This section describes the analytical current sheet method used for the calculation of rotor eddy current power loss using amplitude of rotating flux harmonics. Most analytical methods use a common procedure:

1) Amplitudes of travelling flux harmonics in the rotor reference frame can be estimated either analytically see (Zhu et al., 2001c; Zhu et al., 2001a; Atallah et al., 2000) or from magnetostatic solutions (Sharkh et al., 1999).

2) A multilayer rectilinear or cylindrical model of the PM machine is used to calculate rotor eddy current losses for each harmonic using current sheet method, see (Sharkh et al., 1997; Wills and Kamper, 2010a; Bianchi and Fornasiero, 2009; Bianchi et al., 2007; Zhu et al., 2004).

In current sheet method, each travelling flux harmonic is represented by a current sheet on the surface of the stator bore of a slotless stator, as shown in Figure 3.14.

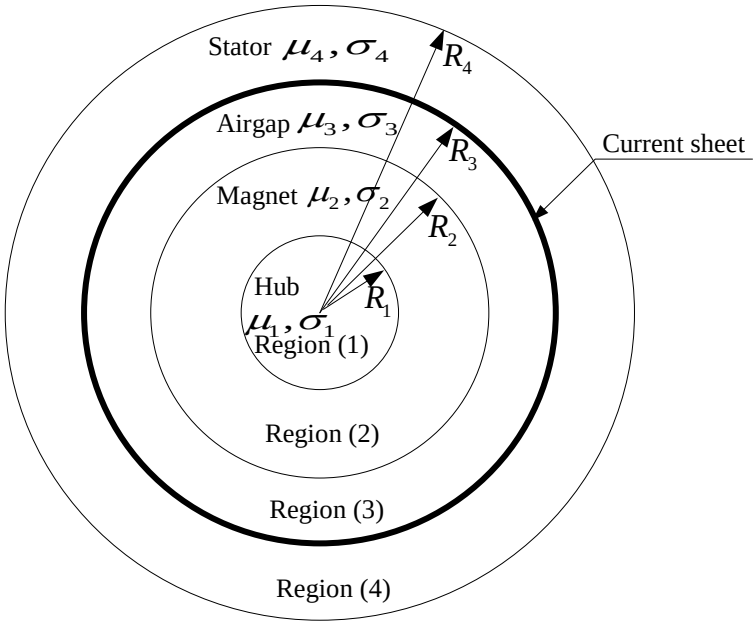

Figure 3.14. Cylindrical slotless model of a PM machine in which each mmf harmonic is represented as an equivalent current sheet

The amplitude of the current sheet is adjusted such that it produces the required amplitude of normal flux density on the surface of the rotor in the absence of eddy

currents see (Stoll and Sykulski, 1992; Sharkh et al., 1999; Irenji, 1998; Atallah et al., 2000) and others. The field solution is derived in each layer of PM machine using Laplace and Poisson field equations, when subjected to the travelling current sheet placed on the slotless stator bore.

3.6.1 **Magnet Flux Tooth Ripple Harmonics and Equivalent Current Sheet**

The general form of the equivalent current sheet for magnet flux harmonics is given by,

$$J_{qk} = \hat{J}_{qk} \cos\left(q\theta + k\omega t\right) = \mathrm{Re}\left(\hat{J}_{qk} e^{iq\theta} e^{jk\omega t}\right) \tag{3.5}$$

In equation (3.5), $\hat{J}_{qk}$ is the amount of current sheet of temporal order *k* and spatial order *q* and J_{qk} is the line density of current in A/m. The amount of current sheet $\hat{J}_{qk}$ in the presence of eddy currents cannot be directly calculated for the given amplitude of harmonics. This situation is later catered for in section 3.7.

3.6.2 **Armature Reaction Stator mmf Harmonics and Equivalent Current Sheets**

The amplitude of the armature reaction flux harmonic F_{qk}, with spatial order *q* and temporal order *k*, is given by McPherson (1981) as:

$$F_{qk} = \frac{3}{2}\frac{4}{\pi}\frac{N_{ph}}{2p}\frac{1}{q}K_{wq}\sqrt{2}\hat{I}_k \tag{3.6}$$

The relation between the amplitude of the flux harmonics F_{qk} and its equivalent current sheet at the stator bore, $\hat{J}_{qk}$ according to (Alger, 1965) is given as:

$$\hat{J}_{qk} = \frac{qp}{R_3} \times F_{qk} \tag{3.7}$$

The equivalent current sheet for the mmf harmonic of an arbitrary space order *h* and time order *k* has the following distribution:

$$J_{qk} = \hat{J}_{qk} \cos\left(q\theta + k\omega t\right) \tag{3.8}$$

In equation (3.8), ω is the angular frequency equal to $2\pi kf$ and f the fundamental frequency.

3.7 Power Loss Calculation using Current Sheet Model

Both rectilinear and cylindrical current sheet models have been used to calculate rotor eddy current power loss caused by magnet flux tooth ripple harmonics and armature reaction stator mmf flux harmonics in PM machines. Examples of rectilinear models can be seen in (Sharkh et al., 1999) and (Zhu et al., 2004), whilst cylindrical current sheet model has been used in Wu et al (2012b), Wu et al (2012a), Zhu et al (2001b) and Zhu et al (2001c). The difference between the models also lies in taking into account the effect of reaction of eddy currents on the amplitude of airgap flux harmonics.

The reaction of eddy currents and their effect on airgap flux harmonics has been taken into account by Sharkh et al (1999), Stoll and Sykulski (1992), Zhu et al (2001c), Zhu et al (2001b) and others. Whereas, in (Wu et al., 2012b; Wu et al., 2012a; Etemadrezaei et al., 2012) this has been neglected for both cases; i.e., PM machines with segmented and ring magnets.

In this section rotor eddy current power loss is calculated for a machine with ring magnets using cylindrical current sheet model and taking into account the effect of reaction eddy current field on airgap flux harmonics. This is achieved by developing two analytical solutions; 1) a solution with eddy currents taken into account, 2) a solution without taking eddy currents into account.

3.7.1 **Field Solution with Eddy Current**

In this section the field solution in the four layers of PM machine model shown in Figure 3.14 is calculated taking into account eddy currents. The Laplace's and Poisson's partial differential equations are solved in each region of the machine model to obtain field quantities such as airgap flux density. The complexity of the analytical problem arises from the presence of Bessel functions with large complex arguments. In principle it is possible to use a series expansion of these Bessel functions to

evaluate their values, however in this Thesis the program suite *Loss1*.mw in Appendix 1 was used to solve these functions.

The solution produces a map of the vector potential *A* in the airgap and magnet layers using Laplace's and Poisson's equations, respectively. Generally, the vector potential *A* is a three dimensional vector dependent on four variables; r, θ, z and t, but for the model under consideration it is assumed to be a one dimensional vector in z direction. This neglects end effects in the machine, reducing the problem to a symmetrical 2D system. In the steady state the complex form of vector potential *A* can be written as:

$$\nabla^2 A = j\omega\mu\sigma A \tag{3.9}$$

In a cylindrical coordinate system the Laplacian of the magnetic vector potential, *A*, assuming no variation in the z direction becomes as follows:

$$\frac{1}{r}\frac{\partial}{\partial r}\left(r\frac{\partial A}{\partial r}\right)+\frac{1}{r^2}\frac{\partial^2 A}{\partial \theta^2}=\nabla^2 A \tag{3.10}$$

The steady state diffusion equation is calculated by substituting equation (3.10) in equation (3.9) as:

$$\frac{1}{r}\frac{\partial}{\partial r}\left(r\frac{\partial A}{\partial r}\right)+\frac{1}{r^2}\frac{\partial^2 A}{\partial \theta^2}= j\omega\mu\sigma A \tag{3.11}$$

Using the separation of variables, and bearing in mind that the applied current sheet varies sinusoidal in time and space in the peripheral direction, the magnetic vector potential *A* can be expressed as:

$$A(r,\theta,t)=R(r)e^{iq\theta}e^{jk\omega t} \tag{3.12}$$

Substituting, equation (3.12) in equation (3.11), it can be shown that:

$$\frac{1}{r}\left(\frac{\partial}{\partial r}R(r)\right)+\left(\frac{\partial^2}{\partial r^2}R(r)\right)=R(r)\left(\left(j\omega\mu\sigma\right)\frac{q^2}{r^2}\right) \tag{3.13}$$

Equation (3.13) is the modified Bessel differential equation whose general equation is gives as:

$$R(k'r)=CI_q\left(q,k'r\right)+DL_q\left(q,k'r\right) \tag{3.14}$$

In equation (3.14), $k' = \sqrt{j\omega\mu\sigma}$, C and D are constants to be determined using boundary conditions, and I_q and L_q are modified Bessel functions of the first and second kinds of order q.

The radial and tangential component of airgap flux density, in terms of vector potential A, are given by:

$$B_r = \frac{1}{r}\frac{\partial A}{\partial \theta} = \frac{1}{r} iq\left[CI_q(k'r) + DL_q(k'r)\right]e^{iq\theta}e^{jk\omega t} \tag{3.15}$$

$$B_\theta = -\frac{\partial A}{\partial r} = -k'\left[CI'_q(k'r) + DL'_q(k'r)\right]e^{iq\theta}e^{jk\omega t} \tag{3.16}$$

The field equations for each region can be written as the following set of equations:

In the rotor hub (region 1):

$$B_{r_1} = \frac{1}{R_1}\frac{\partial A_1}{\partial \theta} = \frac{1}{R_1} iq\left[C_1 I_q(k'_1 R_1) + D_1 L_q(k'_1 R_1)\right]e^{iq\theta}e^{jk\omega t}$$

$$B_{\theta_1} = -\frac{\partial A_1}{\partial R_1} = -k'_1\left[C_1 I'_q(k'_1 R_1) + D_1 L'_q(k'_1 R_1)\right]e^{iq\theta}e^{jk\omega t} \tag{3.17}$$

In the magnet (region 2):

$$B_{r_2} = \frac{1}{R_2}\frac{\partial A_2}{\partial \theta} = \frac{1}{R_2} iq\left[C_2 I_q(k'_2 R_2) + D_2 L_q(k'_2 R_2)\right]e^{iq\theta}e^{jk\omega t}$$

$$B_{\theta_2} = -\frac{\partial A_2}{\partial R_2} = -k'_2\left[C_2 I'_q(k'_2 R_2) + D_2 L'_q(k'_2 R_2)\right]e^{iq\theta}e^{jk\omega t} \tag{3.18}$$

In the airgap (region 3):

$$B_{r_3} = \frac{1}{R_3}\frac{\partial A_3}{\partial \theta} = \frac{1}{R_3} iq\left[C_3 I_q(k'_3 R_3) + D_3 L_q(k'_3 R_3)\right]e^{iq\theta}e^{jk\omega t}$$

$$B_{\theta_3} = -\frac{\partial A_3}{\partial R_3} = -k'_3\left[C_3 I'_q(k'_3 R_3) + D_3 L'_q(k'_3 R_3)\right]e^{iq\theta}e^{jk\omega t} \tag{3.19}$$

In the stator (region 4):

$$B_{r_4} = \frac{1}{R_4}\frac{\partial A_4}{\partial \theta} = \frac{1}{R_4} iq\left[C_4 I_q(k'_4 R_4) + D_4 L_q(k'_4 R_4)\right]e^{iq\theta}e^{jk\omega t}$$

$$B_{\theta_4} = -\frac{\partial A_4}{\partial R_4} = -k_4' \left[C_4 I_q'(k_4' R_4) + D_4 L_q'(k_4' R_4) \right] e^{iq\theta} e^{jk\omega t} \tag{3.20}$$

The constants C_i and D_i in equations (3.17-3.20) can be calculated using the Dirichlet and Neumann boundary conditions. Before applying these boundary conditions they are defined below.

3.7.1.1 Dirichlet Boundary Condition

A Dirichlet boundary condition explicitly defines the value of the vector potential *A* on the boundary. A value of *A*=0 is commonly defined along a boundary to keep the magnetic flux from crossing the boundary.

3.7.1.2 Neumann Boundary Condition

This boundary condition specifies the normal derivative of vector potential along the boundary. In electromagnetic problems, the homogeneous Neumann boundary condition, $\frac{\partial A}{\partial n} = 0$ is defined along a boundary to force flux to pass the boundary at exactly 90^0 to the boundary. This sort of boundary condition is consistent with an interface with a very high permeability.

Applying the Dirichlet and Neumann boundary conditions in PM machine model, the radial flux density B_r is continuous at all interfaces except at $r = R_4$, where the magnetic flux is kept from crossing the stator outer boundary. The boundary conditions can be given by:

$$B_{r_1} = B_{r_2}\Big|_{r=R_1} \qquad B_{r_2} = B_{r_3}\Big|_{r=R_2}$$

$$B_{r_3} = B_{r_4}\Big|_{r=R_3} \qquad B_{r_4}\Big|_{r=R_4} = 0 \tag{3.21}$$

The tangential field intensity H_θ is continuous at the interfaces at $r = R_1$ and R_2, but not at the stator bore $r = R_3$, where there is discontinuity of magnitude equal to the current sheet amplitude J_{qk}.

$$H_{\theta_1} = H_{\theta_2}\Big|_{r=R_1} \qquad H_{\theta_2} = H_{\theta_3}\Big|_{r=R_2}$$

$$H_{\theta_3} = H_{\theta_4}\Big|_{r=R_3} + J_{qk} \tag{3.22}$$

Applying the boundary conditions in equation (3.21) to set of equations in (3.17 - 3.20) results in the following set of equations:

$$\frac{1}{R_1} iq\left[C_1 I_q(k_1' R_1))\right] = \frac{1}{R_1} iq\left[C_2 I_q(k_2' R_1) + D_2 L_q(k_2' R_1)\right]$$

$$\frac{1}{R_2} iq\left[C_2 I_q(k_2' R_2) + D_2 L_q(k_2' R_2)\right] = \frac{1}{R_2} iq\left[C_3 I_q(k_3' R_2) + D_3 L_q(k_3' R_2)\right] \tag{3.23}$$

$$\frac{1}{R_3} iq\left[C_3 I_q(k_3' R_3) + D_3 L_q(k_3' R_3)\right] = \frac{1}{R_3} iq\left[C_4 I_q(k_4' R_3) + D_4 L_q(k_4' R_3)\right]$$

$$\frac{1}{R_4} iq\left[C_4 I_q(k_4' R_4) + D_4 L_q(k_4' R_4)\right] = 0$$

Also, applying the boundary conditions in (3.22) to set of equations in (3.17 - 3.20) will result in:

$$-\frac{1}{\mu_1} k_1'\left[C_1 I_q'(k_1' R_1)\right] = -\frac{1}{\mu_2} k_2'\left[C_2 I_q'(k_2' R_1) + D_2 L_q'(k_2' R_1)\right]$$

$$-\frac{1}{\mu_2} k_2'\left[C_2 I_q'(k_2' R_2) + D_2 L_q'(k_2' R_2)\right] = -\frac{1}{\mu_3} k_3'\left[C_3 I_q'(k_3' R_2) + D_3 L_q'(k_3' R_2)\right] \tag{3.24}$$

$$-\frac{1}{\mu_3} k_3'\left[C_3 I_q'(k_3' R_3) + D_3 L_q'(k_3' R_3)\right] = -\frac{1}{\mu_4} k_4'\left[C_4 I_q'(k_4' R_3) + D_4 L_q'(k_4' R_3)\right] + J_{qk}$$

According to (Abramowitz and Stegun, 1970), functions I_q' and L_q' are derivatives of modified Bessel functions I_q and L_q which may be given by the following relation:

$$I_q'(r) = I_{q-1}(r) - \frac{q}{r} I_q(r)$$

$$L_q'(r) = -L_{q-1}(r) - \frac{q}{r} K_q(r)$$

The analytical solution for the equations (3.23) and (3.24), to calculate constants C_i and D_i in terms of; the applied current sheet amplitude J_{qk}, machine materials and dimensions, is performed using program *Harmonic1.mw* in Appendix 1.

3.7.2 **Eddy Current Power Loss Calculation using Poynting Vector**

Eddy current power loss in the permanent magnets can be calculated using two possible methods as discussed by Zhu et al (2004). In the first method the power loss *P* is given by:

$$P = \frac{1}{2}\int_{V'} \mathrm{Re}\left[E \cdot J\right] dV' \tag{3.25}$$

In equation (3.25), V' denotes the volume of the electrically conducting region in which eddy currents are induced, *E* is the electric field and *J* is the current density.

The alternative method is to use Poynting's vector **P**, which can be written as:

$$\mathbf{P} = \mathbf{E} \times \mathbf{H} \tag{3.26}$$

In equation (3.26), **E** and **H** are vectors representing electric field and magnetic field intensity, respectively.

Both methods result in identical results; Poynting's method however eases the rotor loss calculation when the model is formulated in cylindrical coordinates, as it avoids the problematic integration of Bessel functions with complex arguments.

For a sinusoidal electromagnetic field at steady state, the average power transmitted through the surface as calculated using the Poynting vector is:

$$P = \frac{1}{2}\mathrm{Re}\left(E \times H^*\right) \tag{3.27}$$

In equation (3.27), H^* is the conjugate of the tangential magnetic field intensity amplitude over the surface. The total power loss transmitted through the surface is calculated by integrating equation (3.27) over the total surface area. Let the power transmitted from airgap to the magnet be designated by P_1, the power transmitted to

the rotor hub by P_2, the power loss in the magnet region by P_m and the power loss in the hub region by P_h. In terms of field quantities, these variables may be given as:

$$P_1 = \frac{1}{2}\mathrm{Re}\left\{\left[E_{z_2}\right]_{r=R_2} \times \left[H^*_{\theta_2}\right]_{r=R_2} S_1\right\} \tag{3.28}$$

$$P_2 = \frac{1}{2}\mathrm{Re}\left\{\left[E_{z_1}\right]_{r=R_1} \times \left[H^*_{\theta_1}\right]_{r=R_1} S_2\right\} \tag{3.29}$$

In equations (3.28) and (3.29), S_1 and S_2 are the surface area over the magnet and rotor hub regions, respectively. The power loss in the permanent magnet P_m and in the rotor hub P_h can be calculated as:

$$P_m = P_1 - P_2$$

$$P_h = P_2 \tag{3.30}$$

For a known value of current sheet $\hat{J}_{qk}$, the rotor eddy current power loss can be calculated using the method discussed above.

The difficulty in calculating rotor eddy current power loss arises when the value of the current sheet $\hat{J}_{qk}$ is not known. If this is the case, the flux density over the magnet surface is also not known in the presence of induced eddy currents. This situation is catered for by repeating the above solution for equations (3.28) and (3.29) for the unity current sheet value. Then, as will be discussed in the next section, the airgap flux density on the surface of the magnet with unity current sheet value is calculated in the absence of eddy currents. Finally, the ratio between the given and calculated airgap flux density values is used to scale the field quantities in equations (3.28) and (3.29).

3.7.3 **Field Solution without Eddy Current Effect**

The airgap flux density for a current sheet $\hat{J}_{qk}$ of unit amplitude, in the absence of eddy currents, can be calculated in a cylindrical model of PM machine using the method discussed in section 3.7.2, except that the material conductivity σ in equation (3.11) is

assumed to be zero. This makes the problem magnetostatic, and caters for the fact that no eddy currents are induced in the magnet region.

Using variable separation the solution of equation (3.11) is given by:

$$A(r,\theta,t) = R(r)e^{iq\theta}e^{jk\omega t} \tag{3.31}$$

Substituting equation (3.31) in equation (3.11) it can be shown that:

$$\frac{1}{r}\left(\frac{\partial}{\partial r}R(r)\right)+\left(\frac{\partial^2}{\partial r^2}R(r)\right) = R(r)\left(\frac{q^2}{r^2}\right) \tag{3.32}$$

The solution of equation (3.32) is given as:

$$R(r) = Cr^q + Dr^{-q} \tag{3.33}$$

In the rotor hub (region 1):

$$B_{r_1} = \frac{1}{R_1}\frac{\partial A_1}{\partial \theta} = \frac{1}{R_1}iq\left[C_1 R_1{}^q\right]e^{iq\theta}$$

$$B_{\theta_1} = -\frac{\partial A_1}{\partial R_1} = -\frac{1}{R_1}\left[C_1 R_1{}^q q\right]e^{iq\theta} \tag{3.34}$$

In the magnet (region 2):

$$B_{r_2} = \frac{1}{R_2}\frac{\partial A_1}{\partial \theta} = \frac{1}{R_2}iq\left[C_2 R_2{}^q + D_2 R_2{}^{-q}\right]e^{iq\theta}$$

$$B_{\theta_2} = -\frac{\partial A_1}{\partial R_2} = -\frac{1}{R_2}q\left[C_2 R_2{}^q - D_2 R_2{}^{-q}\right]e^{iq\theta} \tag{3.35}$$

In the airgap (region 3):

$$B_{r_3} = \frac{1}{R_3}\frac{\partial A_1}{\partial \theta} = \frac{1}{R_3}iq\left[C_3 R_3{}^q + D_3 R_3{}^{-q}\right]e^{iq\theta}$$

$$B_{\theta_3} = -\frac{\partial A_1}{\partial R_3} = -\frac{1}{R_3}q\left[C_3 R_3{}^q - D_3 R_3{}^{-q}\right]e^{iq\theta} \tag{3.36}$$

In the stator (region 4):

$$B_{r_4} = \frac{1}{R_4}\frac{\partial A_1}{\partial \theta} = \frac{1}{R_4}iq\left[C_4 R_4{}^q + D_4 R_4{}^{-q}\right] = 0$$

$$B_{\theta_4} = -\frac{\partial A_1}{\partial R_4} = -\frac{1}{R_4} q\left[C_4 R_4^{\,q} - D_4 R_4^{\,-q}\right] e^{iq\theta} \tag{3.37}$$

The constants C_i and D_i in the above field equations can be calculated using boundary conditions. Applying the boundary conditions in equation (3.21) to set of equations in (3.34-3.37) will result in following set of equations:

$$\begin{aligned}
&\frac{1}{R_1} iq\left[C_1 R_1^{\,q} + D_1 R_1^{\,-q}\right] = \frac{1}{R_1} iq\left[C_2 R_1^{\,q} + D_2 R_1^{\,-q}\right] \\
&\frac{1}{R_2} iq\left[C_2 R_2^{\,q} + D_2 R_2^{\,-q}\right] = \frac{1}{R_2} iq\left[C_3 R_2^{\,q} + D_3 R_2^{\,-q}\right] \\
&\frac{1}{R_3} iq\left[C_3 R_3^{\,q} + D_3 R_3^{\,-q}\right] = \frac{1}{R_3} iq\left[C_4 R_3^{\,q} + D_4 R_3^{\,-q}\right] \\
&\frac{1}{R_4} iq\left[C_4 R_4^{\,q} + D_4 R_4^{\,-q}\right] = 0
\end{aligned} \tag{3.38}$$

Similarly, applying the boundary conditions in equation (3.22) to the set (3.34-3.37) will result in following:

$$\begin{aligned}
&-\frac{1}{\mu_1 R_1} q\left[C_1 R_1^{\,q}\right] = -\frac{1}{\mu_2 R_1} q\left[C_2 R_1^{\,q} - D_2 R_1^{\,-q}\right] \\
&-\frac{1}{\mu_2 R_2} q\left[C_2 R_2^{\,q} - D_2 R_2^{\,-q}\right] = -\frac{1}{\mu_3 R_2} q\left[C_3 R_2^{\,q} - D_3 R_2^{\,-q}\right] \\
&-\frac{1}{\mu_3 R_3} q\left[C_3 R_3^{\,q} - D_3 R_3^{\,-q}\right] = -\frac{1}{\mu_4 R_3} q\left[C_4 R_3^{\,q} - D_4 R_3^{\,-q}\right] e^{jq\theta} + J_{qk}
\end{aligned} \tag{3.39}$$

The airgap flux density in the absence of eddy currents can be calculated on the surface of the magnet as:

$$B_{calculated} = B_{r_2}\Big|_{r=R_2} = \frac{1}{R_2} iq\left[C_2 R_2^{\,q} + D_2 R_2^{\,-q}\right] \tag{3.40}$$

3.7.4 **Rotor Eddy Current Power Loss using Magneto-Static Solution**

The rotor eddy current power loss in case of magneto-static solution i.e., neglecting eddy currents cannot be directly calculated using Poynting vector. In order to calculate power loss in the permanent magnet and rotor hub regions from magneto-static solution, the power loss is calculated using method in section 3.7.2. This power loss is then scaled, accordingly. For instance the loss in the permanent magnet region P_m is multiplied with the ratio between B_{given} and $B_{calculated}$ given by:

$$K_b = \frac{B_{given}}{B_{calculated}} \tag{3.41}$$

In equation (3.41), the normal flux density B_{given} is calculated from an FEA static or analytical methods, for instance those given in Table 3.3, whereas $B_{calculated}$ is calculated using method in section 3.7.3, respectively.

The values of the field quantities in equations (3.28) and (3.29) i.e., total eddy current power loss P_t in the magnet is calculated by adjusting the power loss in the magnet (calculated using equation (3.30)) by multiplying it with the flux density ratios as:

$$P_t = \left(\frac{B_{given}}{B_{calculated}} \right)^2 \cdot P_m \tag{3.42}$$

3.8 Limitations of Current Sheet Model

The current sheet method can provide reasonable results for calculating rotor eddy current power loss, but it does make certain simplifying assumptions.

The current sheet model assumes a two dimensional, linear problem for the calculation of rotor eddy current power loss and neglects the three-dimensional features of the PM machine e.g., slotting effect, end effects i.e., the return path of eddy currents. This means the model cannot cater for peripheral magnet segmentation or conducting paths between magnetic poles through the rotor hub. In real three-dimensional situations these paths (airgap between magnets) will largely prevent eddy currents with wavelengths of the order of the magnet segment length from circulating within the

magnets. Current sheet model solutions therefore provide a worst case estimate of rotor loss. Nor do such models directly account for the effect of generated eddy currents on travelling flux harmonics. These eddy currents will themselves generate flux harmonics that interact with the airgap flux harmonics due to slotting or armature reaction flux, and will not only change the amplitude of these harmonics but may also result in the generation of other harmonics.

3.9 Conclusion

This chapter presented the methodology for the calculation of rotor eddy current power loss in PM machines using an FEA transient solution. The method for the calculation of harmonic amplitudes using a static FEA solution is also discussed, along with the use of current sheet models for the calculation of rotor eddy current power loss.

It is shown that FEA transient solutions are capable of solving PM machine models, but meeting the requirement of a very fine mesh for good accuracy may not be possible.

For an FEA static solution, the importance of rotation of the rotor is highlighted in the calculation of the amplitude of harmonics caused by tooth ripple and stator mmf. It is shown that the required range of rotor positions used, depends on the slot-pole combination and the rotor needs to be rotated to the point after which field quantities repeat themselves.

The current sheet model is discussed along with its limitations for the calculation of rotor eddy current power loss. The methodology to cater for the generation of eddy currents and their effect on rotor eddy current power loss is presented.

Though magnet segmentation and end effects were beyond the scope of this chapter it is important to mention that the current sheet model ignores these three-dimensional effects. These effects can be considered by employing 3-D time stepping finite element software.

Chapter 4

Calculation of Magnet Flux Tooth Ripple Loss in PMSG

4.1 Introduction

Generally, two families of analytical methods are used to calculate airgap flux distribution and hence rotor travelling harmonics in slotted PM machines, viz. permeance function and sub-domain methods. This chapter deals only with the permeance function family and compares the accuracy of three analytical methods, developed by Zhu et al (1993), Gieras (2004) and Ẑarko et al (2006), with transient FEA for the calculation of airgap flux density waveforms. The methods are further expanded by the author to allow the calculation of the amplitudes of magnetic flux tooth ripple harmonics in the rotor reference frame. Rotor eddy current power loss is then calculated due to each rotating harmonic using a current sheet model, as discussed in chapter 3. The accuracy of the analytical results, for amplitudes and corresponding rotor eddy current power losses, are then compared with static FEA and transient FEA solutions.

As a simplifying assumption the effect of saturation is generally neglected in analytical methods for the calculation of airgap flux distribution or rotor power loss in

PM machines. Generally the materials used in these machines operate near the saturation point on their B-H curve, and therefore whether saturation occurs depends on many factors including increases in stator current, magnet flux density, temperature, and so on. Saturation is an important aspect of lamination design, affecting the choice of radial depth of the tooth tips in these machines. If these stator tooth tips are too thin they are subject to saturation. As the magnet poles rotate and overlap with the protruding tooth tips, saturation occurs. This results in an increase in rotor power loss. The saturation in the tips has a similar effect to having a very wide slot opening between the teeth. In this chapter the effect of stator tooth tip saturation on rotor eddy current power loss in PM machine under study is also highlighted. Finally, a study is performed to show that reducing saturation by increasing the stator tooth tip thickness reduces the rotor losses.

4.2 Machine under Study

Permanent magnet synchronous generator PMSG1, shown in Figure 3.2, running at no-load with slot-opening of 3mm is used for the study. In addition to the generator parameters shown in Table 3.1, the nonlinear B-H curve for the steel laminations is presented in Figure 4.1 has been used for non-linear transient FEA analysis. The shapes of the tooth tips in PMSG1 under study are not typical and are designed to achieve saturation in case when non-linear BH curve is used for the stator laminations.

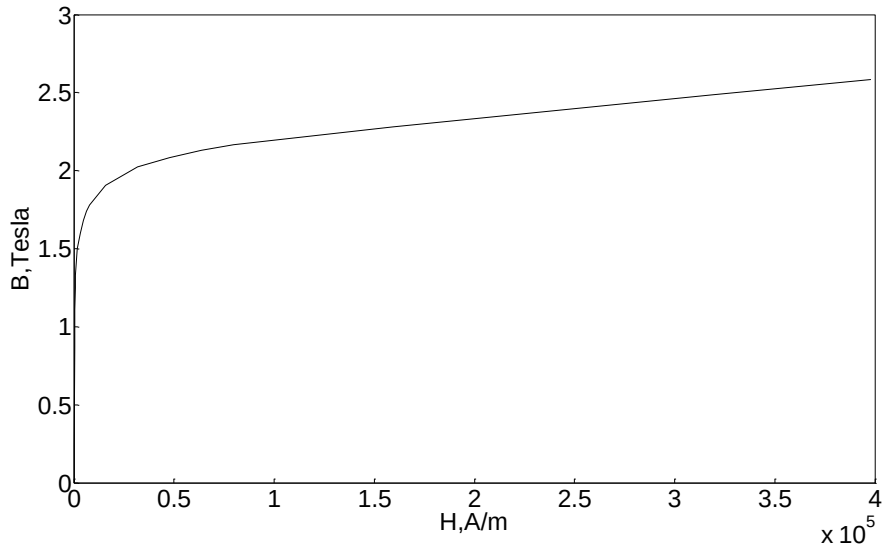

Figure 4.1. Non-Linear B-H curve for stator material in PMSG1

Ring magnet configuration is used in the generator. The issue with the ring magnet configuration is that; it is possible to magnetize these magnets such that their magnetisation direction is parallel (Hallbach machines) but they are very expensive.

4.3 FEA Static Method

Due to magnetic symmetry it is sufficient to model a quarter portion of the PM machine, covering a full pole pitch as shown in Figure 3.2. The boundary conditions along the *x* and *y* axes are defined to have negative symmetry and the normal flux density at the stator outer surface is defined to be zero. The magnet is assumed to be a conducting region with parallel magnetisation. This model assumes that ring magnets are used, and it neglects end effects, which tend to reduce the losses. A mesh was applied to the models as shown in Figure 3.5. Two static FEA solutions are obtained for: 1) Un-saturated stator tooth tip; 2) Saturated stator tooth tip.

4.3.1 **Linear Static FEA Solution for Un-saturated Stator Tooth Tip**

In this section the amplitudes of magnetic flux tooth ripple harmonics in PMSG1 are calculated for an un-saturated stator tooth tip. This is achieved by assigning the stator permeability with high value of 5000. A total of 30 models, representing 30 rotor positions with a step of two electrical degrees, were generated and analysed as discussed in chapter 3. The first position, or the zero degree position, is selected so that the interface of two adjacent poles on the rotor is aligned with the radial line of a certain slot. A one-pole FEA static model of PMSG1, showing the flux density distribution for the position assigned as $\theta = 0$, is illustrated in Figure 4.2. The level of saturation encircled in the tooth tip area is low or in other words the flux density level is higher.

The normal component of airgap flux density distribution just over the magnet surface (at r=27.15mm) at particular rotor position i.e., $\theta = 0$ is shown in Figure 4.3.

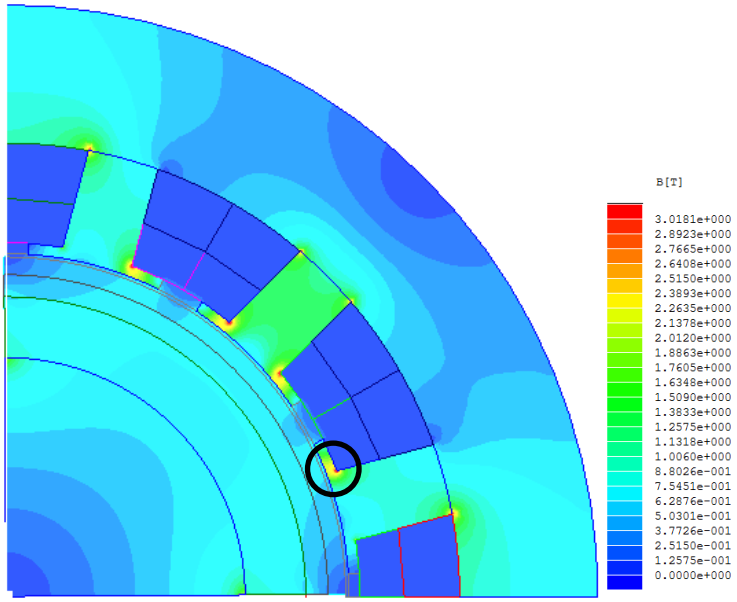

Figure 4.2. Magnet flux density distribution in PMSG1, with un-saturated stator tooth tip

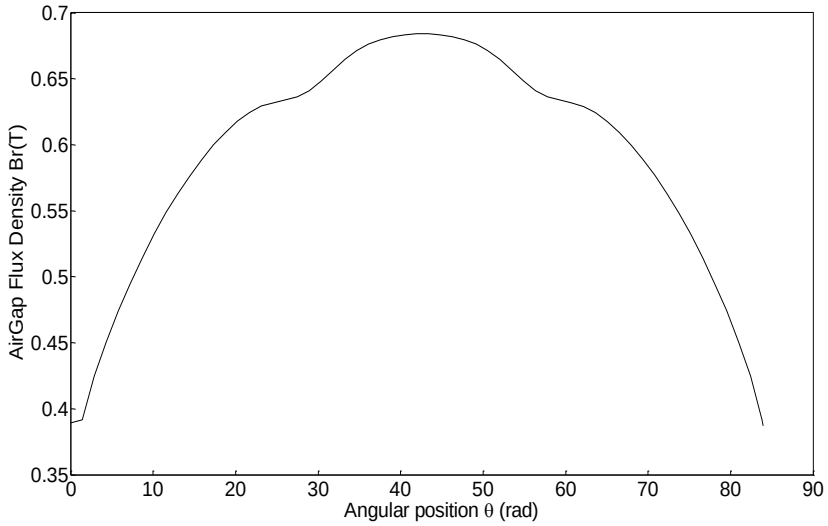

Figure 4.3. No-Load normal flux density just over the magnet surface in PMSG1, with un-saturated stator tooth tip

In order to calculate the spatial and temporal harmonics it is required to calculate normal flux density at various rotor positions as illustrated in Figure 4.4. The waveforms data are then analysed using two dimensional Fourier transform in Matlab using the analytical programs *FFT1*.m and *FFT2*.m, given in Appendix 2, to determine the amplitude of these harmonics. Due to the odd periodicity of flux distribution, even harmonics are absent. The most significant harmonics are given in Table. 4.1. Harmonics rotating CW and CCW with respect to rotor are indicated by - and + superscripts, respectively.

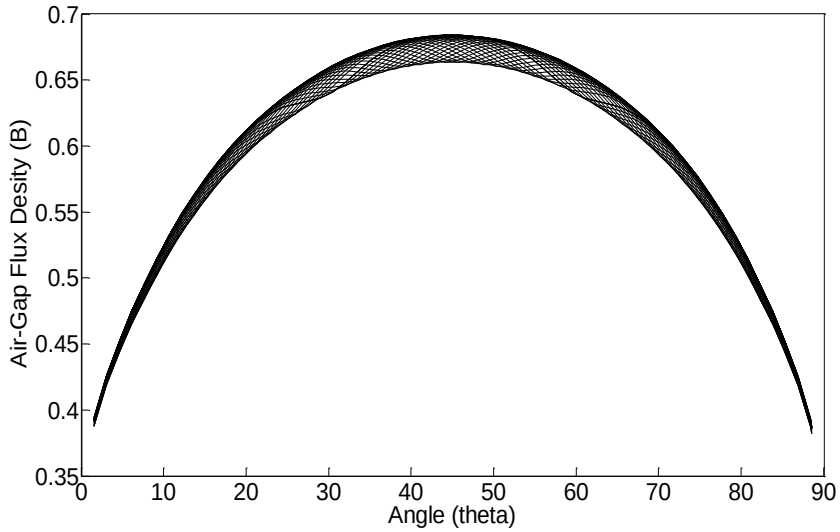

Figure 4.4. No-load normal flux density just over the magnet surface in PMSG1 for 30 rotor positions, with un-saturated stator tooth tip

Spatial order, q (λ_1 = 1 pole pitch)	Temporal order, k (f = 3000 Hz)			
	0	6	12	18
1	0.80550	0.000306^{-} 0.000101^{+}	0.0000349^{-} 0.0000424^{+}	0.0000321^{-}
3	0.19224	0.001069^{-} 0.0000544^{+}	0.0000232^{-} 0.0000293^{+}	0.0000219^{-}
5	0.10530	0.006309^{-} 0.000033^{+}	0.0000865^{-} 0.0000603^{+}	0.0000535^{-}
7	0.07179	0.004625^{-} 0.0000428^{+}	0.000207^{-} 0.0000176^{+}	0.0000246^{-}
9	0.05435	0.000784^{-} 0.0000092^{+}	0.000474^{-} 0.0000173^{+}	0.0000105^{-}
11	0.04362	0.000262^{-}	0.002562^{-}	0.0000388^{-}
13	0.03624	0.000115^{-}	0.00133^{-}	0.0000556^{-}
15	0.03083	0.000061^{-}	0.000219^{-}	0.000111^{-}
17	0.02666	0.000039^{-}	0.0000706^{-}	0.00067^{-}
19	0.02330	0.000032^{-}	0.000024^{-}	0.00027^{-}

Table 4.1. Amplitude of normal flux density harmonics, given in Tesla, over the magnet surface in PMSG1with un-saturated stator tooth tip, obtained from 30 magneto-static models. Positive superscripts indicate CCW rotating and negative superscripts indicate CW rotating harmonics with respect to the rotor

Table 4.1 indicates that among the harmonics of time order 6, those of space order 5 and 7 have the highest amplitudes; among the harmonics of time order 12, those of space order 11 and 13 have the highest amplitudes; and among the harmonics of time

order 18, those of space order 17 and 19 have the highest amplitudes. Almost all combinations of space and time orders are present in the rotor normal airgap flux density as partly shown in Table.4.1.

For the amplitude of harmonics which are obtained using analytical or static FEA methods as shown in Table 4.1, the rotor eddy current power losses due to harmonics with significant amplitude will be calculated using a method which will be termed as "current sheet rotor loss calculation method" here-after. As discussed earlier, in this method, the rotor eddy current power loss calculated using method described in section (3.7.1) is modified using equation (3.42) for the calculation of static rotor eddy current power loss due to significant harmonics taking into account reaction of eddy currents. The method is implemented in analytical programs *Loss1*.mw and *Harmonic1*.mw, given in Appendix 1. Using this method Table 4.2 presents the rotor eddy current power loss from the most significant CW rotating harmonics indicated in Table 4.1; empty cells indicate that the loss is < 0.5W. It is shown that power loss mainly occurs in the PM region, while a small proportion occurs in the rotor hub region. Harmonics with a time order of 6 and a spatial order of 5 and 7 cause the majority of the total power loss.

Spatial order, q	Temporal order, k (f = 3000 Hz)		
	6	12	18
3	2		
5	33		
7	7		
11		2.5	
13		0.5	
17			0.1
19			0.012
Power loss (FEA) = 45 W = 44.84 W in magnet + 0.16 W in hub			

Table 4.2. No-load Rotor eddy current power loss in PMSG1 with un-saturated tooth tip

4.3.2 **Non Linear Static FEA Solution for Saturated Stator Tooth Tip**

In the image of PMSG1 shown in Figure 4.5, the stator tooth tip becomes heavily saturated when the stator is assigned with a non-linear B-H curve. The spatial and temporal order harmonics are calculated using the airgap flux distributions data just

over the magnet surface (at r=27.15mm) calculated for 30 rotor positions, as illustrated in Figure 4.6. *FFT1*.m and *FFT2*.m programs in Appendix 2 are used and the results for the amplitude of harmonics are presented in Table 4.3. The corresponding rotor power losses due to each harmonic is calculated using current sheet rotor loss calculation method, and are presented in Table 4.4.

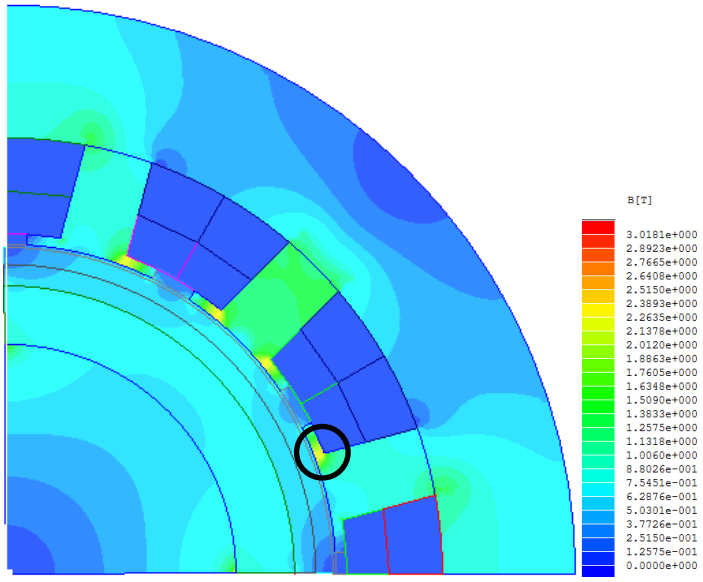

Figure 4.5. Magnet flux density distribution in PMSG1, with saturated stator tooth tip

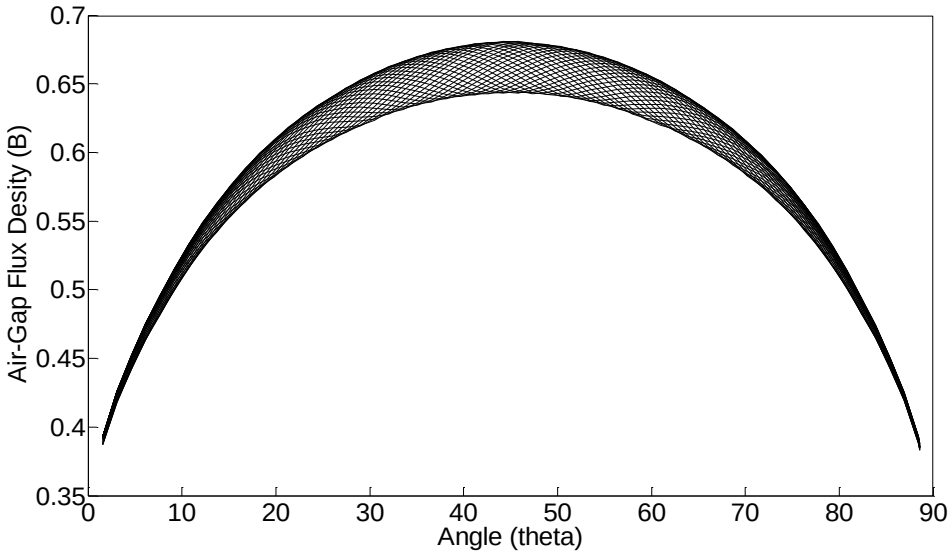

Figure 4.6. No-load normal flux density distribution just over the magnet surface of PMSG1with saturated stator tooth tip at 30 rotor positions

Spatial order, q (λ_1 = 1 pole pitch)	Temporal order, k (f = 3000 Hz)			
	0	6	12	18
1	0.79303	0.000161^{-} 0.0000719^{+}	0.000053^{-} 0.0000478^{+}	0.000033^{-} 0.0000303^{+}
3	0.19368	0.000179^{-} 0.0000275^{+}	0.000043^{-} 0.0000281^{+}	0.0000354^{-} 0.0000182^{+}
5	0.10609	0.010778^{-} 0.0000753^{+}	0.000202^{-} 0.0000653^{+}	0.00000812^{-} 0.0000424^{+}
7	0.07199	0.007689^{-} 0.0000397^{+}	0.00027^{-} 0.0000172^{+}	0.0000872^{-} 0.000014^{+}
9	0.05438	0.000676^{-} 0.0000201^{+}	0.000584^{-} 0.0000156^{+}	0.0000224^{-} 0.00000877^{+}
11	0.04360	0.000233^{-} 0.0000144^{+}	0.001635^{-} 0.0000132^{+}	0.0000758^{-} 0.0000091^{+}
13	0.03625	0.000114^{-} 0.0000142^{+}	0.000825^{-} 0.0000114^{+}	0.000139^{-} 0.00000796^{+}
15	0.03083	0.0000685^{-}	0.000257^{-}	0.000217^{-}
17	0.02665	0.0000489^{-}	0.0000851^{-}	0.000476^{-}
19	0.02331	0.0000351^{-}	0.0000321^{-}	0.000238^{-}

Table 4.3. Amplitudes of normal flux density harmonics in Tesla over the magnet surface of PMSG1 with saturated stator tooth tip, as obtained from 30 magneto-static models. Positive superscripts indicate CCW rotating harmonics while negative superscripts indicate CW rotating harmonics

Spatial order, q	Temporal order, k (f = 3000 Hz)		
	6	12	18
3	0.06		
5	96		
7	20		
11		1	
13		0.15	
17			0.05
19			0.0093
Power loss (FEA-nonlinear) = 117 W = 116.5 W in magnet + 0.5 W in hub			

Table 4.4. No-load rotor eddy current power loss in PMSG1 with saturated stator tooth tip

Table 4.4 indicates that for the saturated stator tooth tips of PMSG1, the rotor losses increase by approximately 3 times. Saturation occurs due to the small magnetic circuit in PM machine, and cause a virtual increase in slot opening, which induces harmonics with higher amplitudes and hence increases overall power loss. To demonstrate this a

comparison was made between the no-load rotor eddy current power losses in PMSG1, with a slot opening of 3mm and the stator permeability defined with non-linear BH curve given in Figure 4.1, against an equivalent machine with a slot opening of 4mm and a fixed stator permeability of 5000 (un-saturated stator tooth tip). The former produced an estimated total power loss of 117W, while the latter showed a loss of 126W (this calculation is shown in chapter 7). The similarity shows that the slot-opening virtually increased by 1mm due to saturation in the stator tooth tips.

4.4 Transient FEA Analysis for Rotor Eddy Current Power Loss Calculation

In order to compare power loss results obtained from static FEA linear (un-saturated stator tooth tip) and non-linear solutions (saturated stator tooth tip) with those from transient FEA solution, transient FEA analysis with a rotating mesh is used for the calculation of rotor eddy current power loss as described in chapter 3. The time step for the FEA transient solution was adjusted to be 6.84×10^{-7} s and about 60000 mesh elements (concentrated mainly in the rotor steel hub and magnets) were set.

Discrepancies in rotor eddy current power loss given by FEA static and FEA transient solutions are observed in case of saturated stator tooth tip and eddy currents assumed to be inductive limited; a comparison of the results is presented in Table 4.5.

Static FEA (un-saturated tooth tip)	Static FEA (saturated tooth tip)	Transient FEA (un-saturated tooth tip)	Transient FEA (saturated tooth tip)
45	117	43	120

Table 4.5. Rotor magnet flux tooth ripple loss comparison for 12-slot, 4-pole, PMSG1

Table 4.5 also indicates that agreement between static FEA and transient FEA solution for the machines with unsaturated stator tooth tip is due to negligible eddy current reaction field effect.

Further, the rotor power loss waveform is also shown in Figure 4.7; the power losses given in Table 4.5 are calculated by taking the average values of these waveforms.

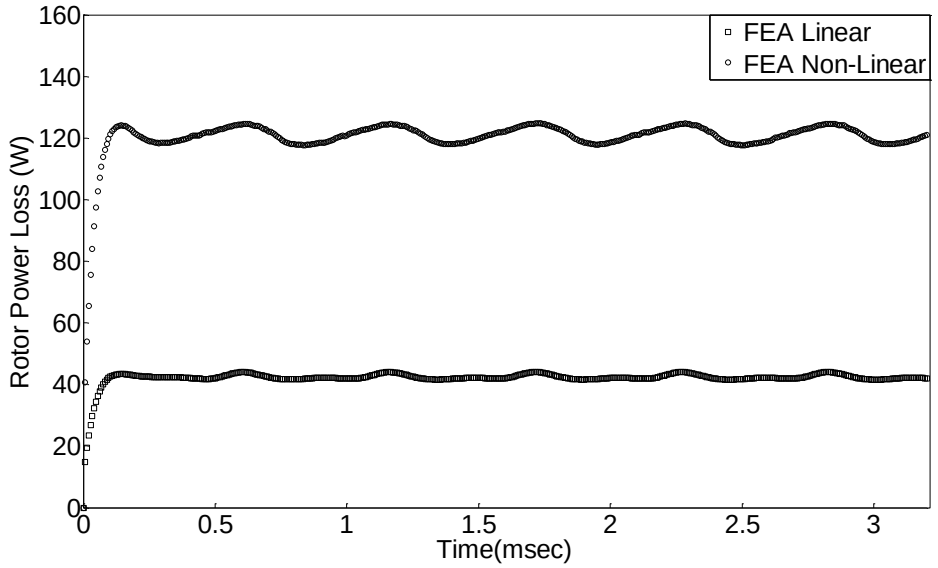

Figure 4.7. Comparison for rotor eddy current power loss in PMSG1 with linear (un-saturated stator tooth tip) and non-linear (saturated stator tooth tip) calculated using transient FEA

4.5 Analytical Method

In this section three analytical methods presented by Zhu and Howe (1993), Gieras (2004) and Ẑarko et al (2006) are developed to calculate the waveforms for magnetic permeance and airgap flux density in PMSG1. The amplitude of each rotating harmonic in space and time is then calculated by transforming the Fourier series for the airgap flux density due to magnet mmf into rotor reference frame. Using the current sheet method the rotor eddy current power loss due to each harmonic is calculated. Finally the accuracy of each analytical method is compared with static and transient FEA methods.

4.5.1 **Magnet Field Distribution in Slotless PM Machine**

The magnetic field distribution in slotless PM machines is calculated using the method developed by Zhu et al (2002). We consider a machine in which the permanent magnets are parallel magnetised with respect to the centre ‘o’ and are of ring shaped, as shown in Figure 4.8. The rotor, permanent magnet and airgap regions are represented by 1, 2 and 3, respectively.

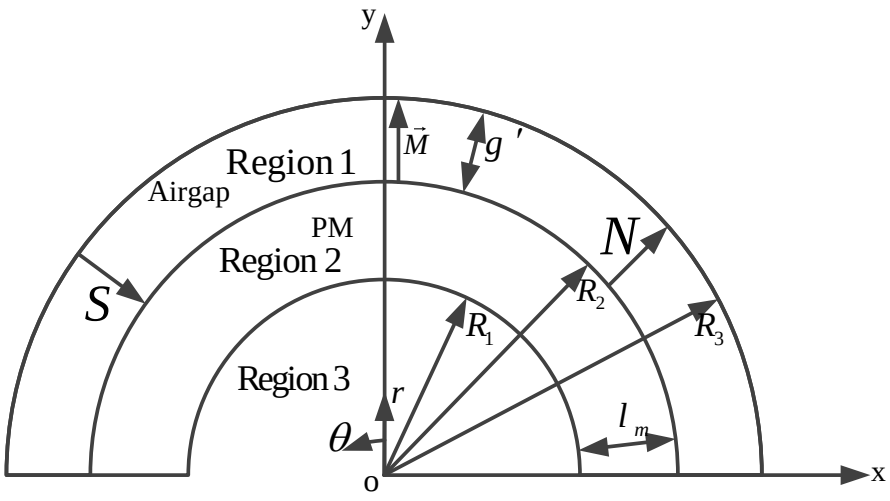

Figure 4.8. Internal rotor PM machine topology

Figure 4.8a shows direction of the vector $\vec{M}$ for parallel magnetization. In this case the direction of magnetisation is always parallel to the centreline of the magnet arc. Hence both radial and tangential components of the vector $\vec{M}$ exist.

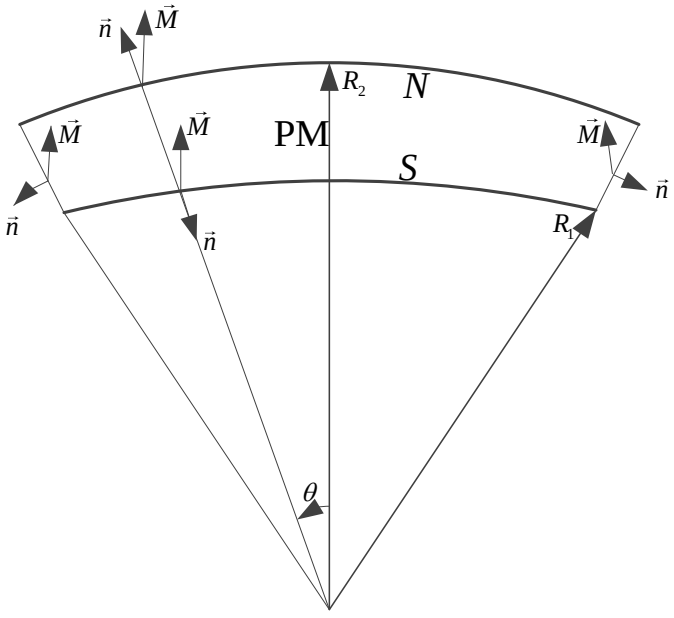

Figure 4.8a. Direction of parallel magnetization

The magnetic field in the airgap and permanent magnet regions is governed by two different equations. In the airgap region the magnetic flux density $\vec{B}$ and the field intensity $\vec{H}$ is related as:

$$\vec{B_1} = \mu_0 \vec{H_1} \tag{4.1}$$

whereas in the permanent magnet region the relationship is given by:

$$\vec{B_2} = \mu_0 \mu_r \vec{H_2} + \mu_0 \vec{M} \tag{4.2}$$

In equation (4.2) $\vec{M}$ is the magnetisation vector and μ_0 and μ_r are the permeability of free space and relative permeability of the permanent magnet, respectively. For magnets with linear magnetisation characteristics (shown in Figure 3.1), the magnetization $\vec{M}$ in terms of remanent flux density $\vec{B}_r$ of the magnetic is written as:

$$\vec{M} = \frac{\vec{B_r}}{\mu_0} \tag{4.3}$$

For the magnetostatic field in a current-free region, the divergence and curl of $\vec{B}$ in free space are:

$$\nabla \cdot \vec{B} = 0 \tag{4.4}$$

$$\nabla \times \vec{B} = 0 \tag{4.5}$$

The magnetic flux density can be expressed as a gradient of a scalar field by assuming:

$$\vec{B} = -\mu_0 \mu_r \nabla \varphi \tag{4.6}$$

The magnetostatic field in the airgap in terms of magnetic scalar potential can be obtained by substituting equation (4.6) in (4.4):

$$\nabla \left(\nabla \varphi_1 \right) = \nabla^2 \varphi_1 = 0 \tag{4.7}$$

In the permanent magnet, for field calculation a magnetised body can be replaced by an equivalent fictitious magnetization volume charge (Hurray, 2010) as:

$$\psi_m = -\nabla \cdot \left(\mu_0 \vec{M} \right) \tag{4.8}$$

From (Hurray, 2010), the Maxwell equation which relates the field $\vec{B}$ to its source magnetisation charge is:

$$\nabla \cdot \vec{B} = \psi_m \tag{4.9}$$

Substituting equations (4.6) and (4.8) in (4.9) will result:

$$\nabla\left(-\mu_0\mu_r\nabla\varphi_2\right)=-\nabla\cdot\left(\mu_0\vec{M}\right) \tag{4.10}$$

Thus the scalar magnetic potential in the permanent magnet can be written as:

$$\Delta\varphi_2=\frac{1}{\mu_r}\nabla\cdot\vec{M} \tag{4.11}$$

The magnetisation vector $\vec{M}$ in polar coordinates can be written as:

$$M=M_r\vec{a}_r+M_\theta\vec{a}_\theta \tag{4.12}$$

Since the direction of magnetisation is always parallel to the centre line of the magnet arc, both radial and tangential components of vector $\vec{M}$ are non-zero; according to (Zhu et al., 2002) their waveforms are presented in Figures 4.9 and 4.10, respectively.

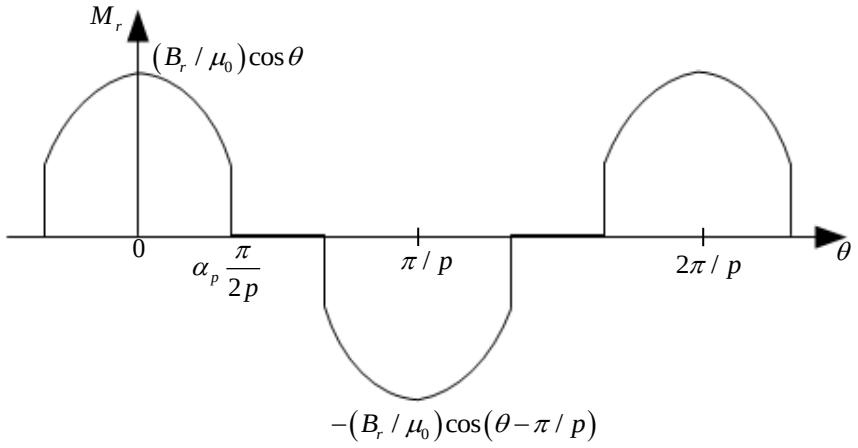

Figure 4.9. Waveform of radial magnetization component M_r

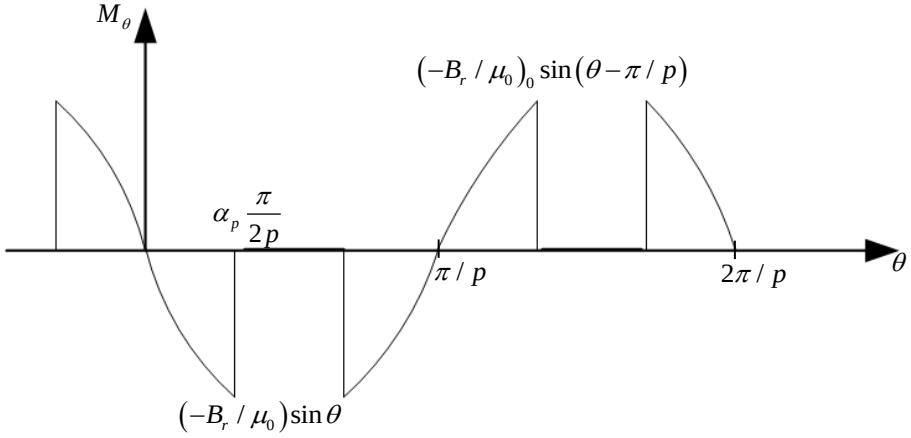

Figure 4.10. Waveform of tangential magnetization component M_θ

In Figures 4.9 and 4.10 α_p is pole arc to pole pitch ratio. For parallel magnetization in permanent magnets the components M_r and M_θ in Figures 4.9 and 4.10 can be expressed as Fourier series:

$$M_r = \sum_{n=1,3,5...}^{\infty} M_{rn} \cos(np\theta) \tag{4.13}$$

$$M_\theta = \sum_{n=1,3,5...}^{\infty} M_{\theta n} \sin(np\theta) \tag{4.14}$$

In equations (4.13) and (4.14), p is the number of pole pairs and θ is the angular displacement from the magnet centre-line. The series coefficients M_{rn} and $M_{\theta n}$ are given by:

$$M_{rn} = \frac{B_r}{\mu_0} \alpha_p \left(A_{1n} + A_{2n} \right) \tag{4.15}$$

$$M_{\theta n} = \frac{B_r}{\mu_0} \alpha_p \left(A_{1n} - A_{2n} \right) \tag{4.16}$$

In equations (4.15) and (4.16), α_p is pole arc to pole pitch ratio and A_{1n} and A_{2n} can be calculated according to (Zhu et al., 2002) as:

$$A_{1n} = \frac{\sin\left((np+1)\alpha_p \frac{\pi}{2p} \right)}{(np+1)\alpha_p \frac{\pi}{2p}} \tag{4.17}$$

For $np = 1$, $A_{2n} = 1$ and for $np \neq 1$

$$A_{2n} = \frac{\sin\left((np-1)\alpha_p \frac{\pi}{2p} \right)}{(np-1)\alpha_p \frac{\pi}{2p}} \tag{4.18}$$

According to equation (4.7), Laplace's equation governs the scalar magnetic potential in the airgap region, which in cylindrical coordinates is written as:

$$\frac{\partial^2 \varphi_1}{\partial r^2} + \frac{1}{r}\frac{\partial \varphi_1}{\partial r} + \frac{1}{r^2}\frac{\partial^2 \varphi_1}{\partial \theta^2} = 0 \tag{4.19}$$

In the permanent magnet, Poisson's equation (4.11) governs the scalar magnetic potential. The divergence of the magnetization vector, with its radial and tangential components in equation (4.13) and (4.14) is given by:

$$\nabla \cdot \vec{M} = \frac{1}{r} M_r + \frac{\partial M_r}{\partial r} + \frac{1}{r}\frac{\partial M_\theta}{\partial \theta} = \sum_{n=1,3,5...}^{\infty} \frac{1}{r} M_n \cos\left(np\theta\right) \tag{4.20}$$

In equation (4.20), M_n is defined as:

$$M_n = M_{rn} + npM_{\theta n} \tag{4.21}$$

Combining equations (4.11) and (4.20) results in:

$$\frac{\partial^2 \varphi_2}{\partial r^2} + \frac{1}{r}\frac{\partial \varphi_2}{\partial r} + \frac{1}{r^2}\frac{\partial^2 \varphi_2}{\partial \theta^2} = \frac{1}{\mu_r} \sum_{n=1,3,5...}^{\infty} \frac{1}{r} M_n \cos\left(np\theta\right) \tag{4.22}$$

The relationship between the radial and tangential components of the field intensity $\vec{H}$ and the scalar magnetic potential φ is:

$$H_r = -\frac{\partial \varphi}{\partial r} \tag{4.23}$$

$$H_\theta = -\frac{1}{r}\frac{\partial \varphi}{\partial \theta} \tag{4.24}$$

4.5.2 **General Solution in Polar Coordinates**

In a PM machine the scalar magnetic potential distribution in the airgap is governed by Laplace's equation in two dimensions, which can be solved using a separation of variable method (Sadiku, 2001). This method seeks a solution which may be broken up into a product of functions, each involving only one of the variables (Žarko, 2004). The unknown scalar magnetic potential $\varphi\left(r,\theta\right)$ is first written as:

$$\varphi_1 = R(r)P\left(\theta\right) \tag{4.25}$$

Substituting equation (4.25) in (4.19) and dividing by RP / r^2 will result in:

$$\frac{r^2}{R}\frac{\partial^2 R}{\partial r^2} + \frac{r}{R}\frac{\partial R}{\partial r} = -\frac{1}{P}\frac{\partial^2 P}{\partial \theta^2} = \Upsilon^2 \tag{4.26}$$

In equation (4.26), Υ is the separation constant. The separated equations are:

$$\frac{\partial^2 P}{\partial \theta^2} + \Upsilon^2 P = 0 \tag{4.27}$$

$$r^2 \frac{\partial^2 R}{\partial r^2} + r \frac{\partial R}{\partial r} - \Upsilon^2 P = 0 \tag{4.28}$$

The known general solution for equation (4.27) is given as:

$$P(\theta) = C_1 \cos(\Upsilon\theta) + C_2 \sin(\Upsilon\theta) \tag{4.29}$$

Due to even periodicity of magnetisation distribution, equation (4.29) with $\Upsilon = np$ and $C_2 = 0$, can be written as:

$$P(\theta) = C_1 \cos(\Upsilon\theta) \tag{4.30}$$

For the airgap region equation (4.28), which is the Cauchy-Euler equation, is solved by substituting $r = e^u$ and reducing to an equation with constant coefficients as:

$$R(r) = C_3 r^{np} + C_4 r^{-np},\ n = 1,2,3,... \tag{4.31}$$

Substituting equations (4.30) and (4.31) in (4.25) results in:

$$\varphi_{n1}(r,\theta) = \left(A_{n1} r^{np} + B_{n1} r^{-np}\right)\cos(np\theta) \tag{4.32}$$

In equation (4.32), A_{n1} and B_{n1} are constants which need to be determined. According to the superposition principle a linear combination of the solutions $\varphi_{n1}(r,\theta)$, each with different values of n and with arbitrary coefficients A_{n1} and B_{n1}, is also a solution of equation (4.19). This solution can be represented as an infinite series (Žarko, 2004):

$$\varphi_1(r,\theta) = \sum_{n=1}^{\infty}\left(A_{n1} r^{np} + B_{n1} r^{-np}\right)\cos(np\theta) \tag{4.33}$$

The solution of the Poisson equation (4.22) in the permanent magnet is the sum of the general solution of the homogeneous equation $\Delta\varphi_2 = 0$ and any particular solution of the inhomogeneous equation (4.22). The general solution of the homogeneous equation is referred to as the complementary solution (Boyce and Diprima, 1986) and is the same as the solution of Laplace's equation (4.33):

$$\varphi_{2c}(r,\theta)=\sum_{n=1}^{\infty}\left(A_{n2}r^{np}+B_{n2}r^{-np}\right)\cos(np\theta) \tag{4.34}$$

The solution for the inhomogeneous equation (4.22) is called the particular solution (Boyce and Diprima, 1986) and is assumed to be of the form:

$$\varphi_{2p}(r,\theta)=\sum_{n=1}^{\infty}C_1 r\cos(np\theta) \tag{4.35}$$

The value of constant C_1 is calculated by substituting equation (4.35) in (4.22) as:

$$C_1=\frac{1}{1-(np)^2}\frac{M_n}{\mu_r} \tag{4.36}$$

$$\varphi_{2p}(r,\theta)=\sum_{n=1,3,5...}^{\infty}\frac{M_n}{\mu_r\left(1-(np)^2\right)}r\cos(np\theta) \tag{4.37}$$

The general form of the solution for equation (4.22), with $np\neq 1$, is then:

$$\begin{aligned}\varphi_2(r,\theta)=\varphi_{2c}(r,\theta)+\varphi_{2p}(r,\theta)&=\sum_{n=1}^{\infty}\left(A_{n2}r^{np}+B_{n2}r^{-np}\right)\cos(np\theta)\\&+\sum_{n=1,3,5...}^{\infty}\frac{M_n}{\mu_r\left(1-(np)^2\right)}r\cos(np\theta)\end{aligned} \tag{4.38}$$

The boundary conditions for the PM machine shown in Figure 4.8 are defined as:

$$H_{\theta_1}(r,\theta)\big|_{r=R_3}=0 \qquad H_{\theta_2}(r,\theta)\big|_{r=R_1}=0$$

$$B_{r_1}(r,\theta)\big|_{r=R_2}=B_{r_2}(r,\theta)\big|_{r=R_2} \quad H_{\theta_1}(r,\theta)\big|_{r=R_2}=H_{\theta_2}(r,\theta)\big|_{r=R_2} \tag{4.39}$$

The field components in equation (4.39) can be calculated by substituting solutions for the scalar magnetic potential from equations (4.33) and (4.38) in equations (4.23) and (4.24) respectively, for the calculation of the unknown coefficients A_{n1}, B_{n1}, A_{n2}, B_{n2}. These solutions for the field components according to (Zhu et al., 2002) are given by the following equations:

For an internal rotor PM machine, in the airgap, $np \neq 1$

$$B_{sr}(r,\theta) = \sum_{n=1,3,5\ldots}^{\infty} \frac{\mu_0 M_n}{\mu_r} \frac{np}{(np)^2 - 1} \left(\left(\frac{r}{R_3}\right)^{np-1} \left(\frac{R_2}{R_3}\right)^{np+1} + \left(\frac{R_2}{r}\right)^{np+1} \right) \left(\frac{(A_{3n} - 1) + 2\left(\frac{R_1}{R_2}\right)^{np+1} - (A_{3n} + 1)\left(\frac{R_1}{R_2}\right)^{2np}}{\frac{\mu_r + 1}{\mu_r}\left(1 - \left(\frac{R_1}{R_3}\right)^{2np}\right) - \frac{\mu_r - 1}{\mu_r}\left(\left(\frac{R_2}{R_3}\right)^{2np} - \left(\frac{R_1}{R_2}\right)^{2np}\right)} \right) \cos(np\theta) \tag{4.40}$$

$$B_{s\theta}(r,\theta) = \sum_{n=1,3,5\ldots}^{\infty} \frac{\mu_0 M_n}{\mu_r} \frac{np}{(np)^2 - 1} \left(-\left(\frac{r}{R_3}\right)^{np-1} \left(\frac{R_2}{R_3}\right)^{np+1} + \left(\frac{R_2}{r}\right)^{np+1} \right) \left(\frac{(A_{3n} - 1) + 2\left(\frac{R_1}{R_2}\right)^{np+1} - (A_{3n} + 1)\left(\frac{R_1}{R_2}\right)^{2np}}{\frac{\mu_r + 1}{\mu_r}\left(1 - \left(\frac{R_1}{R_3}\right)^{2np}\right) - \frac{\mu_r - 1}{\mu_r}\left(\left(\frac{R_2}{R_3}\right)^{2np} - \left(\frac{R_1}{R_2}\right)^{2np}\right)} \right) \sin(np\theta) \tag{4.41}$$

For an internal rotor PM machine, in the permanent magnets, $np \neq 1$

$$B_{sr}(r,\theta) = \sum_{n=1,3,5\ldots}^{\infty} \mu_0 M_n \frac{np}{(np)^2 - 1} \left(\left(\frac{r}{R_2}\right)^{np-1} + \left(\frac{R_1}{R_2}\right)^{np-1} + \left(\frac{R_1}{r}\right)^{np+1} \right) \left(\frac{\left(A_{3n} - \frac{1}{\mu_r}\right) + \left(\frac{R_2}{R_3}\right)^{2np} + \left(1 + \frac{1}{\mu_r}\right)\left(\frac{R_1}{R_2}\right)^{np+1}\left(\frac{R_2}{R_3}\right)^{2np} - \left(A_{3n} + \frac{1}{\mu_r}\right) - \frac{\left(1 - \frac{1}{\mu_r}\right)\left(\frac{R_1}{R_2}\right)^{np+1}}{\frac{\mu_r + 1}{\mu_r}\left(1 - \left(\frac{R_1}{R_3}\right)^{2np}\right) - \frac{\mu_r - 1}{\mu_r}\left(\left(\frac{R_2}{R_3}\right)^{2np} - \left(\frac{R_1}{R_2}\right)^{2np}\right)}}{\frac{\mu_r + 1}{\mu_r}\left(1 - \left(\frac{R_1}{R_3}\right)^{2np}\right) - \frac{\mu_r - 1}{\mu_r}\left(\left(\frac{R_2}{R_3}\right)^{2np} - \left(\frac{R_1}{R_2}\right)^{2np}\right)} \right) \cos(np\theta)$$

$$+ \sum_{n=1,3,5\ldots}^{\infty} \mu_0 M_n \frac{np}{(np)^2 - 1} \left(\left(\frac{R_1}{r}\right)^{np+1} + A_{3n} \right) \cos(np\theta) \tag{4.42}$$

$$B_{s\theta}(r,\theta) = \sum_{n=1,3,5\ldots}^{\infty} -\mu_0 M_n \frac{np}{(np)^2-1}\left(\left(\frac{r}{R_2}\right)^{np-1} - \left(\frac{R_1}{R_2}\right)^{np-1}\left(\frac{R_1}{r}\right)^{np+1}\right)$$
$$\left(\frac{\left(A_{3n}-\frac{1}{\mu_r}\right)+\left(\frac{R_2}{R_3}\right)^{2np}+\left(1+\frac{1}{\mu_r}\right)\left(\frac{R_1}{R_2}\right)^{np+1}\left(\frac{R_2}{R_3}\right)^{2np}-\left(A_{3n}+\frac{1}{\mu_r}\right)-}{\frac{\mu_r+1}{\mu_r}\left(1-\left(\frac{R_1}{R_3}\right)^{2np}\right)-\frac{\mu_r-1}{\mu_r}\left(\left(\frac{R_2}{R_3}\right)^{2np}-\left(\frac{R_1}{R_2}\right)^{2np}\right)}\right.$$
$$\left.\frac{\left(1-\frac{1}{\mu_r}\right)\left(\frac{R_1}{R_2}\right)^{np+1}}{\frac{\mu_r+1}{\mu_r}\left(1-\left(\frac{R_1}{R_3}\right)^{2np}\right)-\frac{\mu_r-1}{\mu_r}\left(\left(\frac{R_2}{R_3}\right)^{2np}-\left(\frac{R_1}{R_2}\right)^{2np}\right)}\right)\sin(np\theta)$$
$$+\sum_{n=1,3,5\ldots}^{\infty}\mu_0 M_n\frac{np}{(np)^2-1}\left(\left(\frac{R_1}{r}\right)^{np+1}-A_{3n}\right)\sin(np\theta) \qquad (4.43)$$

For parallel magnetization, $np \neq 1$

$$A_{3n} = \left(np-\frac{1}{np}\right)\frac{M_{rn}}{M_n}+\frac{1}{np}$$

The radial and tangential component of the airgap flux density in a slotless PM machine is of particular interest for the purpose of rotor eddy current power loss calculation in slotted PM machines. The slotless airgap flux density can be multiplied with the permeance functions developed by (Zhu et al., 1993), (Gieras, 2004) and (Ẑarko et al., 2006) to cater for the effect of slotting.

For internal rotor motors radii within the airgap lie in the range:

$$R_2 < r < R_3$$

The radial and tangential components of field distribution on the surface of the magnet at $r = R_2$ are calculated using equations (4.40) and (4.41) and illustrated in Figure 4.11.

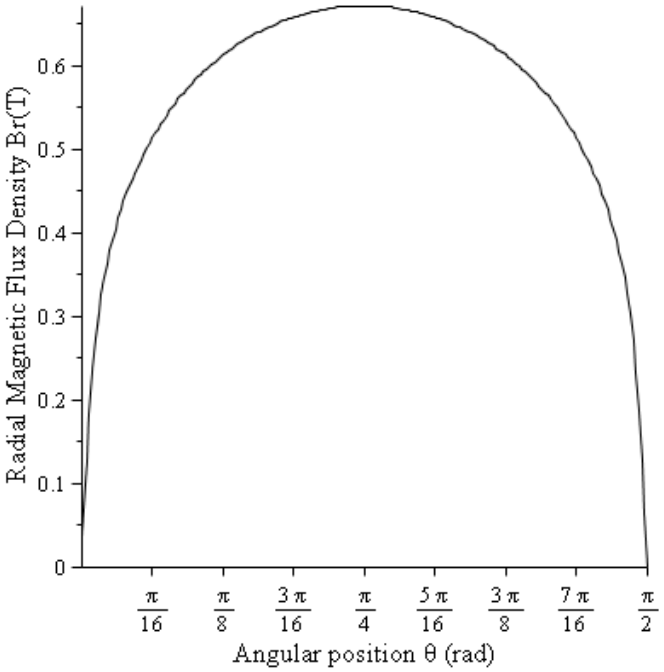

(a)

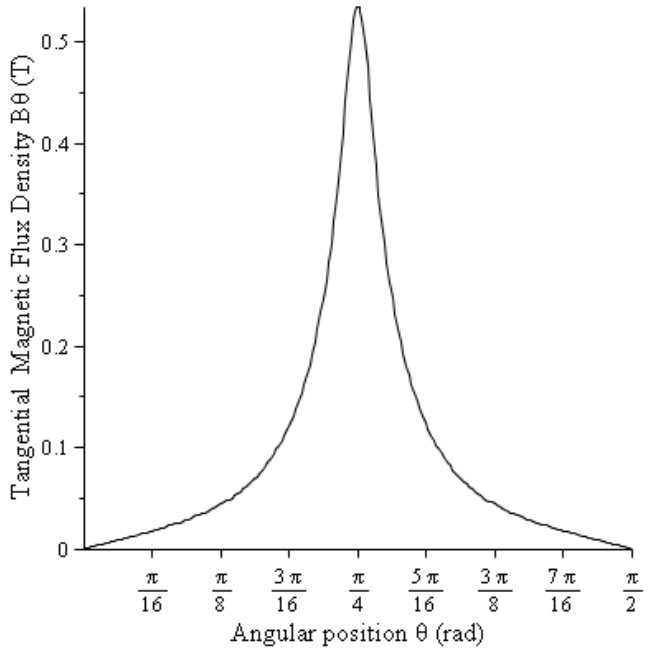

(b)

Figure 4.11. Waveforms of the flux density on the surface of the magnet of a slotless, surface PM machine with parallel magnetized magnets: (a) radial component, (b) tangential component

4.6 Two Dimensional Permeance Methods

Generally, the airgap flux density distribution $\mathbf{B}_g(r,\theta)$ in a slotless PM machine can be modified to cater for the slotting effect. This is achieved by multiplying the airgap flux density $\mathbf{B}_s(r,\theta)$ of the slotless PM machine, with the relative permeance function $\lambda(r,(\theta-\omega t))$ as:

$$\mathbf{B}_g(r,\theta) = \lambda(r,(\theta-\omega t))\mathbf{B}_s(r,\theta) \tag{4.44}$$

In equation (4.44), ω is the angular speed of the rotor. As stated earlier, the permeance function calculated in (Zhu and Howe, 1993; Gieras, 2004) can only give the radial component $B_{gr}(r,\theta)$ of a slotted PM machine, whereas the tangential component is not considered. The permeance function calculated by (Ẑarko et al., 2006) has both radial and tangential components, which can calculate the effect of slotting on both radial $B_{gr}(r,\theta)$ and tangential $B_{g\theta}(r,\theta)$ component of airgap flux density.

4.6.1 **Relative Permeance Method: (Zhu and Howe, 1993)**

Zhu and Howe (1993) used a conformal transformation that transforms the complex slotted geometry into slotless geometry. The relative permeance function $\lambda_{RP}(r,\theta)$ is calculated by analysing a model of one slot of the PM machine. This permeance function is multiplied with the radial component of airgap flux density $B_{sr}(r,\theta)$ to generate the modified flux density. According to equation (4.44) this can be written in rotor reference frame as:

$$B_{gr}(r,\theta) = \lambda_{RP}(r,(\theta-\omega t))\cdot B_{sr}(r,\theta) \tag{4.45}$$

$$B_{g\theta}(r,\theta) = B_{s\theta}(r,\theta) \tag{4.46}$$

The permeance function $\lambda_{RP}(r,\theta)$ according to (Zhu and Howe, 1993) can be given in the rotor reference frame as:

$$\lambda_{RP}(r,\theta)=\Lambda_0(r)+\sum_{n=1}^{\infty}\Lambda_n(r)\cos\left(nQ_s(\theta-\omega_r t)\right) \tag{4.47}$$

In equation (4.47), Q_s is the number of slots, $\Lambda_0(r)$ and $\Lambda_n(r)$ are the Fourier coefficients which are calculated as:

$$\Lambda_0(r)=\frac{1}{k_c}\left(1-1.6\beta(r)\frac{b_0}{\tau_t}\right) \tag{4.48}$$

$$\Lambda_n(r)=-\beta(r)\frac{4}{\pi n}\left(0.5+\frac{\left(n\frac{b_0}{\tau_t}\right)^2}{0.78125-2\left(n\frac{b_0}{\tau_t}\right)^2}\right)\sin\left(1.6\pi n\frac{b_0}{\tau_t}\right) \tag{4.49}$$

In the above equations (4.48) and (4.49), b_0 is the stator slot opening angle in radians, $\beta(r)$ is the variation in the airgap flux due to slotting and k_c is the Carter's coefficient. The coefficient k_c using an effective airgap is given by:

$$k_c=\frac{\tau_t}{\tau_t-\gamma g'} \tag{4.50}$$

In equation (4.50), the tooth pitch τ_t and slot-opening factor γ are calculated as:

$$\tau_t=\frac{2\pi R_3}{Q_s} \tag{4.51}$$

$$\gamma=\frac{4}{\pi}\left(\frac{b_0}{2g_e}\tan^{-1}\left(\frac{b_0}{2g_e}\right)-\ln\sqrt{1+\left(\frac{b_0}{2g_e}\right)^2}\right) \tag{4.52}$$

The reduction in flux per pole due to slotting is catered for by calculating a corrected airgap g_e and a corrected stator bore radius R_{se} as:

$$g_e=g+\left(k_c-1\right)g',\qquad R_{se}=R_3+\left(k_c-1\right)g' \tag{4.53}$$

In equation (4.53), g is the original airgap and g' is the effective airgap calculated as:

$$g'=g+\frac{h_m}{\mu_r} \tag{4.54}$$

In equation (4.54), h_m is the magnet thickness, the factor $\beta(r)$ in equations (4.48) and (4.49) is given as:

$$\beta(r) = \frac{1}{2}\left(1 - \frac{1}{\sqrt{1+\left(\frac{b_0}{2g'}\right)^2\left(1+x^2\right)}}\right) \tag{4.55}$$

In equation (4.55) the value of x is determined as:

$$y\frac{\pi}{b_0} = \frac{1}{2}\ln\left(\frac{\sqrt{a^2+x^2}+x}{\sqrt{a^2+x^2}-x}\right) + \frac{2g'}{b_0}\tan^{-1}\frac{2g'}{b_0}\frac{x}{\sqrt{a^2+x^2}} \tag{4.56}$$

In equation (4.56) the value of a and y is determined as:

$$a^2 = 1+\left(\frac{2g'}{b_0}\right)^2,\ y = r - R_3 + g'$$

The permeance function for one-pole pitch, radial component of airgap flux density in the slotless PM machine, and the airgap flux density in the slotted PM machine (according to equation 4.45) are illustrated in Figures 4.12, 4.13 and 4.14, respectively.

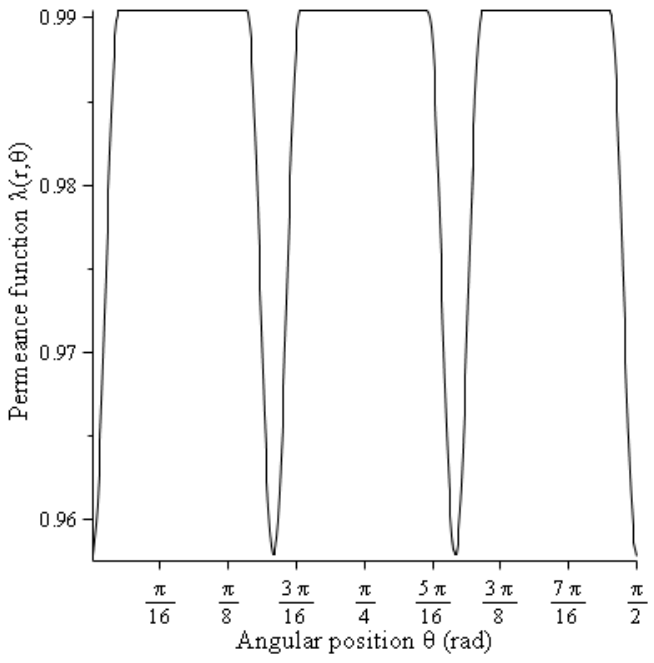

Figure 4.12. Relative permeance function $\lambda_{RP}(r,\theta)$ in PMSG1

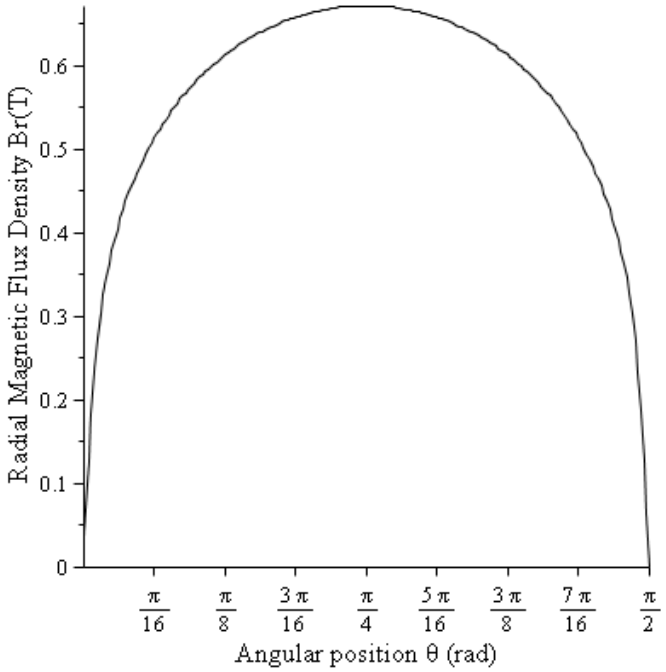

Figure 4.13. Radial airgap flux density in a slotless version of PMSG1

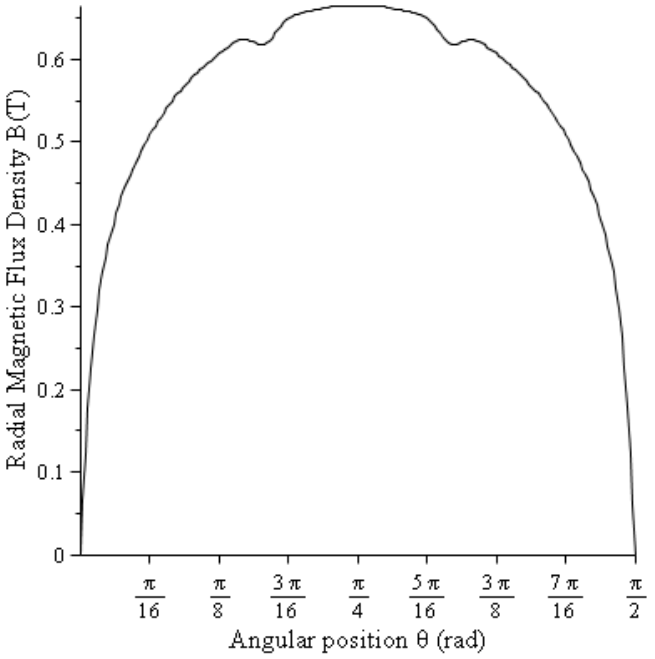

Figure 4.14. Radial airgap flux density in the slotted version of PMSG1

In equation (4.45), the Fourier series of the airgap flux density distribution is extended for the calculation of harmonic amplitude using analytical program *Zhu*.mw in Appendix 1. The results are presented in Table 4.6.

Spatial order, q (λ_1 = 1 pole pitch)	Temporal order, k (f = 3000 Hz)			
	0	6	12	18
1	0.7789	0.00037^- 0.00022^+	0.00009^- 0.00006^+	0.00003^-
3	0.1684	0.00077^- 0.00015^+	0.00012^- 0.00005^+	0.000039^-
5	0.0815	0.0036^- 0.0001^+	0.00019^- 0.00004^+	0.000051^-
7	0.0492	0.0036^- 0.00008^+	0.00031^- 0.00003^+	0.000068^-
9	0.0332	0.00077^- 0.00006^+	0.00065^-	0.000095^-
11	0.0239	0.00037^-	0.00302^-	0.00014^-
13	0.0179	0.00022^-	0.00302^-	0.000233^-
15	0.0137	0.00015^-	0.00065^-	0.00048^-
17	0.0106	0.00011^-	0.00031^-	0.0022^-
19	0.00837		0.00019^-	0.0022^-

Table 4.6. Amplitudes of normal flux density harmonics, in Tesla, over the magnet surface of PMSG1 obtained from relative permeance method by Zhu and Howe, (1993). Positive superscripts indicate CCW rotating harmonics and negative superscripts indicate CW rotating harmonics

Using a current sheet rotor loss calculation method, rotor eddy current power loss due to the most significant harmonics indicated in Table 4.6 has been calculated. The results are presented in Table 4.7, with empty cells showing power loss to be <0.5W.

Spatial order, q	Temporal order, k (f = 3000 Hz)		
	6	12	18
3	1		
5	11		
7	4.4		
11		3.3	
13		2.04	
17			1.1
19			0.8
Power loss (Zhu and Howe, (1993), *RP* method) = 23 W = 22.95 W in magnet + 0.055 W in hub			

Table 4.7. No-Load Rotor eddy current power loss due to CW harmonics in PMSG1

4.6.2 **Relative Permeance Method: (Gieras, 2004)**

Gieras (2004) calculated the permeance function $\lambda_{GR}(r,\theta)$, which is multiplied with the radial component $B_{sr}(r,\theta)$ and tangential component $B_{s\theta}(r,\theta)$ of airgap flux density and according to equation (4.45) is written as:

$$B_{gr}(r,\theta)=\frac{B_{sr}(r,\theta)}{k_c}+\lambda_{GR}\left(r,(\theta-\omega t)\right)\cdot B_{sr}(r,\theta) \tag{4.57}$$

$$B_{g\theta}(r,\theta)=B_{s\theta}(r,\theta) \tag{4.58}$$

The permeance function $\lambda_{GR}(r,\theta)$ is developed using a slightly different approach from that described in (Zhu and Howe, 1993). The function in the rotor reference frame according to (Gieras, 2004) is given as:

$$\lambda_{GR}(\theta)=-2\gamma\frac{g'}{\tau_s}\sum_{n=1}^{\infty}s_{ok}^2\cos\left(nQ_s(\theta-\omega_r t)\right) \tag{4.59}$$

In equation (4.59), s_{ok} is the slot-opening factor and is given as:

$$s_{ok}=\frac{\sin\left(n\rho\pi\frac{b_0}{2\tau_s}\right)}{n\rho\pi\frac{b_0}{2\tau_s}} \tag{4.60}$$

In equation (4.60), τ_s is the slot pitch and ρ is calculated as:

$$\rho=\frac{\frac{b_0}{2\tau_s}}{5+\frac{b_0}{2\tau_s}}\frac{2\sqrt{1+\left(\frac{b_0}{2\tau_s}\right)^2}}{\sqrt{1+\left(\frac{b_0}{2\tau_s}\right)^2}-1} \tag{4.61}$$

Equations (4.59) and (4.57) can be used to calculate the permeance function distribution over one-pole pitch and the airgap flux density distribution in the slotted PMSG1, as illustrated in Figures 4.15 and 4.16, respectively.

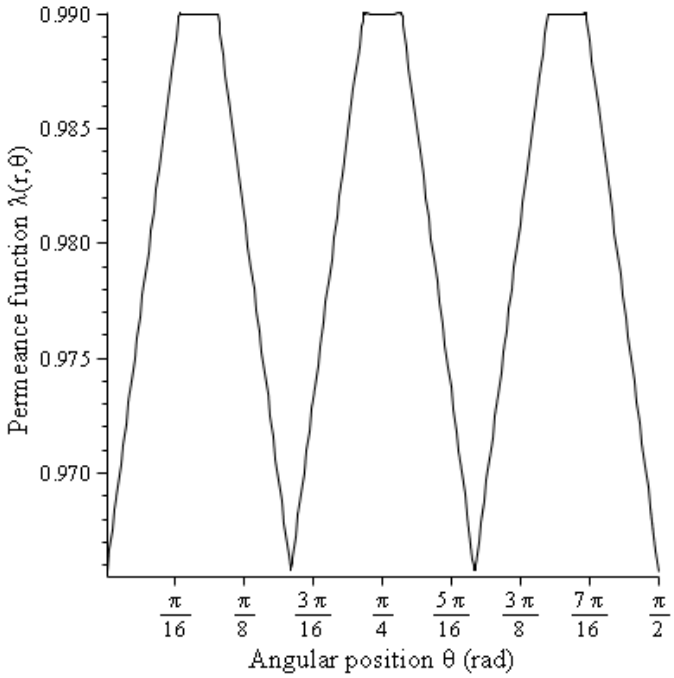

Figure 4.15. Relative permeance function $\lambda_{GR}(r,\theta)$ in PMSG1

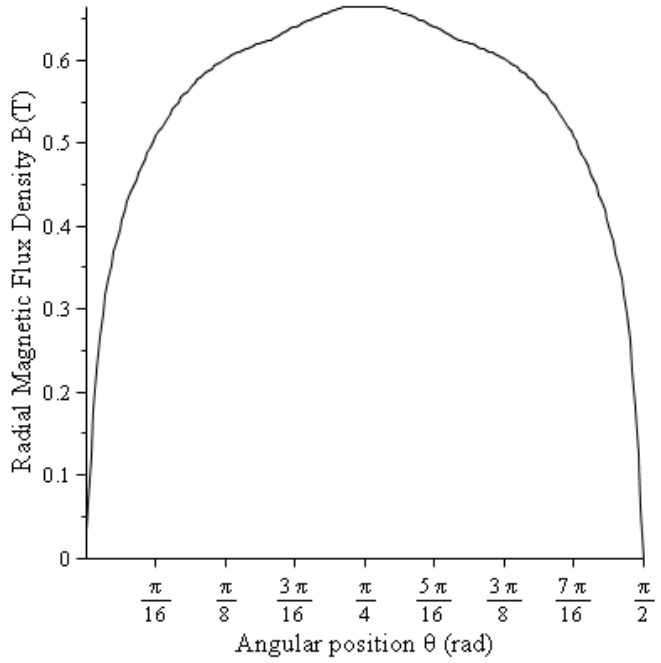

Figure 4.16. Radial airgap flux density in PMSG1

The amplitudes of magnet flux tooth ripple harmonics are calculated by extending equation (4.57). This is achieved in the analytical program *Gieras*.mw in Appendix 1. The amplitude of harmonics are presented in Table 4.8.

Current sheet rotor loss calculation method is then used to calculate respective rotor eddy current power loss due to significant harmonics. The results are presented in Table 4.9.

Spatial order, q (λ_1 = 1 pole pitch)	Temporal order, k (f = 3000 Hz)			
	0	6	12	18
1	0.7806	0.00046^{-} 0.000278^{+}	0.000014^{-} 0.00001^{+}	0.0000022^{-}
3	0.1689	0.000953^{-} 0.000188^{+}	0.000019^{-} 0.000008^{+}	0.0000029^{-}
5	0.08186	0.0044^{-} 0.000135^{+}	0.0000289^{-} 0.000006^{+}	0.0000038^{-}
7	0.0494	0.0044^{-} 0.0001^{+}	0.000047^{-} 0.0000049^{+}	0.0000051^{-}
9	0.0334	0.000953^{-} 0.000077^{+}	0.000098^{-}	0.000007^{-}
11	0.0240	0.00046^{-}	0.00046^{-}	0.0000106
13	0.0179	0.000278^{-}	0.00046^{-}	0.000017^{-}
15	0.0137	0.000188^{-}	0.000098^{-}	0.000036^{-}
17	0.0107	0.000135^{-}		0.000169^{-}
19	0.00841		0.0000289^{-}	0.000169^{-}

Table 4.8. Amplitude of normal flux density harmonics, in Tesla, over the magnet surface of PMSG1 using analytical method by Gieras (2004). Positive superscripts indicates forward rotating harmonics and negative superscripts indicate backward rotating harmonics

Spatial order, q	Temporal order, k (f = 3000 Hz)		
	6	12	18
3	2		
5	17		
7	7		
11		0.1	
13		0.05	
17			0.0065
19			0.0047
Power loss (Gieras (2004), (*GR* method) = 26 W = 25.92 W in magnet + 0.08 W in hub			

Table 4.9. No-Load Rotor eddy current power loss due to CW harmonics in PMSG1

4.6.3 **Complex Relative Permeance Method: (Ẑarko et al., 2006)**

Ẑarko et al (2006) calculated a complex permeance function using conformal transformation to cater for the effect of slotting on both radial and tangential components of airgap flux density. The idea is to use four conformal transformations to transform a slotted airgap into a slotless airgap, where the field solution can be found using the method described in Zhu et al (2002). The solution is then mapped back into the complex plane where the actual slot shape exists. The depth of penetration of the field into the slot opening is assumed to have a negligible effect on airgap flux density distribution in the slotted PM machine.

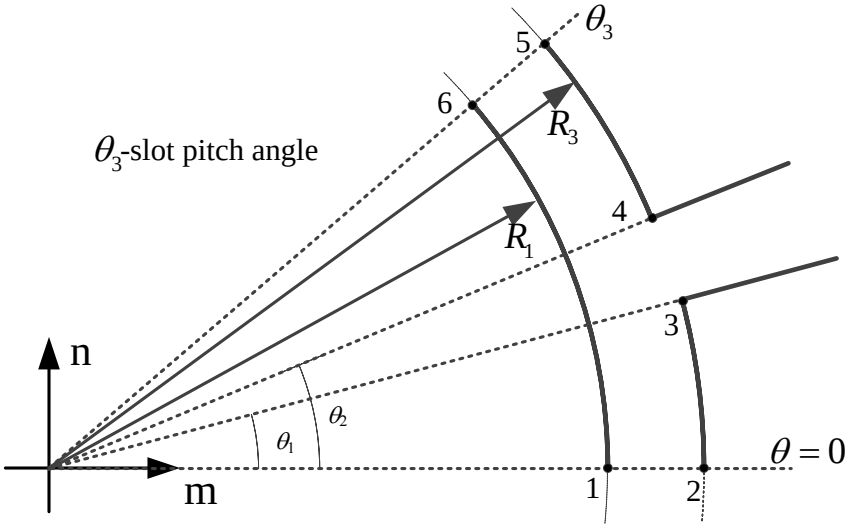

Figure 4.17. One infinitely deep slot opening in the polar ***S*** plane

The slotless airgap flux density $B_s(r,\theta)$ can be written in the form of its radial and tangential components as:

$$B_s(r,\theta) = B_r(r,\theta) + jB_\theta(r,\theta) \tag{4.62}$$

The main steps to transform the slotted airgap geometry into slotless airgap geometry are as follows. The actual one-slot geometry shown in Figure 4.17 is in the ***S*** plane, which in the polar coordinates $S(r,\theta)$ is given by:

$$S = re^{Z} \tag{4.63}$$

The first transformation transforms the polar ***S*** plane into Cartesian ***Z*** plane as:

$$Z = \ln S \tag{4.64}$$

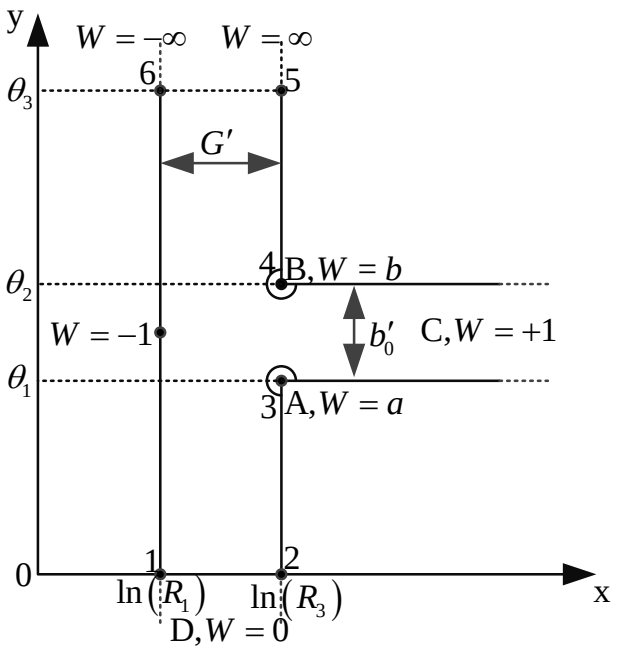

Figure 4.18. Slot opening in the Cartesian ***Z*** plane with values of *W* at the corner points

The second conformal transformation transforms the slot geometry structure defined in the ***Z*** plane into the upper half of the ***W*** plane. This transformation, which opens out the interior of a polygon in the ***Z*** plane into the upper half of the ***W*** plane, is known as a Schwarz-Christoffel transformation as reported in (Gibbs, 1958). There are three corners A, B and C where the value of *W* needs to be fixed, i.e., *a*, *b* and +1, respectively. The transformation is therefore given as:

$$\frac{dZ}{dW} = j\frac{G'}{\pi}\frac{(W-a)^{\frac{1}{2}}(W-b)^{\frac{1}{2}}}{(W-1)W} \tag{4.65}$$

In equation (4.65) the parameters G' and *a* and *b* can be determined as:

$$G' = \ln\frac{R_3}{R_1}, \quad b = \left[\frac{b_0'}{2G'} + \sqrt{\left(\frac{b_0'}{2G'}\right)^2 + 1}\right]^2, a = \frac{1}{b}, \; b_0' = \theta_2 - \theta_1$$

where, G' and b_0' is the airgap length and slot opening, respectively.

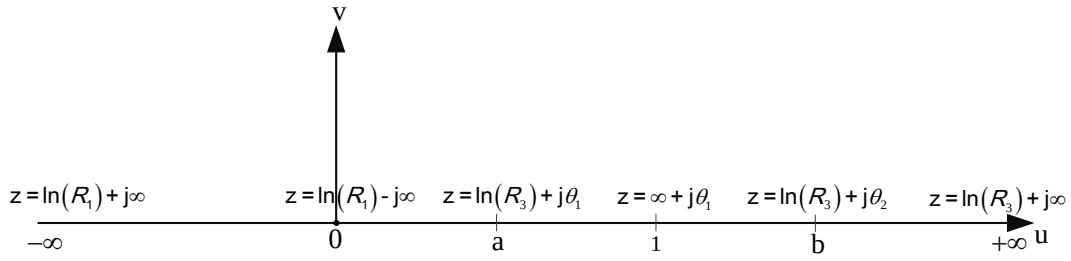

Figure 4.19. Slot Opening in the ***W*** plane

To find the field distribution in the slot area, another transformation from the ***T*** plane to the ***W*** plane is performed. The slot opening in the ***T*** plane represents two parallel plates extending an infinite distance as:

$$T = j\frac{G'}{\pi}\ln W + \ln(R_3) + j\frac{\theta_3}{2} \tag{4.66}$$

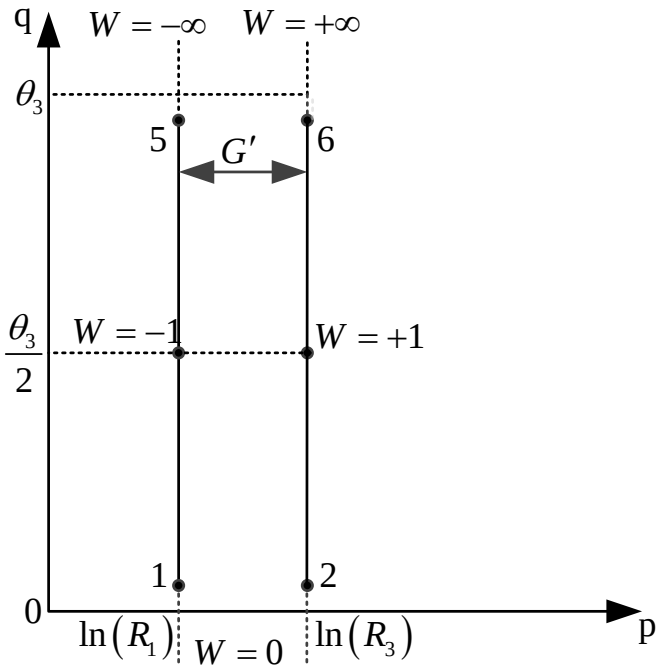

Figure 4.20. Slot opening in the ***T*** plane

The last transformation from the ***T*** plane to the ***K*** plane transforms the two parallel plates shown in Figure 4.20 into a circular shape and models the airgap of a slotless PM machine:

$$K = e^{T} = e^{j\left(\frac{G'}{\pi}\ln W + \ln(R_3)\frac{\theta_3}{2}\right)} \tag{4.67}$$

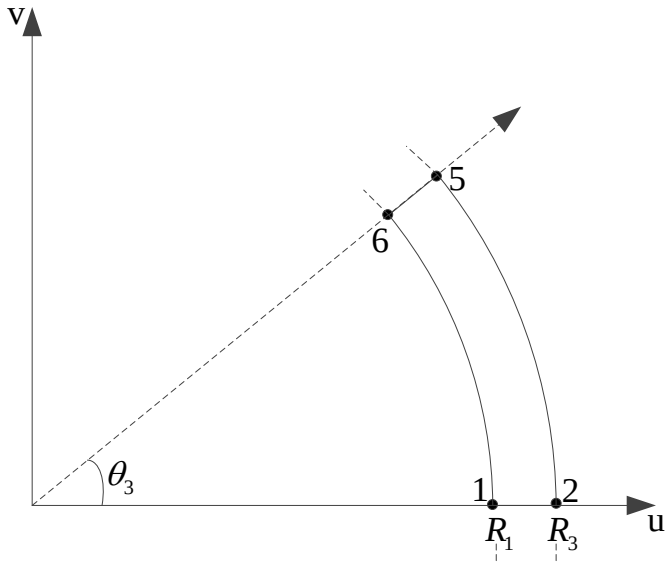

Figure 4.21. Slot opening in the ***K*** plane

According to (Žarko et al., 2006), the complex relative permeance function is determined using the conformal transformations between the corresponding complex planes:

$$\frac{\partial K}{\partial S} = \frac{\partial K}{\partial T}\frac{\partial T}{\partial W}\frac{\partial W}{\partial Z}\frac{\partial Z}{\partial S} \tag{4.68}$$

The partial derivatives in equation (4.68) are defined by conformal transformations between the corresponding complex planes as:

$$\frac{\partial K}{\partial T} = e^{T} = e^{\ln K} = K$$

$$\frac{\partial T}{\partial W} = j\frac{G'}{\pi}\frac{1}{W}$$

$$\frac{\partial W}{\partial Z} = -j\frac{\pi}{G'}\frac{(W-1)W}{(W-a)^{\frac{1}{2}}(W-b)^{\frac{1}{2}}}$$

$$\frac{\partial Z}{\partial S} = \frac{1}{S}$$

Substituting above partial derivatives in equation (4.68) it can be shown:

$$\frac{\partial K}{\partial S} = \lambda^{*} = \frac{K}{S}\frac{W-1}{(W-a)^{\frac{1}{2}}(W-b)^{\frac{1}{2}}} \tag{4.69}$$

The complex relative permeance in equation (4.69) can be written in its real and imaginary components as:

$$\lambda_{CP}(r,\theta) = \lambda_a + j\lambda_b \tag{4.70}$$

The variables *K* and *S* in equation (4.69) are functions of *W*, which according to Equations (4.66) and (4.67) are related as:

$$K = R_3 e^{j\left(\frac{G'}{\pi}\ln W + \frac{\theta_3}{2}\right)}$$

The complex relative permeance function λ^* in equation (4.69) is a non-linear function of *W*. *S* is the known coordinate in the actual geometry which can be transformed in the ***Z*** plane using equation (4.64). The value of *Z* corresponding to that value in the ***W*** plane can be calculated by integrating equation (4.65) and taking into account the location of the origin of the coordinate system in Figure 4.18, variable *Z* becomes:

$$Z = j\frac{G'}{\pi}\left[\ln\left|\frac{1+u}{1-u}\right| - \ln\left|\frac{b+u}{b-u}\right| - 2\frac{b-1}{\sqrt{b}}\tan^{-1}\frac{u}{\sqrt{b}}\right] + C \tag{4.71}$$

In equation (4.71) the parameters *u* and *C* can be determined as:

$$u = \sqrt{\frac{W-b}{W-a}},\ C = \ln R_3 + j\theta_2$$

For example, if it is required to evaluate the flux density at a certain geometric point in the slotted airgap in the ***S*** plane, then the value of *Z* which corresponds to that point in the ***Z*** plane can simply be calculated from equation (4.64). However, the value of *W* which corresponds to that value of *Z* cannot be calculated explicitly from equation (4.71) because that equation is in the form $Z = f(W)$, where *f* is a non-linear function of *W*. The iterative technique is therefore required to solve this non-linear equation and find the value of *W* for the given *Z*. The non-linear least-squares optimisation algorithm built into MATLAB (*lsqnonlin)* has been used to solve the equation.

For PMSG1, the resulting waveforms of the real and imaginary parts of the complex relative permeance function are shown in Figure 4.22.

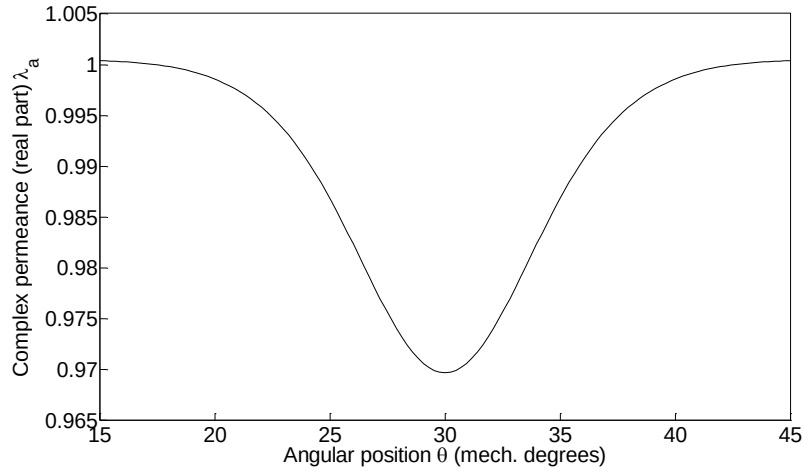

(a)

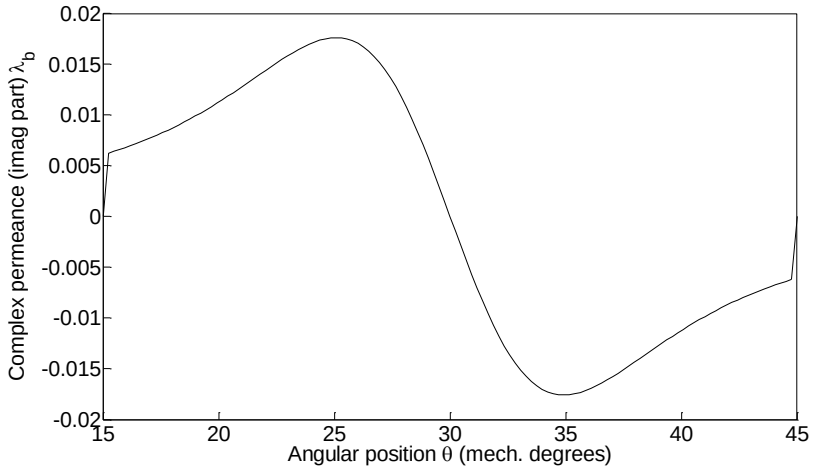

(b)

Figure 4.22. Complex relative permeance over one slot pitch, on the magnet surface PMSG1: (a) Real component (b) Imaginary component

Since these two waveforms in Figure 4.22, will repeat every slot pitch they can be expressed as a Fourier series to give the complex relative permeance function on the surface of the magnet for all rotor positions. This Fourier series is given by:

$$\lambda_a = \lambda_0 + \sum_{n=1}^{\infty} \lambda_{an} + \cos\left(nQ_s\left(\theta - \omega_r t\right)\right) \tag{4.72}$$

$$\lambda_b = \lambda_0 + \sum_{n=1}^{\infty} \lambda_{bn} + \sin\left(nQ_s\left(\theta - \omega_r t\right)\right) \tag{4.73}$$

In equations (4.72) and (4.73), λ_0, λ_{an}, and λ_{bn} are Fourier series coefficients and are calculated from the waveforms in Figure 4.22 using a discrete Fourier transform. The

distribution of radial and tangential components over one pole pitch is illustrated in Figure 4.23.

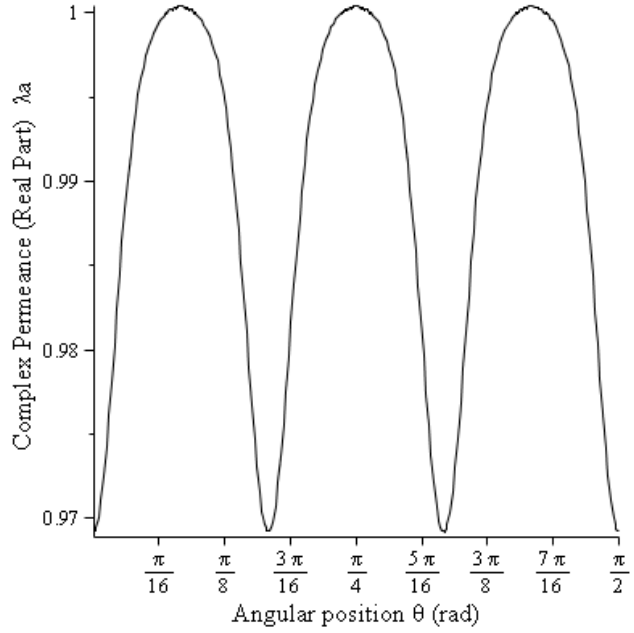

(a)

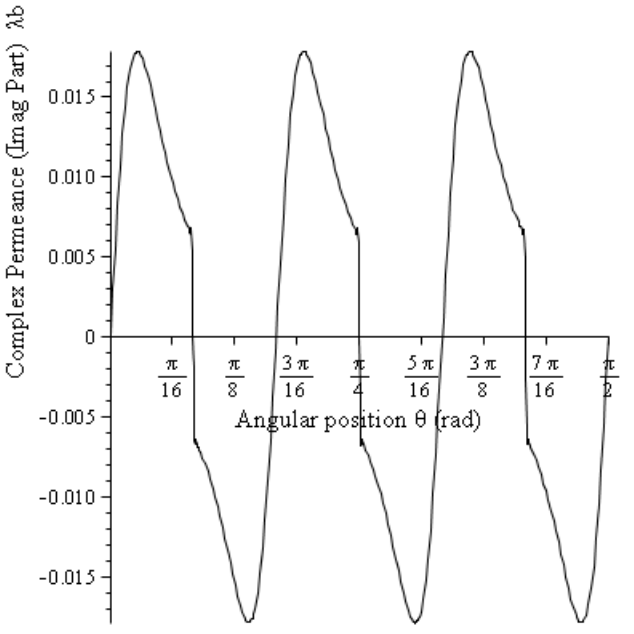

(b)

Figure 4.23. Complex relative permeance per one pole pitch on the surface of the magnet of PMSG1 (a) Real component (b) Imaginary component

According to equation (4.44) the airgap flux density in the slotted PM machine can be written as:

$$\mathbf{B}_g\left(r,\theta\right)=\lambda_{CP}\left(r,\theta\right)\mathbf{B}_s\left(r,\theta\right) \tag{4.74}$$

The radial component can be calculated in the rotor reference frame as:

$$\begin{aligned} B_{gr}\left(r,\theta\right)=\lambda_a\left(r,\left(\theta-\omega t\right)\right)\cdot B_{sr}\left(r,\theta\right)+ \\ \lambda_b\left(r,\left(\theta-\omega t\right)\right)\cdot B_{s\theta}\left(r,\theta\right) \end{aligned} \tag{4.75}$$

Figure 4.24 illustrates the airgap flux distribution in the slotted PM machine obtained using equation (4.75).

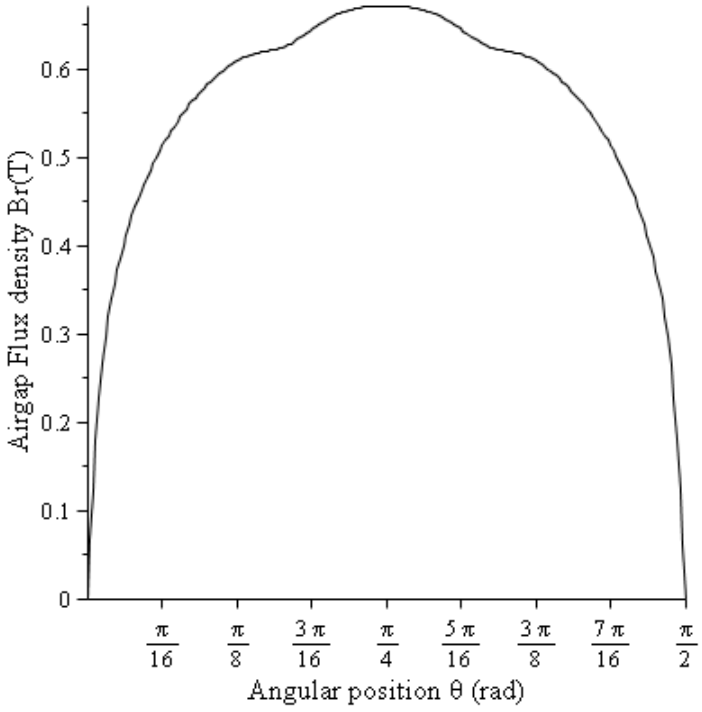

Figure 4.24. Radial airgap flux density in PMSG1

The amplitude of travelling flux harmonics are calculated by extending the equation (4.75). This has been achieved and implemented in the analytical program *Žarko*.mw in Appendix 1. Current sheet rotor loss calculation method is used for the calculation of rotor eddy current power loss due to the most significant harmonics. The results for the amplitude of harmonics and corresponding rotor eddy current power loss are presented in Tables 4.10 and 4.11, respectively.

Spatial order, q (λ_1 = 1 pole pitch)	Temporal order, k (f = 3000 Hz)			
	0	6	12	18
1	0.78238	0.00000537^{-} 0.0000417^{+}	0.000022^{-} 0.0000163^{+}	0.00000673^{-} 0.00000529^{+}
3	0.16917	0.00033^{-} 0.0000411^{+}	0.0000316^{-} 0.0000124^{+}	0.00000863^{-}
5	0.08189	0.00411^{-} 0.000033^{+}	0.00005^{-} 0.00000963^{+}	0.0000112^{-}
7	0.0494	0.00723^{-} 0.0000275^{+}	0.0000972^{-} 0.00000756^{+}	0.0000198^{-}
9	0.0334	0.00211^{-} 0.0000054^{+}	0.00026^{-}	0.0000216^{-}
11	0.0240	0.00118^{-}	0.00168^{-}	0.0000265^{-}
13	0.01798	0.000758^{-}	0.00225^{-}	0.000033^{-}
15	0.01376	0.000526^{-}	0.000591^{-}	0.0000231^{-}
17	0.0107	0.000382^{-}	0.000315^{-}	0.000256^{-}
19	0.0084	0.000287^{-}	0.000198^{-}	0.000698^{-}

Table 4.10. Amplitudes of normal flux density harmonics, in Tesla, over the magnet surface of PMSG1, obtained using analytical method by Ẑarko et al., (2006). Positive superscripts indicate CCW rotating harmonics and negative superscripts indicate CW rotating harmonics

Spatial order, q	Temporal order, k (f = 3000 Hz)		
	6	12	18
3	0.2		
5	14		
7	18		
11		1	
13		1.1	
17			0.015
19			0.08
Power loss ((Ẑarko et al., (2006), (*CR* method) = 34.4 W = 34.31 W in magnet + 0.084 W in hub			

Table 4.11. No-load rotor eddy current power loss due to CW rotating harmonics in PMSG1

It will be shown in the next section that the rotor eddy current power loss result using the analytical method developed by Ẑarko et al., (2006), are closer to FEA for the un-saturated stator tooth tip, in comparison to the analytical methods developed by Zhu and Howe (1993) and Gieras (2004).

4.7 Comparison of Analytical and FEA Methods

Figure 4.25 shows a comparison between the calculated waveforms of airgap flux density distributions on the surface of the magnet, at a particular rotor position $\theta = 0$, using the three analytical methods i.e., the relative permeance (RP) method in [13], the relative permeance method by Gieras (GR) in [14], the complex permeance (CP) method in [15] and the static FE method. Although in this figure the waveforms look similar, there are significant differences between their high order harmonics.

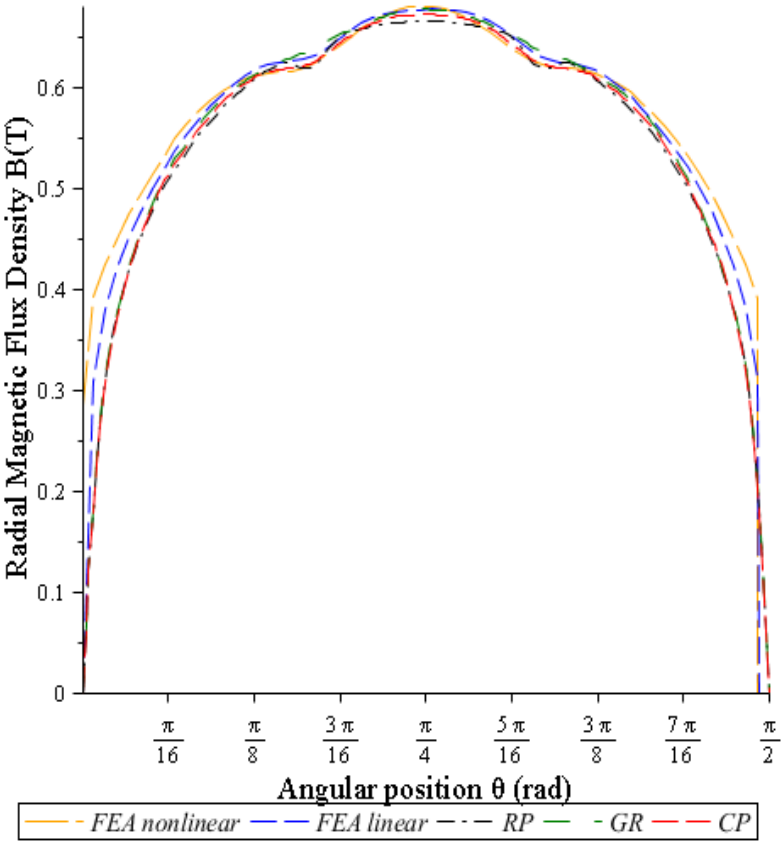

Figure 4.25. Airgap magnetic flux density distribution calculated using FEA and analytical methods

A comparison between harmonic amplitudes calculated using different methods is shown in Figures 4.26–4.28. The results in Figures 4.26–4.28 highlight the discrepancy between amplitude of harmonics calculated using FEA static linear (un-saturated stator tooth tip) and nonlinear (saturated stator tooth tip) solutions and three

analytical methods. The amplitudes of harmonics in the case of a nonlinear static FEA solution with saturated stator tooth tip are the highest.

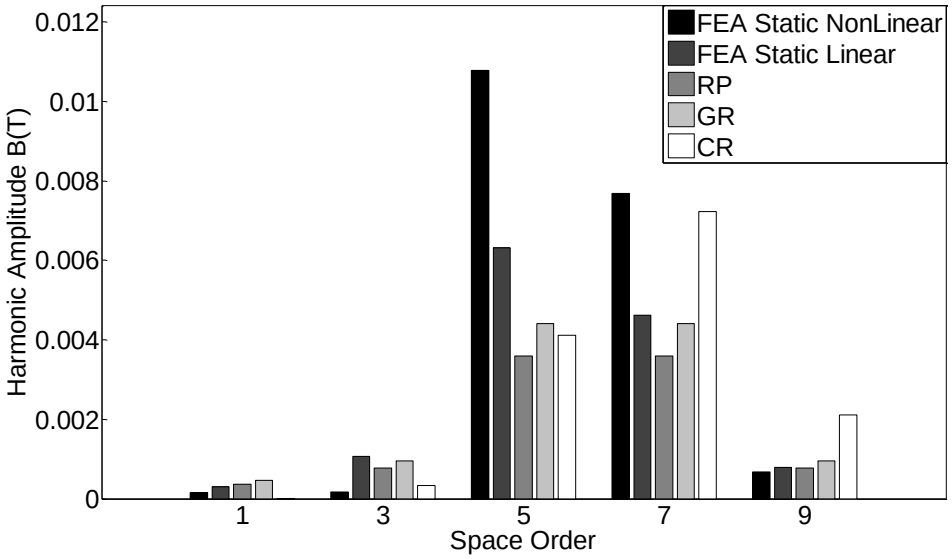

Figure 4.26. No-load amplitude of magnetic induction space harmonics of time order 6

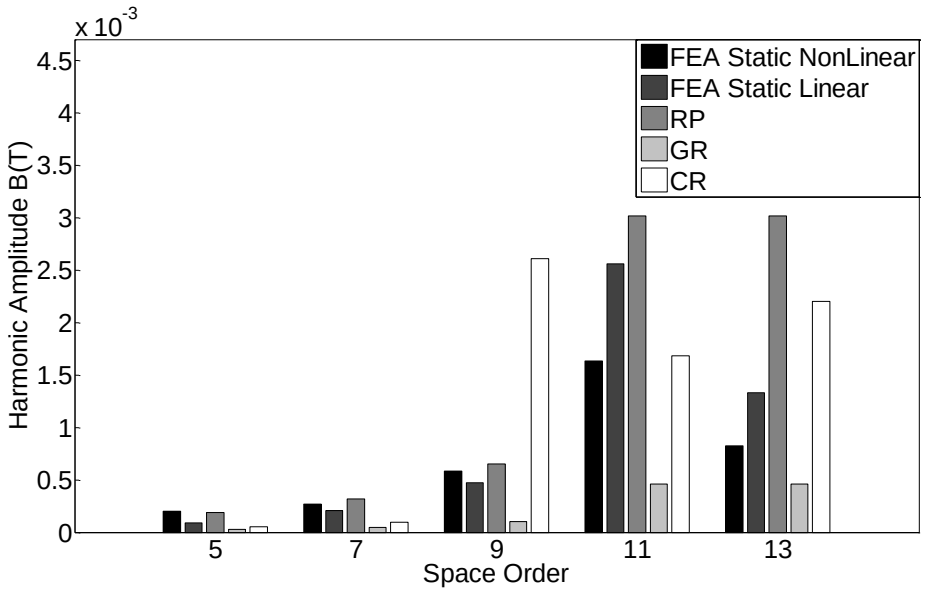

Figure 4.27. No-load Amplitude of magnetic induction space harmonics of time order 12

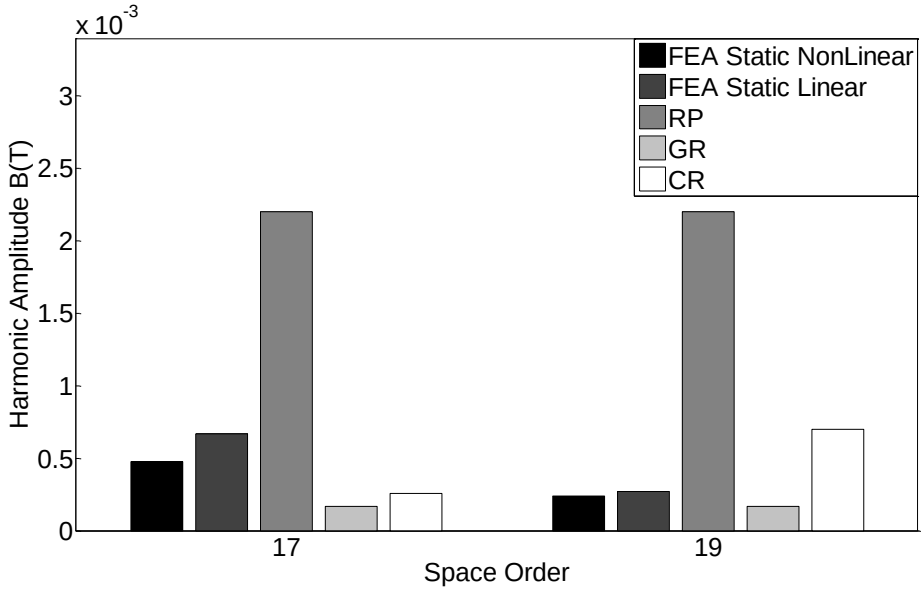

Figure 4.28. No-load Amplitude of magnetic induction space harmonics of time order 18

Rotor eddy current power loss due to each travelling flux harmonic is calculated using the current sheet model. Rotor power losses due to the most significant harmonics, with a power loss > 0.5W, are included in Figures 4.29–4.30. A comparison of the total rotor power loss obtained using the different methods are shown in Figure. 4.31.

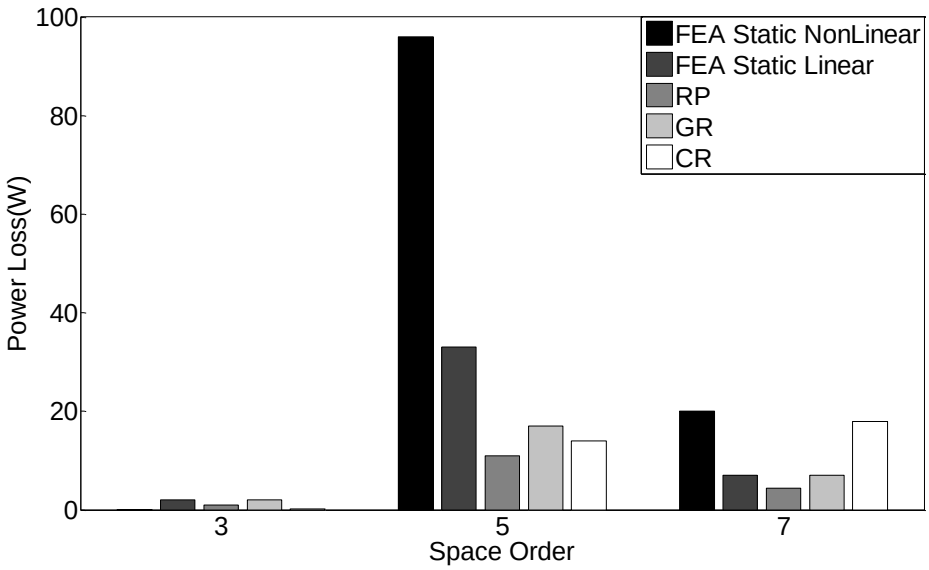

Figure 4.29. No-load power loss due to magnetic induction space harmonics of time order 6

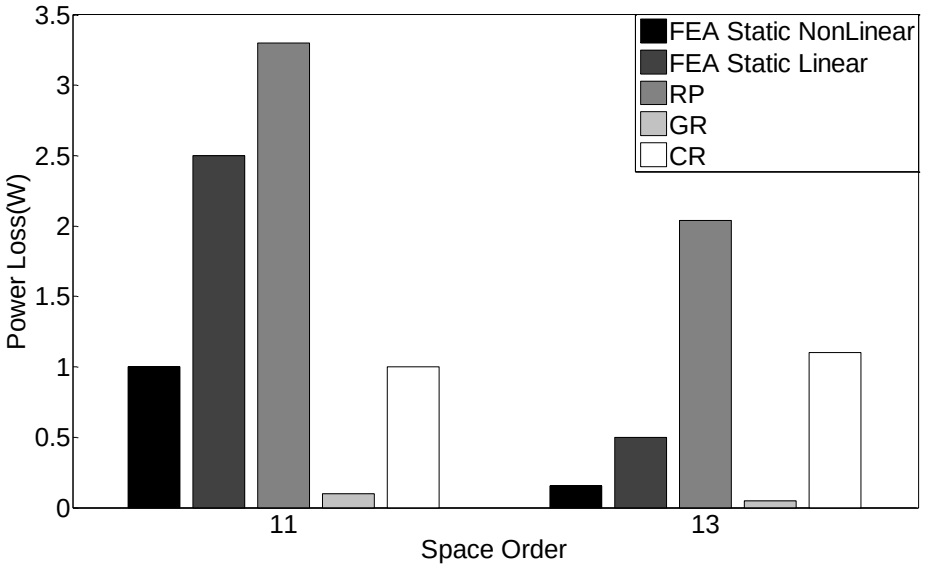

Figure 4.30. No-load rotor power loss due to magnetic induction space harmonics of time order 12

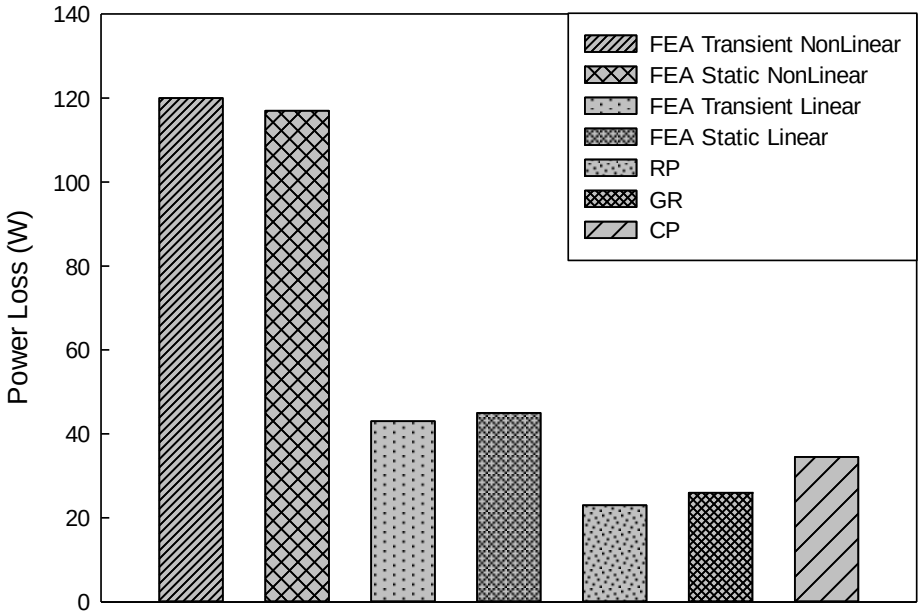

Figure 4.31. No-load total power loss

It can be seen from the results that the discrepancy level between FEA and analytical methods is very significant. There is very good agreement between the losses calculated using transient FEA and those calculated using harmonic analysis of flux density data obtained using a static FEA solution, in both the linear and nonlinear

cases. However, the losses obtained from the nonlinear solutions are about three times those obtained from linear FEA solutions.

In general, the losses calculated using the analytical methods are lower than the linear FEA results, with the complex permeance method being the closest to FEA. It is pertinent to mention here; complex permeance method assumes that permanent magnet surface is not an equal potential. The apparent agreement between the total losses calculated using the complex permeance method (and current sheet eddy current model) and that obtained using linear FEA analysis is however misleading, as it disguises significant differences between the harmonic contents calculated by the two methods.

4.8 Effect of Tooth tip Thickness

Using transient FEA, rotor eddy current power loss is calculated in several variants of PMSG1, with different tooth tip thicknesses, for both linear (un-saturated) and non-linear (saturated) stator tooth tip.

Table 4.12 shows the increase in rotor eddy current power loss with smaller values of stator tooth tip thickness due to saturation. The saturated tooth tip has an effective incremental permeability similar to that of air, and hence saturation effectively increases the slot opening, thus increasing the amplitude of flux harmonics and associated losses.

Tooth Tip Thickness (mm)	Power loss (W) Un-saturated PMSG1 model	Power loss (W) Saturated PMSG1 model
1	43	120
1.5	40	45
2	40	40
3	40	40
4	38	38

Table 4.12. No-load rotor eddy current power loss comparison in PMSG1 for un-saturated and saturated stator tooth tips.

It is worth mentioning that in Table 4.12 (third column), PMSG1 with 1mm stator tooth tip thickness shows saturation effect only. The increase in tooth tip thickness in other variants of PMSG1 reduces the saturation effect and therefore the rotor eddy current power loss remains the same in cases of un-saturated (non-linear) and saturated (linear) stator tooth tip thicknesses.

4.9 Conclusion

The chapter presented a comparison between three analytical methods by Zhu and Howe (1993), Gieras (2004) and Ẑarko et al (2006) and static and transient FEA methods for the calculation of the no-load airgap flux density distribution and asynchronous magnet flux tooth ripple harmonics, in the rotor reference frame. The results presented showed that the complex relative permeance method by Ẑarko et al (2006) provides the closest estimate to FEA solutions when the level of saturation in the machine is negligible. However, in the case of significant saturation of the tooth tip all the methods significantly underestimate the amplitudes of harmonics, and therefore the calculated rotor losses are underestimated (see Table 4.12 with tooth tip thickness of 1mm) in a PM machine with heavy tooth tip saturation.

Increasing tooth tip thickness decreases the rotor loss in PMSG1 with saturated stator tooth tip. Though it is beyond the scope of this chapter, it should be noted that a reduction in rotor loss by increasing tooth tip thickness will be at the expense of increased leakage reactance, voltage regulation and a reduced stator slot fill.

Chapter 5

Rotor Eddy Current Power Loss in PMSG with Sinusoidal Current

5.1 Introduction

In this chapter the accuracy of analytical methods is compared with a static FEA method for the calculation of armature reaction stator mmf harmonics and resultant harmonics. The resultant harmonics considered are the phasor sum of the common harmonics between both magnet flux tooth ripple and armature reaction stator mmf harmonics. The amplitude of resultant harmonics may vary at different current advance angles. A study is therefore also performed to investigate the effect of various current advance angles on the amplitude of resultant harmonics.

An analytical current sheet method is used for the calculation of rotor eddy current power loss, due to harmonics caused by armature reaction stator mmf, resultant mmf and resultant mmf with various current advance angles. A comparison for the rotor eddy current power loss calculation is presented between analytical, static FEA and transient FEA methods. The possible variation in the amplitude of mmf harmonics due to reaction of eddy currents is catered for in the calculation of rotor eddy current power loss.

5.2 Machine under Study

The permanent magnet synchronous generator (PMSG1), shown in Figure. 3.2, is the focus of this study. The generator has 3mm slot opening and double layer, 2/3 fractional pitch winding distribution. The generator's dimensions and material properties have been shown in Table 3.1.

5.3 Analytical Method

In this section analytical methods are presented to calculate; 1) Armature reaction stator mmf flux harmonics using the winding factors derived in (McPherson, 1981) and (Alger, 1965), 2) Resultant harmonics, combining rotor mmf and stator mmf harmonics using vector (phasor) addition.

5.3.1 **Amplitude of Armature Reaction Flux Harmonics**

In a PM machine with a symmetrical three phase stator winding with *p* pole pairs, and with the rotor moving synchronously with the stator fundamental rotating field, the mmf acting across the airgap at any point is equal to the total number of airgap conductors between that point and the nearest peak of the current density wave (Alger, 1965). The amplitude of the armature reaction flux harmonic F_{qk}, with spatial order *q* and temporal order *k*, can be estimated using equation (3.6), which is repeated here as:

$$F_{qk} = \frac{3}{2}\frac{4}{\pi}\frac{N_{ph}}{p}\frac{1}{q}K_{wq}\sqrt{2}\hat{I}_k \tag{5.1}$$

The above equation neglects the effect of saturation, end effects and stator tooth tip on the amplitude of harmonics. For PMSG1 the required parameters in equation (5.1) are: I=100 A, N_{ph}=2×4=8 Turns, p=4. The winding distribution factor K_{wq} is calculated using equation (2.8), the parameters for the equation are: m=1 slot per pole per phase, $\alpha = 0^{o}$, $\beta = \pi/6$ radians, and $\delta' = 2/3$. The frequencies of these harmonics can be determined using equations (2.20) and (2.21). Due to the presence of odd symmetry in the machine under study all harmonics will be clockwise (CW) rotating and even harmonic orders will be absent.

According to equation (3.8), the current sheet distribution is repeated here as:

$$J_{qk} = \hat{J}_{qk} \cos\left(q\theta + k\omega t\right) \tag{5.2}$$

The methodology discussed in section (3.7.1), can be used for the calculation of armature reaction flux harmonics amplitude with magnet conductivity assumed to be zero. Here, another commonly used method is presented for the calculation of armature reaction stator mmf harmonics without taking into account the reaction of eddy currents.

In terms of vector magnetic potential *A*, the field solution in the airgap and permanent magnet regions is obtained using the Laplace and Poisson field equations, respectively. In the airgap region the flux density due to the equivalent current sheet can be calculated using the Laplace equation as:

$$\frac{\partial^2 A(r,\theta)}{\partial r^2} + \frac{1}{r}\frac{\partial A(r,\theta)}{\partial r} + \frac{1}{r^2}\frac{\partial^2 A(r,\theta)}{\partial \theta^2} = 0 \tag{5.3}$$

Using the method of separation of variables the general solution of equation (5.3) is written as:

$$A(r,\theta) = R(r)\cos\left(q\theta + k\omega t\right) \tag{5.4}$$

Substituting equation (5.4) in equation (5.3) it can be shown that:

$$R(r) = Cr^{q} + Dr^{-q} \tag{5.5}$$

In equation (5.5), C and D are constants to be determined using the following two boundary conditions:

$$H_{\theta}\Big|_{r=R_1} = 0, \qquad H_{\theta}\Big|_{r=R_3} = J_{qk} \tag{5.6}$$

The boundary conditions assume infinite permeability for the rotor material and discontinuity in the tangential field intensity at the stator bore by the amount of current sheet J_{qk}. For permanent magnet machines the airgap flux density $\vec{B}$ and $\vec{H}$ in the airgap are coupled by:

$$\vec{B} = \mu_0 \vec{H} \tag{5.7}$$

Therefore the tangential and radial components of the field quantities $\vec{B}$ and $\vec{H}$ can be derived in terms of the vector potential as:

$$B_\theta(r,\theta) = -\frac{\partial A(r,\theta)}{\partial r} \qquad (5.8)$$

$$H_\theta(r,\theta) = \frac{B_\theta(r,\theta)}{\mu_0} \qquad (5.9)$$

$$B_r(r,\theta) = \frac{1}{r}\frac{\partial A(r,\theta)}{\partial \theta} \qquad (5.10)$$

$$H_r(r,\theta) = \frac{B_r(r,\theta)}{\mu_0} \qquad (5.11)$$

Applying the boundary conditions in equation (5.6) to the field equations (5.8-5.11) allows the values of C and D to be written as:

$$C = \frac{DR_1^{-q}}{R_1^q} \qquad (5.12)$$

$$D = \frac{J_{qk}R_3\mu_0}{q\left(R_1^{-2q}R_3^q - R_1^{-q}\right)} \qquad (5.13)$$

The final field solution can be obtained by first substituting equations (5.12) and (5.13) in equation (5.5). From equation (5.5) the value of $R(r)$ is then substituted in equation (5.4). Finally the value of vector potential from (5.4) is used in (5.10) and (5.11) to calculate the radial and tangential airgap flux density as:

$$B_r(r,\theta) = \frac{J_{qk}R_3\mu_0\left(R_1^{-2q}r^q + r^{-q}\right)}{r\left(R_1^{-2q}R_3^q - R_3^{-q}\right)} \qquad (5.14)$$

$$B_\theta(r,\theta) = \frac{J_{qk}R_3\mu_0\left(R_1^{-2q}r^q - r^{-q}\right)}{r\left(R_1^{-2q}R_3^q - R_3^{-q}\right)} \qquad (5.15)$$

5.3.2 **Resultant Airgap Flux Harmonics**

Analytically, the magnet flux tooth ripple harmonics and stator mmf flux harmonics of same order can be added vectorially to obtain the resultant harmonics. Following Figures 5.1 and 5.2 can be used to specify the correct phase angle between the two flux harmonics. In these Figures the phase angle φ is defined as the angle between stator voltage V and resulting stator current I, angle δ is defined as the angle between stator voltage V and rotor induced fundamental emf, E, while the load angle ψ is defined as the angle between stator current I and rotor induced emf E. The resistance of the winding is assumed to be negligible in these phasor diagrams.

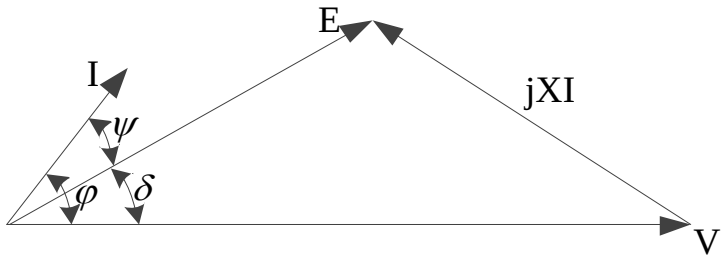

Figure 5.1. Phasor diagram of synchronous generator with capacitive load

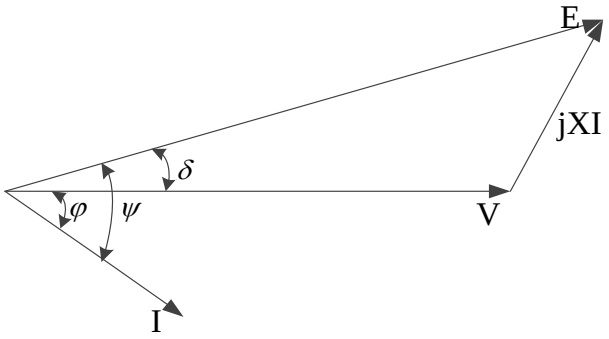

Figure 5.2. Phasor diagram of synchronous generator with inductive load

For PMSG1, the load angle ψ can be related to angle δ and phase angle φ, considering the phase angle φ being negative for an inductive load and positive for a capacitive load and ψ being positive for a generator, allows the following to be written:

$$\delta = \sin^{-1}\left(\frac{XI\cos\varphi}{E}\right) \tag{5.16}$$

$$\psi = \varphi - \delta \tag{5.17}$$

In equation (5.16) *X*, *I* and *E* represent the reactance, current and back emf of the generator, respectively. In the purely capacitive case the angle δ is zero, φ is +90 and the resulting load angle ψ is +90 degrees. For a purely inductive case the angle δ is zero, φ is -90 and the load angle ψ is -90 degrees. The angle between the rotor and the stator magnetic field axes is always 90-ψ degrees. The stator emf *E* induced by the fundamental rotor field can be calculated as:

$$E = 4.44\, fK_{w1}N_{ph}\phi \tag{5.18}$$

ϕ is the flux linkages. Using equations (5.16) and (5.18) for PMSG1, with X=0.528 Ω,

f = 3000Hz, K_{w1}=0.866, N_{ph}=8 and ϕ=3.5mWb, E is calculated to be 330 V.

For each harmonic at different phase angle φ, the angle "α" between magnet flux tooth ripple harmonic and stator mmf harmonic component, producing the resultant harmonic is calculated by using trigonometry relations as shown in program *Vadd1*.mw in Appendix 1. The result of the calculation is shown in Table 5.1. From the Table, it is clear that all harmonics present a relation of either $\alpha_{qk}+\psi=90$ or $\alpha_{qk}-\psi=90$. The harmonics 5th, 11th and 17th behaves the same as the fundamental, whereas, the harmonics 7th 13th are 180 degrees out of phase with the fundamental harmonic.

Temporal Order, k	Spatial Harmonic, q	ψ(deg) $(\varphi(\text{deg}))$						
		-90 (-90)	-60 (-54)	-30 (-21)	0 (10)	30 (38)	60 (65)	90 (90)
		$\alpha_{qk}=90-\psi$ or $\alpha_{qk}=90+\psi$						
6	5	180	150	120	90	60	30	0
	7	0	30	60	90	120	150	180
12	11	180	150	120	90	60	30	0
	13	0	30	60	90	120	150	180
18	17	180	150	120	90	60	30	0
	19	0	30	60	90	120	150	180

Table 5.1. Angle (in degrees) between rotor and stator fields for different harmonics and phase angles in PMSG1

For the calculation of resultant airgap flux harmonics, the radial airgap flux density in PMSG1 is calculated using the complex relative permeance method by Ẑarko et al., (2006) given by:

$$B_{gr}(r,\theta)=\lambda_a\left(r,(\theta-\omega t)\right)\cdot B_{sr}(r,\theta)+\lambda_b\left(r,(\theta-\omega t)\right)\cdot B_{s\theta}(r,\theta) \tag{5.19}$$

The vector addition of equation (5.14) and (5.19) can be performed as:

$$B_t=\sum_{k=0}^{\infty}\sum_{h=1}^{\infty}B_{gr}(r,\theta)\cos(q\theta+k\omega t)+B_r(r,\theta)\cos\left(q\theta+k\omega t+\alpha_{qk}\right) \tag{5.20}$$

It is informative to express equation (5.20) as:

$$B_t = \sum_{k=0}^{\infty}\sum_{h=1}^{\infty} B_{gr}(r,\theta)\cos(q\theta + k\omega t) + B_r(r,\theta)\begin{pmatrix}\cos(q\theta + k\omega t)\cos(\alpha_{qk}) \\ -\sin(q\theta + k\omega t)\sin(\alpha_{qk})\end{pmatrix} \quad (5.21)$$

From equation (5.21) it can be observed that if the load angle ψ between back EMF E and current I is 0 degrees, the angle α_{qk} is 90 degrees then superposition, (viz. direct addition of tooth ripple and stator mmf harmonics) can be performed and equation (5.21) becomes:

$$B_t = \sum_{k=0}^{\infty}\sum_{h=1}^{\infty} B_{gr}(r,\theta)\cos(h\theta + k\omega t) + B_r(r,\theta)\left(\cos(h\theta + k\omega t)\right) \quad (5.22)$$

For all other values of α_{qk} superposition can't be employed, as the amplitude of harmonics will increase or decrease depending on angle α_{qk} .

5.4 Transient FEA Method

Transient FEA analysis (discussed in chapter 3) is performed to calculate the effect of current advance angles on rotor eddy current power loss. In addition the effect of un-saturated and saturated stator tooth tips on rotor eddy current power loss is also investigated. The transient FEA results are then compared with those calculated using analytical and static FEA method in the Tables here after.

5.5 Static FEA Method

In this section the static FEA method is discussed for the calculation of the amplitudes of harmonics caused by armature reaction stator mmf and resultant mmf in PMSG1. Firstly, the section describes the methodology for the calculation of airgap flux density data due to each mmf at various rotor positions. Then the data is analysed using Fourier transform to calculate the amplitude of each harmonic. Finally, comparison between analytical and static FEA is presented for the amplitude of harmonics and respective rotor eddy current power loss.

5.5.1 **Airgap Flux Density Data due to Armature Reaction Stator mmf**

The stator current in the windings of PMSG1is considered to be sinusoidal, therefore higher order mmf space harmonics will be produced whose flux densities rotate with synchronous speed relative to the stator; this may be in the same direction to the fundamental mmf or in the opposite direction. These slowly rotating space harmonics, relative to the stator, behave as fast rotating time harmonics relative to the rotor because of their high number of poles.

A quarter of the PMSG1 covering a full pole pitch is modelled in the Maxwell 2D software, as shown in Figure 5.3. The stator and rotor permeability's for the model are defined in Table 3.1. The magnets are considered to be a kind of neodymium-iron-boron (NdFeB), having a typical remanence of 1.07 Tesla and coercive force of about 781 kA/m at the working temperature of 160^0. The permeability of the magnet is equal to the slope of its B-H curve (shown in Figure 3.1) while magnet conductivity is defined in Table 3.1. The remanence B_r of the magnet is assumed to be zero (magnets are not magnetised), to ensure that the airgap flux is from the armature reaction stator mmf, only The boundary conditions along the *x* and *y* axis in Figure 5.3 are defined to have negative symmetry, to comply with field quantities. Normal flux density at the stator outer surface is defined to be zero. The flux pattern due to the three phase stator current in PMSG1 at rotor position $\theta = 0$ is shown in Figure 5.3.

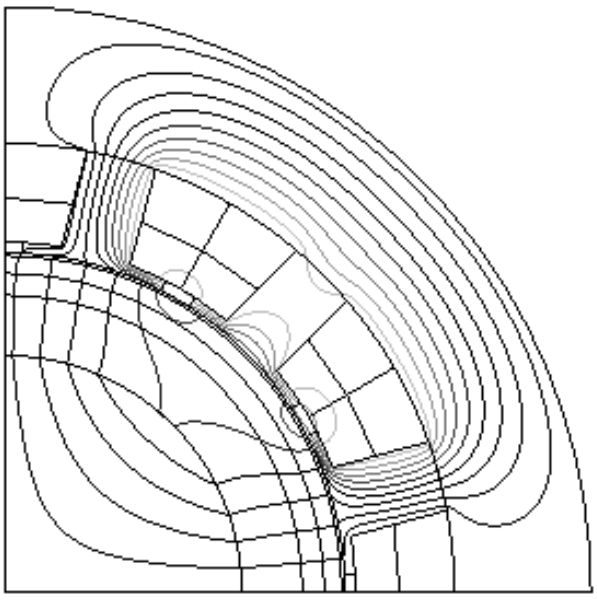

Figure 5.3. Flux pattern due to three phase stator current only, i.e., no magnets at $\theta = 0$ in PMSG1

As the three phase stator current is considered to be sinusoidal, it is also supposed that the axis of rotor and stator fields are at 90 degrees to each other, i.e., stator current phasor and stator emf phasor are in the same direction. Two conductors per coil are defined and therefore the current in phase A winding is $200\times\sqrt{2}\cos\theta$. The angle θ is the rotor position in electrical degrees, which varies from zero to 58 degrees to produce 30 models over one slot pitch. The reference axis $\theta = 0$ lies through the centre of the slot accommodating phase A and C′ windings. The currents in phase B and C are shifted by 120^0 and 240^0 respectively with respect to A.

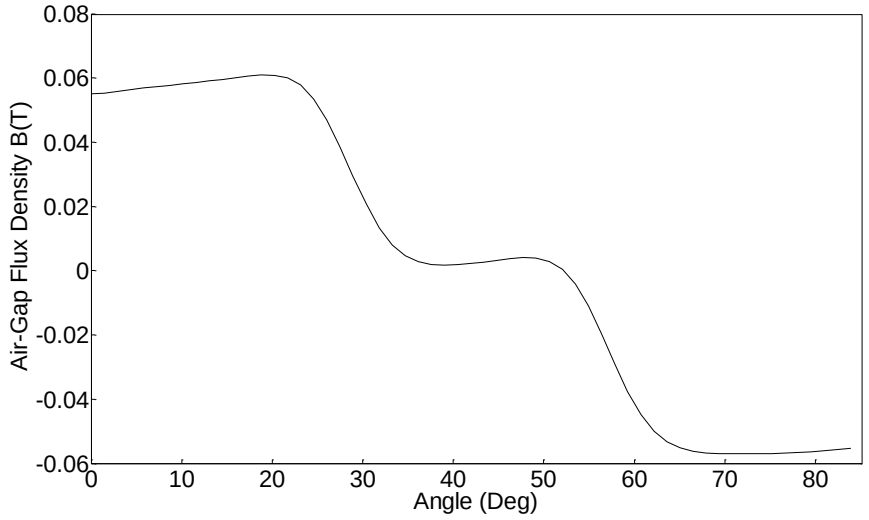

Figure 5.4. One FEA static solution for airgap flux density distribution due to armature reaction stator mmf only, just above the surface of the magnet

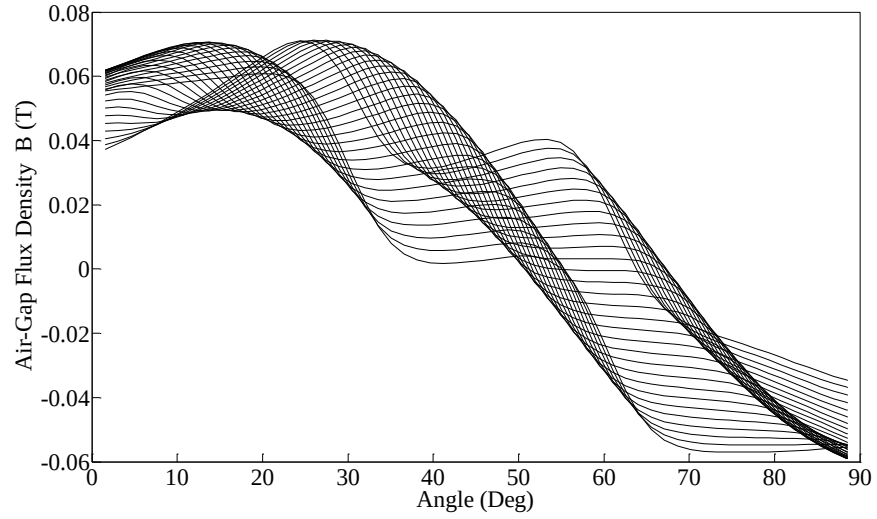

Figure 5.5. 30 FEA static solutions for airgap flux density distribution due to armature reaction stator mmf only, just above the surface of the magnet

Previous Figure 5.4 shows the static FEA solutions for the airgap flux density distribution due to armature reaction stator mmf on the surface of the magnet at rotor position $\theta = 0$. A plot showing all 30 FEA static solutions for airgap flux density covering one slot-pitch is shown in Figure 5.5.

5.5.2 **Airgap Flux Density Data due to Resultant mmf**

The resultant flux harmonics due to combined tooth ripple and armature reaction flux can be calculated using a static FEA method. The permanent magnets are made active i.e., B_r=1.07 and sinusoidal three phase current is assigned to the phases of PMSG1, so that the airgap flux density is due to the interaction of both sources. Figure 5.6 shows the resulting flux distribution due to interaction of rotor and stator mmf in PMSG1.

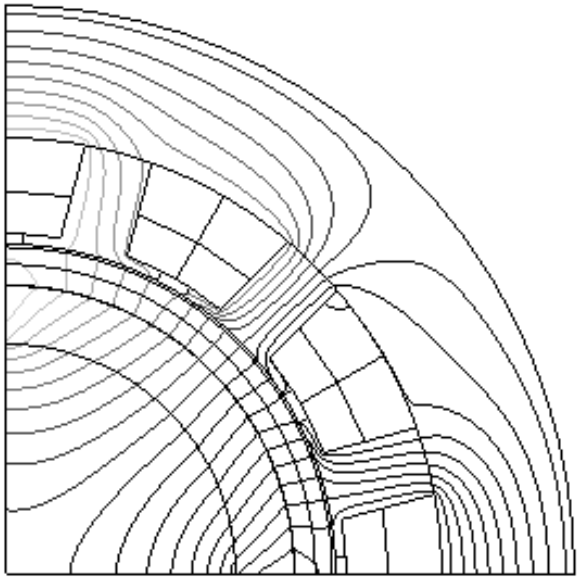

Figure 5.6. Flux distribution due to combined stator mmf and permanent magnet mmf, for a particular rotor position

Following, Figure 5.7 shows the airgap flux density distribution just above the magnet surface due to interaction between both sources, at $\theta = 0$ rotor position. The combined data for all 30 rotor positions covering one slot pitch is shown in Figure 5.8.

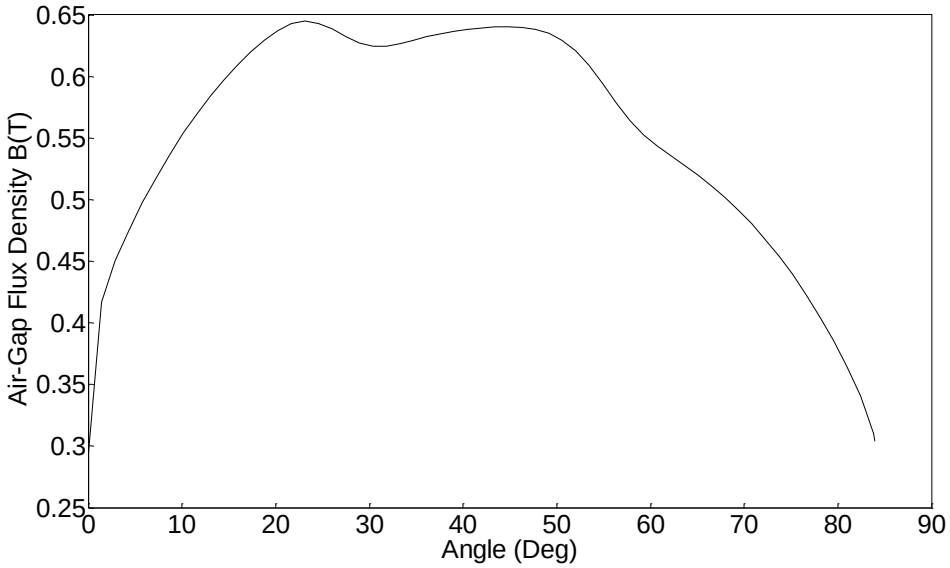

Figure 5.7. Normal airgap flux density on the surface of the magnet, obtained from one FEA static solution combining both magnet flux and armature reaction stator mmf

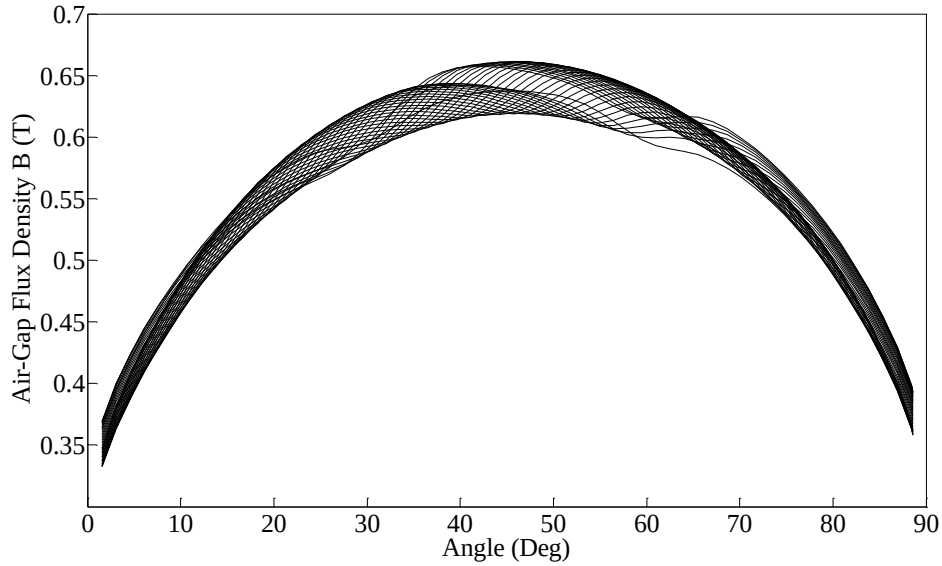

Figure 5.8. Normal airgap flux density on the surface of the magnet, obtained from 30 FEA static solutions combining both magnet flux and armature reaction stator mmf

5.5.3 **Amplitude of Magnet flux tooth ripple Harmonics**

The amplitude of magnet flux tooth ripple harmonics using the analytical method from Ẑarko et al (2006) had been presented in Table 4.10. The amplitude of these harmonics are used later in the section for the calculation of resultant harmonics.

5.5.4 **Armature Reaction Stator mmf Harmonics**

Two dimensional Fourier analysis is performed on the airgap flux density data in Figure 5.5 using analytical programs *FFT1*.m and *FFT2*.m to calculate the amplitudes of armature reaction stator mmf harmonics in the rotor reference frame. Even travelling spatial harmonics are absent due to the presence of odd symmetry in the spatial distribution of the stator mmf.

The analytical method discussed in section 5.3.1, is also used for the calculation of armature reaction stator mmf harmonics. The method has been implemented in the program *Current1*.mw in Appendix 1. Table 5.2 presents a comparison between amplitude of harmonics; calculated using both analytical and static FEA methods.

Spatial order, q	Temporal order, k				
		0	6	12	18
1	Static FEA Analytical	0.0591 0.0608			
5	Static FEA Analytical		0.0115^- 0.0114^-		
7	Static FEA Analytical		0.0054^- 0.0066^-		
11	Static FEA Analytical			0.0021^- 0.0022^-	
13	Static FEA Analytical			0.0007^- 0.0013^-	
17	Static FEA Analytical				0.0003^- 0.0004^-
19	Static FEA Analytical				0.0006^- 0.00026^-

Table 5.2. Comparison between analytical and static FEA methods for the calculation of armature reaction flux harmonic amplitudes at a current advance angle of 0 degrees and a fundamental frequency f of 3000Hz

The rotor eddy current power loss due to each harmonic shown in Table 5.2 is calculated using same *Current1*.mw program in Appendix 1. A comparison between analytical and static FEA method for rotor eddy current power loss due to each harmonic is presented in Table 5.3. While the individual harmonics of flux density are very different, the total power loss shows good agreement. This is because the contribution to loss of those harmonics whose amplitudes are very different is only small. The results presented show that the majority of rotor eddy current power loss is due to temporal order 6 with space order of 5 and 7.

Spatial order, q	Temporal order, k			
		6	12	18
5	Static FEA Analytical	109 122		
7	Static FEA Analytical	10 15		
11	Static FEA Analytical		1.5 2	
13	Static FEA Analytical		0.1 0.4	
17	Static FEA Analytical			0.02 0.03
19	Static FEA Analytical			<0.01 0.01
Power loss (Analytical)				≈ 139 W
Power loss (Static FEA)				≈ 121 W
Power loss (Transient FEA (un-saturated tooth tip)				≈ 130 W
Power loss (Transient FEA (saturated tooth tip)				≈ 130 W

Table 5.3. Comparison between analytical, static and transient FEA methods for the calculation of rotor power loss caused by armature reaction stator mmf harmonics

5.5.5 **Amplitude of Resultant Harmonics**

Two dimensional Fourier analysis is performed using the analytical programs *FFT1*.m and *FFT2*.m on the resultant airgap flux density data in Figure 5.8 in order to calculate the amplitudes of resultant flux harmonics. Analytically, the resultant flux harmonics are calculated using methodology discussed in section 5.3.2. This has been implemented in the program *Vadd1*.mw in Appendix 1. Table 5.4 presents a comparison for the amplitude of resultant harmonics calculated using both analytical and static FEA methods.

Spatial order, q	Temporal order, k				
		0	6	12	18
1	Static FEA Analytical	0.7767 0.7916			
5	Static FEA Analytical	0.1922 0.1652			
7	Static FEA Analytical	0.1053 0.0799	0.0128^{-} 0.0125^{-}		
11	Static FEA Analytical	0.0717 0.0482	0.0047^{-} 0.009^{-}		
13	Static FEA Analytical	0.0436 0.0235		0.00315^{-} 0.0025^{-}	
17	Static FEA Analytical	0.0362 0.0175		0.0014^{-} 0.0027^{-}	
19	Static FEA Analytical	0.0266 0.0104			0.00069^{-} 0.00067^{-}

Table 5.4. Comparison between analytical and static FEA methods for the calculation of resultant flux harmonic amplitudes

A comparison for the rotor eddy current power loss due to asynchronous harmonics shown in Table 5.4, is presented in Table 5.5. The rotor eddy current power loss is calculated taking into account reaction of eddy current field using equation 3.42. This has been implemented in analytical programs *Harmonic1.mw* and *Loss1*.mw in Appendix 1.

Spatial order, q	Temporal order, k			
		6	12	18
5	Static FEA Analytical	136 129		
7	Static FEA Analytical	8 28		
11	Static FEA Analytical		4 2	
13	Static FEA Analytical		0.4 2	
17	Static FEA Analytical			0.1 0.1
19	Static FEA Analytical			0.01 0.01
Power loss (Analytical)				≈ **161** W
Power loss (Static FEA)				≈ **149** W
Power loss (Transient FEA (un-saturated tooth tip))				≈ **157** W
Power loss (Transient FEA (saturated tooth tip))				≈ **180** W

Table 5.5. Comparison between analytical, transient and static FEA methods for the calculation of rotor eddy current power loss caused by resultant harmonics

5.6 Effect of current advance load angle

The rotor power loss calculation presented in Table 5.5 is performed with a load angle ψ, between the back EMF E and current I, taken to be zero degrees, for which the angle α_{qk} is 90 degrees.

As well as the armature reaction in PMSGs changes the airgap flux density. It strengthens the flux density for a capacitive load and weakens it for an inductive load. This results in a change in the amplitude of rotating harmonics from the rotor mmf / stator mmf / resultant mmf, which in turn changes the power loss.

This section investigates the effect of current advance angle on the amplitudes of airgap flux harmonics and corresponding rotor eddy current power loss. The amplitude of resultant harmonics are calculated using the analytical program *Vadd1*.mw in Appendix 1, the results are presented in Table 5.6. The corresponding

rotor eddy current power loss due to each harmonic over a range of current advance angles is shown in Table 5.7. The results show that rotor eddy current power loss is mainly caused by harmonics of temporal order 6 and spatial orders 5 and 7.

Spatial order, q	Temporal order, k			
	Current advance angles, φ	6	12	18
5	-90	0.0067		
	-60	0.0076		
	-30	0.0099		
	30	0.0143		
	60	0.0156		
	90	0.0161		
7	-90	0.0128		
	-60	0.0123		
	-30	0.011		
	30	0.0064		
	60	0.0033		
	90	0.0004		
11	-90		0.0004	
	-60		0.0011	
	-30		0.002	
	30		0.0034	
	60		0.0037	
	90		0.004	
13	-90		0.0037	
	-60		0.0035	
	-30		0.0032	
	30		0.002	
	60		0.00124	
	90		0.0011	

Table 5.6. Analytical calculation of harmonics amplitudes at current advance angles ranging from an inductive to capacitive load

Since the 5^{th} and 7^{th} harmonics due to the stator mmf is the largest harmonic, tooth ripple 5^{th} harmonic is weakened for the pure inductive load and are strengthened for the pure capacitive load and opposite is true for 7^{th} harmonic.

Table 5.7 shows that the, space 5^{th} harmonic loss increases with increase in the phase angle (from -90 to +90 degrees), whereas it reduces for the 7^{th} space harmonic. Behaviour of the 11^{th} is similar to that of the 5^{th} harmonic and behaviour of the 13^{th} space harmonic is similar to that of the 7^{th} harmonic, the same as the corresponding harmonic's amplitude. Similar behaviour may not be valid for harmonics not shown in the table, however they are not significant.

Spatial order, q	Temporal order, k			
	Current advance angles	6	12	18
5	-90 -60 -30 30 60 90	37 48 81 169 201 214		
7	-90 -60 -30 30 60 90	56 52 41 14 4 0.05		
11	-90 -60 -30 30 60 90		0.057 0.43 1.5 4 5 6	
13	-90 -60 -30 30 60 90		3 3 2 1 0.34 0.27	
Total Power loss (Analytical) Total Power loss (Transient FEA (un-saturated tooth tip)) Total Power loss (Transient FEA (saturated tooth tip))	-90	96W 85W 73W		
Total Power loss (Analytical) Total Power loss (Transient FEA (un-saturated tooth tip)) Total Power loss (Transient FEA (saturated tooth tip))	-60	103W 102W 88W		
Total Power loss (Analytical) Total Power loss (Transient FEA (un-saturated tooth tip)) Total Power loss (Transient FEA (saturated tooth tip))	-30	126W 130W 125W		
Total Power loss (Analytical) Total Power loss (Transient FEA (un-saturated tooth tip)) Total Power loss (Transient FEA (saturated tooth tip))	30	188W 200W 245W		
Total Power loss (Analytical) Total Power loss (Transient FEA (un-saturated tooth tip)) Total Power loss (Transient FEA (saturated tooth tip))	60	210W 218W 280W		
Total Power loss (Analytical) Total Power loss (Transient FEA (un-saturated tooth tip)) Total Power loss (Transient FEA (saturated tooth tip))	90	220W 250W 360W		

Table 5.7. Comparison between analytical and transient FEA solutions for rotor eddy current power loss with current advance angles ranging from an inductive to capacitive load

The improvement in accuracy obtained by using vector addition, for the calculation of losses due to resultant mmf (magnet flux and stator mmf), is highlighted in following Figure 5.9. Good agreement is observed between analytical and FEA results when vector addition is used. The results presented also show the high discrepancy between FEA and analytical methods in the case of superposition. The losses are significantly overestimated when the load is inductive and underestimated when it is capacitive.

The superposition of losses (or the amplitude of harmonics) is correct only when the phase advance angle is zero.

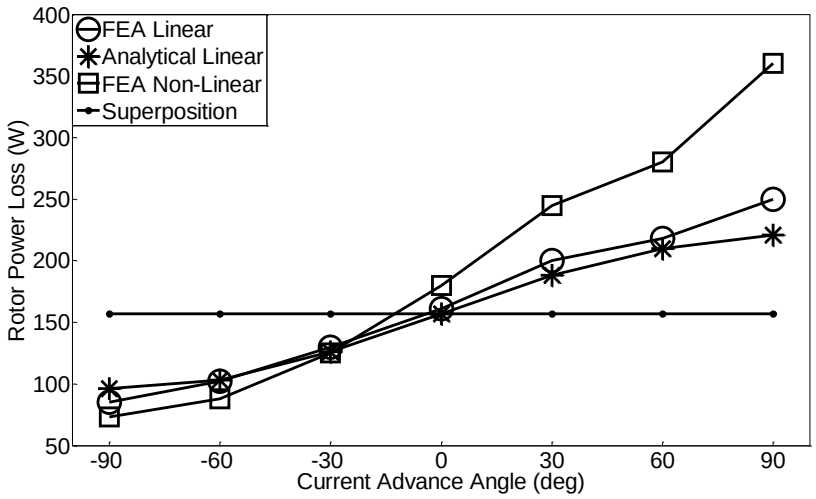

Figure 5.9. Comparison for rotor eddy current power loss using superposition, vector addition and FEA methods

5.7 Conclusion

This chapter compared the accuracy of analytical methods with FEA for the calculation of the amplitudes of harmonics caused by first armature reaction stator mmf alone, then combined rotor and stator mmf in PMSG1. The corresponding rotor eddy current power loss due to these harmonics is calculated using the analytical current sheet method and the results are compared with those using static FEA and transient FEA methods. The reaction of eddy currents is catered for in the rotor loss calculation.

Good agreement is seen between analytical and FEA methods for the calculation of armature reaction stator mmf harmonics and corresponding rotor eddy current power loss. Since the winding factor equation doesn't cater for the effects of slot opening and stator tooth tip saturation, the observed good agreement between analytical and FEA methods demonstrates that armature reaction stator mmf is not significantly dependent on slot openings or the saturation of stator tooth tips.

It has been shown that tooth ripple loss can be significant in some PM machines, e.g. PMSG1, and if ignored may lead to inaccurate rotor power loss calculation. In the

context of adding tooth ripple and armature reaction flux harmonics it has been shown that, in comparison to superposition, vector addition of the two field harmonics results in a significantly more accurate power loss calculation.

Discrepancy between analytical and FEA results for the calculation of resultant harmonics is observed in the case of saturated stator tooth tips (i.e., the case where stator permeability assigned as non-linear BH curve).

Chapter 6

Rotor Eddy Current Power Loss in PMSG Connected to an Uncontrolled Rectifier

6.1 Introduction

High speed permanent magnet synchronous generators are used in many applications, including gas turbine CHP (combined heat and power) generators and exhaust energy recovery systems used in micro grids. The output of the generator is usually conditioned (rectified) using an uncontrolled rectifier, in which power diodes are used for switching, followed by a dc/dc converter and a three-phase grid connected inverter (Abusara et al., 2014).

The use of uncontrolled rectifiers in high-speed PM machines can be justified. In these machines high fundamental frequencies (in our case it is 3000 Hz), and high power levels (> 50 kW), mean using an active rectifier can be fraught with difficulties. To synthesise a good PWM waveform and maintain current ripple at an acceptable level the PWM frequency needs to be so high (> 30 kHz) it is outside the range of high power IGBTs. Additionally, PWM ripple can cause significant rotor losses in the machine. The PWM current ripple could be reduced by using an inductor, but that adds size and cost to an already complex converter.

Due to the high rotational speed and high harmonic content of the stator current, rotor losses in PM machines connected to rectifier loads can be significant and could lead to overheating of the magnets and the retaining sleeve (Vadher et al., 1986; Seok-Myeong Jang, 2006; Van der Veen et al., 1997; Nagarkatti et al., 1982).

This chapter compares the accuracy of analytical and transient FEA methods for the calculation of rotor eddy current power loss in a permanent magnet synchronous generator connected to an uncontrolled bridge rectifier. Two winding and rectifier topologies are considered: (1) a 3-phase winding with a 3-phase bridge rectifier and (2) a double 3-phase winding, with a 3-phase rectifier for each winding, connected in series. The cases of constant current and constant voltage rectifier DC links are investigated. Both magnet flux tooth ripple and stator mmf harmonics are considered in the calculation of rotor loss. Vector addition is used to calculate the resultant harmonics from the interaction of sources, taking into account the phase angle between each harmonic for rotor eddy current power loss calculation.

6.2 Machine under Study

PM synchronous generator PMSG2, shown in Figure 3.2, is used for the study. The generator has 4mm slot opening and other dimensions and material properties are shown in Table 3.1. The terminals of the generator are connected to an uncontrolled rectifier, feeding a constant current, highly inductive load and constant voltage, highly capacitive load. The values of inductance and capacitance are assumed to be infinite.

6.2.1 **Winding and Rectifier Configurations**

Two winding and rectifier configurations were considered and investigated. In the first configuration, the winding is a 3-phase fully pitched, double layer winding with two slots per pole per phase, feeding one rectifier as shown in Figure 6.1.

In the second configuration, the winding is split into two sets of fully pitched, double layer, 3-phase windings with 1 slot per pole per phase each. Each set is connected to a 3-phase bridge rectifier and the two rectifiers are connected in series as shown in Figure 6.2. There is a 30 electrical degrees phase shift between the emf's of the two

sets of windings as they are displaced in space by 1 slot pitch.

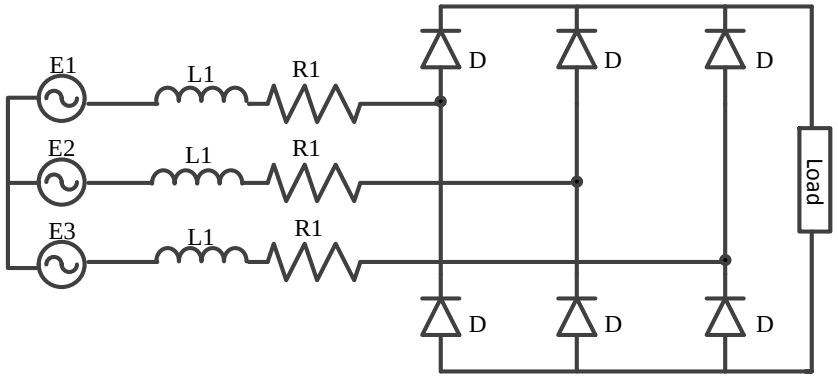

Figure 6.1. PMSG2 with one three phase winding connected to a single three phase bridge rectifier

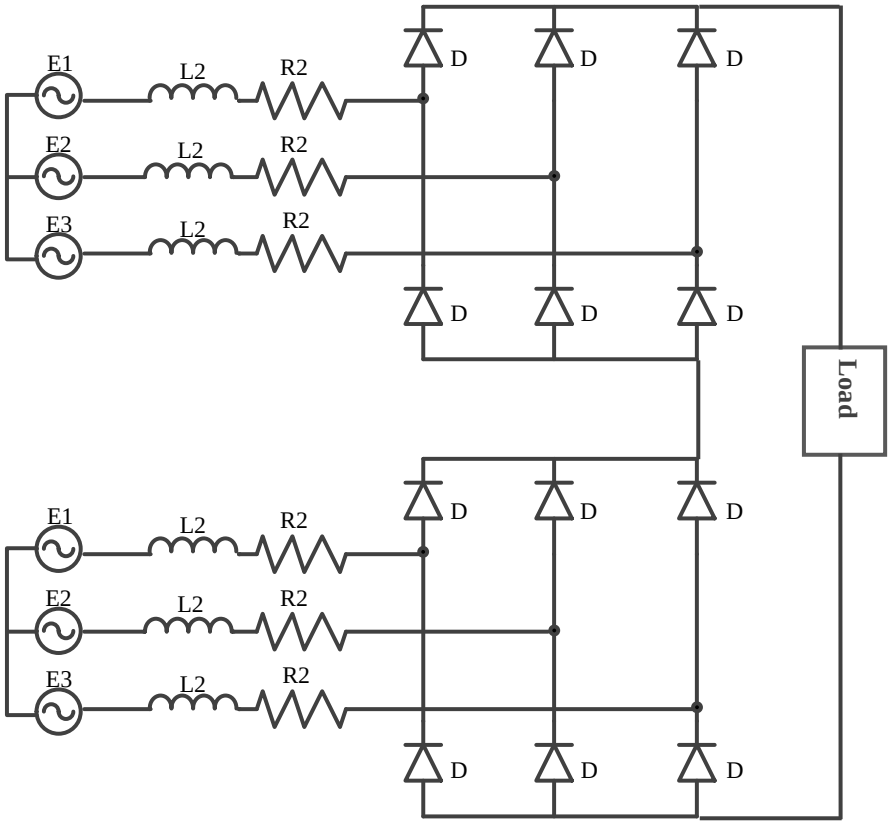

Figure 6.2. PMSG2 with two sets of three phase windings, connected to two rectifiers

6.2.2 **Rectifier Current Waveforms**

In principle the rectifier current could be calculated from a circuit simulation including the emf, resistance and inductance of the winding. For accuracy the winding inductance needs to be frequency dependent and saturation needs to be taken into account. But to enable direct comparison between FEA and analytical calculation, the

current produced by FEA is prescribed in the analytical model. A typical phase current waveform for a machine connected in a two rectifier topology, and with a constant dc link current (CC) source, is shown in Figure 6.3. The constant current source value was set to 128 A to give an average torque of 7.5 Nm at a speed of 90,000 rpm. The waveform for a machine with one rectifier is similar.

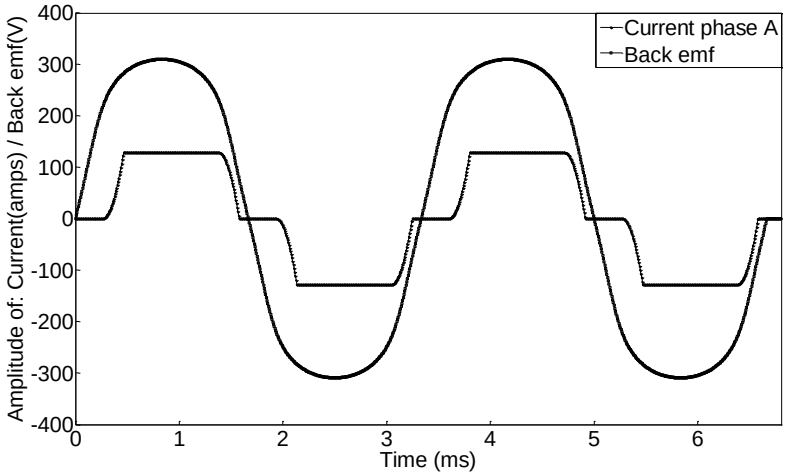

Figure 6.3. Phase current of a generator connected to both rectifier topologies with a constant current (CC) dc link. DC link current is 128A, speed is 90,000 rpm and torque is 7.5 Nm

The spectrum of harmonic amplitudes and corresponding phase angles for both wave forms is presented in the following Figures 6.3a and 6.3b.

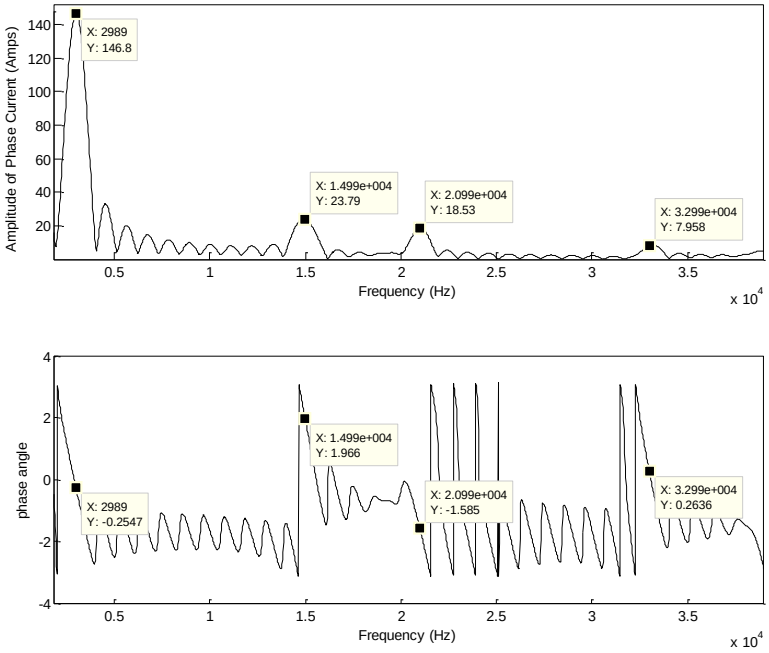

Figure 6.3a: Amplitude and phase angles spectrum for the current waveform shown in Figure 6.3.

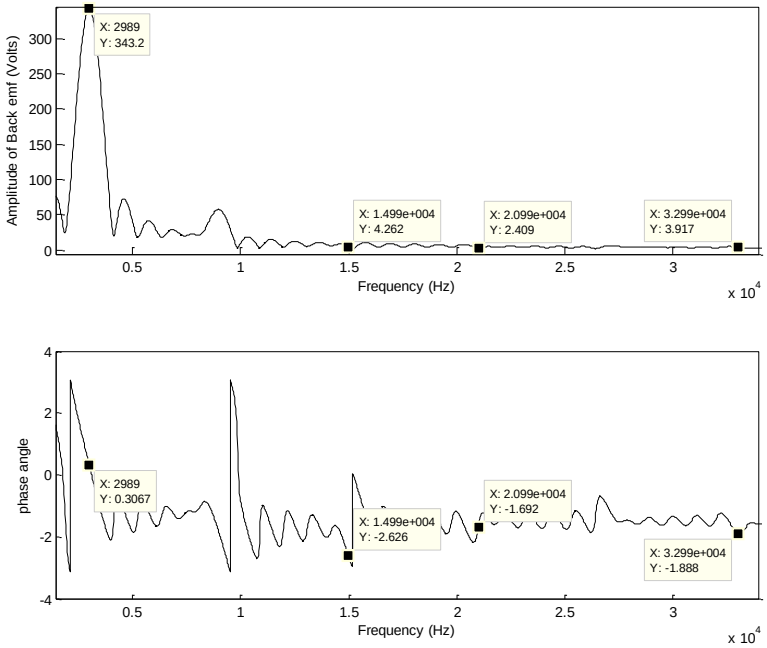

Figure 6.3b: Amplitude and phase angles spectrum for the back emf waveform shown in Figure 6.3.

The phase current waveform of a machine connected to one rectifier with a constant dc link voltage (CV) is shown in Figure 6.4. The waveform for a machine with two rectifiers with a constant dc link voltage is shown in Figure 6.5.

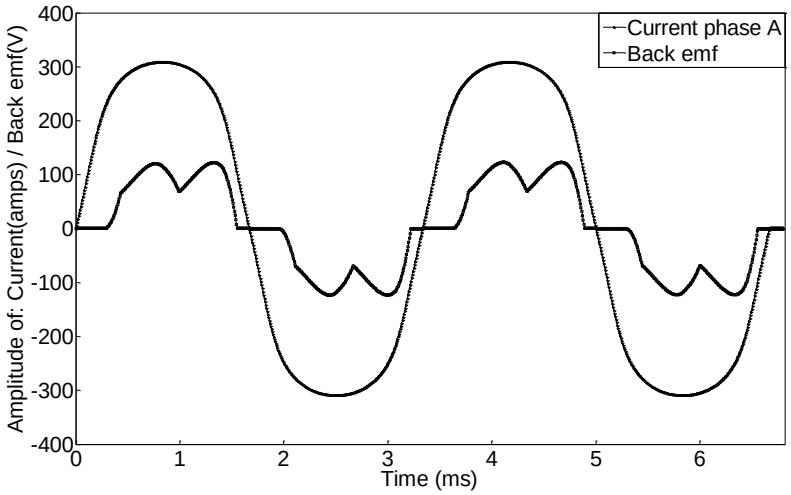

Figure 6.4. Phase current waveform of a generator connected to one rectifier with a constant voltage (CV) dc link. DC link voltage=543 V, speed =90,000 rpm, current =121 A and torque = 6 Nm

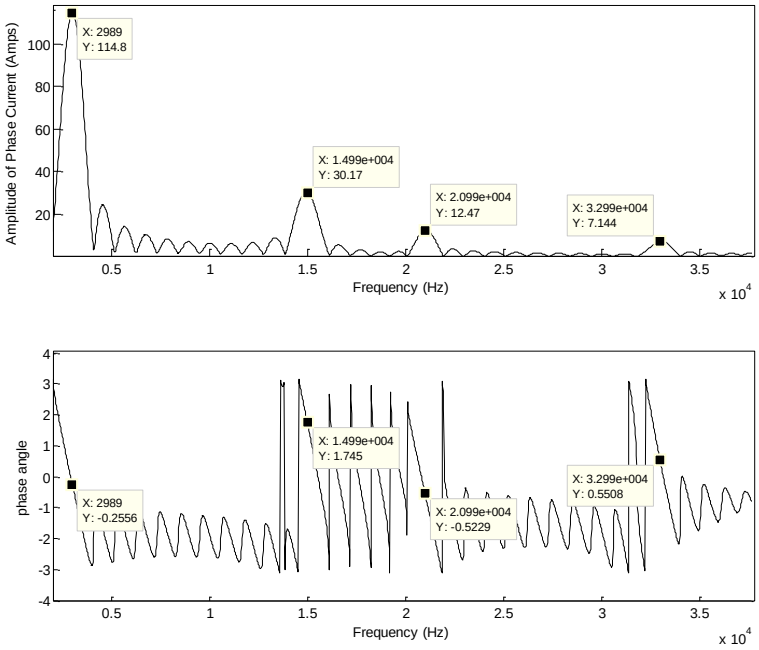

Figure 6.4a: Amplitude and phase angles spectrum for the current waveform shown in Figure 6.4.

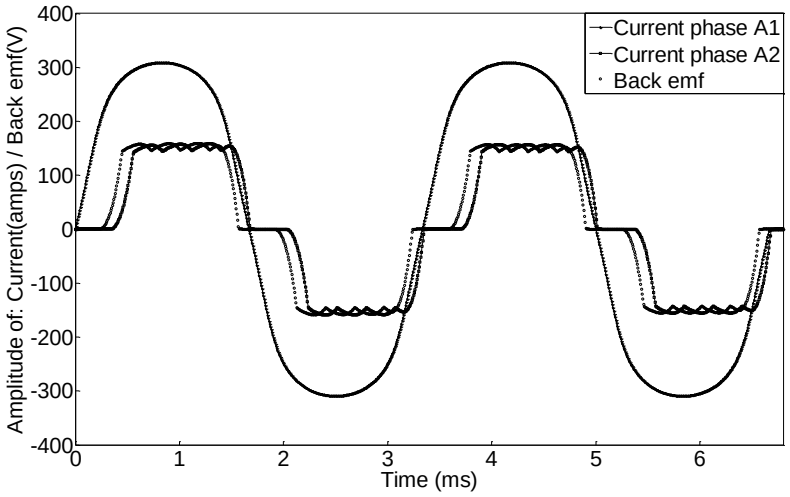

Figure 6.5. Phase current waveform of a generator connected to two rectifiers with a constant voltage (CV) dc link. DC link voltage = 543 V, speed =90,000 rpm, current = 121 A and torque = 7.5 Nm

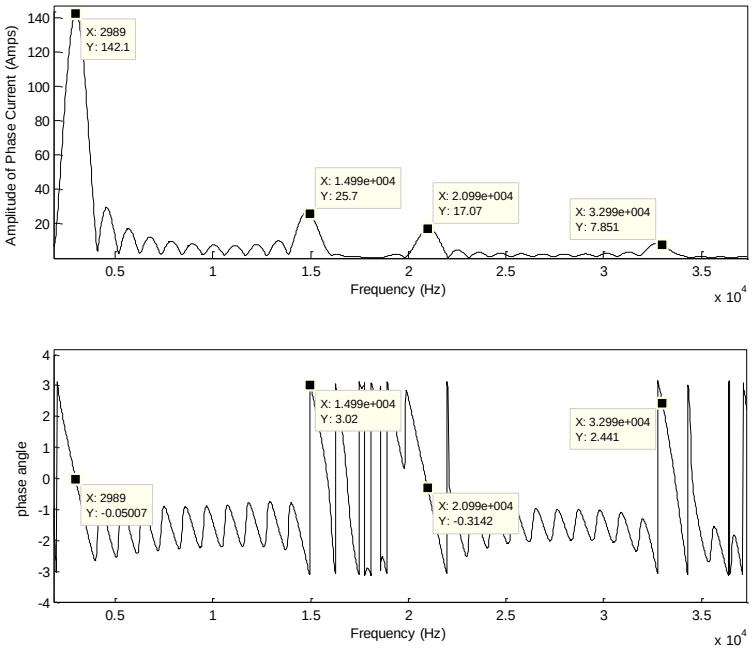

Figure 6.5a: Amplitude and phase angles spectrum for the current waveform (A1) shown in Figure 6.5.

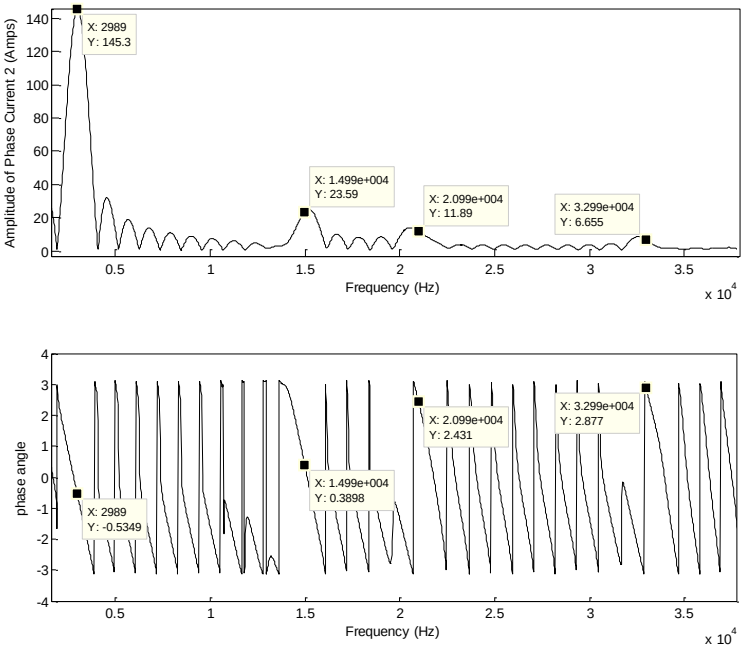

Figure 6.6a: Amplitude and phase angles spectrum for the current waveform (A2) shown in Figure 6.5.

6.2.3 **Vector (phasor) Addition**

To add the tooth ripple and armature reaction flux harmonics vectorially, one must first calculate the load angle ψ between each current harmonic I and the back emf E.

It is worth noting that the load angle at the terminals of the generator when feeding a purely resistive load is always less than unity, mainly due to delay angle of the current introduced by the switching. It is 0.956 for a three phase, uncontrolled, full bridge rectifier feeding a resistive load, and 0.955 for a highly inductive load. For a capacitive load the load angle is $0.955\cos\alpha$ where α is the firing angle, which in the case of an uncontrolled rectifier is zero (Shephard W et al., 1995).

Using program *FFTI2*.m in Appendix 2, Fourier analysis is performed on the current and back emf waveforms shown in Figures 6.3, 6.4 and 6.5, in order to calculate the amplitude and phase angle of each harmonic in the stator reference frame. The load angle ψ for both rectifier topologies when connected to a constant current dc link is calculated using the analytical program *Vadd2*.mw in Appendix 1. The results for the load angle are shown in Table 6.1. Using the same program *Vadd2*.mw the load angle for both rectifier topologies when connected to a constant voltage dc link is calculated. The results for the constant voltage dc link case are shown in Table 6.2.

Harmonic	One Rectifier Topology ψ(rad)	Two Rectifier Topology ψ(rad)
Fundamental	-0.56	-0.6
5^{th}	4.5	4.2
7^{th}	0.1	-0.65
11^{th}	2.1	1.71
13^{th}	-1.5	2.2
17^{th}	0.13	2
19^{th}	1.6	2.8

Table 6.1. Phase angle ψ between Back EMF *E* and Current *I* for the constant current dc link case

Harmonic	One Rectifier Topology ψ(rad)	Two Rectifier Topology ψ(rad)
Fundamental	-0.56	-0.349
5^{th}	1.43	2.7
7^{th}	-0.82	-0.61
11^{th}	0.24	2.13
13^{th}	-2.2	-0.635
17^{th}	-1.23	1.8
19^{th}	2.6	-1.77

Table 6.2. Phase angle ψ between Back EMF *E* and Current *I* for constant voltage dc link case

6.3 Methodology for Analytical Method

In this section, analytical method by Ẑarko et al., (2006) is used to calculate airgap magnet flux distribution waveform in PMSG2. The waveform is compared with the one calculated using transient FEA. The methodology is presented for the calculation of stator mmf harmonic amplitudes in PMSG2, when connected to the two winding and rectifier topologies.

6.3.1 **Airgap Magnet Flux Density Distribution**

The radial and tangential components of airgap complex permeance function over the magnet surface, covering a range of one slot pitch, is calculated using the analytical program *Ẑarko*.mw in Appendix 1; the results are shown in Figures 6.6a and 6.6b.

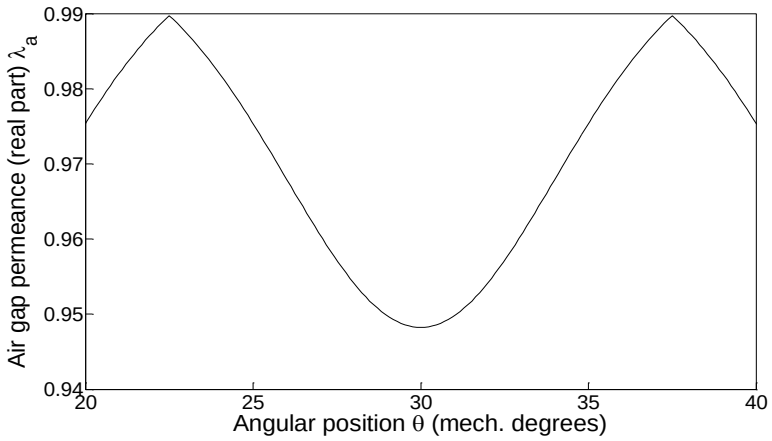

(a)

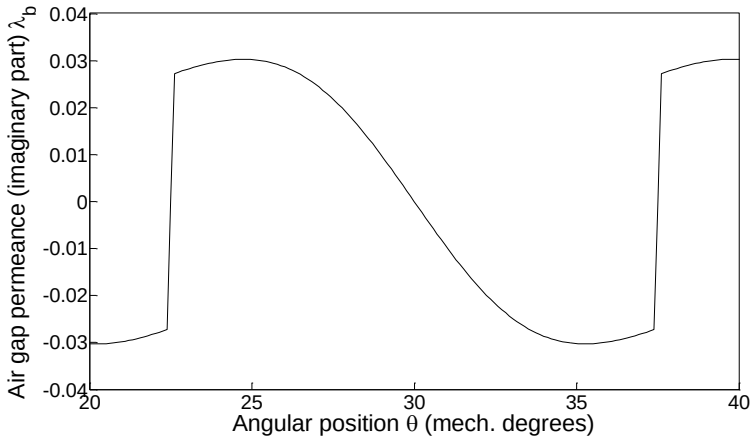

(b)

Figure 6.6. Complex relative air-gap permeance over the surface of the magnet covering one slot pitch of the machine under study (a) Real component (b) Imaginary component

The complex permeance function λ^* is then multiplied with the radial component of slotless airgap flux density to cater for the effect of slotting as:

$$B_{gr}(r,\theta) = \lambda_a\left(r,(\theta-\omega t)\right)\cdot B_{sr}(r,\theta) + \lambda_b\left(r,(\theta-\omega t)\right)\cdot B_{s\theta}(r,\theta) \tag{6.1}$$

The accuracy of the analytical method is compared with transient FEA for the calculation of radial airgap flux distribution, as illustrated in Figure 6.7.

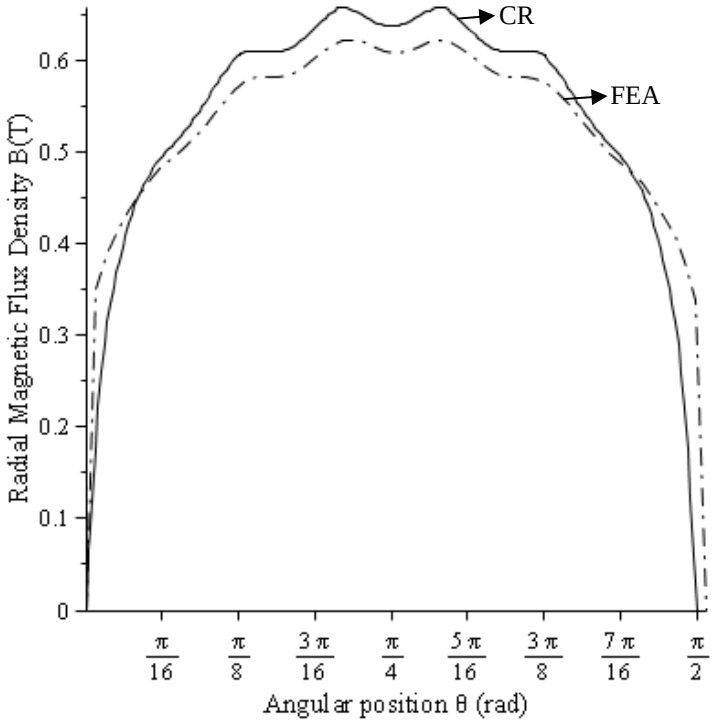

Figure 6.7. Comparison between analytical and transient FEA method for airgap flux density distribution in PMSG2 due to magnet flux

6.3.2 Armature Reaction Flux Harmonics in PMSG2 Connected to the One Rectifier Topology

In case of PMSG2 connected to one rectifier topology, the amplitude of the armature reaction flux harmonics F_{qk} , with spatial order q and temporal order k, can be estimated using analytical equation (5.1); the equivalent current sheet is calculated using equation (5.2). Thus, using the equivalent current sheet the amplitude of radial and tangential airgap flux density on the surface of magnet (as discussed in chapter 3) can be calculated as:

$$B_r(r,\theta) = \frac{J_{qk} R_3 \mu_0 \left(R_1^{-2q} r^q + r^{-q} \right)}{r\left(R_1^{-2q} R_3^q - R_3^{-q} \right)} \tag{6.2}$$

$$B_\theta(r,\theta) = \frac{J_{qk} R_3 \mu_0 \left(R_1^{-2q} r^q - r^{-q} \right)}{r\left(R_1^{-2q} R_3^q - R_3^{-q} \right)} \tag{6.3}$$

It is important to correctly calculate winding distribution factor K_{wq} in equation (5.2). For spatial harmonics due to fully pitched, double layer winding configuration in the generator under study, the methodology for the calculation of K_{wq} is presented. The mmf distribution due to each set of windings shown in Figure 3.2, can be shown as:

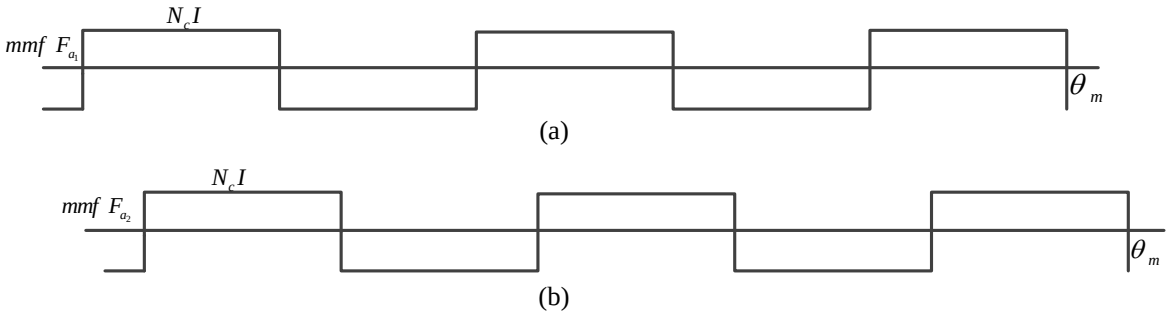

Figure 6.8. mmf distribution due to each winding configuration

In Figure 6.8, N_c, I and θ_m represents turns per coil, current in the winding and mechanical angle in degrees, respectively. The number of turns per coil N_c can be written as:

$$N_c = \frac{N_{ph}}{2p \times spp} \tag{6.4}$$

In equation (6.4), N_{ph}, p and spp represents number of phases, number of pole pairs and number of slots per pole per phase, respectively. The sum of mmfs shown in Figure 6.8 from two slots takes the form shown in Figure 6.9 and is given by:

$$\vec{F} = \vec{f}_{a1} + \vec{f}_{a2} \tag{6.5}$$

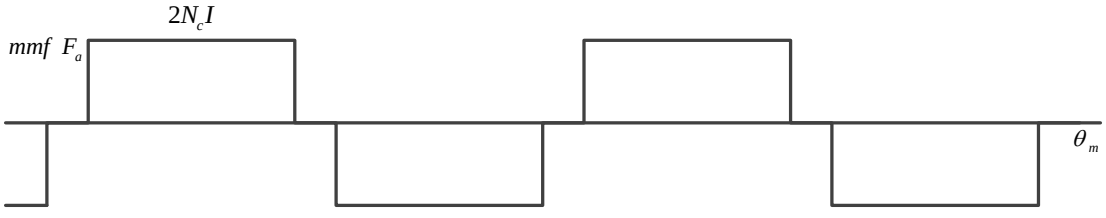

Figure 6.9. Total mmf due to two sets of three phase winding

The mmf magnitude is proportional to twice the number of turns per coil and the contributions from each slot are separated by 30 electrical degrees. The total mmf F is given by:

$$F^2 = \vec{F} \cdot \vec{F} = \left(\vec{f}_{a1} + \vec{f}_{a2} \right) \cdot \left(\vec{f}_{a1} + \vec{f}_{a2} \right) \tag{6.6}$$

$$F^2 = \vec{F} \cdot \vec{F} = \vec{f}_{a1}^{\,2} + \vec{f}_{a2}^{\,2} + 2\,\vec{f}_{a1}\vec{f}_{a2} \cos\left(\frac{q\pi}{6} \right) \tag{6.7}$$

Since $\vec{f}_{a1}$ and $\vec{f}_{a2}$ are similar in magnitude, the equation (6.7) can be simplified as:

$$F^2 = \vec{F} \cdot \vec{F} = 2\,\vec{f}^{\,2} + 2\,\vec{f}^{\,2} \cos\left(\frac{q\pi}{6} \right) \tag{6.8}$$

As the pitch and skew factors are equal to 1, the distribution factor can be deduced from equation (6.8) as:

$$\left(\frac{F}{2f} \right)^2 = K_{wq}^2 = \frac{1}{2}\left(1 + \cos\left(\frac{q\pi}{6} \right) \right) \tag{6.9}$$

$$K_{wq} = \sqrt{\left(\cos^2\left(\frac{q\pi}{12} \right) \right)} \tag{6.10}$$

$$K_{wq} = \cos\left(\frac{q\pi}{12} \right) \tag{6.11}$$

The validity of equation (6.11) can be proved by also deriving it from the general winding distribution factor K_{wq} expression, which is given as:

$$K_{wq} = \frac{\sin\left(q \cdot \frac{\pi}{2 \cdot m} \right)}{S_{pp} \cdot \sin\left(\frac{q \cdot \pi}{2 \cdot m \cdot S_{pp}} \right)} \tag{6.12}$$

In equation (6.12), m and S_{pp} are number of phases and slots per pole per phase, respectively. For PMSG2, by substituting m = 3 and S_{pp} = 2 in equation (6.10), and let,

$$x = q.\frac{\pi}{2mS_{pp}} = \frac{q\pi}{12}$$

Then equation (6.12) can be written as:

$$K_{wq} = \frac{\sin 2x}{2\sin x} = \frac{2\sin x\cos x}{2\sin x} = \cos x = \cos\left(\frac{q\pi}{12}\right) \tag{6.13}$$

6.3.3 **Armature Reaction Flux Harmonics in PMSG2 Connected to the Two Rectifier Topology**

The armature reaction flux harmonics for PMSG2 connected to two rectifiers are calculated by defining the mmf distribution for the phase A, in two winding sets, as:

$$F_{a_1} = F_1\cos\left(\frac{\Omega}{\omega}(\omega t)\right)\left(\cos\theta - \frac{1}{3}\cos(3\theta) + \frac{1}{5}\cos(5\theta).....\right), \tag{6.14}$$

$$F_{a_2} = F_1\cos\left(\frac{\Omega}{\omega}\left(\omega t - \frac{\pi}{6}\right)\right)\left(\begin{array}{r}\cos\left(\theta - \frac{\pi}{6}\right) - \frac{1}{3}\cos\left(3\left(\theta - \frac{\pi}{6}\right)\right) \\ + \frac{1}{5}\cos\left(5\left(\theta - \frac{\pi}{6}\right)\right).....\end{array}\right) \tag{6.15}$$

In equation (6.14) and (6.15), Ω and F_1 are given by:

$$\Omega = n\omega \tag{6.16}$$

$$F_1 = \frac{4}{\pi}N_c\hat{I}_k \tag{6.17}$$

In equation (6.16) and equation (6.17), n, N_c, $\hat{I}_k$ are the number of harmonics, number of turns per coil and rms value of the stator current, respectively.

The mmf distribution of phase B, represented by F_{b_1}, F_{b_2}, and of phase C represented by F_{c_1}, F_{c_2}, will be 120^0 and 240^0 apart from phase A, respectively. The total mmf sum from the three phases F_{qk} is given by:

$$F_{qk} = F_{a_1} + F_{a_2} + F_{b_1} + F_{b_2} + F_{c_1} + F_{c_2} \tag{6.18}$$

Using equation (6.18), the amplitude of armature reaction flux harmonics F_{qk} can be calculated in rotor reference frame. The equivalent current sheet $\hat{J}_{qk}$ for each harmonic at the stator bore is then calculated as:

$$\hat{J}_{qk} = \frac{q \cdot p}{R_3} \cdot F_{qk}$$

Equations (5.2-5.14) are then employed to calculate the amplitude of radial and tangential airgap flux density on the surface of magnet for the two rectifier topology.

6.3.4 **Amplitude of Resultant Harmonic**

The vector addition of magnet flux tooth ripple harmonics calculated in equation (6.1) and armature reaction stator mmf harmonics calculated in equation (6.2), in the case of both rectifier topologies is calculated as:

$$B_t = \sum_{k=0}^{\infty}\sum_{h=1}^{\infty} B_{gr}(r,\theta)\cos(h\theta + k\omega t) + B_r(r,\theta)\begin{pmatrix}\cos(h\theta + k\omega t)\cos(\alpha_{qk}) \\ -\sin(h\theta + k\omega t)\sin(\alpha_{qk})\end{pmatrix} \quad (6.19)$$

6.4 Analytical vs. Transient FEA Methods

This section compares the analytical and FEA methods for the calculation of harmonic amplitude and corresponding rotor eddy current power losses in PMSG2. In contrast to the sinusoidal current case (discussed in chapter 5), the amplitude of armature reaction stator mmf harmonics of fundamental spatial order are now significant. In addition, the amplitudes of other rotating harmonics have increased. This section also highlights the importance of vector addition for accurate analytical results.

6.4.1 **Amplitude of Magnet Flux Tooth Ripple Harmonics and Corresponding Rotor Power Loss**

The amplitudes of magnet flux tooth ripple harmonics in PMSG2 using the analytical method by Žarko et al., (2006) (program *Žarko*.mw in Appendix 1) are presented in Table 6.3. The rotor eddy current power loss due to each harmonic taking into account reaction of eddy current field is calculated using equation (3.42), which is implemented in analytical programs *Harmonic1*.mw and *Loss1*.mw in Appendix1

(procedure known as current sheet rotor loss calculation method). The results are presented in Table 6.4; in which empty cells indicates that power loss is < 0.5 W and is therefore neglected – this is henceforth applicable to all Tables.

Spatial order q	Temporal order k	
	12	24
11	0.0047^{-}	
13	0.0104^{-}	
15	0.0032^{-}	
17	0.0018^{-}	
23		0.000318^{-}
25		0.0017^{-}

Table 6.3. Magnet flux tooth ripple harmonic amplitudes in T, at f_1 = 3000 Hz. Negative sign indicate CW rotating harmonics

Spatial order q	Temporal order k	
	12	24
11	8	
13	24	
15	1.5	
17	0.5	
23		<0.5
25		0.5
Power loss (Analytical)		≈ **34** W
Power loss (FEA Transient Linear Solution)		≈ **24** W

Table 6.4. Rotor eddy current loss due to magnet flux tooth ripple harmonic in PMSG2

6.4.2 **Amplitude of Armature Reaction Stator mmf Harmonics and Corresponding Rotor Power Loss (Constant Current dc link load)**

For PMSG2 connected to a one rectifier topology and feeding a constant load current of 128A, the armature reaction stator mmf harmonics can be calculated by defining the magnet regions as a material that has permeability equal to the recoil permeability of the magnets and a conductivity equal to zero. Fourier transform is performed on Figure 6.3 using program *FFT12*.m in Appendix 2 to calculate the value of stator winding current at different time order. This current value is then used in program *Current1*.mw in Appendix 1 to calculate amplitude of armature reaction stator mmf

harmonics travelling in space and time, as presented in Table 6.5. The value of winding distribution factor K_{wq} for each spatial harmonic in the program *Current1*.mw is calculated using equation (6.11). The corresponding rotor eddy current power loss due to each harmonic is then calculated using the same analytical program *Current1*.mw, with results shown in Table 6.6.

Spatial order q	Temporal order k		
	6	12	18
1	0.0114^{-} 0.0088^{+}	0.0038^{-} 0.0023^{+}	0.00167^{-}
5	0.0031^{-}	0.00045^{-}	
7	0.0018^{-}		
11		0.00227^{-}	
13		0.00133^{-}	

Table 6.5. Amplitudes of armature reaction stator mmf harmonics at f_1 = 3000 Hz for PMSG2 connected to a one rectifier topology and supplying a CC load

Spatial order q	Temporal order k		
	6	12	18
1	110 66	18 7	2
5	8	1	
7	1		
11		2	
13		<0.5	
Total Power loss (Analytical)		≈ 213 W	

Table 6.6. Analytical calculation of rotor eddy current power loss due to armature reaction stator mmf harmonics in PMSG2 connected to one rectifier topology supplying a CC load

Table 6.6 shows that a significant amount of rotor power loss is generated by harmonics of fundamental spatial wavelength shown in Table 6.5. The presence of these harmonics has been discussed in chapter 2.

6.4.3 **Amplitude of Resultant Harmonics and Corresponding Rotor Eddy Current Power Losses (Constant Current DC Link Case)**

The resultant harmonics are calculated from the vector addition of common harmonics

in magnet flux tooth ripple and armature reaction stator mmf. Examining Tables 6.3 and 6.5 indicates that harmonics of temporal order 12 and those of spatial order 11 and 13 are common between both mmfs.

These common harmonics are vectorially added using equation (6.19), which is implemented in the analytical program *Vadd2*.mw in Appendix 1. The load angle ψ between back emf E and current I calculated in Tables 6.1 and 6.2 is used to calculate α_{qk} in equation (6.19). The amplitudes of common resultant harmonics along with other harmonics are presented in Table 6.7. The rotor eddy current power loss due to each harmonic taking into account reaction of eddy current field is calculated using current sheet rotor loss calculation method; the results are presented in Table 6.8.

Spatial order q	Temporal order k		
	6	12	18
1	0.0114^{-} 0.0088^{+}	0.0038^{-} 0.0023^{+}	0.00167^{-}
5	0.0031^{-}	0.00045^{-}	
7	0.0018^{-}		
11		0.004^{-}	
13		0.011^{-}	

Table 6.7. Resultant **h**armonic amplitudes for PMSG2, when connected to a one rectifier topology supplying a CC load at f_1 = 3000 Hz. Negative and positive indices show harmonics rotating CW and CCW, respectively

Spatial order q	Temporal order k		
	6	12	18
1	110 66	18 7	2
5	8	1	
7	1		
11		6	
13		27	
Total Power loss (Analytical)			≈ 246 W
Power loss (FEA Transient Linear Solution)			≈ 240 W

Table 6.8. Rotor power loss due to each resultant harmonic in PMSG2 when connected to a one rectifier topology supplying a CC load

The accuracy of analytical method for the calculation of rotor eddy current power loss in Table 6.8 is compared with transient FEA solution (shown in Figure 6.10). Good

agreement is observed for the rotor power loss calculation between both methods.

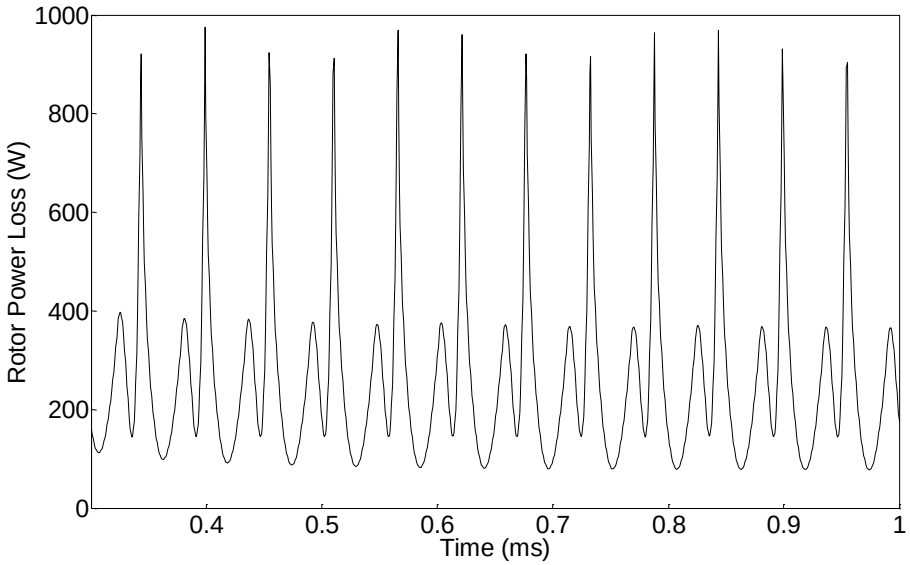

Figure 6.10. Transient FEA rotor eddy current power loss for PMSG2, when connected to a one rectifier topology supplying a constant current DC link

Tables 6.7 and 6.8 also highlight the importance of magnet flux tooth ripple harmonics, which are generally ignored in the rotor loss calculation. Had these harmonics been ignored a discrepancy of 33W between analytical and transient FEA would have resulted. Similarly, had superposition been applied for the calculation of rotor eddy current power loss, a discrepancy of 31W between analytical and transient FEA would have resulted.

For PMSG2, connected to a two rectifier topology and feeding a constant load current of 128A, the amplitude of harmonics due to armature reaction stator mmf only is calculated using the methodology discussed in section 6.3.4. This is implemented by performing Fourier transform on Figure 6.3, using *FFT12*.m in Appendix 2 to calculate the value of stator winding current at various time order. This current value is then used in program *Rec2*.mw to calculate the amplitude of armature reaction stator mmf harmonics travelling in time and space, in the rotor reference frame. Program *Current2*.mw in Appendix 1 is used to calculate the amount / value for the current sheet, which is then used to calculate the radial and tangential airgap flux density harmonic using equations (6.2) and (6.3), respectively.

The resultant harmonics between magnet flux tooth ripple in Table 6.4 and armature reaction stator mmf harmonics are calculated using program *Vadd2*.mw in Appendix 1, and are presented in Table 6.9.

Spatial order q	Temporal order k	
	12	24
1	0.004^{-} 0.003^{+}	
5	0.002^{-}	
7	0.0013^{-}	
11	0.0038^{-}	0.00007^{-}
13	0.011	0.00005^{-}

Table 6.9. Resultant harmonic amplitudes for PMSG2 connected to a two rectifier topology and supplying a CC load at f_1 = 3000 Hz. Negative or positive indices denote harmonics that are CW or CCW rotating, respectively

In Table 6.9, it is interesting to see that in case of a generator connected to a two rectifier topology with 2 slot / pole, some harmonics due to armature reaction stator mmf cancels out including harmonics of temporal order 6 and spatial order 1, 5 and 7.

The respective rotor eddy current power loss for each resultant harmonic is calculated using current sheet rotor loss calculation method and the results are presented in Table 6.10. The accuracy of the analytical method for the calculation of rotor eddy current power loss is also compared with a transient FEA solution (shown in Figure 6.11).

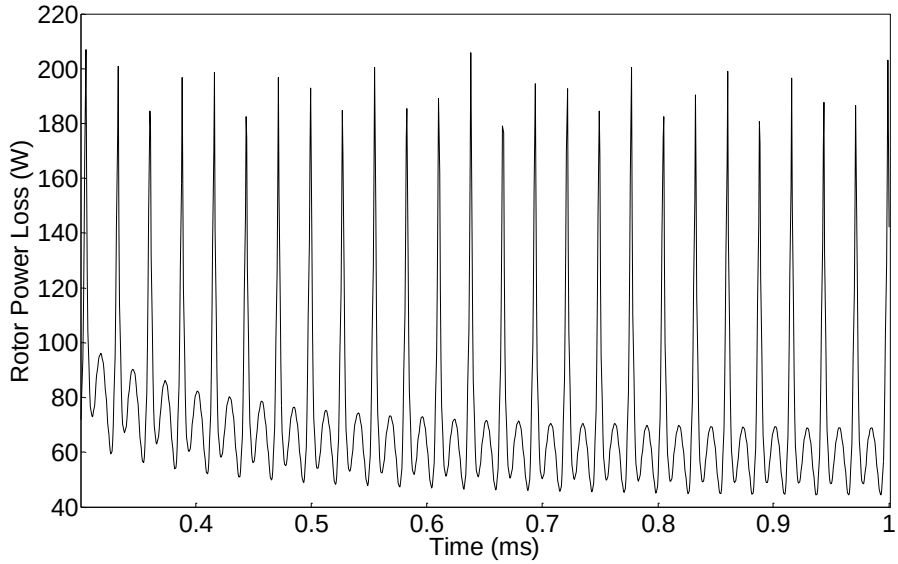

Figure 6.11. Transient FEA rotor eddy current power loss for PMSG2 connected to a two rectifier topology and supplying a constant current DC link

Spatial order q	Temporal order k	
	12	24
1	20	
	11	
5	10	
7	2	
11	5	<0.5
13	27	<0.5
Total Power loss (Analytical)	≈ 75 W	
Power loss (FEA Transient)	≈ 70 W	

Table 6.10. Rotor eddy current power loss in PMSG2 due to resultant harmonics, when connected to a two rectifier topology and supplying a CC load

Further analytical and transient FEA studies are performed to calculate rotor eddy current power loss in PMSG2, when connected to both rectifier topologies, running at a constant speed of 90,000 rpm and connected to various constant current loads; the results are shown in Figure 6.12.

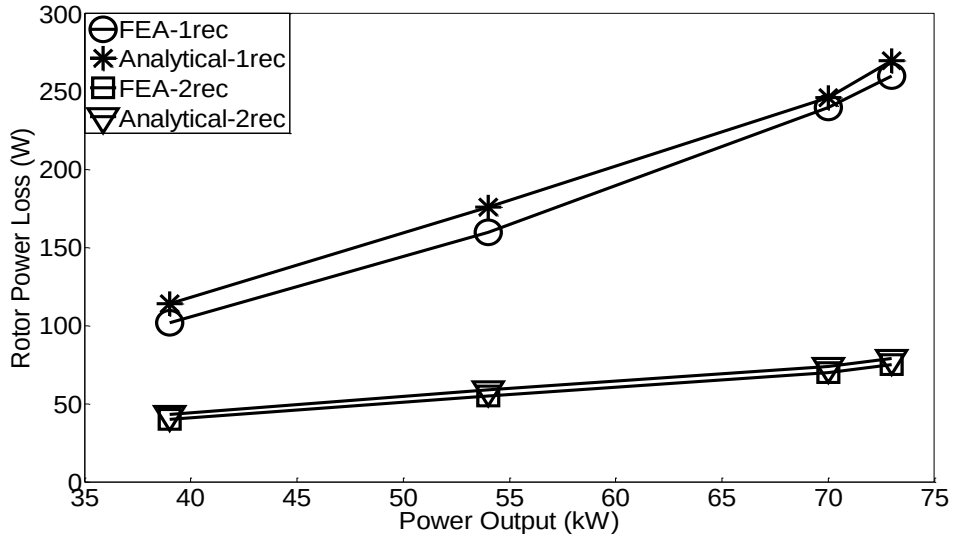

Figure 6.12. Eddy current power loss vs. power at 90,000 rpm for a constant current DC link

In addition, Figure 6.13 presents a comparison between analytical and FEA methods for the calculation of eddy current power loss when connected to a constant current load of 128A, for a range of different speeds. Good agreement is observed between the analytical and FEA results for both studies.

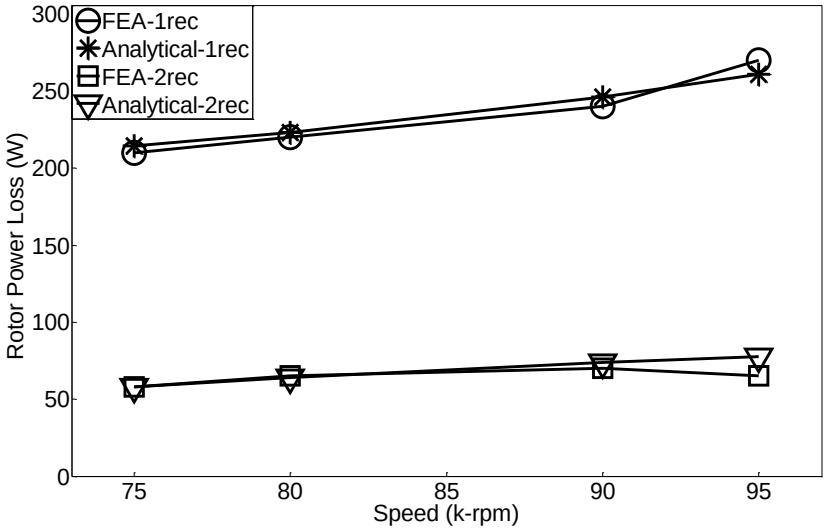

Figure 6.13. Eddy current power loss vs. speed when supplying a constant current DC link

6.4.4 **Amplitude of Resultant Harmonics and corresponding Rotor Eddy Current Power Loss (Constant Voltage dc link)**

In this section we first consider the case of PMSG2 connected to a one rectifier topology, running at 90,000rpm and supplying a constant DC link voltage of 543V. The value of peak current flowing at this voltage is equal to 121A. Using analytical method the amplitude of resultant harmonics and their corresponding rotor eddy current power losses are calculated. The accuracy of analytical results for rotor eddy current power loss is compared with transient FEA solution (shown in Figure 6.14).

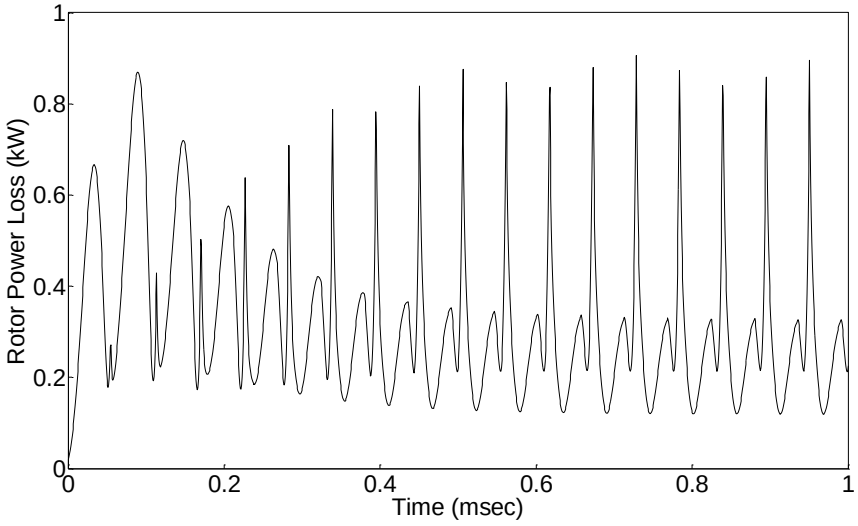

Figure 6.14. Transient FEA rotor eddy current power loss for PMSG2, when connected to a one rectifier topology and supplying a constant voltage DC link

Same procedure as discussed for the constant current dc link has been used for the calculation of resultant harmonics in case of constant voltage dc link. The magnet flux tooth ripple harmonics are obtained from Table 6.4. The Fourier transform is performed on Figures 6.4 using *FFT12*.mw program in Appendix 1, to calculate the value of stator winding current at various time order. These current values are then used in program *Current1*.mw along with K_{wq} to calculate the amplitudes of armature reaction stator mmf harmonics travelling in time and space. *Vadd2*.mw in Appendix 1 is used for vector addition of common harmonics due to magnet flux tooth ripple and armature reaction stator mmf, the results are shown in Table 6.11.

Spatial order q	Temporal order k		
	6	12	18
1	0.0145^{-} 0.006^{+}	0.0034^{-} 0.0025^{+}	0.0018^{-} 0.00145^{+}
5	0.0029^{-}	0.000602	
7	0.0016^{-}	0.0008	
11		0.004^{-}	
13		0.011^{-}	

Table 6.11. Resultant harmonic amplitudes for PMSG2 when connected to a one rectifier topology and supplying CV load at f_1 = 3000 Hz. Negative and positive indices denote harmonics rotating CW or CCW, respectively

The rotor eddy current power loss due to each harmonic in Table 6.11 is calculated using current sheet rotor loss calculation method, the results are presented in Table 6.12.

Spatial order q	Temporal order k		
	6	12	18
1	178 30	14.5 7.5	1.5 1
5	7	0.8	
7	1	0.7	
11		6	
13		27	
Total Power loss (Analytical)		≈ 275 W	
Power loss (FEA Transient)		≈ 282W	

Table 6.12. Rotor power loss due to resultant harmonics in PMSG2 connected to one rectifier topology supplying CV load

Table 6.12 indicates that, similar to the case of a constant current source, harmonics of a fundamental spatial order have the most significant amplitudes and result in the highest rotor eddy current power losses.

We next consider the case of PMSG2 connected to two rectifiers, again with a constant DC link voltage of 543V and peak current of 121A. As discussed earlier the amplitude of resultant harmonics are calculated using programs *FFT12*.m, *Rec2*.mw, *Current2*.mw and *Vadd2*.mw. The amplitudes of these harmonics are presented in Table 6.13. The accuracy of analytical method in terms of rotor eddy current power loss is compared with transient FEA solution.

Spatial order q	Temporal order k	
	12	24
1	0.004^{-} 0.003^{+}	
5	0.0016^{-}	
7	0.0014^{-}	
11	0.0038^{-}	0.00007^{-}
13	0.0112^{-}	0.00005^{-}

Table 6.13. Harmonic amplitudes for PMSG2 when connected to a two rectifier topology, supplying a CV load at f_1 = 3000 Hz. Negative and positive indices denote harmonics that are CW and CCW rotating, respectively

Finally, rotor eddy current power loss due to each resultant harmonic is calculated using current sheet rotor loss calculation method, the results are shown in Table 6.14. The Table also presents comparison between analytical and transient FEA (shown in Figure 6.15) results for the calculation of rotor eddy current power loss.

Spatial order q	Temporal order k	
	12	24
1	20 12	
5	6	
7	2	
11	5	<0.5
13	28	<0.5
Total Power loss (Analytical)	≈ 72 W	
Power loss (FEA Transient)	≈ 78 W	

Table 6.14. Rotor eddy current power loss due to each harmonic, for PMSG2 connected to a two rectifier topology and supplying a CV load

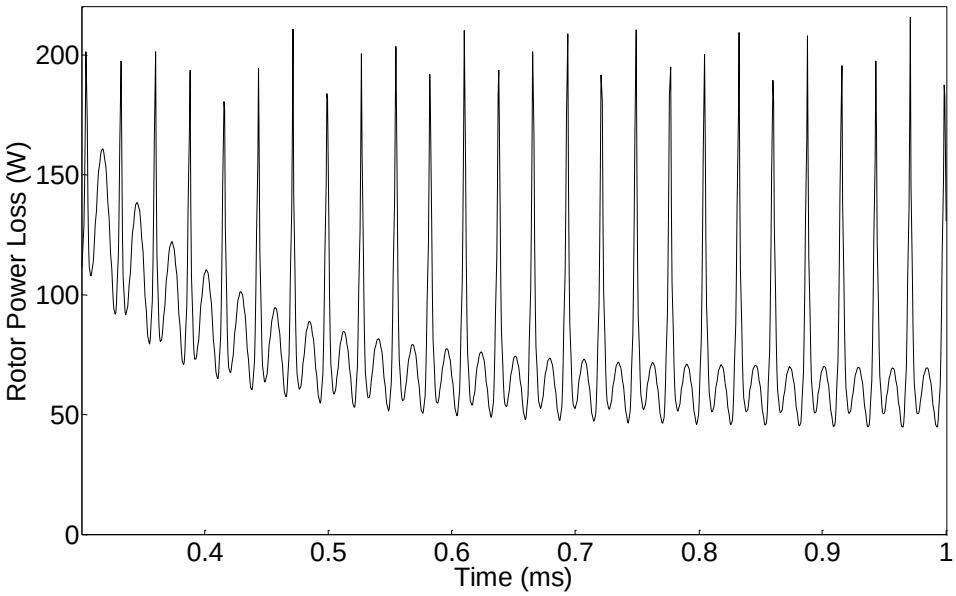

Figure 6.15. Transient FEA eddy current power loss for PMSG2, when connected to a two rectifier topology and supplying a constant voltage DC link

Following, Figures 6.16 and 6.17 illustrate calculations of rotor eddy current power loss in PMSG2, when connected to a two rectifier topology, for different voltages and speeds, using both analytical and FEA methods. Good agreement is observed between the analytical and FEA results. Again the two rectifier machine has significantly lower eddy current losses due to the cancellation of some harmonics.

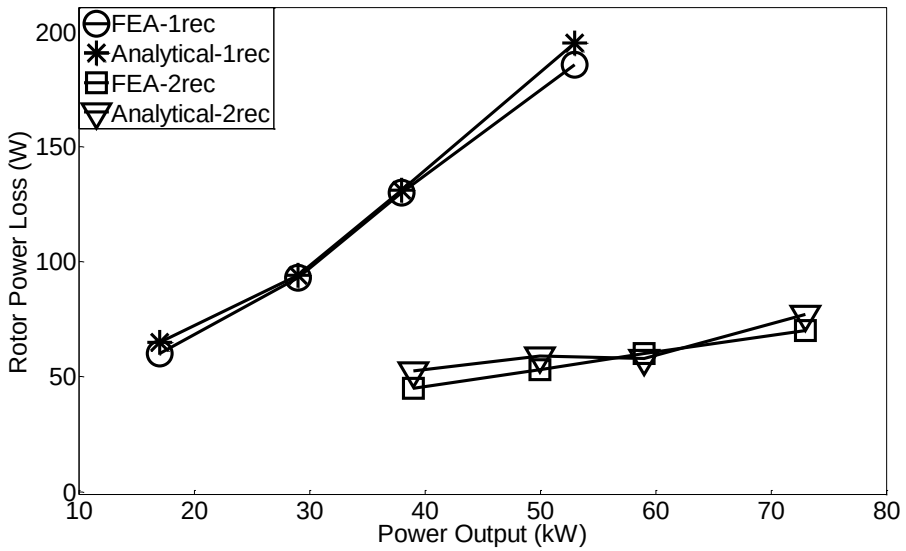

Figure 6.16. Rotor eddy current power loss vs. power output at 90,000 rpm, for a constant voltage DC link

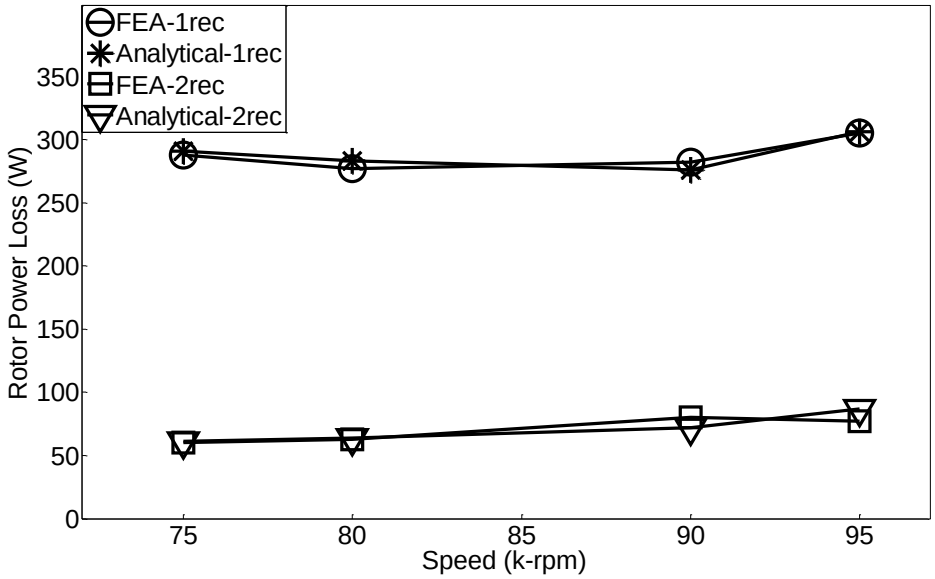

Figure 6.17. Rotor eddy current power loss vs. speed when supplying a constant voltage DC link

It is worth noting that the machine under study has negligible saturation. If, however, the tooth tip thickness is halved to 0.5 mm, which increases the level of saturation significantly, then the rotor losses in the constant current, one rectifier case, for example, will increase from 240W to 286W, as saturation of the tooth tips virtually increases the slot opening and therefore the amplitudes of asynchronous harmonics increases.

6.5 Conclusions

This chapter presented the effect of two winding and rectifier topologies on rotor eddy current power loss in PM synchronous generators connected to rectifier loads. It is shown that rotor eddy current losses in a PM synchronous generator feeding into an un-controlled rectifier can be reduced significantly by splitting the three-phase winding into two sections, with a 30 degree phase shift between their emfs, and with each winding connected to its own rectifier. The rectifiers may be connected in series or in parallel. Due to the 30 degree phase shift between the two sets of windings, some of the stator mmf harmonics and their corresponding rotor losses will be eliminated. This double winding, 12 pulse configuration has the additional benefit of reducing the DC link voltage ripple.

Good agreement has been observed between the rotor losses found from analytical calculations and 2D FEA. But it is essential that the armature and magnet flux harmonics are added vectorially to calculate the resultant travelling flux harmonics and their corresponding losses. The losses due to armature and magnet flux harmonics should not be calculated independently and then added together.

Chapter 7

Parametric Study

7.1 Introduction

In this chapter, computational and analytical parametric study is performed to investigate the effect of different number of slots, slot-opening, winding configuration, magnet and airgap thicknesses and magnet segmentation on rotor electromagnetic losses in a number of permanent magnet synchronous generators (PMSGs). This chapter is divided into two parts.

The first part of the chapter develops a normalisation technique to highlight the effect of variation in machine parameters on rotor eddy current power loss and also enables quick calculations of these losses in similar PM machines. In the development of this technique, all machines studied have the same overall diameter; stator bore diameter and active length. They were all designed to have approximately the same open circuit emf; the magnet thickness was adjusted in proportion to the gap to achieve this. All machines were assumed to output the same sinusoidal current, at the same load angle of the load.

The second part of the chapter presents a limited transient FEA study for the calculation of rotor losses in three PMSGs connected to a rectifier load. The effect of

different winding configuration, slot-pole combination, rectifier topologies and magnet segmentation on rotor eddy current power loss has been investigated in these PMSGs.

7.2 Methodology

In this section, the methodology for transient FEA, static FEA and analytical methods is briefly described for the calculation of rotor eddy current power loss in PMSGs.

7.2.1 **Transient FEA**

In transient FEA solution, machine is modelled and boundary conditions are applied. Time step of 6.84×10^{-7} s and a total number of elements of about 60000 is used for analysis.

7.2.2 **Static FEA**

A number of 2D magneto-static models of the machine, for different rotor positions, corresponding to different time steps, are analysed. Data of the normal flux density on the surface of the rotor are extracted from the models and assembled in a matrix. Each row in the matrix represents the flux density on the surface of the rotor at a different time step and rotor position. Double Fourier transform is used to obtain the time and space orders of the normal flux density travelling waves on the surface of the rotor. Rotor eddy current loss caused by each harmonic is then calculated by solving the diffusion equation in a 2D multilayer slotless model of the machine as illustrated in Figure 3.14. The amplitude, frequency and wavelength of the current sheet are adjusted to produce the corresponding normal flux density travelling wave on the surface of the rotor.

7.2.3 **Analytical Method**

The analytical rotor eddy current power loss due to magnet flux tooth ripple harmonics and armature reaction stator mmf harmonics are calculated using the current sheet rotor loss calculation method. The amplitude of these harmonics are calculated using

the analytical method derived by Ẑarko et al (2006) and winding factor equation (3.6), respectively.

7.3 Effect of Machine Parameters on Rotor Eddy Current Power Loss

In this section transient FEA is used to investigate the effect of different slot openings, magnet thickness and airgap length on the rotor eddy current power loss in PMSG1. The results are compared with those using static FEA and analytical methods. Then normalization technique is developed for quick estimate of rotor losses in different variants of PMSG1.

Figure 7.1 shows a typical transient FEA curves of on-load rotor eddy current power loss for PMSG1 having different slot-openings. An initial transient is observed, followed by a slowly varying curve. The average of the last 50 microseconds was used as an estimate of the average power loss. The rotor loss in PMSG1 with 4mm slot opening shows the highest amount.

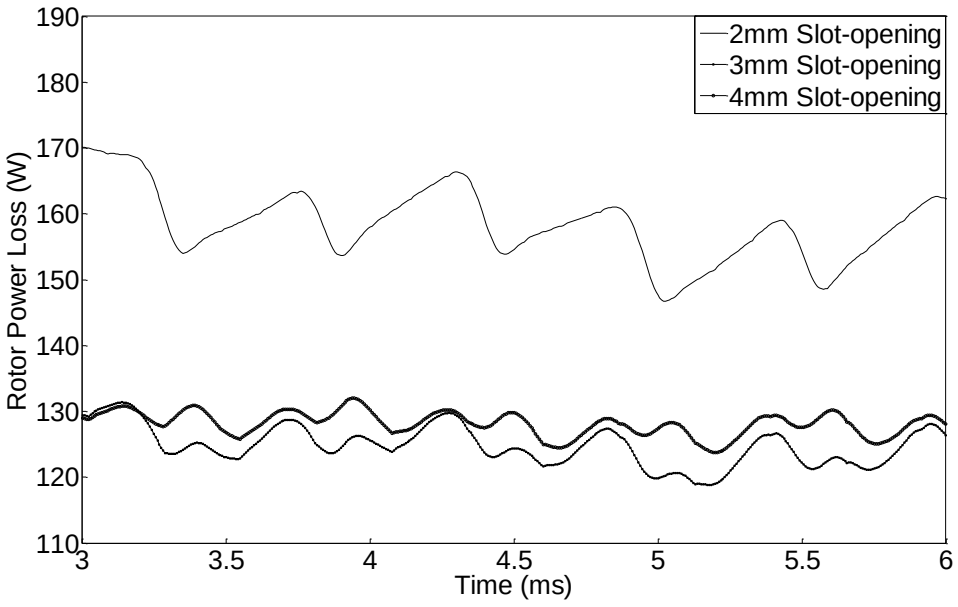

Figure 7.1. On load rotor power loss vs. time in PMSG1

A comparison between transient FEA, static FEA and analytical methods for the no-load and on-load rotor eddy current power loss in variants of PMSG1 designs is

presented in following Table 7.1 and 7.2. A reasonably good agreement is observed between the methods for rotor eddy current power loss.

	Slot opening (mm)	Magnet thickness (mm)	Airgap (mm)	Analytical result (W)	Static FEA result (W)	Transient FEA result (W)
PMSG1	2	3.5	2.5	40	44	45
	3	4.5	3.2	68	85	89
	4	5.5	3.9	100	112	120

Table 7.1. Comparison for no-load rotor eddy current power loss in PMSG1 using analytical, static FEA and transient FEA methods

	Slot opening (mm)	Magnet thickness (mm)	Airgap (mm)	Analytical result (W)	Static FEA result (W)	Transient FEA result (W)
PMSG1	2	3.5	2.5	125	140	148
	3	4.5	3.2	126	122	127
	4	5.5	3.9	129	131	135

Table 7.2. Comparison for on-load rotor eddy current power loss in PMSG1 using analytical, static FEA and transient FEA methods

The solution time for transient FEA analysis for the three design variants of PMSG1 presented in Tables 7.1 and 7.2 took approximately 5 hours. These losses can be estimated quickly using normalisation technique, discussed in next section.

7.3.1 **Normalization Technique**

In the development of normalisation technique, the radial magnet thickness in PMSG1 was adjusted when the gap is changed such that the fundamental component flux, and hence the emf, remain roughly the same for all machines. This is illustrated in Table 7.3, which shows the fundamental space order harmonic of the no-load normal flux density on the surface of the magnet for a series of PMSG1.

Slot Opening (mm)	Magnet Thickness (mm)							
	1.5	2.5	3.5	4.5	5.5	6.5	7.5	8.5
1	0.7	0.71	0.73	0.74	0.74	0.75	0.75	0.75
2	0.69	0.71	0.72	0.73	0.74	0.75	0.75	0.75
3	0.68	0.70	0.72	0.73	0.74	0.74	0.75	0.75
4	0.66	0.69	0.71	0.72	0.74	0.74	0.74	0.75
5	0.64	0.68	0.70	0.71	0.73	0.74	0.74	0.74
6	0.61	0.66	0.69	0.71	0.72	0.70	0.73	0.74
7	0.59	0.64	0.67	0.70	0.71	0.72	0.73	0.73
8	0.56	0.62	0.66	0.68	0.70	0.71	0.72	0.73

Table 7.3. Amplitude of flux density harmonic with space fundamental order and zero time order of normal flux density over the magnet surface at no-load.

However, for a fairer comparison between the machines, the calculated rotor losses for given winding current need to be adjusted to compensate for this variation. It is useful to normalise the data so that it may be used to estimate rotor losses in similar machines, but with different dimensions and speeds.

In most machines, it was observed that the losses were mainly in the magnets, except when the magnets were thin and the airgap was also small. In the latter cases, there were significant losses in the rotor steel hub. For the cases when the losses are mostly in the magnet, in which the skin depth at the lowest harmonic frequency (18 kHz) is 4 mm, it is reasonable to assume that the losses are resistance limited and that the eddy currents do not vary radially. In this case it can be readily shown from Faraday's law that the loss per unit area for each harmonic with frequency ω_q , wavelength λ_q and peak normal flux density B_q is given by:

$$P = \frac{\sigma \tau \omega_q^2 \lambda_q^2 B_q^2}{8\pi^2} \tag{7.1}$$

In equation (7.1), σ , τ are magnet's conductivity and thickness, respectively. The above equation can be derived using cylindrical coordinates. Assuming, variation in magnetic flux density *B* in time *t* and θ is given by:

$$B(t,\theta) = B_m \cos\left(\omega t - \frac{N_p}{2}\theta\right) \tag{7.2}$$

In equation (7.2), N_p is the number of poles. From Maxwell equations current density *J* is given by:

$$J = \sigma E \tag{7.3}$$

In equation (7.3), electric field *E* can be calculated as;

$$\nabla \times E = \begin{vmatrix} U_r & U_\theta & U_z \\ \dfrac{\partial}{\partial r} & \dfrac{1}{r}\dfrac{\partial}{\partial \theta} & \dfrac{\partial}{\partial z} \\ 0 & 0 & E_z \end{vmatrix} \tag{7.4}$$

Substituting value of E in equation (7.3), the following can be written:

$$J = \sigma E = \sigma r \omega B_m \frac{2}{N_p} \cos\left(\omega t - \frac{N_p}{2}\theta\right) \tag{7.5}$$

The eddy current power loss in the magnet region can be calculated by integrating the volume v of the permanent magnet as:

$$P_{eddy} = \int_v \sigma E_{rms}^2 \mathrm{d}v \tag{7.6}$$

Using equation (7.6), and after some algebraic manipulation equation (7.1) can be determined. Equation (7.1) suggests a possible method of normalising the rotor loss data so that it may be used to calculate the losses in similar machines, with similar harmonic content. The amplitude, frequency and asynchronous flux harmonics in a machine, for given fundamental magnet airgap flux and armature mmf, is determined largely by the total gap g between the stator bore and rotor hub OD (Outer Diameter), number of slots and slot opening s. Machines with similar s/λ and g/λ have similar flux harmonic content, for given average gap flux density (Freeman, 1962). The results in (Freeman, 1962) apply strictly to machines with large number of teeth per pole e.g., 30 or more, but it could be a reasonable first assumption that may be used as a basis for establishing a similarity between two machines from the point of view or rotor loss per unit area of its surface. Such machines will have flux density harmonics with similar amplitudes relative to the fundamental value provided that the ratios of their wavelength to slot pitch are the same. Their frequency will depend on the speed of the machine, number of poles and number of slots. Based, on equation (7.1), rotor losses in one machine could be estimated from those calculated in a similar machine with same s/λ and g/λ in proportion to the square of the frequency of the fundamental tooth ripple harmonic (calculated by multiplying the number of teeth by the rotor speed in revolutions per second), square of the slot pitch λ, square of the fundamental airgap flux density, magnet thickness and magnet conductivity. This suggests normalising rotor power loss by dividing the loss per unit area of rotor surface by the square of the slot pitch, square of the fundamental slot pitch, and square of the fundamental airgap flux density.

Contour plots of the normalised no-load and on-load rotor power loss per unit area of rotor surface for all variants design of PMSG1 are shown in Figure 7.3 and Figure 7.4, respectively. As expected, with increase in slot-opening and reduction in airgap length causes increased rotor eddy current loss.

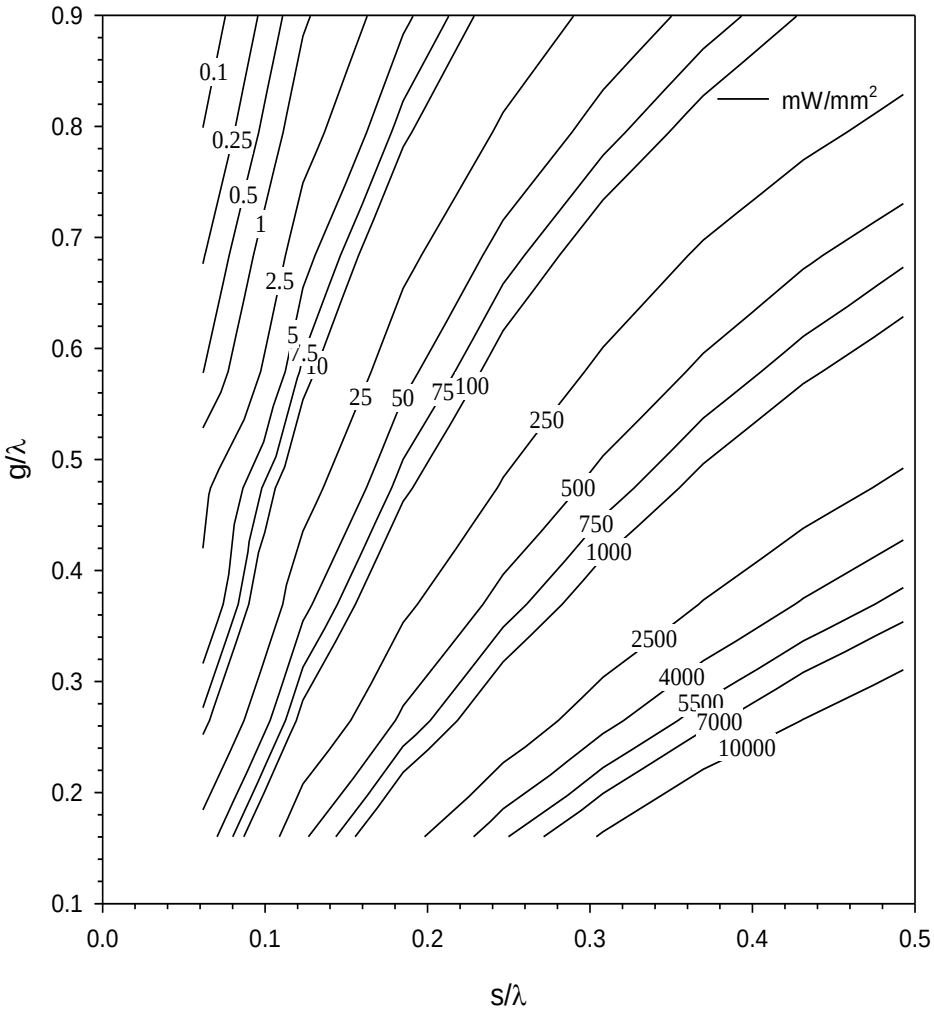

Figure 7.2. Normalised no-load power loss density

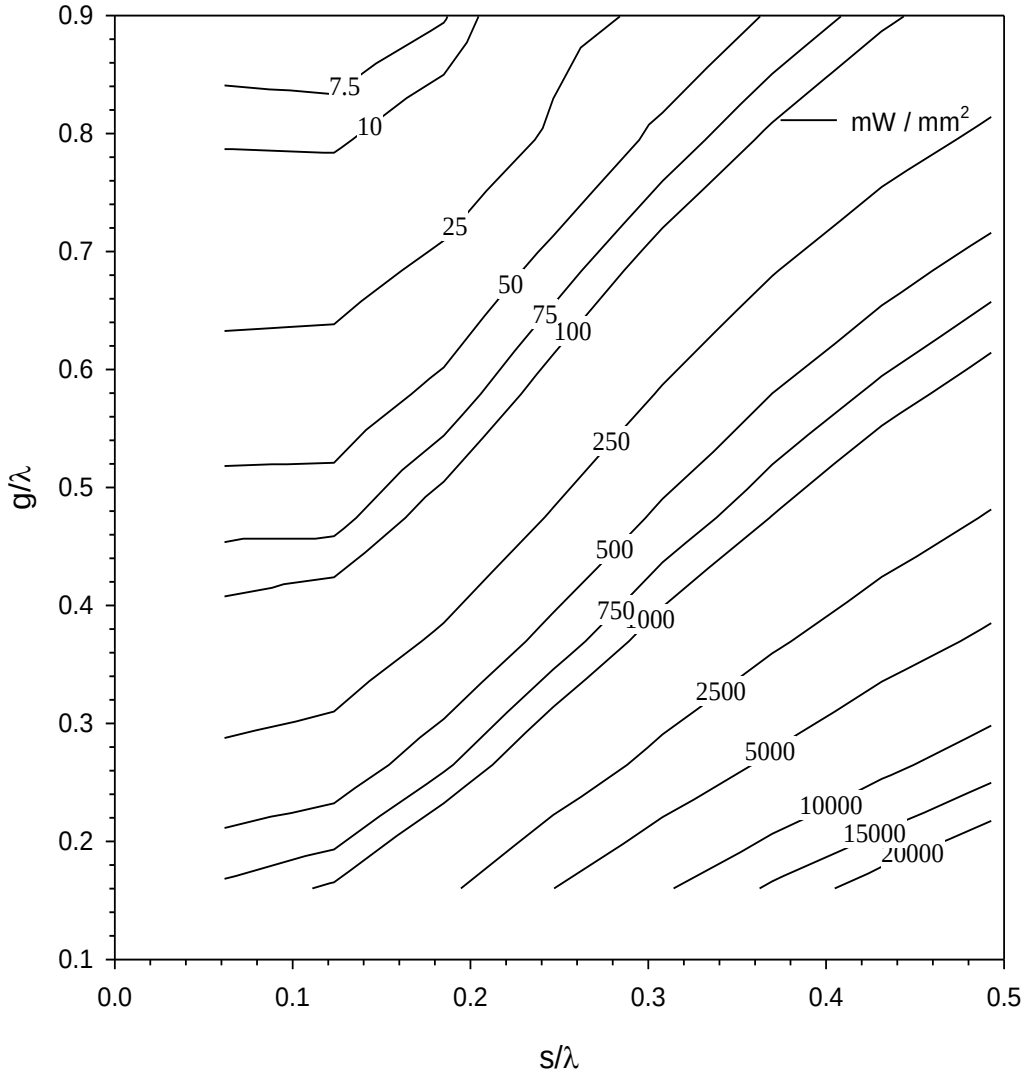

Figure 7.3. Normalised on-load power loss density

The data in Figure 7.2 and 7.3 were used to estimate the no-load and on-load power loss in similar machines with 3 and 6 slots per pole. The results are shown Table 7.4 and 7.5, which also compares the estimated rotor losses with those calculated using transient FEA. A reasonable agreement is observed between the full load losses estimated using the normalised data and those estimated from FEA, especially at high values of g / λ, when the losses are mainly in the magnets. However, the agreement in the no-load case for some machines is not as good. However, the trend of the data is similar in both cases.

Slot-opening s (mm)	Airgap + Magnet thickness g (mm)	Slot-pitch λ (mm)	s/λ	g/λ	Power Loss (W)	
					Normalised data	Transient FEA
2	6	16.23	0.123	0.369	38	40
3	7.7	16.23	0.184	0.474	75	89
4	9.4	16.23	0.246	0.579	100	120
2	6	8.115	0.246	0.739	36	26
3	6	8.115	0.369	0.739	170	110
4	6	8.115	0.492	0.739	438	264

Table 7.4. Comparison for no-load power loss estimated from normalised loss graphs and transient FEA

Slot-opening s (mm)	Airgap + Magnet thickness g (mm)	Slot-pitch λ (mm)	s/λ	g/λ	Power Loss (W)	
					Normalised data	Transient FEA
2	6	16.23	0.123	0.369	120	148
3	7.7	16.23	0.184	0.474	95	127
4	9.4	16.23	0.246	0.579	130	135
2	6	8.115	0.246	0.739	50	60
3	6	8.115	0.369	0.739	180	115
4	6	8.115	0.492	0.739	490	455

Table 7.5. Comparison for on-load power loss estimated from normalised loss graphs and transient FEA

7.4 Rotor Eddy Current Power Loss in PMSGs Connected to Rectifier DC-Link Loads

In this second part of the chapter, transient FEA is used for the mesh and time step dependence studies on rotor eddy current power loss in three PMSGs. Then rotor eddy current power losses in these generators are calculated at no-load and on-load conditions. Finally, limited study is performed to investigate the effect of magnet segmentation on rotor eddy current power loss at no-load and on-load conditions in these generators.

For the calculation of on-load rotor eddy current power loss case, one of the three phase generator, PMSG1, shown in Figure 3.2, is connected to 6 pulse bridge rectifier (shown in Figure 6.1). The second generator, PMSG2, shown in Figure 3.3, with two separate sets of 3 phase windings having a phase difference of 30 degrees is connected to a 12 pulse bridge rectifier as shown in Figures 6.1 and 6.2. The third generator,

PMSG3, has 0.5 slots per pole per phase shown in Figure 3.4 and its concentrated three phase windings are connected to a 6 pulse full bridge rectifier.

The three generators have slot-openings of 4mm, 2 pairs of poles, and are running at 90,000 rpm. They have ring shaped parallel magnetized permanent magnets. Other dimensions of generators and properties of materials are showed in Table 3.1.

7.4.1 **Mesh Analysis**

Table 7.6 presents the variation in rotor eddy current power loss in PMSGs due to the number of mesh elements. It is illustrated that with increase in number of mesh elements rotor eddy current power loss decreases in PMSGs for which reason is explained in section (3.2.3). The time for calculating eddy current power loss in each model was dependent on number of elements and computer configuration. With computer configuration of Intel(R) Core™2 Duo @ 3.33GHz; highest number of mesh elements i.e., 70000 in machine model approximately took 4 hours to calculate rotor eddy current power loss, while rotor eddy current power loss were calculated in 2 hours in model with 10000 elements.

PMSGs	Rotor Eddy Current Power Loss (W)				
	Number of Elements				
	10000	30000	50000	60000	70000
PMSG1	378	369	368	368	367
PMSG2	249	248	248	248	248
PMSG3	1615	1610	1599	1588	1570

Table 7.6. No-load rotor eddy current power loss in PMSGs with various numbers of mesh elements

7.4.2 **Time Step Analysis**

Table 7.7 illustrates the variation in rotor eddy current power loss in PMSGs at various time steps. The number of elements for each case were 60000. The losses increase at smaller time step for all cases; this is due to the fact that more harmonics are captured at smaller step and hence higher losses. In terms of eddy current power loss calculation, models using smallest time step i.e., 1e-7 took approximately 4-5 hours, while it took 2 hours to calculate rotor eddy current power loss in models using time

step of 1.5 e-6. But accuracy has been compromised for the solution as shown in Table 7.7.

PMSGs	Rotor Eddy Current Power Loss (W)			
	Time Steps			
	1.5e-6	1e-6	1.5e-7	1e-7
PMSG1	374	405	413	427
PMSG2	249	266	278	279
PMSG3	1510	1518	1527	1560

Table 7.7. No-Load rotor eddy current power loss in PMSGs at various time steps

7.4.3 **No-Load (Open Circuit) Rotor Eddy Current Power Loss**

Using transient FEA method, the no-load rotor eddy current power loss is calculated in three PMSGs using time step of 6.84×10^{-7} s and a total number of elements of about 60000. The tooth tip thickness is 1mm for all the three generators. A comparison for no-load rotor eddy current power loss is presented in Table 7.8 for these PMSGs.

PMSGs	Magnet Flux Tooth Ripple Loss (W)
	Stator Tooth Tip 1mm
PMSG1	127
PMSG2	24
PMSG3	90

Table 7.8. No-load rotor eddy current power loss in PMSGs

The no-load power loss results illustrated in Table 7.8 shows highest rotor loss in PMSG1. This is due to the fact that this generator has 3 slots per pole and therefore the amplitude of temporal order 6 and spatial orders 5 and 7 in rotor reference frame are highest (shown in chapter 4), which results in higher rotor loss. On the other hand these temporal and spatial order harmonics are absent in PMSG2 with 6 slots per pole (shown in chapter 6), hence the power loss is the lowest. PMSG3 has even symmetry, therefore in addition to temporal order of 6 and spatial orders of 5, 7, there are additional temporal harmonic of order 3 with even spatial orders of 2, 4. In this generator the contribution towards the rotor loss from temporal order 6 and spatial orders 5 and 7, compared to those in PMSG1 is much lower.

7.4.4 **Effect of Stator Tooth Tip Saturation**

The effect of stator tooth tip saturation on rotor eddy current power loss in three PMSGs is illustrated in Table 7.9 and 7.10. This is achieved by calculating linear (permeability of stator assumed 5000) and non-linear (BH curve assigned to stator material) solutions. Except PMSG2 in which stator tooth tip saturation is negligible, the results for other two generators show increased rotor eddy current power loss for the saturated stator tooth tip compared to un-saturated one, this being due to smaller magnetic circuit. The increase in magnetic circuit can be achieved by increasing stator tooth tip thickness which reduces saturation, resulting in reduced rotor eddy current power loss (illustrated in Table 7.10).

PMSGs	Magnet Flux Tooth Ripple Loss (W) Un-Saturated stator tooth tip (linear solution)
	Stator Tooth Tip 1.5mm
PMSG1	107
PMSG2	23
PMSG3	84

Table 7.9. No-load rotor eddy current power loss in PMSGs with un-saturated stator tooth tip

In comparison to Table 7.8, the no-load rotor eddy current power loss in PMSGs with increased stator tooth tip thickness show decreased rotor losses.

PMSGs	Magnet Flux Tooth Ripple Loss (W) Saturated stator tooth tip (non-linear solution)	
	Stator Tooth Tip1mm	Stator Tooth Tip 1.5mm
PMSG1	160	109
PMSG2	23	23
PMSG3	2181	866

Table 7.10. No-load rotor eddy current power loss in PMSGs with saturated stator tooth tip

Table 7.10 illustrates rotor eddy current power loss in PMSGs assigned with non-linear BH curve. In this case the rotor losses also decrease with increase in stator tooth tip thickness, but in comparison to Tables 7.8 and 7.9 where permeability of the stator material was high, these losses are higher in PMSG1 and PMSG3.

7.4.5 **On-Load Rotor Eddy Current Power Loss**

In order to calculate the on-load rotor eddy current power loss in the PMSGs under study, the terminals of these generators are connected to an uncontrolled rectifier feeding a constant current highly inductive load and constant voltage highly capacitive loads. For the case of constant current dc link the values are assumed to be 100A and 128A. The corresponding terminal voltages or induced emf for the PMSG1 and PMSG2 are 550V, while for PMSG3 is 500V. In case of constant current dc link voltage, the values are assumed to be 543V and 550V. The corresponding values for the current in PMSG1 and PMSG2 are 128 A and 100 A, while for PMSG3 the values are 120 A and 90 A, respectively.

The fact that splitting the winding by 30 degrees in PMSG2 significantly reduces rotor losses in the generator has been re-established for constant current dc link and constant voltage dc link. The rotor eddy current power loss calculations are presented in Tables 7.11 and 7.12, respectively.

PMSGs	Rotor Eddy Current Power Loss (W)	
	Constant Current dc link (Amps)	
	100A	128A
PMSG1(connected to one rectifier topology)	265W	367W
PMSG2(connected to one rectifier topology)	181W	240W
PMSG3(connected to one rectifier topology)	1039W	1556W
PMSG2 (connected to two rectifier topology)	57W	70W

Table 7.11. Rotor eddy current power loss in PMSGs connected to constant current dc link load of 100A and 128A. PMSGs are running at a speed of 90,000 rpm

PMSGs	Rotor Eddy Current Power Loss (W)	
	Constant Voltage dc link (V)	
	543V	550V
PMSG1(connected to one rectifier topology)	364W	292W
PMSG2(connected to one rectifier topology)	282W	212W
PMSG3(connected to one rectifier topology)	1132W	1095
PMSG2 (connected to two rectifier topology)	78W	74W

Table 7.12. Rotor eddy current power loss in PMSGs connected to uncontrolled rectifier feeding constant voltage dc link of 543V and 550V. PMSGs are running at a speed of 90,000 rpm

Table 7.12 shows that in comparison to 543 V, the rotor eddy current power loss in PMSGs for the 550 V volts is lower. This is due to the fact that the potential

difference between generator voltage *E* and the dc link load voltage *V* is reduced and therefore low amount of current will flow in the magnets, causing reduced losses.

7.4.6 **Effect of Magnet Segmentation in PMSGs at No-Load**

The eddy currents flow in a rectangular path between pairs of magnet poles, causing magnet power loss. The path of these currents can be restricted by segmenting the permanent magnets. Though segmentation is a laborious process it may reduce rotor eddy current power loss in PM machines provided certain conditions are met (as will be discussed later in this section). A limited study was performed to investigate the effect of circumferential magnet segmentation on rotor eddy current power loss in PMSGs. The permanent magnets are isolated using mica, which has μ_r = 1 and conductivity of 1e-15. Stator tooth tip saturation is included in the study using linear and non-linear models of the generators. In addition to magnet segmentation, increasing the tooth tip thickness may further reduce rotor losses in PMSGs.

PMSGs	Rotor Eddy Current Power Loss (W)					
	Circumferential Magnet Segments					
	0		2		4	
	Stator tooth Tip thickness		Stator tooth Tip thickness		Stator tooth Tip thickness	
	1mm	1mm	1mm	1mm	1mm	1mm
	Un-Saturated	Saturated	Un-Saturated	Saturated	Un-Saturated	Saturated
PMSG1	127	**160**	115	**160**	106	134
PMSG2	24	23	24	26	24	24
PMSG3	90	2181	**91**	**1735**	87	**1778**

Table 7.13. Effect of magnet segmentation on no-load rotor eddy current power loss in PMSGs connected to uncontrolled rectifier. The stator tooth tip thickness is 1mm

PMSGs	Rotor Eddy Current Power Loss (W)					
	Circumferential Magnet Segments					
	0		2		4	
	Stator tooth Tip thickness		Stator tooth Tip thickness		Stator tooth Tip thickness	
	1.5mm	1.5mm	1.5mm	1.5mm	1.5mm	1.5mm
	Un-Saturated	Saturated	Un-Saturated	Saturated	Un-Saturated	Saturated
PMSG1	**107**	**109**	**113**	**113**	103	103
PMSG2	23	23	24	24	23	23
PMSG3	84	866	82	650	78	619

Table 7.14. Effect of magnet segmentation on no-load rotor eddy current power loss in PMSGs connected to uncontrolled rectifier. The stator tooth tip thickness is 1.5mm

From Table 7.13 and 7.14, it is interesting to see that magnet segmentation not always reduces rotor eddy current power loss. For example, the rotor loss may remain the same in PMSG1 with saturated stator tooth tip thickness having either 0 or 2 magnet segments. Also, the rotor loss may increase rather than decrease due to magnet segmentation. For example, in Table 7.13, the rotor loss increased by 43 W in case of PMSG3 with 4 magnet segments compared to one with 2 magnet segments.

The anomaly in rotor eddy current power loss due to magnet segmentation is due to the fact that; magnet segmentation will only reduce rotor losses if the eddy currents are resistive limited in the magnets, flux density on the magnet surface is homogeneous, and end effects are negligible. For all other cases, magnet segmentation may not result in reduced rotor power loss.

Following models show the eddy current distribution at no-load in the permanent magnet region of three PMSGs. For comparison, the scaling factor for each PMSG with linear (unsaturated stator tooth tip) and non-linear (saturated stator tooth tip) is kept constant.

Stator Tooth Tip Thickness 1mm

Case 1: No-Magnet Segmentation

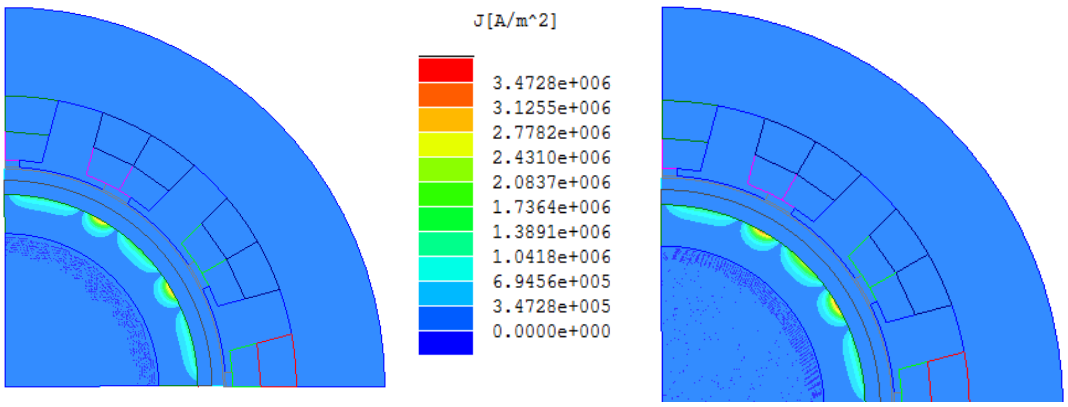

PMSG1 linear model with 1mm tooth tip thickness

PMSG1 non-linear model with 1mm tooth tip thickness

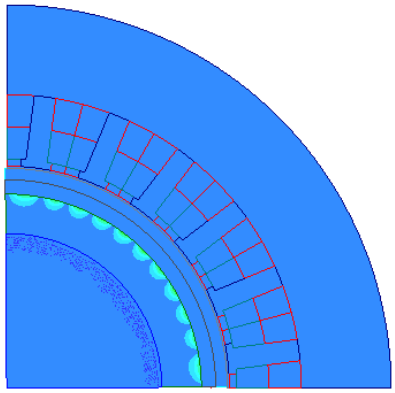

PMSG2 linear model with 1mm tooth tip thickness

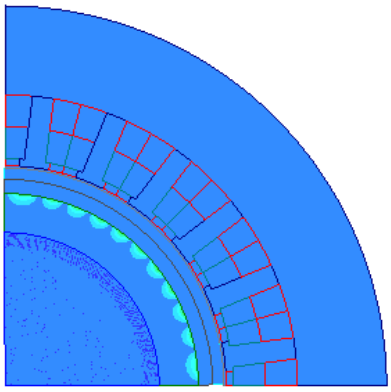

PMSG2 non-linear model with 1mm tooth tip thickness

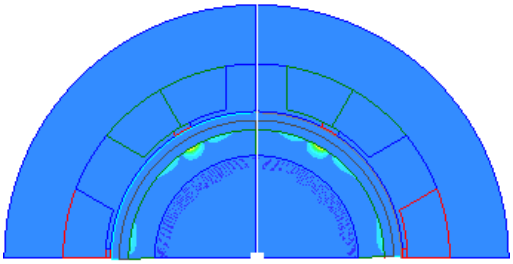

PMSG3 linear model with 1mm tooth tip thickness

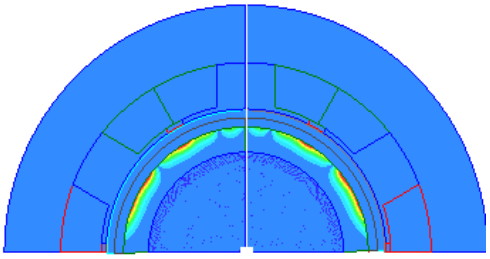

PMSG3 non-linear model with 1mm tooth tip thickness

Figure 7.4. Distribution of eddy currents in the permanent magnet region of PMSGs with 1mm stator tooth tip thickness and 0 magnet segments at no-load (open circuit).

Case 2: Two-Magnet Segments

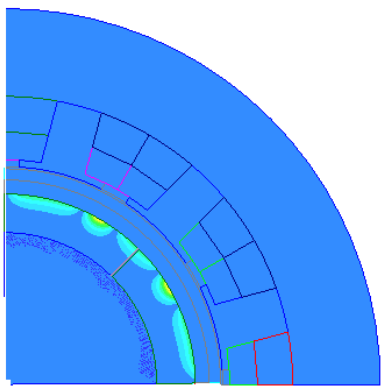

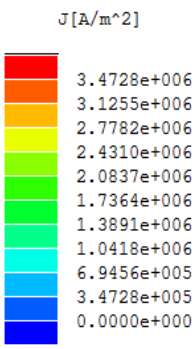

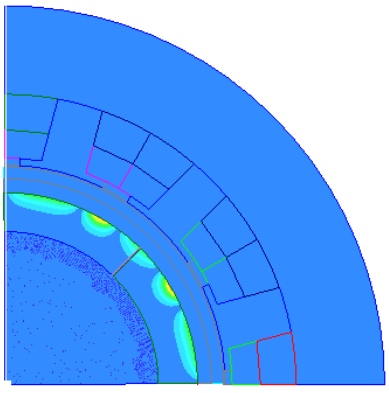

PMSG1 linear model with 1mm tooth tip thickness

PMSG1 non-linear model with 1mm tooth tip thickness

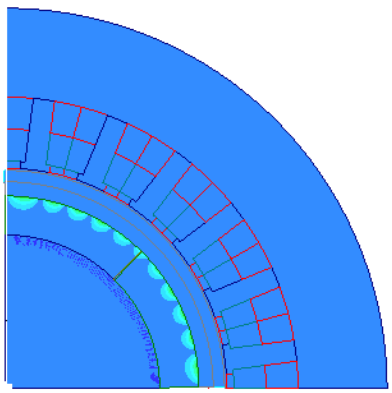

PMSG2 linear model with 1mm tooth tip thickness

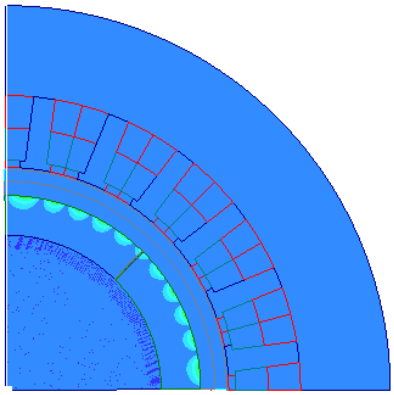

PMSG2 non-linear model with 1mm tooth tip thickness

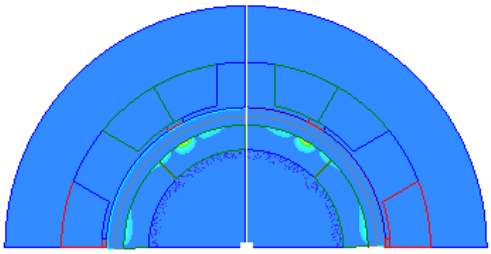

PMSG3 linear model with 1mm tooth tip thickness

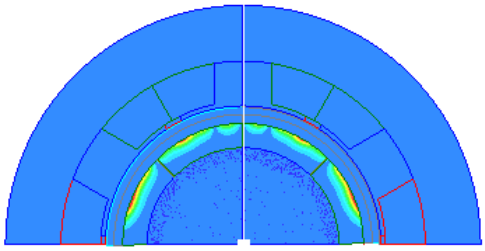

PMSG3 non-linear model with 1mm tooth tip thickness

Figure 7.5. Distribution of eddy currents in the permanent magnet region of PMSGs with 1mm stator tooth tip thickness and 2 magnet segments at no-load (open circuit).

Case 3: Four-Magnet Segments

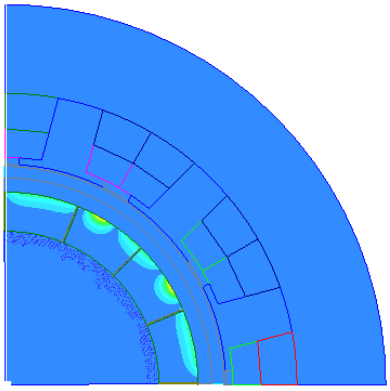

PMSG1 linear model with 1mm tooth tip thickness

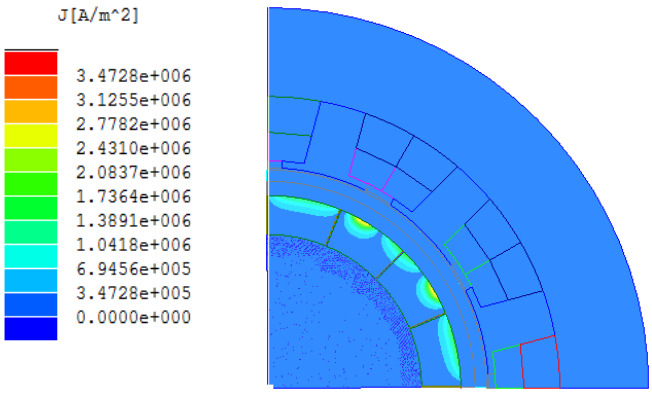

PMSG1 non-linear model with 1mm tooth tip thickness

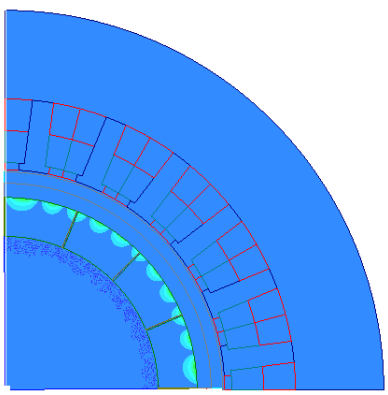

PMSG2 linear model with 1mm tooth tip thickness

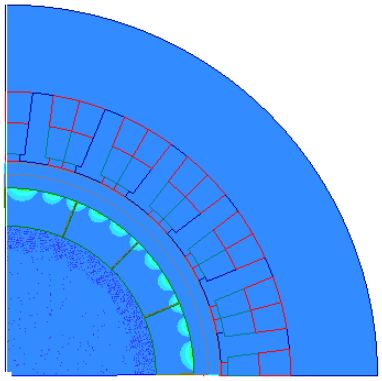

PMSG2 non-linear model with 1mm tooth tip thickness

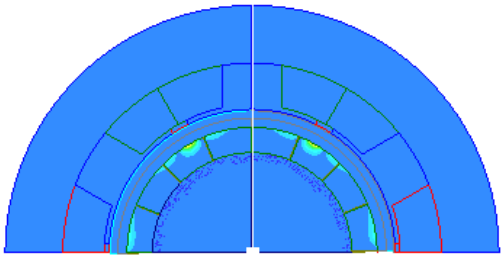

PMSG3 linear model with 1mm tooth tip thickness

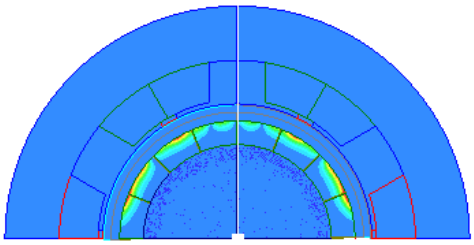

PMSG3 non-linear model with 1mm tooth tip thickness

Figure 7.6. Distribution of eddy currents in the permanent magnet region of PMSGs with 1mm stator tooth tip thickness and 4 magnet segments at no-load (open circuit).

Stator Tooth Tip Thickness 1.5 mm

Case 1: No-Magnet Segmentation

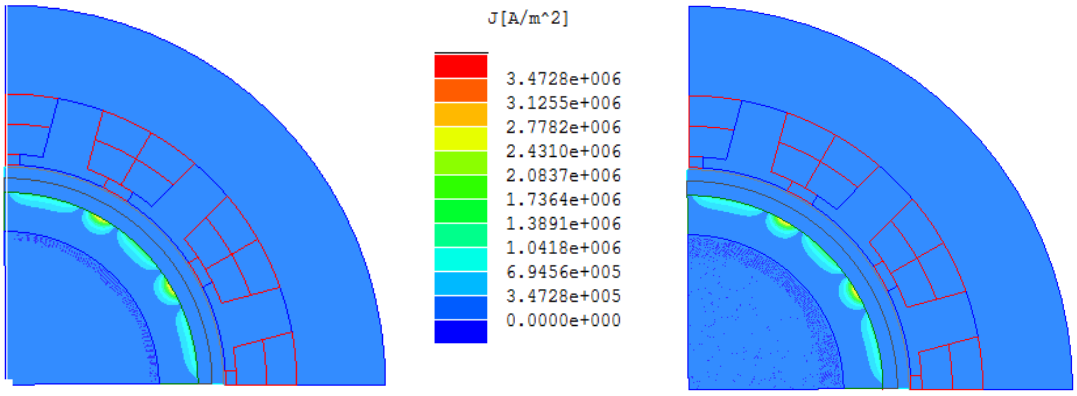

PMSG1 linear model with 1.5mm tooth tip thickness

PMSG1 non-linear model with 1.5mm tooth tip thickness

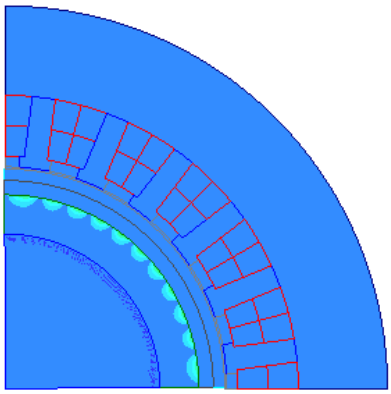

PMSG2 linear model with 1.5mm tooth tip thickness

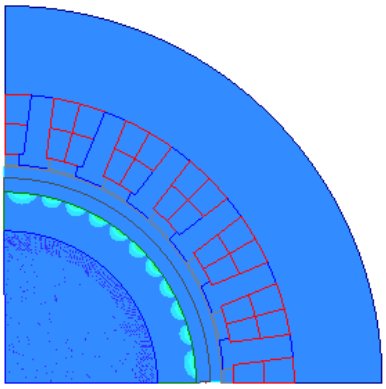

PMSG2 non-linear model with 1.5mm tooth tip thickness

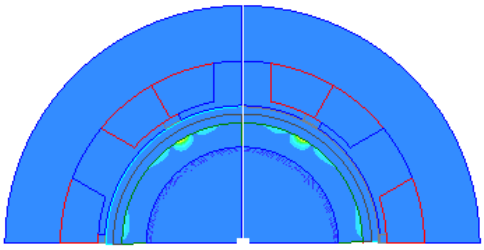

PMSG3 linear model with 1.5mm tooth tip thickness

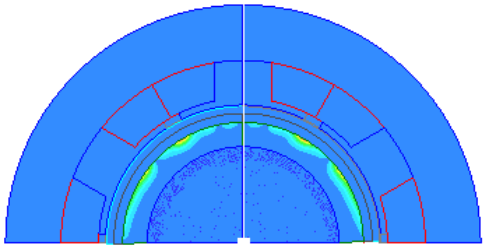

PMSG3 non-linear model with 1.5mm tooth tip thickness

Figure 7.7. Distribution of eddy currents in the permanent magnet region of PMSGs with 1.5mm stator tooth tip thickness and 0 magnet segments at no-load (open circuit).

Case 2: Two-Magnet Segments

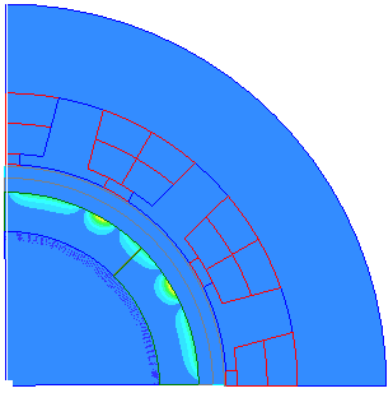

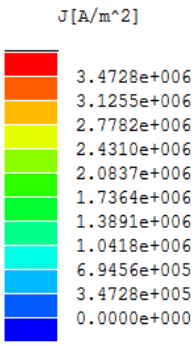

PMSG1 linear model with 1.5mm tooth tip thickness

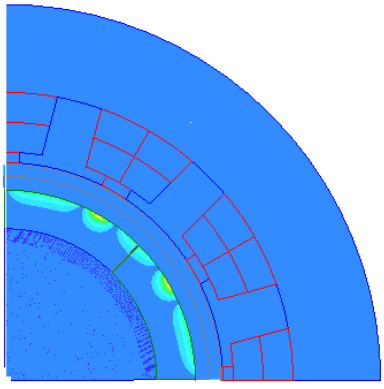

PMSG1 non-linear model with 1.5mm tooth tip thickness

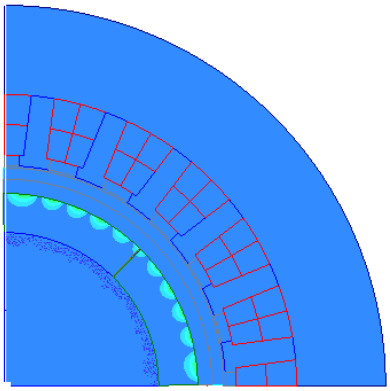

PMSG2 linear model with 1.5mm tooth tip thickness

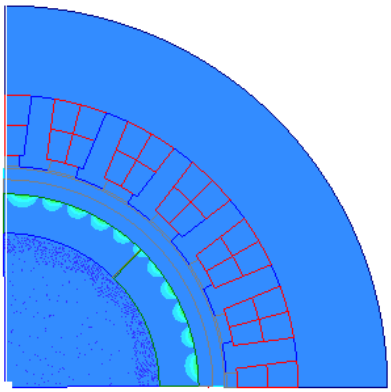

PMSG2 non-linear model with 1.5mm tooth tip thickness

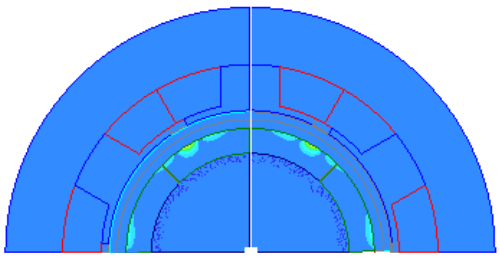

PMSG3 linear model with 1.5mm tooth tip thickness

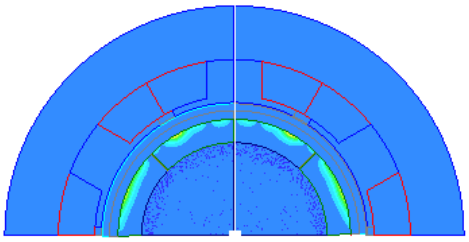

PMSG3 non-linear model with 1.5mm tooth tip thickness

Figure 7.8. Distribution of eddy currents in the permanent magnet region of PMSGs with 1.5mm stator tooth tip thickness and 2 magnet segments at no-load (open circuit).

Case 3: Four-Magnet Segments

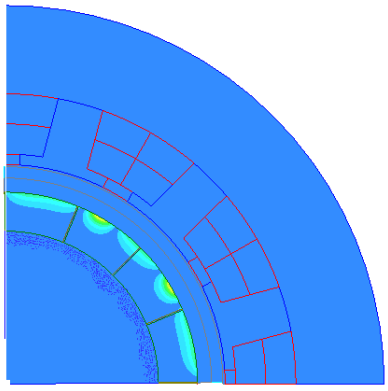

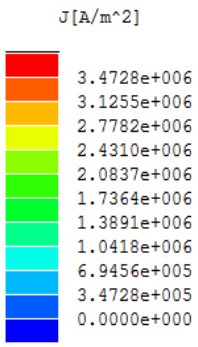

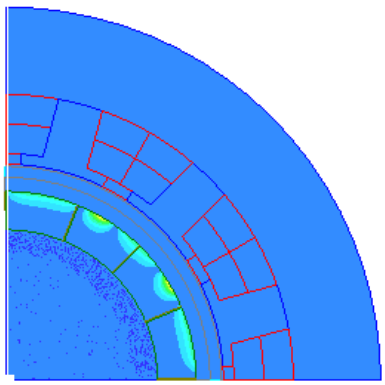

PMSG1 linear model with 1.5mm tooth tip thickness

PMSG1 non-linear model with 1.5mm tooth tip thickness

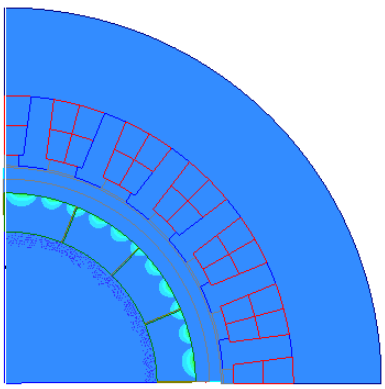

PMSG2 linear model with 1.5mm tooth tip thickness

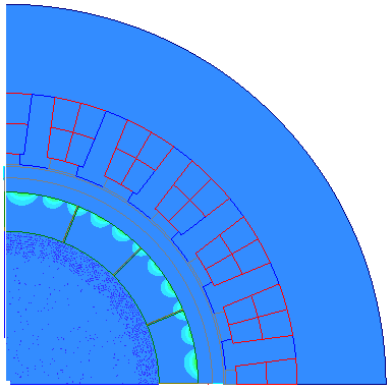

PMSG2 non-linear model with 1.5mm tooth tip thickness

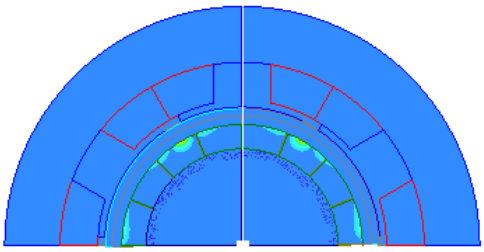

PMSG3 linear model with 1.5mm tooth tip thickness

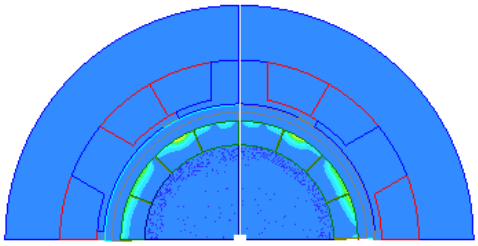

PMSG3 non-linear model with 1.5mm tooth tip thickness

Figure 7.9. Distribution of eddy currents in the permanent magnet region of PMSGs with 1.5mm stator tooth tip thickness and 4 magnet segments at no-load (open circuit).

7.4.7 **Effect of Magnet Segmentation in PMSGs at On-Load**

In this study, PMSGs are connected to an uncontrolled rectifier feeding a constant dc link current load of 128 A. In this case magnet segmentation again didn't always result in reducing rotor eddy current power loss in studied PMSGs.

PMSGs	Rotor Eddy Current Power Loss (W)					
	Circumferential Magnet Segments					
	0		2		4	
	Stator tooth Tip thickness		Stator tooth Tip thickness		Stator tooth Tip thickness	
	1mm	1mm	1mm	1mm	1mm	1mm
	Un-Saturated	Saturated	Un-Saturated	Saturated	Un-Saturated	Saturated
PMSG1	367W	371W	**338W**	391W	**347W**	361W
PMSG2	**240W**	287W	**259W**	277W	274W	247W
PMSG3	1039W	2381W	**1551W**	2117W	**1599W**	2211W

Table 7.15. Effect of magnet segmentation on on-load rotor eddy current power loss in PMSGs connected to uncontrolled one rectifier topology. The stator tooth tip thickness is 1mm. The dc link constant current is 128 A

PMSGs	Rotor Eddy Current Power Loss (W)					
	Circumferential Magnet Segments					
	0		2		4	
	Stator tooth Tip thickness		Stator tooth Tip thickness		Stator tooth Tip thickness	
	1.5mm	1.5mm	1.5mm	1.5mm	1.5mm	1.5mm
	Un-Saturated	Saturated	Un-Saturated	Saturated	Un-Saturated	Saturated
PMSG1	175W	176W	182W	184W	174W	174W
PMSG2	247W	245W	249W	251W	256W	301W
PMSG3	185W	860W	183W	**313W**	183W	**664W**

Table 7.16. Effect of magnet segmentation on on-load rotor eddy current power loss in PMSGs connected to uncontrolled one rectifier topology. The stator tooth tip thickness is 1.5mm. The dc link constant current is 128 A

Table 7.15 indicates that in comparison to PMSG2 with 0 magnet segment, the rotor eddy current power loss in PMSG2 with 2 magnet segments increased by 19W. Also, Table 7.16 shows an increase of 315W in rotor eddy current power loss in PMSG3 with 4 magnet segments compared to PMSG3 with 2 magnet segments.

The eddy current distribution in the permanent magnet region at on-load condition in three PMSGs is indicated in the following figures;

Stator Tooth Tip Thickness 1mm

Case 1: No-Magnet Segmentation

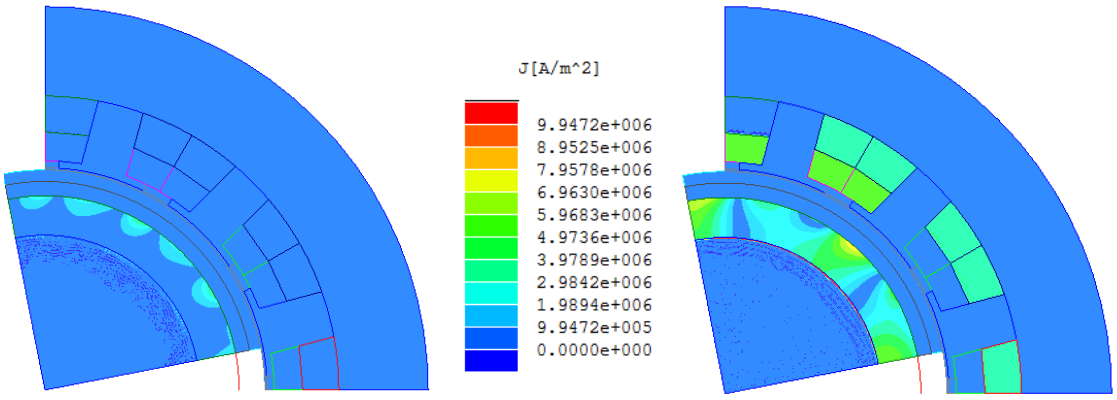

PMSG1 linear model with 1mm tooth tip thickness PMSG1 non-linear model with 1mm tooth tip thickness

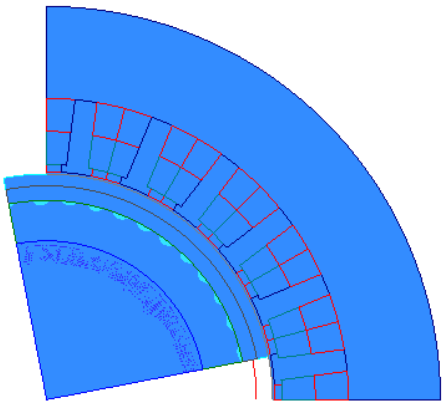

PMSG2 linear model with 1mm tooth tip thickness

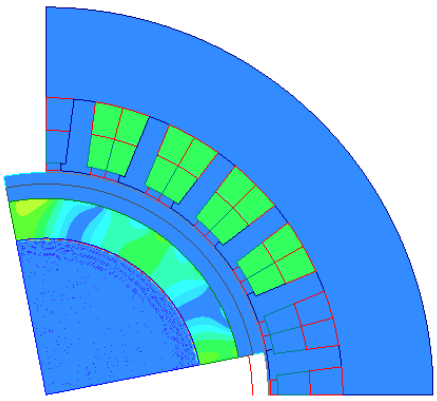

PMSG2 non-linear model with 1mm tooth tip thickness

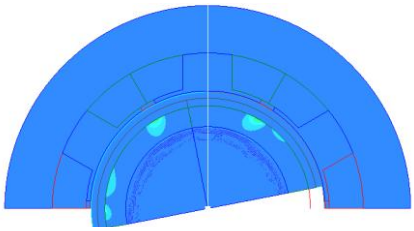

PMSG3 linear model with 1mm tooth tip thickness

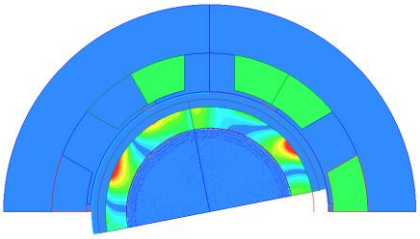

PMSG3 non-linear model with 1mm tooth tip thickness

Figure 7.10. Distribution of eddy currents in the permanent magnet region of PMSGs with 1mm stator tooth tip thickness and 0 magnet segments at on-load condition.

Case 2: Two-Magnet Segmentation

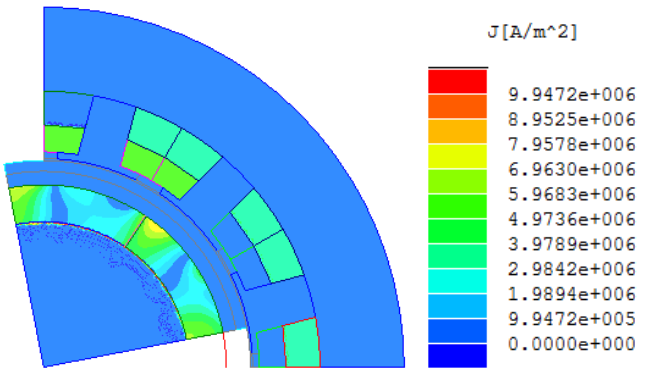

PMSG1 linear model with 1mm tooth tip thickness

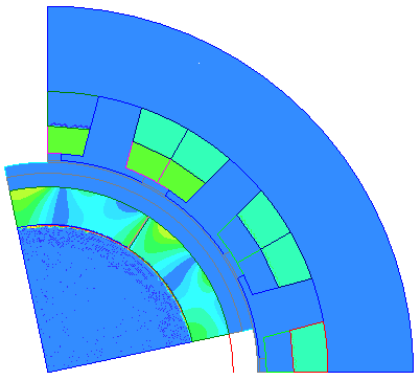

PMSG1 non-linear model with 1mm tooth tip thickness

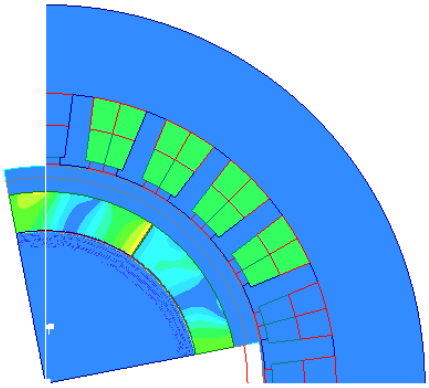

PMSG2 linear model with 1mm tooth tip thickness

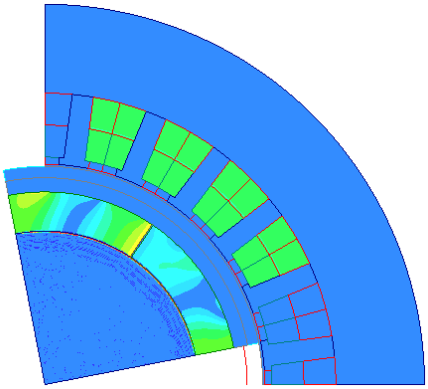

PMSG2 non-linear model with 1mm tooth tip thickness

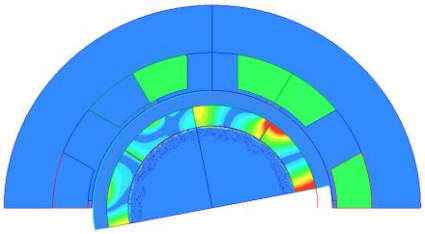

PMSG3 linear model with 1mm tooth tip thickness

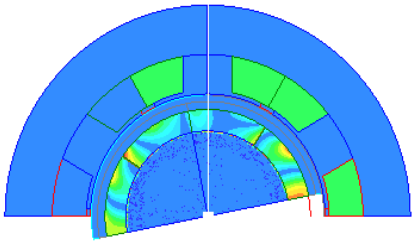

PMSG3 non-linear model with 1mm tooth tip thickness

Figure 7.11. Distribution of eddy currents in the permanent magnet region of PMSGs with 1mm stator tooth tip thickness and 2 magnet segments at on-load condition.

Case 4: Four-Magnet Segmentation

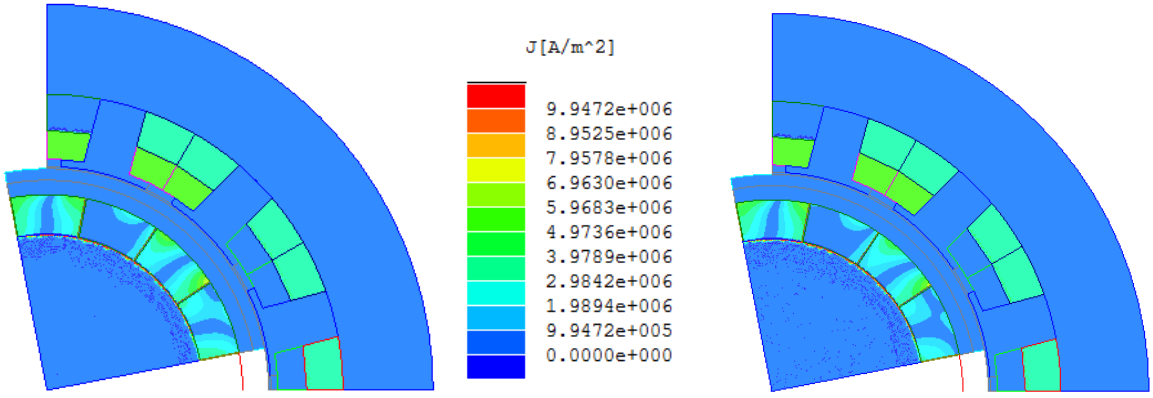

PMSG1 linear model with 1mm tooth tip thickness

PMSG1 non-linear model with 1mm tooth tip thickness

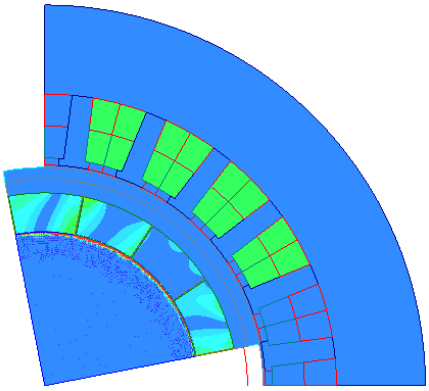

PMSG2 linear model with 1mm tooth tip thickness

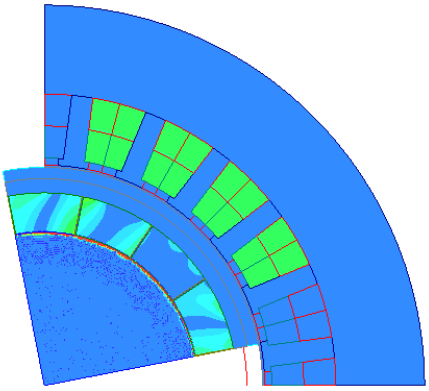

PMSG2 non-linear model with 1mm tooth tip thickness

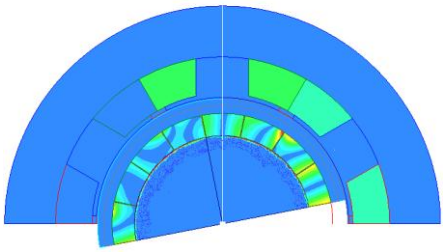

PMSG3 linear model with 1mm tooth tip thickness

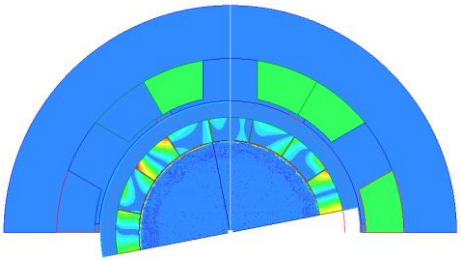

PMSG3 non-linear model with 1mm tooth tip thickness

Figure 7.12. Distribution of eddy currents in the permanent magnet region of PMSGs with 1mm stator tooth tip thickness and 4 magnet segments at on-load condition.

Stator Tooth Tip Thickness 1.5 mm

Case 1: No-Magnet Segmentation

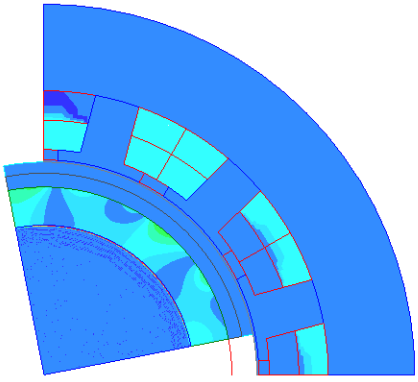

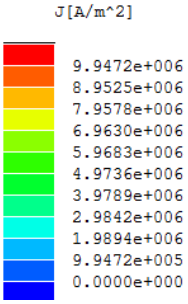

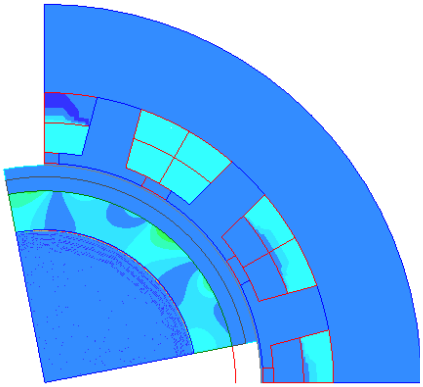

PMSG1 linear model with 1.5mm tooth tip thickness

PMSG1 non-linear model with 1.5mm tooth tip thickness

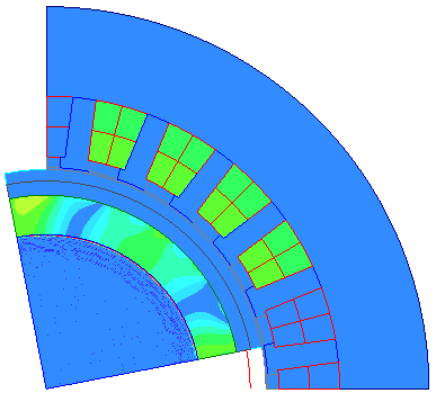

PMSG2 linear model with 1.5mm tooth tip thickness

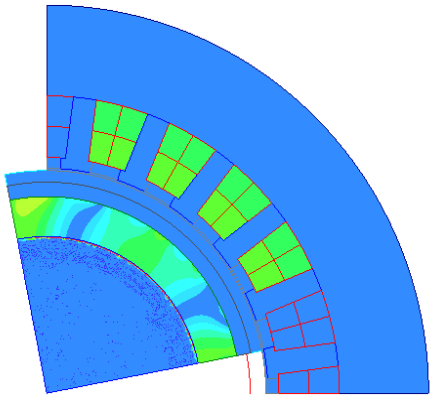

PMSG2 non-linear model with 1.5mm tooth tip thickness

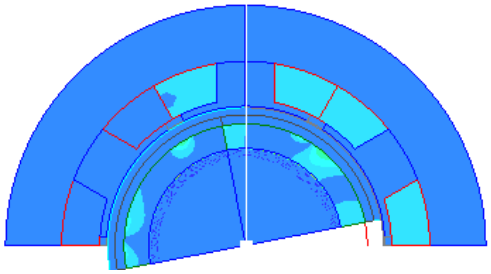

PMSG3 linear model with 1.5mm tooth tip thickness

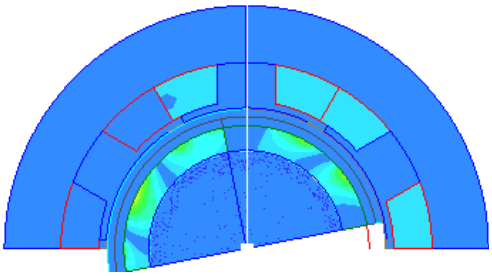

PMSG3 non-linear model with 1.5mm tooth tip thickness

Figure 7.13. Distribution of eddy currents in the permanent magnet region of PMSGs with 1.5mm stator tooth tip thickness and 0 magnet segments at on-load condition.

Case 2: Two-Magnet Segmentation

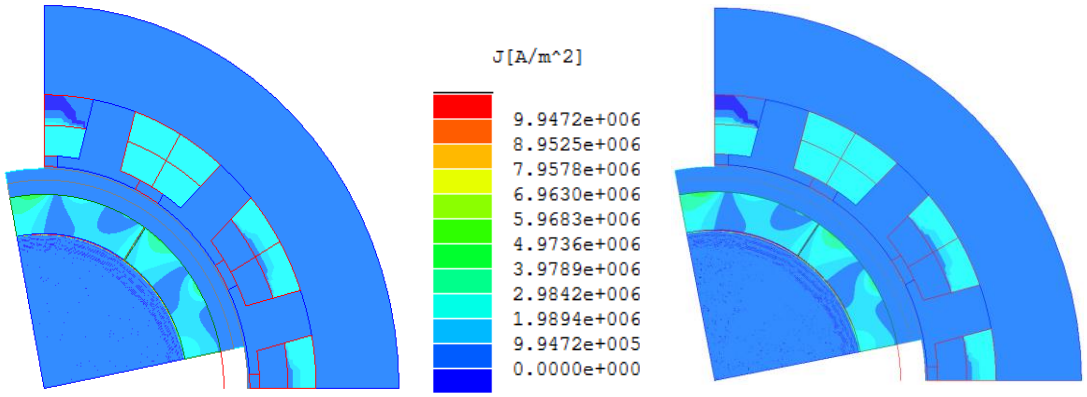

PMSG1 linear model with 1.5mm tooth tip thickness

PMSG1 non-linear model with 1.5mm tooth tip thickness

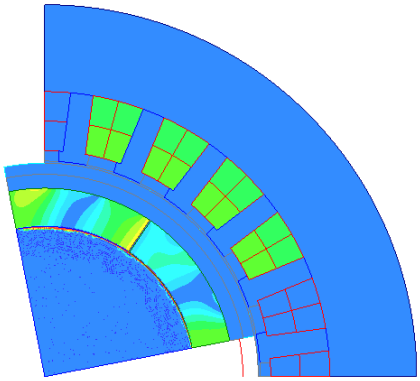

PMSG2 linear model with 1.5mm tooth tip thickness

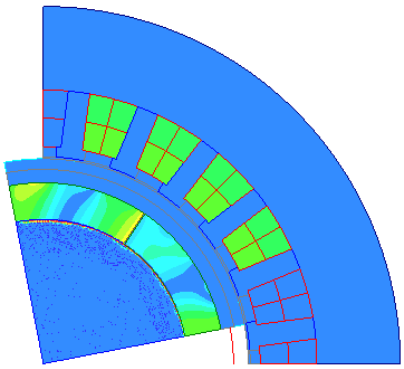

PMSG2 non-linear model with 1.5mm tooth tip thickness

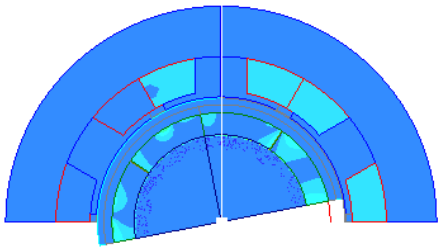

PMSG3 linear model with 1.5mm tooth tip thickness

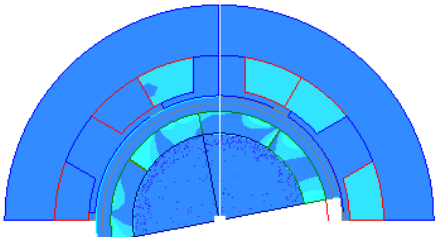

PMSG3 non-linear model with 1.5mm tooth tip thickness

Figure 7.14. Distribution of eddy currents in the permanent magnet region of PMSGs with 1.5mm stator tooth tip thickness and 2 magnet segments at on-load condition.

Case 3: Four-Magnet Segmentation

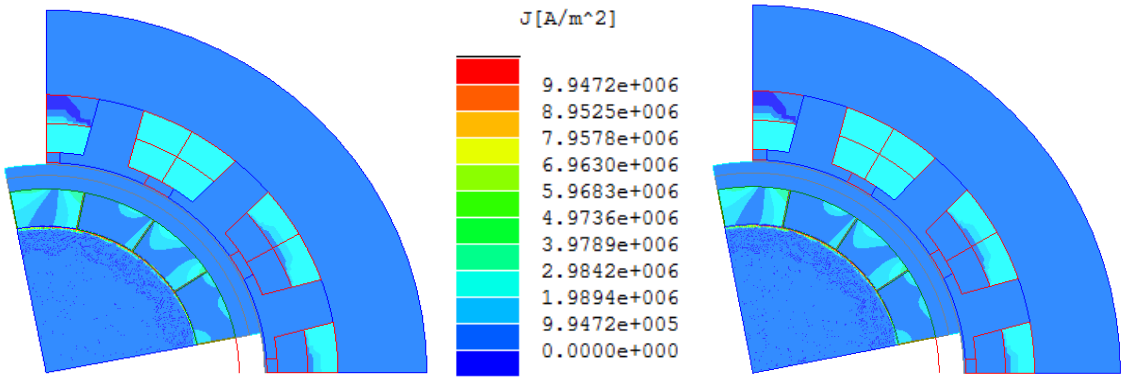

PMSG1 linear model with 1.5mm tooth tip thickness

PMSG1 non-linear model with 1.5mm tooth tip thickness

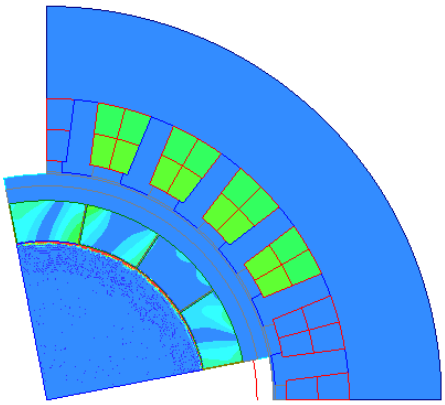

PMSG2 linear model with 1.5mm tooth tip thickness

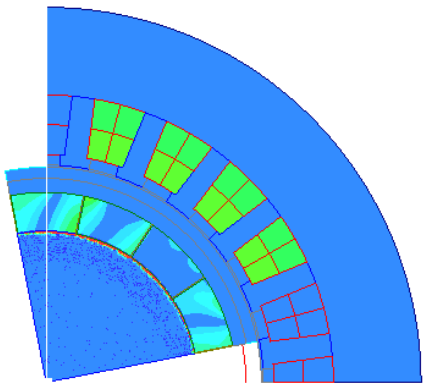

PMSG2 non-linear model with 1.5mm tooth tip thickness

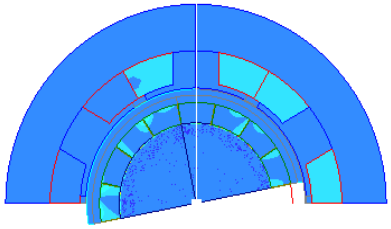

PMSG3 linear model with 1.5mm tooth tip thickness

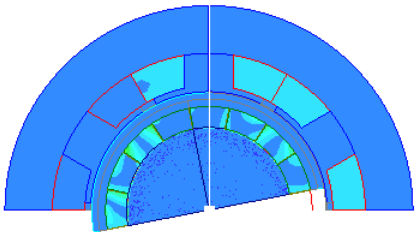

PMSG3 non-linear model with 1.5mm tooth tip thickness

Figure 7.15. Distribution of eddy currents in the permanent magnet region of PMSGs with 1.5mm stator tooth tip thickness and 4 magnet segments at on-load condition.

7.5 Conclusion

This chapter proposed a rotor eddy current power loss normalisation technique, which demonstrated to provide quick and reasonable estimates of full load rotor losses in similar generators. However, the agreement between no-load rotor losses estimated from the normalised data and those computed using FEA was not as good for some PMSGs e.g., in case of PMSG1 with slot opening of 3mm and 4mm. Although there was agreement on data trend which shows a decrease in rotor losses by reducing the slot opening and increasing the airgap.

The normalised data presented should be used with extreme care. It is only applicable to surface PM machines similar to those described Table 3.1. The calculations used to obtain the data also ignore end effects.

The number of mesh elements and time step dependence studies for rotor eddy current power loss calculation in PMSGs showed higher number of mesh elements and smaller time step is required for accurate transient FEA solution.

Finally, it is shown that circumferential magnet segmentation doesn't always result in reducing rotor eddy current power loss. The rotor losses will only reduce if eddy currents are resistive limited and their wavelengths are smaller than magnet width, flux density on the magnet surface is homogeneous and end effects are ignored.

Chapter 8

Conclusions

8.1 Thesis contributions and conclusions

In this thesis the accuracy of analytical methods used for the calculation of harmonic amplitudes and their corresponding rotor eddy current power losses has been compared with finite element analysis (FEA) in high-speed permanent magnet synchronous generators (PMSGs). The reaction of induced eddy currents field effect on the amplitudes of these harmonics was catered for in the calculation of the rotor eddy current power loss.

Three PMSGs i.e., PMSG1, PMSG2 and PMSG3, were the focus of study. The generators each have 4 poles , a rated speed of 90,000 rpm and a rated power of 50kW. The permanent magnets used in these generators are parallel magnetized, surface mounted ring magnets. In practice magnets are made in sectors of a ring. Even for a single pole, magnet is manufactured in a number of segments that depends on the magnet thickness. A kind of thickness to length ratio is considered by magnet manufacturers.

Ideally in the generators under study, each pole should have 4-6 pieces of magnet segments, and each segment being magnetized in the direction of its centre. It is possible to parallel magnetize segments of each pole but it’s not cost effective. As the

difference in rotor eddy current power loss in case of parallel magnetised one magnet pole piece (unsegment magnet) and segmented magnets in the generators under study was smaller i.e., 16% , therefore segmentation had been neglected. A non-conducting, non-magnetic sleeve is assumed to hold the magnets. The rotor is assumed to be made of solid steel for essential strength. The generators have the same overall diameter; stator bore diameter and active length, but have different numbers of slots per pole and winding configurations. The first machine, PMSG1, has 1 slot per pole per phase, with a short-pitched (by 2/3) three phase winding. The second machine, PMSG2, has 6 slots per pole, with 2 slots per pole per phase and a full pitched three phase winding. The third machine, PMSG3, has 0.5 slots per pole per phase and a concentrated three phase winding.

Firstly, a suite of analytical programs was developed in cylindrical coordinates for the calculation of harmonic amplitudes and corresponding rotor eddy current power losses in PMSG1 and PMSG2. The current sheet method was used for the calculation of rotor eddy current power loss. In this method each travelling flux harmonic caused by airgap permeance variation due to slotting and/or airgap mmf variation in space or time is represented by a rotating current sheet on the surface of a slotless stator. The current sheet value is adjusted to produce the same magnetostatic normal flux density on the surface of the magnet as that of the corresponding harmonic. The two-dimensional diffusion equation is then solved for each harmonic respective current sheet to calculate the corresponding rotor eddy current power loss.

Next, a static FEA method was used to calculate the amplitudes of rotating harmonics on the surface of the magnet, caused by permanent magnet mmf, armature reaction stator mmf and combined resultant mmf. In this method a two-dimensional Fourier transform is performed on the airgap flux density data, obtained at various rotor positions using the Maxwell 2D FEA software for the calculation of amplitude of airgap flux harmonics. The static FEA method was also used to investigate the effect of reduced stator tooth tip thickness and resulting saturation, on the amplitudes of harmonics and rotor eddy current power loss.

Finally, a two-dimensional transient FEA method was also employed for the rotor eddy current power loss calculation, which included rotor rotation and the external

circuit. The level of mesh refinement and time interval were established through a verification study, in which several solutions at different levels of refinement were obtained, and rotor losses were calculated as function of time step and number of mesh elements. This study established a minimum time step of 6.84×10^{-7} s and a minimum number of elements of 60000, beyond which the steady state average power loss did not change. Values equal to these thresholds were used for successive studies. The mesh elements were most concentrated in the rotor region.

The amplitude of magnet flux tooth ripple harmonics in PMSG1 (at no-load) were calculated using three analytical relative permeance methods, developed by Zhu et al (1993), Gieras (2004) and Ẑarko et al (2006). The corresponding rotor eddy current power loss due to each harmonic was calculated using the current sheet method. The differences in rotor power loss obtained from each analytical method vs. FEA, with negligible stator tooth tip saturation, were 20W, 17W and 9W, respectively. The discrepancy between the analytical and FEA results was the smallest for the complex permeance method by Ẑarko et al (2006).

Using the amplitude of airgap flux harmonics calculated from static FEA method, the current sheet method showed good agreement with transient FEA in terms of total rotor eddy current power loss. This finding has also been verified by (Irenji, 1998). This indirectly verifies that the current sheet method is accurate enough, and the critical step is the calculation of harmonic amplitudes. When the stator tooth tip is saturated, all three analytical methods failed to provide accurate results, and the difference between total power losses calculated using the analytical methods and FEA increased by 3 times. The study is also presented to show that reducing saturation by increasing the stator tooth tip thickness reduces the rotor losses.

To calculate on-load rotor eddy current power loss in PMSG1, with a sinusoidal stator current, the amplitude of each rotating flux harmonic in space and time was calculated using the winding factor equations (McPherson, 1981). The accuracy of the analytical results in terms of rotor eddy current power loss due to each flux harmonic was verified using both static and transient FEA. Good agreement was observed between the analytical and FEA methods for both un-saturated (stator permeability of 5000) and saturated (stator assigned non-linear BH curve) stator tooth tips, with differences

less than ±7%. This shows that armature reaction stator mmf is independent of slot-opening and stator tooth tip thickness.

It was highlighted that although a significant part of the total rotor losses was due to armature reaction stator mmf harmonics, the losses due to magnet flux tooth ripple losses cannot be neglected in the machines under study. It was shown that the total rotor losses in the machine are dependent on the load angle between the emf *E* and current *I*, and cannot be simply calculated by adding the no-load losses due to magnet flux tooth ripple harmonics with those due to stator mmf asynchronous harmonics. This is due to the interaction between the stator mmf harmonics and the magnet flux tooth ripple harmonics, which needs to be added vectorially. This was verified by comparing the analytical rotor eddy current power loss calculated using resultant harmonics, with those obtained from FEA, in a PM machine with un-saturated and saturated stator tooth tip thicknesses. Good agreement between analytical and FEA results was observed for total rotor eddy current power loss caused by resultant harmonics in the case of un-saturated stator tooth tips, although the difference between the results increased by 10% in the case of saturated stator tooth tip.

The effect of phase advance angle on rotor eddy current power loss in PMSG1 was also investigated. It was shown that rotor losses increase as the load angle moves from lagging to leading. The ratio of rotor losses when supplying a purely capacitive load to those when supplying a purely inductive load was found to be 3 by FEA transient linear solution. This power loss variation is due to the magnetising or demagnetising effect of the armature reaction field.

The accuracy of analytical and FEA methods was compared for the calculation of rotor eddy current power loss in PMSG2, when connected to an uncontrolled bridge rectifier. Two winding and rectifier topologies were considered: a 3-phase winding with a 3-phase bridge rectifier and a double 3-phase winding with a 3-phase rectifier for each, connected in series. Both magnet flux tooth ripple and armature reaction stator mmf harmonics were considered in the calculation of rotor loss; the harmonics were added vectorially. It was shown that the machine with a double 3-phase winding has considerably lower rotor loss, i.e., 25% less than the machine with a single 3-phase

winding, due to cancellation of some of the higher spatial order harmonics of time order 6.

A transient FEA parametric study was also performed to investigate the effect of slotting; i.e., number of slots, slot opening and airgap and magnet thicknesses, on rotor eddy current losses in PMSGs. For this study the generators were all designed to have approximately the same open circuit emf. This was achieved by adjusting the magnet thickness in proportion to the airgap. All generators were assumed to output the same sinusoidal current, at the same current advance angle.

The results were presented in a normalised fashion, showing losses per unit surface area of the rotor surface versus slot opening to slot pitch (s/λ) and total airgap (magnet + sleeve+ clearance gap) to slot pitch (g/λ). It was shown that no-load magnet flux tooth ripple loss is a strong function of both (s/λ) and (g/λ), and the losses decrease significantly with decreasing slot opening, increasing airgap length and increasing number of slots. Rotor on-load losses also decreased with reducing (s/λ) and (g/λ) ratios, but the decrease was not significant compared to the no-load loss. This showed that there is little dependence of on-load rotor loss on the ratios, although the losses can be reduced significantly by increasing the total airgap.

A limited transient FEA study was performed on three permanent magnet synchronous generators PMSG1, PMSG2 and PMSG3, connected to rectifiers with a constant current and voltage dc link loads, to investigate the effects of the different numbers of slots per pole, winding and rectifier configurations, and circumferential magnet segmentation. Rotor eddy current power loss is calculated under both no-load and on-load conditions. The results showed that the machine with 1.5 slots per pole has the highest on-load rotor loss due to the presence of the odd temporal and second spatial harmonic. The losses can be reduced considerably by increasing the number of slots to two slots per pole and splitting the windings into two independent three-phase sets, with a rectifier for each and with the outputs of the rectifiers connected in series or parallel. It was also shown that magnet segmentation doesn't always reduce rotor eddy current power loss in PM machines, either at no-load or on-load conditions. Segmentation will only reduce rotor losses in those PM machines in which eddy

currents are resistive limited, the flux density on the magnet surface is assumed to be homogeneous and end effects are neglected.

8.2 Future Work

It is clear that the analytical methods used here for calculating magnet flux tooth ripple harmonics are not accurate, especially when there is saturation in the stator tooth tip. It would therefore be useful to investigate the accuracy of other analytical methods, such as those by (Liu and Li, 2007; Dubas and Espanet, 2009; Zhu et al., 2010; Wu et al., 2011). These methods may be replicated in the Maple suite for the airgap flux density distribution. This distribution can then be translated into the rotor reference frame, and by expanding the Fourier form of the solution one could estimate the amplitudes of harmonics. The accuracy of analytical results for the calculation of harmonic amplitude and their respective rotor eddy current power loss could then be compared with static FEA and transient FEA methods.

Winding factor equations could be used for the calculation of amplitude of harmonics in concentrated wound PMSG for two cases: 1) A PMSG connected to a sinusoidal current distribution 2) A PMSG connected to a rectifier load with a non-sinusoidal current distribution. In chapter 6 of this Thesis, the current waveform of PMSG2 is produced by FEA analysis and was prescribed in the analytical model. This method could instead be developed so that the rectifier current is calculated from an accurate circuit model taking eddy currents into account.

As opposed to generators the PM machines could also be modelled as motors. Using both analytical and FEA methods; the rotor eddy current power loss in these motors can be calculated. Two cases needs to be considered for comparison; 1) A PM motor supplied with a sinusoidal current 2) A PM motor connected to a PWM (pulse width modulation) excitation. In the case of a PM machine connected to a PWM current source the temporal harmonics in the current will be significant, and will induce increased rotor eddy current power losses of an amount depending on the winding and slot / pole configuration. The rotor losses could be calculated for different winding configurations, for which an accurate analytical calculation of the winding distribution factor will be important.

Practical experimental work supported by 3D analysis is also needed to establish the accuracy of 2D analytical and FEA results for the calculation of rotor eddy current power loss. The analysis will cater for realistic features of the generators including end effects and magnet segmentation. Though the solution time for the analysis is high, but it can be reduced by using the method discussed by Saban et al., (2007). In this method the resultant current sheet due to magnet flux tooth ripple harmonics and stator mmf harmonics is calculated using a 2D analytical method. The resultant current sheet is then formulated in the rotor reference frame. Following this the 2D current sheet is axially extended for use in a 3D FEA analysis. The accuracy of this method can be further improved by using vector addition for the calculation of the resultant current sheet in 2D.

The work presented in the Thesis was based on two-dimensional analytical and FEA calculations in PMSGs with ring magnets configuration. The effects of the conducting shield and rotor iron laminations on rotor eddy current power loss have been neglected, and therefore further analytical development needs to be performed. The current sheet method doesn't allow for the effect of interactions between the rotor eddy currents and the stator slots. Moreover, the method also doesn't account for end effects and for axial or circumferential magnet segmentation. The result of this will be that calculated losses are likely to be overestimates.

Appendix1

Symbols used in the programs

f = frequency
k = time order
h = space order
q = wavelength
Rs = radius of stator
Rg = radius of airgap
Rm = radius of magnet
Anm = current sheet
ω = angular frequency
$S1$ = surface area of magnet
$S2$ = surface area of rotor hub
p = number of pair of poles
$\mu 0$ = Permeability of free space
$\mu r1$ = relative permeability of rotor
$\mu r2$ = relative permeability of magnet
$\mu r3$ =relative permeability of airgap
$\mu r4$ = relative permeability of steel
$\sigma 1$ = conductivity of magnet material
$\sigma 2$ = conductivity of stator material
$\sigma 3$ = conductivity of rotor hub material

Programs in Maple

% Author: A. Ali Qazalbash
% Program: *HRS*.mw

% **Programs to calculate spatial and temporal harmonic order**

% **Harmonics due to Rotor Saliency**

```
restart:
% Permeance variation
Ph := Poh + P2h·cos(2(theta − wt)) + P4h·cos(4(theta − wt)):                    (1)

% Rotor mmf
Frs := unapply(F1·cos(theta − wt) − F3·cos(3(theta − wt)) + F5·cos(5(theta
       − wt)) − F7·cos(7(theta − wt)), t, theta):                               (2)

% Multiplying (1) and (2)
Pa := P0h·(F1·cos(theta − wt) − F3·cos(3(theta − wt)) + F5·cos(5(theta
       − wt)) − F7·cos(7(theta − wt))):

  evalf(combine(Pa)):
```

****

% Author: A. Ali Qazalbash
% Program: *HSS*.mw

%**Harmonics due to Stator Slotting**
restart :
% Permeance variation
$Ph := Poh + P2h \cdot \cos(2 \cdot n \cdot \text{theta}) + P4h \cdot \cos(4 \cdot n \cdot \text{theta})$: (1)

% Rotor mmf
$Frs := unapply(F1 \cdot \cos(\text{theta} - wt) - F3 \cdot \cos(3(\text{theta} - wt)) + F5 \cdot \cos(5(\text{theta} - wt)) - F7 \cdot \cos(7(\text{theta} - wt)), t, \text{theta})$: (2)

%Multiplying (1) and (2)
$Pa := P0h \cdot (F1 \cdot \cos(\text{theta} - wt) - F3 \cdot \cos(3(\text{theta} - wt)) + F5 \cdot \cos(5(\text{theta} - wt)) - F7 \cdot \cos(7(\text{theta} - wt)))$:

$evalf(combine(Pa))$:

****

% Author: A. Ali Qazalbash
% Program: *HMS*.mw

%**Harmonics due to Stator mmf Space Distribution**
restart :
%Permeance variation
$Ph := Poh + P2h \cdot \cos(2 \cdot n \cdot \text{theta}) + P4h \cdot \cos(4 \cdot n \cdot \text{theta})$: (1)

%Non-sinusoidal mmf spatial distribution
$Fss := unapply(F1 \cdot \cos(wt - \text{theta}) + F5 \cdot \cos(wt + 5 \cdot \text{theta}) + F7 \cdot \cos(wt - 7 \cdot \text{theta}), t, \text{theta})$: (2)

%Multiplying (1) and (2)
$Pa := P2h \cdot \cos(2 \cdot 3 \cdot \text{theta}) \cdot (F1 \cdot \cos(wt - \text{theta}) + F5 \cdot \cos(wt + 5 \cdot \text{theta}) + F7 \cdot \cos(wt - 7 \cdot \text{theta}))$:

$evalf(combine(Pa))$:

****

% Author: A. Ali Qazalbash
% Program: *HMSR*.mw

%**Harmonics due to Interaction between Stator mmf Spatial harmonics and Rotor saliency**
restart :
%Stator mmf spatial harmonics
$Fsr := unapply(F1 \cdot \cos(wt + \text{theta}) + F5 \cdot \cos(6 \cdot wt + 5 \cdot \text{theta}) + F7 \cdot \cos(6 \cdot wt + 7 \cdot \text{theta}), t, \text{theta})$: (1)

%Permeance variation
$Ph := Poh + P2h \cos(2\theta) + P4h \cos(4\theta)$ (2)

%Multiplying (1) and (2)
$Pa := P2h \cdot \cos(4 \cdot 3 \cdot (\text{theta})) \cdot (F1 \cdot \cos(wt + \text{theta}) + F5 \cdot \cos(6 \cdot wt + 5 \cdot \text{theta}) + F7 \cdot \cos(6 \cdot wt + 7 \cdot \text{theta}))$:

$evalf(combine(Pa))$:

****

% Author: A. Ali Qazalbash
% Program: *HMTR*.mw

%**Harmonics due to Interaction between Stator mmf time harmonics and Rotor saliency**
restart :

%Stator mmf time harmonics

$Fsr := unapply(F1\cdot\cos(\text{theta}) + F2\cdot\cos(3\cdot wt + \text{theta}) + F4\cdot\cos(3\cdot wt - \text{theta}), t, \text{theta})$: (1)

%Permeance variation

$Ph := Poh + P2h\cdot\cos(2\cdot n\cdot(\text{theta})) + P4h\cdot\cos(4\cdot n\cdot(\text{theta}))$: (2)

%Multiplying (1) and (2)

$Pa := P2h\cdot\cos(2\cdot 3\cdot(\text{theta}))\cdot(F1\cdot\cos(\text{theta}) + F2\cdot\cos(3\cdot wt + \text{theta}) + F4\cdot\cos(3\cdot wt - \text{theta}))$:

$evalf(combine(Pa))$:

****

% Author: A. Ali Qazalbash
% Program: *HST*.mw

%**Harmonics due to Stator slotting**

restart :

%Stator mmf time harmonics

$Fsr := unapply(F1\cdot\cos(\text{theta}) + F2\cdot\cos(3\cdot\text{theta}) + F4\cdot\cos(3\cdot wt - \text{theta}), t, \text{theta})$: (1)

%Permeance variation

$Ph := Poh + P2h\cdot\cos(2\cdot n\cdot(\text{theta} + wt)) + P4h\cdot\cos(4\cdot n\cdot(\text{theta} + wt))$: (2)

%Multiplying (1) and (2)

$Pa := P2h\cdot\cos(2\cdot 3\cdot(\text{theta} + wt))\cdot(F1\cdot\cos(\text{theta}) + F3\cdot\cos(3\cdot\text{theta}) + F5\cdot\cos(5\cdot\text{theta}))$:

$evalf(combine(Pa))$:

****

% Author: A. Ali Qazalbash
% Program: *Loss1*.mw

% **The program calculates rotor eddy current power loss taking into account eddy current**

restart :

withVectorCalculus :

SetCoordinates(*'cylindrical'*[*r*, theta, *z*]) :

% **Magnetic Flux density in Rotor hub**

% using Poisson equation in the rotor hub region

$Poissons := \left(diff\left(Ar\left(r,theta\right),r\right)r + r^2 diff\left(Ar\left(r,theta\right),\text{'\$'}\left(r,2\right)\right) + diff\left(Ar\left(r,theta\right),\text{'\$'}\left(r,2\right)\right)\right) / r^2 = -\tau 1^2 Ar\left(r,theta\right)$:

% **The solution of the above equation can be written as:**

$Ar := (r, \text{theta}) \rightarrow Rc(r) * \exp(I\cdot q\cdot\text{theta})$:

Poissons :

$ODEC := simplify\left(\frac{Poissons}{\exp(I\cdot q\cdot theta)}\right)$

% solving for *Rc(r)*

$lr := dsolve(ODEC, Rc(r))$:

% taking right hand side (rhs) of *lr* and multiplying it with $exp(I\cdot q\cdot theta)$

$Ar := unapply(rhs(lr) * \exp(I\cdot q\cdot\text{theta}), r, \text{theta})$:

% taking into account Bessel function

$Ar := unapply((\_C1\ \text{BesselJ}(q, \tau l\, r) * \exp(I\cdot q\cdot\text{theta})), r, \text{theta})$:

% calculating radial component of magnet flux density using vector potential

$Br := unapply((1/r) * \text{D}[2](Ar)(r, \text{theta}), r, \text{theta})$:

% calculating tangential component of airgap flux density

```
Btr := unapply( -D[1](Ar)(r, theta), r, theta) :
% calculating radial component of magnet flux intensity
Hr := unapply(Br(r, theta) / (mu0·mur1), r, theta) :
% calculating tangential component of magnet flux intensity
Htr := unapply( (Btr(r, theta) / (mu0·mur1)), r, theta) :
```

% **Magnetic Flux density in Magnet**

```
Poissons := (diff (Ar(r,theta),r)r + r^2 diff (Ar(r,theta),'$'(r,2)) + diff (Ar(r,theta),'$'(r,2)))/ r^2 = -τ2^2 Ar(r,theta):
Az := (r, theta) → Rs(r) * exp(I·q·theta) :
Poissons :
ODES := simplify(Poissons / exp(I·q·theta)) :
lm := dsolve(ODES, Rs(r)) :
Az := unapply(rhs(lm) * exp(I·q·theta), r, theta) :
Az := unapply(((_C2 BesselJ(q, τ2·r) + _C3 BesselY(q, τ2·r)) e^(Iqθ)), r, theta)
Bmr := unapply( ( 1 / r ) * D[2](Az)(r, theta), r, theta) :
Hmr := unapply( ( (Bmr(r, theta)) ) / (mu0 * mur2), r, theta) :
Bmt := unapply( -D[1](Az)(r, theta), r, theta) :
Hmt := unapply( ( (Bmt(r, theta)) ) / (mu0 * mur2), r, theta) :
```

% **Magnetic Flux density in Air-Gap**

```
Poissons := (diff (Ar(r,theta),r)r + r^2 diff (Ar(r,theta),'$'(r,2)) + diff (Ar(r,theta),'$'(r,2)))/ r^2 = -τ3^2 Ar(r,theta):
Aa := (r, theta) → Rs(r) * exp(I·q·theta) :
Poissons :
ODES := simplify(Poissons / exp(I·q·theta)) :
Rsin := subs(_C1 = _C4, _C2 = _C5, rhs(dsolve(ODES, Rs(r)))) :
Rsin := collect(Rsin, {BesselJ, BesselY}) :
Aa := unapply(Rsin * exp(I·q·theta), r, theta) :
Bar := unapply( ( 1 / r ) * D[2](Aa)(r, theta), r, theta) :
Har := unapply( ( (Bar(r, theta)) ) / (mu0 * mur3), r, theta) :
Bat := unapply( -D[1](Aa)(r, theta), r, theta) :
Hat := unapply( ( (Bat(r, theta)) ) / (mu0 * mur3), r, theta) :
```

% **Magnetic Flux density in Stator**

```
Poissons := (diff (Ar(r,theta),r)r + r^2 diff (Ar(r,theta),'$'(r,2)) + diff (Ar(r,theta),'$'(r,2)))/ r^2 = -τ4^2 Ar(r,theta):
As := (r, theta) → Rs(r) * exp(I·q·theta) :
Poissons :
ODES := simplify(Poissons / exp(I·q·theta)) :
Rsin := subs(_C1 = _C6, _C2 = _C7, rhs(dsolve(ODES, Rs(r)))) :
Rsin := collect(Rsin, {BesselJ, BesselY}) :
As := unapply(Rsin * exp(I·q·theta), r, theta) :
Bs := unapply( ( 1 / r ) * D[2](As)(r, theta), r, theta) :
Hs := unapply( ( (Bs(r, theta)) ) / (mu0 * mur4), r, theta) :
Bst := unapply( -D[1](As)(r, theta), r, theta) :
Hst := unapply( ( (Bst(r, theta)) ) / (mu0 * mur4), r, theta) :
```

% **Boundary Conditions**

```
eq1 := Bs(Rs, theta) = 0 :
eq2 := Hat(Rg, theta) = Hst(Rg, theta) + Anm·e^(I q θ) :
eq3 := Bar(Rg, theta) = Bs(Rg, theta) :
eq4 := Hmt(Rm, theta) = Hat(Rm, theta) :
eq5 := Bmr(Rm, theta) = Bar(Rm, theta) :
eq6 := Htr(Rr, theta) = Hmt(Rr, theta) :
eq7 := Br(Rr, theta) = Bmr(Rr, theta) :
```

% from eq1, we have:

```
s1 := coeff(lhs(eq1), exp(I·q·theta)) = 0 :
```

% from eq2, we have:
$s2 := coeff(lhs(eq2), (\exp(I \cdot q \cdot \text{theta}))) = coeff(rhs(eq2), \exp(I \cdot q \cdot \text{theta}))$:
% from eq3, we have:
$s3 := coeff(lhs(eq3), \exp(I \cdot q \cdot \text{theta})) = coeff(rhs(eq3), \exp(I \cdot q \cdot \text{theta}))$:
% from eq4, we have:
$s4 := coeff(lhs(eq4), \exp(I \cdot q \cdot \text{theta})) = coeff(rhs(eq4), \exp(I \cdot q \cdot \text{theta}))$:
% from eq5, we have:
$s5 := coeff(lhs(eq5), \exp(I \cdot q \cdot \text{theta})) = coeff(rhs(eq5), \exp(I \cdot q \cdot \text{theta}))$:
% from eq6, we have:
$s6 := coeff(lhs(eq6), \exp(I \cdot q \cdot \text{theta})) = coeff(rhs(eq6), \exp(I \cdot q \cdot \text{theta}))$:
% from eq7, we have:
$s7 := coeff(lhs(eq7), \exp(I \cdot q \cdot \text{theta})) = coeff(rhs(eq7), \exp(I \cdot q \cdot \text{theta}))$:

% we have 4 equations with 4 variables therefore it can be solved as:
$sol := solve(\{s1, s2, s3, s4, s5, s6, s7\}, \{\_C1, \_C2, \_C3, \_C4, \_C5, \_C6, \_C7\})$:

% **Eddy Currents taken into account**

$$Az := unapply\left(\left(rhs(sol[2])\,\text{BesselJ}(q, \tau 2 \cdot r) + rhs(sol[3])\,\text{BesselY}(q, \tau 2 \cdot r)\right), r, theta\right)$$

$$Bmr := unapply\left(\frac{1}{r}.\frac{\mathrm{d}}{\mathrm{d}\,theta}(Az)(r, theta), r\right)$$

$Hmr := unapply(((Bmr(r))) / (mu0 * mur), r)$:

$$Bmt := unapply\left(-\frac{\mathrm{d}}{\mathrm{d}\,r}(Az)(r, theta), r\right):$$

$Hmt := unapply(((Bmt(r))) / (mu0 * mur2), r)$:

% **Field quantities to calculate rotor loss**

$$Ar := unapply\left(\left(rhs(sol[1]) \cdot \text{BesselJ}(q, \tau 1 \cdot r)\right), r, theta\right):$$

$$Br := unapply\left(\frac{1}{r}.\frac{\mathrm{d}}{\mathrm{d}\,theta}(Ar)(r, theta), r\right):$$

$$Hr := unapply\left(\left((Br(r))\right) / (mu0 \cdot mur), r\right):$$

$$Brt := unapply\left(\left(-\frac{\mathrm{d}}{\mathrm{d}\,r} Ar(r, theta)\right), r\right):$$

$Hrt := unapply(((Brt(r))) / (mu0 * mur1), r)$:

%**Machine Parameters**

$\omega := 2\pi kf$: $f := 3000$: $\mu 0 := 4\pi \times 10^{-7}$: $p := 2$: $\sigma 1 := 6666667$: $\sigma 2 := 769231$: $\sigma 3 := 3.5 \times 10^{-15}$: $\mu r1 := 750$: $\mu r2 := 1.07$: $\mu r3 := 1$: $\mu r4 := 5000$

$Rm := 27.1 \times 10^{-3}$: $Rs := 31 \times 10^{-3}$: $Rr := 21.6 \times 10^{-3}$: $Rg := \left(Rm + 3.8 \times 10^{-3}\right)$: $Anm :=$ current sheet value : $k :=$ time order :

$h :=$ space order

$q := p \times h$: $S1 := \left(\pi(2Rm) 125 \times 10^{-3}\right)$: $S2 := \left(\pi(2Rr) 125 \times 10^{-3}\right)$: $\tau 1 := \sqrt{I\omega\sigma 1\mu 0\mu r1}$: $\tau 2 := \sqrt{I\omega\sigma 2\mu 0\mu r2}$: $\tau 3 := \sqrt{I\omega\sigma 3\mu 0\mu r3}$:

$\tau 4 := \sqrt{I\omega\mu 0\mu r4}$:

% **Power Loss Calculation**
% Poynting theorem is used for the calculation of power loss

% **Power transmitted from airgap to magnet**

$Emt := evalf(-I \cdot \omega \cdot Az(Rm))$:
$Hmt := evalf(conjugate(Hmt(Rm)))$:

$$P_1 := evalf\left(\frac{1}{2} \cdot \text{Re}(Emt \cdot Hmt) \cdot S_1\right):$$

% **Power transmitted from magnet layer to rotor hub**

$Ert := evalf(-I \cdot \omega \cdot Az(Rr))$:
$Hrt := evalf(conjugate(Hrt(Rr)))$:

$P_2 := evalf\left(\frac{1}{2}\cdot \mathrm{Re}(Ert\cdot Hrt)\cdot S_2\right):$

% **Power Loss in magnet**
$Pmag := P_1 - P_2 :$

% **Power Loss in rotor hub**
$Phub := P_2 :$

****

% Author: A. Ali Qazalbash
% Program: *Harmonic1*.mw

% **The program calculates airgap flux density harmonic in time and space without taking into account reaction of eddy currents**

```
restart :
withVectorCalculus :
SetCoordinates( 'cylindrical'[r, theta, z] ) :
```

% **Magnetic Flux density in Rotor hub**

% **Using Laplace equation in the rotor hub region**

$Lar := \left(diff\left(Ar(r,theta),r\right)r + r^2 diff\left(Ar(r,theta),\$'(r,2)\right) + diff\left(Ar(r,theta),\$'(r,2)\right)\right)/r^2 = 0:$

```
Ar := (r, theta) → Rc(r) * exp(I·q·theta) :
Lar :
ODEC := simplify( Lar / exp(I·q·theta) ) :
lr := dsolve( ODEC, Rc(r) ) :
Ar := unapply( rhs(lr) * exp(I·q·theta), r, theta) :
Ar := unapply( ( (_C1· r^q)·e^(I q θ) ), r, theta) :
Br := unapply( (1/r) * D[2](Ar) (r, theta), r, theta) :
Btr := unapply( -D[1](Ar) (r, theta), r, theta) :
Hr := unapply( Br(r, theta) / (mu0·mur1), r, theta) :
Htr := unapply( (Btr(r, theta) / (mu0·mur1)), r, theta) :
```

% **Magnetic Flux density in Magnet**

% **Using Laplace equation in the magnet region**

$Lar := \left(diff\left(Ar(r,theta),r\right)r + r^2 diff\left(Ar(r,theta),\$'(r,2)\right) + diff\left(Ar(r,theta),\$'(r,2)\right)\right)/r^2 = 0:$

```
Az := (r, theta) → Rs(r) * exp(I·q·theta) :
Lar :
ODES := simplify(Lar / exp(I · q · θ))
lm := dsolve( ODES, Rs(r) ) :
Az := unapply( rhs(lm) * exp(I·q·theta), r, theta) :
Az := unapply( ( (_C2 r^(-q) + _C3 r^q)·e^(I q θ) ), r, theta) :
Bmr := unapply( ( 1/r ) * D[2](Az) (r, theta), r, theta ) :
Hmr := unapply( ( (Bmr(r, theta)) ) / (mu0 * mur2), r, theta) :
Bmt := unapply( -D[1](Az) (r, theta), r, theta) :
Hmt := unapply( ( (Bmt(r, theta)) ) / (mu0 * mur2), r, theta) :
```

% **Magnetic Flux density in Air-Gap**

$Lar := \left(diff\left(Ar(r,theta),r\right)r + r^2 diff\left(Ar(r,theta),\$'(r,2)\right) + diff\left(Ar(r,theta),\$'(r,2)\right)\right)/r^2 = 0:$

```
Aa := (r, theta) → Rs(r) * exp(I·q·theta) :
Lar :
```

$ODES := simplify(Lar / exp(I \cdot q \cdot \theta))$

```
Rsin := subs(_C1 = _C4, _C2 = _C5, rhs(dsolve(ODES, Rs(r)))):
Aa := unapply(Rsin * exp(I·q·theta), r, theta):
Bar := unapply((1/r) * D[2](Aa)(r, theta), r, theta):
Har := unapply(((Bar(r, theta)))/(mu0*mur3), r, theta):
Bat := unapply(-D[1](Aa)(r, theta), r, theta):
Hat := unapply(((Bat(r, theta)))/(mu0*mur3), r, theta):
```

% **Magnetic Flux density in Stator**

$$Lar := \left(diff\left(Ar(r,theta),r\right)r + r^2 diff\left(Ar(r,theta),\text{'\$'}(r,2)\right) + diff\left(Ar(r,theta),\text{'\$'}(r,2)\right)\right)/r^2 = 0:$$

```
As := (r, theta) → Rs(r) * exp(I·q·theta):
Lar:
ODES := simplify(Lar / exp(I·q·θ))
Rsin := subs(_C1 = _C6, _C2 = _C7, rhs(dsolve(ODES, Rs(r)))):
As := unapply(Rsin * exp(I·q·theta), r, theta):
Bs := unapply((1/r) * D[2](As)(r, theta), r, theta):
Hs := unapply(((Bs(r, theta)))/(mu0*mur4), r, theta):
Bst := unapply(-D[1](As)(r, theta), r, theta):
Hst := unapply(((Bst(r, theta)))/(mu0*mur4), r, theta):
```

% **Boundary Conditions**

```
eq1 := Hst(Rs, theta) = 0:
eq2 := Hat(Rg, theta) = Hst(Rg, theta) + Anm·e^(I q θ):
eq3 := Bar(Rg, theta) = Bs(Rg, theta):
eq4 := Hmt(Rm, theta) = Hat(Rm, theta):
eq5 := Bmr(Rm, theta) = Bar(Rm, theta):
eq6 := Htr(Rr, theta) = Hmt(Rr, theta):
eq7 := Br(Rr, theta) = Bmr(Rr, theta):

% from eq1, we have:
 s1 := coeff(lhs(eq1), exp(I·q·theta)) = 0:
% from eq2, we have:
s2 := coeff(lhs(eq2), (exp(I·q·theta))) = coeff(rhs(eq2), exp(I·q·theta)):
% from eq3, we have:
s3 := coeff(lhs(eq3), exp(I·q·theta)) = coeff(rhs(eq3), exp(I·q·theta)):
% from eq4, we have:
s4 := coeff(lhs(eq4), exp(I·q·theta)) = coeff(rhs(eq4), exp(I·q·theta)):
% from eq5, we have:
s5 := coeff(lhs(eq5), exp(I·q·theta)) = coeff(rhs(eq5), exp(I·q·theta)):
% from eq6, we have:
s6 := coeff(lhs(eq6), exp(I·q·theta)) = coeff(rhs(eq6), exp(I·q·theta)):
% from eq7, we have:
s7 := coeff(lhs(eq7), exp(I·q·theta)) = coeff(rhs(eq7), exp(I·q·theta)):
% we have 4 equations with 4 variables, can be solved as:
 sol := solve({s1, s2, s3, s4, s5, s6, s7}, {_C1, _C2, _C3, _C4, _C5, _C6, _C7}):
```

% **Without Eddy Currents taken into account**

% calculating magnet vector potential

$$Az := unapply\left(\left(rhs(sol[2])\,\text{BesselJ}(q,\tau 2\cdot r) + rhs(sol[3])\,\text{BesselY}(q,\tau 2\cdot r)\right),r\right)$$

% calculating radial airgap flux density

$$Bmr := unapply\left(\frac{1}{r}.\frac{d}{d\,theta}(Az)(r,theta),r\right)$$

% **Machine Parameters**

$Rm := 27.1\times10^{-3} : Rs := 31\times10^{-3} : Rr := 21.6\times10^{-3} : Rg := \left(Rm + 3.8\times10^{-3}\right) : Anm :=$ current sheet value : $k :=$ time order :

$h :=$ space order

$q := p\times h : S1 := \left(\pi(2Rm)125\times10^{-3}\right) : S2 := \left(\pi(2Rr)125\times10^{-3}\right) : \tau1 := \sqrt{I\omega\sigma1\mu0\mu r1} : \tau2 := \sqrt{I\omega\sigma2\mu0\mu r2} : \tau3 := \sqrt{I\omega\sigma3\mu0\mu r3}$:

$\tau4 := \sqrt{I\omega\mu0\mu r4}$:

% **Harmonic amplitude on the surface of the magnet**

evalf((*Bmr*(*Rm*))) :

****

% Author: A. Ali Qazalbash
% Program: *Current1*.mw

% **The program calculates rotor eddy current power loss taking into account eddy current due to armature reaction stator mmf harmonics only, for the known value of current sheet for each harmonic**

restart : *with*(*VectorCalculus*) :
SetCoordinates(*'cylindrical'*[*r*, theta, *z*]) :

% **Magnetic Flux density in Rotor Hub**

Lar := (*diff* (*Ar*(*r*, theta), *r*) * *r* + *r*^2 * *diff* (*Ar*(*r*, theta), `$`(*r*, 2))
+ *diff* (*Ar*(*r*, theta), `$`(theta, 2))) / *r*^2 = - $\tau1^2 \cdot$ *Ar*(*r*, theta) :

Ar := (*r*, theta) → *Rc*(*r*) * exp(*I*·*q*·theta) :

Lar :

ODEC := *simplify*$\left(\dfrac{Lar}{\exp(I\cdot q\cdot\text{theta})}\right)$:

lr := *dsolve*(*ODEC*, *Rc*(*r*)) :

Ar := *unapply*(*rhs*(*lr*) * exp(*I*·*q*·theta), *r*, theta) :

Ar := *unapply*((*_C1* BesselJ(*q*, $\tau1$ *r*) * exp(*I*·*q*·theta)), *r*, theta) :

Br := *unapply*((1 / *r*) * D[2] (*Ar*) (*r*, theta), *r*, theta) :

Btr := *unapply*(- D[1] (*Ar*) (*r*, theta), *r*, theta) :

Hr := *unapply*(*Br*(*r*, theta) / (*mu0*·*mur1*), *r*, theta) :
Htr := *unapply*((*Btr*(*r*, theta) / (*mu0*·*mur1*)), *r*, theta) :

% **Magnetic Flux density in Magnet**

Poissons := (*diff* (*Az*(*r*, theta), *r*) * *r* + *r*^2 * *diff* (*Az*(*r*, theta), `$`(*r*, 2))
+ *diff* (*Az*(*r*, theta), `$`(theta, 2))) / *r*^2 = - $\tau2^2 \cdot$ *Az*(*r*, theta) :

Az := (*r*, theta) → *Rs*(*r*) * exp(*I*·*q*·theta) :

Poissons :

ODES := *simplify*(*Poissons* / exp(*I*·*q*·theta)) :

lm := *dsolve*(*ODES*, *Rs*(*r*)) :

Az := *unapply*(*rhs*(*lm*) * exp(*I*·*q*·theta), *r*, theta) :

Az := *unapply*$\left(\left(\left(\text{\_C2}\ \text{BesselJ}(q, \tau2\cdot r) + \text{\_C3}\ \text{BesselY}(q, \tau2\cdot r)\right) e^{I q \theta}\right), r, \text{theta}\right)$:

Bmr := *unapply*$\left(\left(\dfrac{1}{r}\right) * \text{D}[2](Az)(r, \text{theta}), r, \text{theta}\right)$:

Hmr := *unapply*(((*Bmr*(*r*, theta))) / (*mu0* * *mur2*), *r*, theta) :

Bmt := *unapply*(- D[1] (*Az*) (*r*, theta), *r*, theta) :

Hmt := *unapply*(((*Bmt*(*r*, theta))) / (*mu0* * *mur2*), *r*, theta) :

% **Magnetic Flux density in Air-Gap**

Poissons := (*diff* (*Aa*(*r*, theta), *r*) * *r* + *r*^2 * *diff* (*Aa*(*r*, theta), `$`(*r*, 2))
+ *diff* (*Aa*(*r*, theta), `$`(theta, 2))) / *r*^2 = - $\tau3^2 \cdot$ *Aa*(*r*, theta) :

$Aa := (r, \text{theta}) \rightarrow Rs(r) * \exp(I \cdot q \cdot \text{theta})$:

Poissons :

$ODES := simplify(Poissons / \exp(I \cdot q \cdot \text{theta}))$:

$Rsin := subs(\_C1 = \_C4, \_C2 = \_C5, rhs(dsolve(ODES, Rs(r))))$:

$Rsin := collect(Rsin, \{\text{BesselJ}, \text{BesselY}\})$:

$Aa := unapply(Rsin * \exp(I \cdot q \cdot \text{theta}), r, \text{theta})$:

$Bar := unapply\left(\left(\frac{1}{r}\right) * \text{D}[2](Aa)(r, \text{theta}), r, \text{theta}\right)$:

$Har := unapply(((Bar(r, \text{theta}))) / (mu0 * mur3), r, \text{theta})$:

$Bat := unapply(-\text{D}[1](Aa)(r, \text{theta}), r, \text{theta})$:

$Hat := unapply(((Bat(r, \text{theta}))) / (mu0 * mur3), r, \text{theta})$:

% **Magnetic Flux density in Stator**

$Poissons := (diff(As(r, \text{theta}), r) * r + r\text{^}2 * diff(As(r, \text{theta}), \text{`\$`}(r, 2))$
$+ diff(As(r, \text{theta}), \text{`\$`}(\text{theta}, 2))) / r\text{^}2 = -\tau 4^2 \cdot As(r, \text{theta})$:

$As := (r, \text{theta}) \rightarrow Rs(r) * \exp(I \cdot q \cdot \text{theta})$:

Poissons :

$ODES := simplify(Poissons / \exp(I \cdot q \cdot \text{theta}))$:

$Rsin := subs(\_C1 = \_C6, \_C2 = \_C7, rhs(dsolve(ODES, Rs(r))))$:

$Rsin := collect(Rsin, \{\text{BesselJ}, \text{BesselY}\})$:

$As := unapply(Rsin * \exp(I \cdot q \cdot \text{theta}), r, \text{theta})$:

$Bs := unapply\left(\left(\frac{1}{r}\right) * \text{D}[2](As)(r, \text{theta}), r, \text{theta}\right)$:

$Hs := unapply(((Bs(r, \text{theta}))) / (mu0 * mur4), r, \text{theta})$:

$Bst := unapply(-\text{D}[1](As)(r, \text{theta}), r, \text{theta})$:
$Hst := unapply(((Bst(r, \text{theta}))) / (mu0 * mur4), r, \text{theta})$:

% **Boundary Conditions**

$eq1 := Bs(Rs, \text{theta}) = 0$:

$eq2 := Hat(Rg, \text{theta}) = Hst(Rg, \text{theta}) + Anm \cdot e^{I q \theta}$:

$eq3 := Bar(Rg, \text{theta}) = Bs(Rg, \text{theta})$:

$eq4 := Hmt(Rm, \text{theta}) = Hat(Rm, \text{theta})$:

$eq5 := Bmr(Rm, \text{theta}) = Bar(Rm, \text{theta})$:

$eq6 := Htr(Rr, \text{theta}) = Hmt(Rr, \text{theta})$:

$eq7 := Br(Rr, \text{theta}) = Bmr(Rr, \text{theta})$:

% from eq1, we have:
$s1 := coeff(lhs(eq1), \exp(I \cdot q \cdot \text{theta})) = 0$:
% from eq2, we have:
$s2 := coeff(lhs(eq2), (exp(I \cdot q \cdot theta))) = coeff(rhs(eq2), exp(I \cdot q \cdot theta))$:
% from eq3, we have:
$s3 := coeff(lhs(eq3), (exp(I \cdot q \cdot theta))) = coeff(rhs(eq3), exp(I \cdot q \cdot theta))$:
% from eq4, we have:
$s4 := coeff(lhs(eq4), (exp(I \cdot q \cdot theta))) = coeff(rhs(eq4), exp(I \cdot q \cdot theta))$:
% from eq5, we have:
$s5 := coeff(lhs(eq5), (exp(I \cdot q \cdot theta))) = coeff(rhs(eq5), exp(I \cdot q \cdot theta))$:
% from eq6, we have:
$s6 := coeff(lhs(eq6), (exp(I \cdot q \cdot theta))) = coeff(rhs(eq6), exp(I \cdot q \cdot theta))$:
% from eq7, we have:
$s7 := coeff(lhs(eq7), (exp(I \cdot q \cdot theta))) = coeff(rhs(eq7), exp(I \cdot q \cdot theta))$:

% we have 4 equations with 4 variables. The solution is given by:

$sol := solve(\{s1, s2, s3, s4, s5, s6, s7\}, \{\_C1, \_C2, \_C3, \_C4, \_C5, \_C6, \_C7\})$:

%**With Eddy Currents taken into account**

$Az := unapply\left(\left(\left(rhs\left(sol[2]\right)\text{BesselJ}\left(q, \tau 2 \cdot r\right) + rhs\left(sol[3]\right)\text{BesselY}\left(q, \tau 2 \cdot r\right)\right)\right), r, theta\right):$

$Bmr := unapply\left(\frac{1}{r} \cdot \frac{\mathrm{d}}{\mathrm{d}\, theta}\left(Az\right)(r, theta), r\right):$

$Hmr := unapply(((Bmr(r)))/(mu0 * mur), r):$

$Bmt := unapply\left(-\frac{\mathrm{d}}{\mathrm{d}\, r}\left(Az\right)(r, theta), r\right):$

$Hmt := unapply(((Bmt(r)))/(mu0 * mur2), r):$

%**Rotor Loss**

$Ar := unapply\left(\left(rhs\left(sol[1]\right) \cdot \text{BesselJ}\left(q, \tau 1 \cdot r\right)\right), r, theta\right):$

$Br := unapply\left(\frac{1}{r} \cdot \frac{\mathrm{d}}{\mathrm{d}\, theta}\left(Ar\right)(r, theta), r\right):$

$Hr := unapply\left(\left(\left(Br(r)\right)\right)/\left(mu0 \cdot mur\right), r\right):$

$Brt := unapply\left(-\frac{\mathrm{d}}{\mathrm{d}\, r} Ar(r, theta), r\right):$

$Hrt := unapply(((Brt(r)))/(mu0 * mur1), r):$

%**Machine Parameters**

$\omega := 2\pi kf : f := 3000 : \mu 0 := 4\pi \times 10^{-7} : p := 2 : \sigma 1 := 6666667 : \sigma 2 := 0.00000001 : \sigma 3 := 3.5 \times 10^{-15} : \mu r1 := 750 : \mu r2 := 1.07 : \mu r3 := 1:$
$\mu r4 := 5000$

$Rm := 27.1 \times 10^{-3} : Rs := 31 \times 10^{-3} : Rr := 21.6 \times 10^{-3} : Rg := \left(Rm + 3.8 \times 10^{-3}\right) : Anm :=$ current sheet value $: k :=$ time order :

$h :=$ space order

$q := p \times h : S1 := \left(\pi(2Rm)125 \times 10^{-3}\right) : S2 := \left(\pi(2Rr)125 \times 10^{-3}\right) : \tau 1 := \sqrt{I\omega\sigma 1\mu 0\mu r1} : \tau 2 := \sqrt{I\omega\sigma 2\mu 0\mu r2} : \tau 3 := \sqrt{I\omega\sigma 3\mu 0\mu r3}:$

$\tau 4 := \sqrt{I\omega\mu 0\mu r4} : Ik :=$ Peak current $: Kwq :=$ Winding factor $: Nph :=$ Number of turns per phase :

% **Current sheet value**

$Anm := evalf\left(\frac{h \cdot p}{2 \cdot R_s} \cdot \frac{3}{2} \cdot \frac{4}{Pi} \cdot \frac{Nph}{p} \cdot \frac{1}{h} \cdot Kwq \cdot \sqrt{2} \cdot Ik\right):$

% **Amplitude of harmonics, this value can also be calculated using the following program *Current2*.mw**

$evalf(Bmr(Rm)):$

% **Power Loss Calculation**

% Poynting theorem is used for the calculation of power loss

% **Power transmitted from airgap to magnet**

$Emt := evalf(-I \cdot \omega \cdot Az(Rm)):$
$Hmt := evalf(conjugate(Hmt(Rm))):$
$P_1 := evalf\left(\frac{1}{2} \cdot \text{Re}\left(Emt \cdot Hmt\right) \cdot S_1\right):$

% **Power transmitted from magnet layer to rotor hub**

$Ert := evalf(-I \cdot \omega \cdot Az(Rr)):$

$Hrt := evalf(conjugate(Hrt(Rr))):$

$P_2 := evalf\left(\frac{1}{2} \cdot \text{Re}\left(Ert \cdot Hrt\right) \cdot S_2\right):$

% **Power Loss in magnet**

$Pmag := P_1 - P_2:$

% **Power Loss in rotor hub**

$Phub := P_2$:

****

% Author: A. Ali Qazalbash
% Program: *Current2*.mw

% **The program calculates the amplitude of harmonics caused by armature reaction stator mmf harmonics only and calculates the amplitude of each harmonic**

restart : *with*(*VectorCalculus*) :

SetCoordinates('cylindrical'[*r*, theta, *z*]) :

% **Laplace equation in the Airgap**

$Lar := \left(diff\left(Ar\left(r,theta\right),r\right)r + r^2 diff\left(Ar\left(r,theta\right),\text{'\$'}\left(r,2\right)\right) + diff\left(Ar\left(r,theta\right),\text{'\$'}\left(r,2\right)\right)\right)/r^2 = 0$:

Ar := (*r*, theta) → *Rc*(*r*) * exp(*I*·*q*·theta) :

Lar :

$ODEC := simplify\left(\frac{Lar}{exp\left(I\cdot q\cdot theta\right)}\right)$:

lr := *dsolve*(*ODEC*, *Rc*(*r*)) :

Ar := *unapply*(*rhs*(*lr*) * exp(*I*·*q*·theta), *r*, theta) :

Ar := *unapply*(((*_C1*· r^{q} + *_C2* r^{-q}) ·$e^{I\,q\,\theta}$), *r*, theta) :

Bri := (1/*r*) * D[2](*Ar*)(*r*, theta) :

Hri := *Bri*/(*mu0*) :

Bti := - D[1](*Ar*)(*r*, theta) :

Hti := (*Bti*/(*mu0*)) :

% **Boundary Conditions**

HthRr := *eval*(*Hti*, *r* = *Rr*) :

_C1 := *solve*(*HthRr* = 0, *_C1*) :

_C1 := *simplify*(*_C1*) :

HthRs := *eval*(*Hti*, *r* = *Rs*) :

_C2 := *solve*(*HthRs* = - *Anm*, *_C2*) :

Xri := *factor*(*Bri*) :

Xti := *factor*(*Bti*) :

xx := *factor*(*combine*(*Xri*)) :

$Bmr := unapply\left(\left(\frac{xx}{I}\right),r\right)$

yy := *factor*(*combine*(*Xti*)) :

Bmt := *unapply*((*yy*), *r*) :

%**Machine Parameters**

$\omega := 2\pi kf$: $f := 3000$: $\mu 0 := 4\pi\times 10^{-7}$: $p := 2$: $\sigma 1 := 6666667$: $\sigma 2 := 769231$: $\sigma 3 := 3.5\times 10^{-15}$: $\mu r1 := 750$: $\mu r2 := 1.07$: $\mu r3 := 1$:
$\mu r4 := 5000$

$Rm := 27.1\times 10^{-3}$: $Rs := 31\times 10^{-3}$: $Rr := 21.6\times 10^{-3}$: $Rg := \left(Rm + 3.8\times 10^{-3}\right)$: *Anm* := current sheet value : *k* := time order :

h := space order

$q := p\times h$: $S1 := \left(\pi(2Rm)125\times 10^{-3}\right)$: $S2 := \left(\pi(2Rr)125\times 10^{-3}\right)$: $\tau 1 := \sqrt{I\omega\sigma 1\mu 0\mu r1}$: $\tau 2 := \sqrt{I\omega\sigma 2\mu 0\mu r2}$: $\tau 3 := \sqrt{I\omega\sigma 3\mu 0\mu r3}$:

$\tau 4 := \sqrt{I\omega\mu 0\mu r4}$: *Ik* := Peak current : *Kwq* := Winding factor : *Nph* := Number of turns per phase :

%**Current Sheet value**

$Anm := evalf\left(\frac{h\cdot p}{2\cdot R_s}.B\ value\ from\ program\ Rec2\right)$:

%**AirGap Flux Density**

$evalf((Bmr(Rm)))$:

****

% Author: Z.Q.Zhu & A. Ali Qazalbash
% Program: *Zhu*.mw

% **The program calculates the airgap flux density in the slotless machine using method developed by Zhu et al., (2002) and multiplies it with relative permeance function developed by Zhu et al., (1993). Then the amplitude of magnet flux tooth ripple harmonics is calculated.**

$restart$:

$withVectorCalculus$:

$SetCoordinates('cylindrical'[r, \text{theta}, z])$:

% **The airgap flux density in the slotless PM machine is calculated using Zhu et al., (2002)**

$A1 := n \to \sin((np+1)alpha\_p \cdot \text{Pi}/(2p))/((np+1)alpha\_p \cdot \text{Pi}/(2p))$:

$A2 := n \to \sin((np-1)alpha\_p \cdot \text{Pi}/(2p))/((np-1)alpha\_p \cdot \text{Pi}/(2p))$:

$Mr := n \to \frac{Br}{mu0} \cdot alpha\_p * (A1(n) + A2(n))$:

$Mth := n \to \frac{Br}{mu0} \cdot alpha\_p * (A1(n) - A2(n))$:

$Mm := n \to (Mr(n) + n \cdot p \cdot Mth(n))$:

$A3 := n \to \left(\left(n \cdot p - \frac{1}{n \cdot p}\right) \cdot \frac{Mr(n)}{Mm(n)} + \frac{1}{n \cdot p}\right)$:

$$Br1 := n \to \left(\frac{\mu 0 Mm(n) np}{mur(n^2 p^2 - 1)}\left(\left(\left(\frac{R}{Rs}\right)^{np-1}\left(\frac{Rm}{Rs}\right)^{np+1} + \left(\frac{Rm}{R}\right)^{np+1}\right)\left(A3(n) - 1 + 2\left(\frac{Rr}{Rm}\right)^{np+1} - (A3(n)+1)\left(\frac{Rr}{Rm}\right)^{2np}\right)/\left(\frac{(mur+1)\left(1-\frac{Rr}{Rs}\right)^{2np}}{mur}\right) - \frac{(mur-1)\left(\left(\frac{Rm}{Rs}\right)^{2np} - \left(\frac{Rr}{Rm}\right)^{2np}\right)}{mur}\right)\right):$$

%**Machine Parameters**

$mu0 := 4\pi \times 10^{-7} : p := 2 : mur := 1.07 : Rm := 27.1 \times 10^{-3} : Rs := 31 \times 10^{-3} : Rr := 21.6 \times 10^{-3} : Br := 1.12$:
$alpha\_p := 1 : R := Rm : Qs :=$ number of slots $: nh :=$ *number of harmonics* $:$ pe $:=$ slot opening in radians

% **Airgap flux density in the slotless PM machine**

$Bar := theta \to add\left(\left(Br1(2n+1)\cos((2n+1)p \cdot theta), n = 0..nh\right)\right)$

$evalf(Bar(theta))$

% **Calculation of relative permeance function**
% Slot opening
b0 := evalf(pe·Rs) :
% Airgap
$g := Rs - Rm$:
% Magnet height
$hm := Rm - Rr$:
% Radius on the surface of the magnet
$r := Rm$
% effective airgap
$gp := g + \frac{hm}{mur}$:
$y := r - Rs + gp$:
$a := \sqrt{1 + \left(\frac{2 \cdot gp}{b0}\right)^2}$:

% Slot pitch

$$taut := \frac{2\cdot \mathrm{Pi}\cdot Rs}{Qs} :$$

$$eq := \frac{y\cdot \mathrm{Pi}}{b0} = \frac{1}{2}\cdot \ln\left(\frac{\mathrm{sqrt}\left(a^2+v^2\right)+v}{\mathrm{sqrt}\left(a^2+v^2\right)-v} \right) + \frac{2\cdot gp}{b0}\cdot \arctan\left(\frac{2\cdot gp}{b0} \cdot \frac{v}{\mathrm{sqrt}\left(a^2+v^2\right)} \right) :$$

$$v := fsolve(evalf(eq), v) :$$

$$\mathrm{beta} := evalf\left(\frac{1}{2}\cdot \left(1 - \frac{1}{\mathrm{sqrt}\left(1+\left(\frac{b0}{2\cdot gp} \right)^2 \cdot \left(1+v^2\right) \right)} \right) \right) :$$

% Carters Coefficient

$$kc := \frac{taut}{taut - gam\cdot gp} :$$

$$gam := evalf\left(\frac{4}{\mathrm{Pi}} \cdot \left(\frac{b0}{2\cdot gp}\cdot \arctan\left(\frac{b0}{2\cdot gp} \right) - \ln\left(\mathrm{sqrt}\left(1+\left(\frac{b0}{2\cdot gp} \right)^2 \right) \right) \right) \right) :$$

$$lam0 := evalf\left(\frac{1}{kc}\cdot \left(1 - \frac{1.6\cdot \mathrm{beta}(r)\cdot b0}{taut} \right) \right) :$$

$$lam := n \to -\frac{\mathrm{beta}(r)\cdot 4}{\mathrm{Pi}\cdot n} \left(0.5 + \frac{\left(\frac{n\cdot b0}{taut} \right)^2}{0.78125 - 2\cdot \left(\frac{n\cdot b0}{taut} \right)^2} \right) \cdot \sin\left(\frac{1.6\cdot \mathrm{Pi}\cdot n\cdot b0}{taut} \right) :$$

% Relative permeance function

$$xlam := theta \to lam0 + Sum\left(lam(n)\cdot cos\left(n\cdot Qs\cdot \left(\frac{theta - wr\cdot t1}{2} \right) \right), n = 1..nh \right) :$$

% **Multiplying slotless airgap flux density with permeance function**

$$Brs := theta \quad \left(evalf\left(xlam(theta)\left(Bar(theta) \right) \right) \right) :$$

% **The amplitude of harmonics can be calculated as**

$$Q := evalf(xlam(\mathrm{theta})) :$$

$$Q1 := simplify(Q) :$$

$$R := evalf\left(Sum\left(\left(Br1\left(2n+1\right)\cos\left(\left(2n+1\right) p\cdot theta \right), n = 0..nh \right) \right) \right) :$$

$$V := combine(R\cdot Q_1) :$$

****

% Author: Gieras & A. Ali Qazalbash
% Program: *Gieras*.mw

% **The program calculates the relative permeance function developed by Gieras et al., (2004), the function is applied with the airgap flux density in slotless PM machine calculated by Zhu et al., (2002). Then the amplitude of magnet flux tooth ripple harmonics is calculated.**

% **Calculation of relative permeance function**

% Effective airgap

$$gp := g + \frac{hm}{mur} :$$

$$s := \frac{\left(\frac{b0}{ts} \right)}{5 + \frac{b0}{ts}} \cdot \frac{2\cdot \mathrm{sqrt}\left(1+\left(\frac{b0}{ts} \right)^2 \right)}{\mathrm{sqrt}\left(1+\left(\frac{b0}{ts} \right)^2 \right) - 1} :$$

$$gam := evalf\left(\frac{4}{\mathrm{Pi}} \left(\frac{b0}{2\cdot gp}\arctan\left(\frac{b0}{2\cdot gp} \right) - \ln\left(sqrt\left(1+\left(\frac{b0}{2\cdot gp} \right)^2 \right) \right) \right) \right) :$$

% Slot opening factor

$$ko := \left(\frac{\sin\left(k \cdot s \cdot \mathrm{Pi} \cdot \frac{b0}{2 \cdot ts} \right)}{k \cdot s \cdot \mathrm{Pi} \cdot \frac{b0}{2 \cdot ts}} \right) :$$

% Carters Coefficient

$$Kc := \frac{ts}{ts - gam \cdot gp} :$$

% Permeance function

$$lam := unapply\left(\left(\tfrac{1}{Kc} - 2 \cdot gam \cdot \tfrac{gp}{ts} \cdot Sum\left(ko^2 \cos\left(k \cdot Qs\left(\tfrac{theta - wrt1}{2} \right) \right), k = 1..nh \right) \right), theta \right):$$

$$Q := evalf(lam(\mathrm{theta})) :$$

$$Q1 := simplify(Q)$$

$$R := evalf\left(Sum\left(\left(Br1(2n+1) \cos\left((2n+1)\, p \cdot theta \right), n = 0..nh \right) \right) \right)$$

% Harmonic Amplitude rotating in space and time

$$V := combine(R \cdot Q_1) :$$

****

% Author: Ẑarko & A. Ali Qazalbash
% Program: *Ẑarko*.mw

% **The program calculates the complex relative permeance function developed by Ẑarko et al., (2006), the function is applied with the airgap flux density in slotless PM machine calculated by Zhu et al., (2002). Then the amplitude of magnet flux tooth ripple harmonics is calculated.**

% **Calculation of complex relative permeance function**
% the value of lambda is calculated using the Matlab program *Ẑarko*.m.

```
with(Matlab) :
Matlab[setvar]("x", 3.14) :
```

% the real and imaginary components of lambda are plotted

```
lambdaa := Matlab[getvar]("lambdaa") :
Q := transpose( (lambdaa) ) :
N := 128 :  thetas := 2·Pi/4 :
pos := Vector(N + 1, i→ (i − 1) * thetas / N) :
plot( pos, Re(lambdaa) ) :
plot( pos, Im(lambdaa) ) :
T := 2·Pi/p :
```

% applying Discrete Fourier transforms

```
with(DiscreteTransforms) : with(plots) :
Pk := Array( indets( plot( pos, Re(Q) ), listlist)[ ], datatype = float[8]) :
ArrayDims(Pk) :
N := op( [2, 1, 2], Pk); [min, max](seq(Pk[i + 1, 1] - Pk[i, 1], i = 1 ..N − 1) ) :
pointplot(Pk) :
Z := FourierTransform( ⟨seq(Pk[i, 2], i = 1 ..N)⟩, normalization = full) :
a0 :=  2· Re(Z[1]) :
A := Array( 1 .. trunc( (N)/2 ), datatype = float[8] ) :
ArrayTools:-Copy( 2 * Re(Z), 1, A) :
```

$$fdftreal := theta \rightarrow \left(a0/2 \right) + add\left(A[i] \cos\left(iQs\left(\tfrac{(theta - wrt1)}{2} \right) \right), i = 1..nh \right):$$

```
K := evalf( ( fdftreal(theta) ) ) :
Pkk := Array( indets( plot( pos, Im(Q) ), listlist)[ ], datatype = float[8]) :
ArrayDims(Pkk) :
```

$$N := op\left([2,1,2], Pkk \right); [\min, \max]\left(seq\left(Pkk[i+1,1] - Pkk[i,1], i = 1..N-1 \right) \right):$$

```
pointplot(Pkk) :
Z1 := FourierTransform( ⟨seq(Pkk[ i, 2], i = 1 ..N) ⟩, normalization = full) :
B1 := Array( 1 .. trunc( (N) /2), datatype = float[ 8]) :
ArrayTools:-Copy( -2 * Im(Z1), 1, B1) :
fdftimg := theta → add( B1[i] · sin( i · Qs( (theta−wrt1) / 2 ) ), i = 1..nh ):
K := evalf( ( fdftreal( theta) ) ) :
L := evalf( ( fdftimg( theta) ) ) :
% calculating radial component of airgap flux density
H := evalf (X (theta)) :
% calculating tangential component of airgap flux density
J := evalf (Y (theta))
% combining both parts of airgap flux density
eqa := evalc( H + I·J) :
Q1 := combine( eqa) :
% combining real and tangential part of lambda
eqb := evalc( K + I·L) :
eqbb := conjugate( eqb) :
Q2 := combine( eqbb) :
eqf := evalc( Q1·Q2) :
% Harmonics in time and space
eqff := combine( eqf) :

**********************************************************************************

% Author: A. Ali Qazalbash
% Program: Vadd1.mw

% The program performs vector (phasor) addition between magnet flux tooth ripple harmonics and stator mmf harmonics.
restart :
withVectorCalculus :
X := reactance : E := back emf : phii := ( 0·Pi / 180 ) : i := current value

h:=space harmonics: k:=time harmonics: M:=Magnet mmf harmonics: W:=Stator mmf harmonics: angle:=angle1:
angle:=angle2:

c := X·i·cos( phii) / E :

S := sin^-1 ( c) : floor( evalf( S·180 / Pi ) ) :

sigh := evalf ( phii − S) :

sian := evalf( sigh·180 / Pi ) :

if sian < 1 then
sian := round( evalf( sigh·180 / Pi ) )
else
sian := floor( evalf( sigh·180 / Pi ) )
end if:

angle1 := -90 + sian :   angle1 for Harmonics 1, 5, 11, 17
angle2 := 90 + sian :    angle2 for Harmonics 7, 13
```

$A := algsubs(h\cdot \text{theta} + k\cdot w\cdot t = u,\ M\cdot\cos(h\cdot \text{theta} + k\cdot w\cdot t))$:

$B := expand\left(algsubs\left(h\cdot \text{theta} + k\cdot w\cdot t = u,\ W * \cos\left(h\cdot \text{theta} + k\cdot w\cdot t + \left(\frac{angle\cdot \text{Pi}}{180}\right)\right)\right)\right)$:

$T := simplify(eval(convert(collect(A + B, \cos(u)), phaseamp, u), u = h\cdot \text{theta} + k\cdot w\cdot t))$;

****

% Author: A. Ali Qazalbash
% Program: *Vadd2*.mw

% **The program performs vector (phasor) addition between magnet flux tooth ripple harmonics and stator mmf harmonics in case of generators connected to rectifier loads.**

h:=*space harmonics*: *k*:=*time harmonics*: *M*:=*Magnet mmf harmonics*: *W*:=*Stator mmf harmonics*: *angle*:=*angle1*: *angle*:=*angle2*:

$Ian := current\ harmonic\ phase\ angle$:

$Ea := back\ emf\ harmonic\ phase\ angle$:

$sigh := evalf(Ian - Ea)$:

$sian := evalf\left(\frac{sigh\cdot 180}{\text{Pi}}\right)$:

if $sian < 1$ **then**

$sian := \text{round}\left(evalf\left(\frac{sigh\cdot 180}{\text{Pi}}\right)\right)$

else

$sian := \text{floor}\left(evalf\left(\frac{sigh\cdot 180}{\text{Pi}}\right)\right)$

end if:

$angle1 := -90 + sian$: angle1 for Harmonics 1, 5, 11, 17

$angle2 := 90 + sian$: angle2 for Harmonics 7, 13

$A := algsubs(h\cdot \text{theta} + k\cdot w\cdot t = u,\ M\cdot\cos(h\cdot \text{theta} + k\cdot w\cdot t))$:

$B := expand\left(algsubs\left(h\cdot \text{theta} + k\cdot w\cdot t = u,\ W * \cos\left(h\cdot \text{theta} + k\cdot w\cdot t + \left(\frac{angle\cdot \text{Pi}}{180}\right)\right)\right)\right)$:

$T := simplify(eval(convert(collect(A + B, \cos(u)), phaseamp, u), u = h\cdot \text{theta} + k\cdot w\cdot t))$;

****

% Author: A. Ali Qazalbash
% Program: *Rec2*.mw

% **The program calculates the amplitude of stator mmf harmonics in stator reference frame for the generator with two winding rectifier topology.**

restart :

$Nc := Number\ of\ turns\ per\ coil : \Omega := harmonic\ order\cdot\ w : Ik := value\ of\ peak\ current : w := angular\ frequency$:

$$Fa1 := \frac{4}{\mathrm{Pi}} \cdot Nc \cdot Ik \cdot \cos\left(\frac{\Omega}{w} \cdot (w \cdot t)\right) \cdot \left(\cos(\mathrm{theta}) - \frac{1}{3} \cdot \cos(3 \cdot \mathrm{theta}) + \frac{1}{5} \cdot \cos(5 \cdot \mathrm{theta}) - \frac{1}{7} \cdot \cos(7 \cdot \mathrm{theta}) + \frac{1}{9} \cdot \cos(9 \cdot \mathrm{theta}) - \frac{1}{11} \cdot \cos(11 \cdot \mathrm{theta}) + \frac{1}{13} \cdot \cos(13 \cdot \mathrm{theta}) - \frac{1}{15} \cdot \cos(15 \cdot \mathrm{theta}) + \frac{1}{17} \cdot \cos(17 \cdot \mathrm{theta}) - \frac{1}{19} \cdot \cos(19 \cdot \mathrm{theta})\right) :$$

$$Fa2 := \frac{4}{\mathrm{Pi}} \cdot Nc \cdot Ik \cdot \cos\left(\frac{\Omega}{w} \cdot \left(w \cdot t - \frac{\mathrm{Pi}}{6}\right)\right) \cdot \left(\cos\left(\mathrm{theta} - \frac{\mathrm{Pi}}{6}\right) - \frac{1}{3} \cdot \cos\left(3 \cdot \left(\mathrm{theta} - \frac{\mathrm{Pi}}{6}\right)\right) + \frac{1}{5} \cdot \cos\left(5 \cdot \left(\mathrm{theta} - \frac{\mathrm{Pi}}{6}\right)\right) - \frac{1}{7} \cdot \cos\left(7 \cdot \left(\mathrm{theta} - \frac{\mathrm{Pi}}{6}\right)\right) + \frac{1}{9} \cdot \cos\left(9 \cdot \left(\mathrm{theta} - \frac{\mathrm{Pi}}{6}\right)\right) - \frac{1}{11} \cdot \cos\left(11 \cdot \left(\mathrm{theta} - \frac{\mathrm{Pi}}{6}\right)\right) + \frac{1}{13} \cdot \cos\left(13 \cdot \left(\mathrm{theta} - \frac{\mathrm{Pi}}{6}\right)\right) - \frac{1}{15} \cdot \cos\left(15 \cdot \left(\mathrm{theta} - \frac{\mathrm{Pi}}{6}\right)\right) + \frac{1}{17} \cdot \cos\left(17 \cdot \left(\mathrm{theta} - \frac{\mathrm{Pi}}{6}\right)\right) - \frac{1}{19} \cdot \cos\left(19 \cdot \left(\mathrm{theta} - \frac{\mathrm{Pi}}{6}\right)\right)\right) :$$

$$Fb1 := \frac{4}{\mathrm{Pi}} \cdot Nc \cdot Ik \cdot \cos\left(\frac{\Omega}{w} \cdot \left(w \cdot t - \frac{2 \cdot \mathrm{Pi}}{3}\right)\right) \cdot \left(\cos\left(\theta - \left(\frac{2 \cdot \mathrm{Pi}}{3}\right)\right) - \frac{1}{3} \cdot \cos\left(3 \cdot \left(\theta - \frac{2 \cdot \mathrm{Pi}}{3}\right)\right) + \frac{1}{5} \cdot \cos\left(5 \cdot \left(\theta - \frac{2 \cdot \mathrm{Pi}}{3}\right)\right) - \frac{1}{7} \cdot \cos\left(7 \cdot \left(\theta - \frac{2 \cdot \mathrm{Pi}}{3}\right)\right) + \frac{1}{9} \cdot \cos\left(9 \cdot \left(\theta - \frac{2 \cdot \mathrm{Pi}}{3}\right)\right) - \frac{1}{11} \cdot \cos\left(11 \cdot \left(\theta - \frac{2 \cdot \mathrm{Pi}}{3}\right)\right) + \frac{1}{13} \cdot \cos\left(13 \cdot \left(\theta - \frac{2 \cdot \mathrm{Pi}}{3}\right)\right) - \frac{1}{15} \cdot \cos\left(15 \cdot \left(\theta - \frac{2 \cdot \mathrm{Pi}}{3}\right)\right) + \frac{1}{17} \cdot \cos\left(17 \cdot \left(\theta - \frac{2 \cdot \mathrm{Pi}}{3}\right)\right) - \frac{1}{19} \cdot \cos\left(19 \cdot \left(\theta - \frac{2 \cdot \mathrm{Pi}}{3}\right)\right)\right) :$$

$$Fb2 := \frac{4}{\mathrm{Pi}} \cdot Nc \cdot Ik \cdot \cos\left(\frac{\Omega}{w} \cdot \left(w \cdot t - \frac{5 \cdot \mathrm{Pi}}{6}\right)\right) \cdot \left(\cos\left(\mathrm{theta} - \left(\frac{5 \cdot \mathrm{Pi}}{6}\right)\right) - \frac{1}{3} \cdot \cos\left(3 \cdot \left(\mathrm{theta} - \left(\frac{5 \cdot \mathrm{Pi}}{6}\right)\right)\right) + \frac{1}{5} \cdot \cos\left(5 \cdot \left(\mathrm{theta} - \left(\frac{5 \cdot \mathrm{Pi}}{6}\right)\right)\right) - \frac{1}{7} \cdot \cos\left(7 \cdot \left(\mathrm{theta} - \left(\frac{5 \cdot \mathrm{Pi}}{6}\right)\right)\right) + \frac{1}{9} \cdot \cos\left(9 \cdot \left(\mathrm{theta} - \left(\frac{5 \cdot \mathrm{Pi}}{6}\right)\right)\right) - \frac{1}{11} \cdot \cos\left(11 \cdot \left(\mathrm{theta} - \left(\frac{5 \cdot \mathrm{Pi}}{6}\right)\right)\right) + \frac{1}{13} \cdot \cos\left(13 \cdot \left(\mathrm{theta} - \left(\frac{5 \cdot \mathrm{Pi}}{6}\right)\right)\right) - \frac{1}{15} \cdot \cos\left(15 \cdot \left(\mathrm{theta} - \left(\frac{5 \cdot \mathrm{Pi}}{6}\right)\right)\right) + \frac{1}{17} \cdot \cos\left(17 \cdot \left(\mathrm{theta} - \left(\frac{5 \cdot \mathrm{Pi}}{6}\right)\right)\right) - \frac{1}{19} \cdot \cos\left(19 \cdot \left(\mathrm{theta} - \left(\frac{5 \cdot \mathrm{Pi}}{6}\right)\right)\right)\right) :$$

$$Fc1 := \frac{4}{\mathrm{Pi}} \cdot Nc \cdot Ik \cdot \cos\left(\frac{\Omega}{w} \cdot \left(w \cdot t - \frac{4 \cdot \mathrm{Pi}}{3}\right)\right) \cdot \left(\cos\left(\theta - \frac{4 \cdot \mathrm{Pi}}{3}\right) - \frac{1}{3} \cdot \cos\left(3 \cdot \left(\theta - \frac{4 \cdot \mathrm{Pi}}{3}\right)\right) + \frac{1}{5} \cdot \cos\left(5 \cdot \left(\theta - \frac{4 \cdot \mathrm{Pi}}{3}\right)\right) - \frac{1}{7} \cdot \cos\left(7 \cdot \left(\theta - \frac{4 \cdot \mathrm{Pi}}{3}\right)\right) + \frac{1}{9} \cdot \cos\left(9 \cdot \left(\theta - \frac{4 \cdot \mathrm{Pi}}{3}\right)\right) - \frac{1}{11} \cdot \cos\left(11 \cdot \left(\theta - \frac{4 \cdot \mathrm{Pi}}{3}\right)\right) + \frac{1}{13} \cdot \cos\left(13 \cdot \left(\theta - \frac{4 \cdot \mathrm{Pi}}{3}\right)\right) - \frac{1}{15} \cdot \cos\left(15 \cdot \left(\theta - \frac{4 \cdot \mathrm{Pi}}{3}\right)\right) + \frac{1}{17} \cdot \cos\left(17 \cdot \left(\theta - \frac{4 \cdot \mathrm{Pi}}{3}\right)\right) - \frac{1}{19} \cdot \cos\left(19 \cdot \left(\theta - \frac{4 \cdot \mathrm{Pi}}{3}\right)\right)\right) :$$

$$Fc2 := \frac{4}{\mathrm{Pi}} \cdot Nc \cdot Ik \cdot \cos\left(\frac{\Omega}{w} \cdot \left(w \cdot t - \frac{3 \cdot \mathrm{Pi}}{2}\right)\right) \cdot \left(\cos\left(\mathrm{theta} - \left(\frac{3 \cdot \mathrm{Pi}}{2}\right)\right) - \frac{1}{3}\right.$$
$$\cdot \cos\left(3 \cdot \left(\mathrm{theta} - \left(\frac{3 \cdot \mathrm{Pi}}{2}\right)\right)\right) + \frac{1}{5} \cdot \cos\left(5 \cdot \left(\mathrm{theta} - \left(\frac{3 \cdot \mathrm{Pi}}{2}\right)\right)\right) - \frac{1}{7}$$
$$\cdot \cos\left(7 \cdot \left(\mathrm{theta} - \left(\frac{3 \cdot \mathrm{Pi}}{2}\right)\right)\right) + \frac{1}{9} \cdot \cos\left(9 \cdot \left(\mathrm{theta} - \left(\frac{3 \cdot \mathrm{Pi}}{2}\right)\right)\right) - \frac{1}{11}$$
$$\cdot \cos\left(11 \cdot \left(\mathrm{theta} - \left(\frac{3 \cdot \mathrm{Pi}}{2}\right)\right)\right) + \frac{1}{13} \cdot \cos\left(13 \cdot \left(\mathrm{theta} - \left(\frac{3 \cdot \mathrm{Pi}}{2}\right)\right)\right) - \frac{1}{15}$$
$$\cdot \cos\left(15 \cdot \left(\mathrm{theta} - \left(\frac{3 \cdot \mathrm{Pi}}{2}\right)\right)\right) + \frac{1}{17} \cdot \cos\left(17 \cdot \left(\mathrm{theta} - \left(\frac{3 \cdot \mathrm{Pi}}{2}\right)\right)\right) - \frac{1}{19}$$
$$\left. \cdot \cos\left(19 \cdot \left(\mathrm{theta} - \left(\frac{3 \cdot \mathrm{Pi}}{2}\right)\right)\right)\right) :$$

$K := evalf((Fa1 + Fb1 + Fc1)) :$

$K1 := evalf((Fa2 + Fb2 + FC2)) :$

$Harmonics := evalf(K + K1) :$

$expand(\%) :$

$combine(\%) :$

****

Appendix2

Programs in Matlab

```
% Author: A. Ali Qazalbash
% Program: Current3.m

% The program is used to define current values to be defined for the calculation of armature reaction stator
mmf harmonics using static FEA
close all
clear

for theta =0*pi/180          %theta in electrical degrees
Ia=I*cos(theta);
Ib=I*cos(theta-(2*pi/3));
Ic=I*cos(theta-(4*pi/3));
end

disp(Ia);%Current in phase A
disp(Ib);%Current in phase B
disp(Ic);%Current in phase C
```

****

```
% Author: Neamat T Irenji & A. Ali Qazalbash
% Program: FFT1.m

% Two dimensional Fourier Transform
%The program is used to read excel files containing airgap flux density data for each rotor position.
clear

%Defining path to read excel files
folderpath  =  'C:\local\PhD-Third-Year\JP1-Power-loss-calculation-using-various-methods\Harmonics-mag5p5-30-
models\Harmonics-5p5-30-models-excel';
filenames = dir((folderpath,'.\*xlsx'));
for i = 1 : size(filenames,1)filepath = (folderpath , '\' , filenames(i).name);
data{i} = xlsread(filepath,1, 'C2:D61');
x(:,i) = data{i}(2:end,2);
end
time = data{1}(2:end,1)' * 180/pi;
%Plot figure
figure,
hold on
for i = 1 : size(x,2)
p=plot(time, x(:,i))
set(p,'Color','k')
end

% All the data is saved in a file to be further analysed
```

```
cd('C:\local\PhD-Third-Year\JP1-Power-loss-calculation-using-various-methods\Harmonics-mag5p5-30-
models\Harmonics-5p5-30-models-excel')

save 'No_Load_5P5' 'x'
ylabel('Air-Gap Flux Desity (B)','FontSize',30)
xlabel('Angle (theta)','FontSize',30)

*********************************************************************************

% Author: Neamat T Irenji & A. Ali Qazalbash
% Program: FFT2.m

% The program calculates the 2D Fourier transform of the data from previous program FFT1.m.
clear

%Reading the file containing airgap flux density data in the matrix form
Load'C:\local\PhD-Third-Year\JP1-Power-loss-calculation-using-various-methods\Harmonics-mag5p5-30-
models\Harmonics-5p5-30-models-excel\No_Load_5P5.mat';
%Reading x-axis time data
Load 'C:\local\PhD-Third-Year\JP3-Power Factor\Harmonics_analysis_final_data\Load_only_
Harmonics_3p5_5p5\Load_Harmonics_3p5_5p5_excel\time.mat';

[m1,n1]=size(x);
%Matrix manipulation
%Data for N-pole Xn
%
x1=(x(1,:)-x(m1,:))/2;
x1n=x(2:m1-1,:);
Xn=[x1;x1n];
%Generating points for S-pole, data for S-pole is the negative of data for N-pole
Xs=-Xn;
%
Xns=[Xn;Xs];
time2 = linspace(0,time(end)*2,size(Xns,1));
figure(1),plot(time2,Xns)
[m,n]=size(Xns);
Xnsfft2=fft2(Xns);
Xnsabs=abs(Xnsfft2)/(m*n);

%Matrix manipulation
X=Xnsabs;

if rem(m,2)==0,
   X1m0=X(2:m/2,1);
   X2m0=X(m/2+2:m,1);
   X2m0=flipud(X2m0);
   Xm0=X1m0+X2m0;
   %
   X13=X(2:m/2,2:n);
   X24=X(m/2+2:m,2:n);
   X24=flipud(fliplr(X24));
   X1234=X13+X24;
   Y=zeros(m/2,n);
   Y(1,:)=X(1,:);
   Y(2:m/2,1)=Xm0;
   Y(2:m/2,2:n)=X1234;
else
   X1m0=X(2:m/2+0.5,1);
   X2m0=X(m/2+1:m,1);
   X2m0=flipud(X2m0);
   Xm0=X1m0+X2m0;
   %
   X13=X(2:m/2+0.5,2:n);
   X24=X(m/2+1:m,2:n);
   X24=flipud(fliplr(X24));
```

```
   X1234=X13+X24;
   %
   Y=zeros(m/2+0.5,n);
   Y(1,:)=X(1,:);
   Y(2:m/2+0.5,1)=Xm0;
   Y(2:m/2+0.5,2:n)=X1234;
end

% if Y is partitioned from the middle column, then the first part represent the forward rotating waves and second part the backward rotating waves.

Xfft2=Y;

%Mat_to_write = Y(2:2:20,1:6);
Mat_to_write = Y;

%Writing results to a file
xlswrite('C:\local\PhD-Third-Year\JP1-Power-loss-calculation-using-various-methods\Harmonics-mag5p5-30-models\No_Load_5p5_all_harmonics',Mat_to_write)

**********************************************************************************************


% Author: A. Ali Qazalbash
% Program: FFTE.m

% Program to calculate Harmonics in Back emf E. (Reactance Calculation)
clear

data = xlsread('C:\local\PhD-Third-Year\JP2-PM-machine-connected-to-rectifier\Complete_Final_Data_PMSG_Connected_to_Rectifier\1rec_Different_Current_CC\1rec_1285amps_inductive\I_1000Hz_FFT.xlsx');

x = data(:,2);
time = data(:,1);
plot(time,x)
y = fft(x)/length(x)
fs = 1/(time(2)-time(1));
f = linspace(0,1,length(x)/2+1)*fs/2;
plot(f,2*abs(y(1:end/2+1)))
plot(f,(angle(y(1:end/2+1))))
% startm from time t1 to t2 where t2 - t1 is a complete cycle

ts1 = 200;
t1 = time(ts1); % use this time in current
t2 = t1 + 1/100;
ts2 = find (abs(time - t2) == min(abs(time - t2)));
plot(time(ts1:ts2),x(ts1:ts2))
x1 = x (ts1:ts2);
time1 = time(ts1:ts2);
y1 = fft(x1)/length(x1);
f1 = linspace(0,1,length(x1)/2+1)*fs/2;
plot(f1,2*abs(y1(1:end/2+1)),'LineWidth',2.5,'color','k')
plot(f1,(phase(y1(1:end/2+1))))

**********************************************************************************************


% Author: A Ali Qazalbash
% Program: FFTI.m

% This program calculates the harmonics in current I. (Reactance calculation)
clear

data = xlsread('C:\local\PhD-Third-Year\JP2-PM-machine-connected-to-rectifier\Inductance_Calculation_for_Various_speeds\br_i_1_rec_fp_3000.xlsx');
```

```
x = data(:,2);
time = data(:,1);
plot(time,x)
y = fft(x)/length(x);
fs = 1/(time(2)-time(1));
f = linspace(0,1,length(x)/2+1)*fs/2;
plot(f,2*abs(y(1:end/2+1)))
plot(f,(angle(y(1:end/2+1))))
%% startm from time t1 to t2 where t2 - t1 is a complete cycle

t_from_E = time; % this time should be the same as in E (previous program)
ts1 = find (abs(time - t_from_E) == min(abs(time - t_from_E)));
t1 = time(ts1);
t2 = t1 + 1/100;
ts2 = find (abs(time - t2) == min(abs(time - t2)));
plot(time(ts1:ts2),x(ts1:ts2))
x1 = x (ts1:ts2);
time1 = time(ts1:ts2);
y1 = fft(x1)/length(x1);
f1 = linspace(0,1,length(x1)/2+1)*fs/2;
plot(f1,2*abs(y1(1:end/2+1)))
plot(f1,(angle(y1(1:end/2+1))))
```

****

```
% Author: A. Ali Qazalbash
% Program: FFTI2.m

% This program performs FFT on the current wave forms for the rectifier case

clear

data = xlsread('C:\local\PhD-Third-Year\JP2-PM-machine-connected-to-rectifier\rectifier_current_fft.xlsx');

x = data(8:end,2);
time = data(8:end,1);
plot(time,x)
NFFT = 2^16; %interpolating the spectrum i.e.
y = fft(x, NFFT)/length(x);
fs = 1/(time(2)-time(1));
f = linspace(0,1,NFFT/2+1)*fs/2;

plot(f,2*abs(y(1:end/2+1)))
plot(f,(angle(y(1:end/2+1))))
ah(1) = subplot(2,1,1)
plot(f,2*abs(y(1:end/2+1)));
ah(2) = subplot(2,1,2)
plot(f,(angle(y(1:end/2+1))));
linkaxes(ah,'x')
```

****

```
% Author: Ẑarko & A. Ali Qazalbash
% Program: Ẑarko.m

% The program calculates the value of lambda

close all;
clear all;
clc
 %-----------------------------------------------------------------------
    nr=90000; %Rated speed [r/min]
    Do=107e-3; %stator outer dimater
    Ds=62e-3; %stator inner dimater
    la=125e-3; %core length
```

```
   Qs=12; %number of slots
   p=2; %number of poles
   alpha_p=0.99; %relative magnet angular span
   lm=5.5e-3; %magnet thickness
   g=3.9e-3; %air gap size
   mur=1.07; % relative permeability
   Br = 1.12677618751;

%    bo=5.3e-3; %slot opening width
   Rs=Ds*0.5; %stator inner radius

   bo=5.55*Rs*pi/180;  %slot opening width

   do=1e-3; %slot opening depth

   dslot=10e-3; %slot depth

 %-------------------------------------------------------------------------
   Mtype='P'; %Type of magnetization
   Nlambda=64; %Number of Fourier coefficients in the relative air gap
            %permeance distribution (max. 128)
   NB=301; %Number of Fourier coefficients in the flux density distribution
   N=128; %number of evaluation points (always use an even number!)
%-------------------------------------------------------------------------
%DEFINE PARAMETERS FOR FLUX DENSITY FOURIER COEFFICIENTS
   Rs=Ds*0.5; %stator inner radius
   Rm=Rs-g; %Magnet radius
   Rr=Rs-g-lm; %Rotor radius
   R=Rm+0.05e-3;

   RmRs=Rm/Rs;
   RrRm=Rr/Rm;
   RrRs=Rr/Rs;
   RRs=R/Rs;
   RmR=Rm/R;
%-------------------------------------------------------------------------

%-------------------------------------------------------------------------
   mu0=4*pi*1e-7;
%-------------------------------------------------------------------------

%-------------------------------------------------------------------------
%Polar coordinates of the characteristic points on the slot outline
   Rp1=Rr;
   Rp2=Rs;
   Rp3=Rs;
   Rp4=Rs;
   thetas=2*pi/Qs; %slot pitch in rad
   alphao=2*asin(0.5*bo/Rs); %slot opening in rad
   theta1=thetas/2-alphao/2;
   theta2=theta1+alphao;
%-------------------------------------------------------------------------
%CONFORMAL MAPPING OF THE SLOT STRUCTURE
   clear j
%Coefficients of the conformal mapping function
   boprime=theta2-theta1;
   gprime=log(Rp2/Rp1);
   bCM=(boprime/2/gprime+sqrt((boprime/2/gprime)^2+1))^2;
   aCM=1/bCM;

%CALCULATE COMPLEX RELATIVE AIR GAP PERMEANCE
   clear z_real z_imag
   z_imag=j*[0:thetas/N:thetas];
   z_real(1:length(z_imag))=log(R);
   z=z_real+z_imag; %Coordinates of the points in the Z plane
   s=exp(z);

%Define conformal mapping function
   FCM=inline('j*gprime/pi*(log((1+s)/(1-s))-log((b+s)/(b-s))-2*(b-1)/sqrt(b)*atan(s/sqrt(b)))+log(Rp2)+j*theta2',...
      's','b','gprime','Rp2','theta2');

%START OPTIMIZATION
   w0=[0.01*aCM]; %initial values
```

```
for i=1:length(z)
   res=@(w0)(FCM(sqrt((w0-bCM)/(w0-aCM)),bCM,gprime,Rp2,theta2)-z(i));
   [w(i),resnorm,residual,exitflag]=lsqnonlin(res,w0,[],[]);  % Call optimizer
   k(i)=exp(j*gprime/pi*log(w(i))+log(Rp2)+j*thetas/2);
   lambda(i)=k(i)*(w(i)-1)/(w(i)-aCM)^(1/2)/(w(i)-bCM)^(1/2)/s(i);
   %fprintf(1,'Iteration: %d,   dt/dz: %f\n',i,lambda(i));
   w0=w(i);
end

      lambda=[conj(lambda(N/2+1:-1:1)) lambda(2:N/2)];

figure;plot(real(lambda));grid
figure;plot(imag(lambda));grid
```

List of References

Abramowitz M and Stegun IA, (1970), “Handbook of Mathematical Functions”, *Dover Publications,* Inc., New York, USA. ISBN-10: 0160002028

Abusara, M. A., Guerrero, J. M. and Sharkh, S. M. (2014) 'Line-Interactive UPS for Microgrids', *IEEE Transactions on Industrial Electronics,*vol. 61, no. 3, pp. 1292-1300.

Alger, PL. (1965) 'The nature of induction machines', *Gordon and Breach, Science Publishers Inc., London* ISBN-149:36843684

Al-Naemi, F. I. and Moses, A. J. (2006) 'FEM modeling of rotor losses in PM motors', *Journal of Magnetism and Magnetic Materials,* vol. 304, no. 2, pp. e794-e797.

Ansoft Corporation (2006), [version 5.0.909], "Maxwell 2D", USA

Atallah, K., Howe, D., Mellor, P. H. and Stone, D. A. (2000) 'Rotor loss in permanent-magnet brushless AC machines', *IEEE Transactions on Industry Applications,* vol. 36, no. 6, pp. 1612-1618.

Bakshi, U. A. and Bakshi, M. V. (2009) 'Electric Machines III', *Technical publishers Pune, India,*ISBN-9788184312539

Bedrich Heller and Hamata, V. (1977) 'Harmonic field effects in induction machines', *Elsevier scientific publishing company, New york, USA.*

Belli, Z. and Mekideche, M. R. (2013) 'Optimization of magnets segmentation for eddy current losses reduction in permanent magnets electrical machines', *8th International Conference and Exhibition on Ecological Vehicles and Renewable Energies (EVER), 13',* pp.1-7.

Bianchi, N., Bolognani, S. and Fornasiero, E. (2007) 'A General Approach to Determine the Rotor Losses in Three-Phase Fractional-Slot PM Machines',

IEEE International Conference on Electric Machines and Drives, IEMDC 07', vol. 1. pp. 634-641.

Bianchi, N. and Fornasiero, E. (2009) 'Impact of MMF Space Harmonic on Rotor Losses in Fractional-Slot Permanent-Magnet Machines', *IEEE Transactions on Energy Conversion,* vol. 24, no. 2, pp. 323-328.

Binns, K. J. and Schmid, E. (1975) 'Some concepts involved in the analysis of the magnetic field in cage induction machines', *Proceedings of the Institution of Electrical Engineers, ,* vol. 122, no. 2, pp. 169-175.

Boules, N. (1981) 'Impact of slot harmonics on losses of high-speed permanent magnet machines with a magnet retaining ring', *Elect. Mach. Power Syst.,,* vol. 6, no. 6, pp. 527-539.

Boyce, W. E. and Diprima, R. C. (1986) 'Elementary Differential Equations and Boundary Value Problems.', *John Wiley &Sons*, 1986 ISBN-10:0470458313

Carter, F. W. (1900) 'Note on Air-gap and Interpolar Induction', *I.E.E,* vol. 29, no.146, pp. 925-933.

Dajaku, G. and Gerling, D. (2010) 'Stator Slotting Effect on the Magnetic Field Distribution of Salient Pole Synchronous Permanent-Magnet Machines', *IEEE Transactions on Magnetics,* vol. 46, no. 9, pp. 3676-3683.

Drubel, O. and Stoll, R. L. (2001) 'Comparison between analytical and numerical methods of calculating tooth ripple losses in salient pole synchronous machines', *IEEE Transactions on Energy Conversion,* vol. 16, no. 1, pp. 61-67.

Dubas, F. and Espanet, C. (2009) 'Analytical Solution of the Magnetic Field in Permanent-Magnet Motors Taking Into Account Slotting Effect: No-Load Vector Potential and Flux Density Calculation', *IEEE Transactions on Magnetics,* vol. 45, no. 5, pp. 2097-2109.

Ede, J. D., Atallah, K., Jewell, G. W., Wang, J. B. and Howe, D. (2004) 'Effect of axial segmentation of permanent magnets on rotor loss of modular brushless machines', *IEEE Industry Application Conference, 04',* vol.3, pp. 1703-1708.

Ede, J. D., Atallah, K., Jewell, G. W., Wang, J. B. and Howe, D. (2007) 'Effect of Axial Segmentation of Permanent Magnets on Rotor Loss in Modular

Permanent-Magnet Brushless Machines', *IEEE Transactions on Industry Applications, ,* vol. 43, no. 5, pp. 1207-1213.

El-Refaie, A. M. (2010) 'Fractional-Slot Concentrated-Windings Synchronous Permanent Magnet Machines: Opportunities and Challenges', *IEEE Transactions on Industrial Electronics, ,* vol. 57, no. 1, pp. 107-121.

Etemadrezaei, M., Wolmarans, J. J., Polinder, H. and Ferreira, J. A. (2012) 'Precise calculation and optimization of rotor eddy current losses in high speed permanent magnet machine*', International Conference on Electric Machines (ICEM), 12'*, pp.1399-1404.

Fang, D. (1997) 'Commutation-caused eddy-current losses in permanent-magnet brushless DC motors', *IEEE Transactions on Magnetics,* vol. 33, no. 5, pp. 4310-4318.

Freeman, E. M. (1962) 'The calculation of harmonics, due to slotting, in the flux-density waveform of a dynamo-electric machine', *Proceedings of the IEE - Part C: Monographs,* vol. 109, no. 16, pp. 581-588.

Gibbs, W. J. (1947) 'Tooth-ripple losses in unwound pole-shoes', *Electrical Engineers - Part II: Power Engineering, Journal of the Institution of,* vol. 94, no. 37, pp. 2.

Gibbs, W. J. (1958) 'Conformal Transformations in Electrical Engineering', *37 Essex Street W.C.2: Chapman & Hall LTD* ISBN-10:0412060302

Gieras, J. F. (2004) 'Analytical approach to cogging torque calculation of PM brushless motors', *IEEE Transactions on Industry Applications,* vol. 40, no. 5, pp. 1310-1316.

Hurray, P. G. (2010) 'Maxwell's Equations', *John Wiley & Sons*ISBN-10:0470542764

Irenji, N. T. (1998) 'Calculation of electromagnetic rotor losses in high speed permanent magnet machines', *PhD Thesis University of Southampton.*

Ishak, D., Zhu, Z. Q. and Howe, D. (2005) 'Eddy-current loss in the rotor magnets of permanent-magnet brushless machines having a fractional number of slots per pole', *IEEE Transactions on Magnetics,* vol. 41, no. 9, pp. 2462-2469.

Jiabin, W., Atallah, K., Chin, R., Arshad, W. M. and Lendenmann, H. (2010) 'Rotor Eddy-Current Loss in Permanent-Magnet Brushless AC Machines', *IEEE Transactions on Magnetics*, vol. 46, no. 7, pp. 2701-2707.

Kaczmarek, R., Wan-Ying, H. and Vannier, J. C. (2007) 'Magnetic losses simulation in PMSM drive by FE: Harmonic superposition by method of locked rotor', in *9th International Conference on Electrical Power Quality and Utilisation, EPQU 2007*, pp. 1-4.

Kirtley, J. L., Tolikas, M., Long, J. H., Ng, C. W. and ROche, R. (1998) 'Rotor loss models for high speed PM motor-generators', *ICEMS, 98'*, pp. 1832-1837.

Kumar, P. and Bauer, P. (2008) 'Improved Analytical Model of a Permanent-Magnet Brushless DC Motor', *IEEE Transactions on Magnetics*, vol. 44, no. 10, pp. 2299-2309.

Langsddorf, A. (1955) '*Theory of alternating-current machinery*', McGraw-Hill Book Company, Inc., USA, ISBN-0070994234

Lawrenson, P. J., Reece, P. and Ralph, M. C. (1966) 'Tooth-ripple losses in solid poles', *Proceedings of the Institution of Electrical Engineers*, vol. 113, no. 4, pp. 657-662.

Liu, Z. J. and Li, J. T. (2007) 'Analytical Solution of Air-Gap Field in Permanent-Magnet Motors Taking Into Account the Effect of Pole Transition Over Slots', *IEEE Transactions on Magnetics, ,* vol. 43, no. 10, pp. 3872-3883.

McPherson, G. (1981) 'An Introduction to Electrical Machines and Transformers', *John Wiley & Sons, USA*, ISBN-0471635294

Nagarkatti, A. K., Mohammed, O. A. and Demerdash, N. A. (1982) 'Special Losses in Rotors of Electronically Commutated Brushless DC Motors Induced by Non-Uniformly Rotating Armature MMFS', *IEEE Power Engineering Review*, vol. PER-2, no. 12, pp. 33-33.

Nakano, M., Kometani, H. and Kawamura, M. (2006) 'A study on eddy-current losses in rotors of surface permanent-magnet synchronous machines', *IEEE Transactions on Industry Applications*, vol. 42, no. 2, pp. 429-435.

Nuscheler, R. (2008) 'Two-dimensional analytical model for eddy-current loss calculation in the magnets and solid rotor yokes of permanent magnet

synchronous machines', *18th International Conference on Electrical Machines,(ICEM),08',* pp. 1-6.

Oberretl, K. (1972) 'Eddy Current Losses in Solid Pole Shoes of Synchronous Machines at No-Load and on Load', *IEEE Transactions on Power Apparatus and Systems,* vol. PAS-91, no. 1, pp. 152-160.

Polinder, H. and Hoeijmakers, M. J. (1997) 'Eddy-current losses in the permanent magnets of a PM machine*',8th International Conference on Electric Machines and Drives (IEMDC),* no. 444, pp. 138-142.

Polinder, H. and Hoeijmakers, M. J. (1999) 'Eddy-current losses in the segmented surface-mounted magnets of a PM machine', *IEE Proceedings of Electric Power Applications,* vol. 146, no. 3, pp. 261-266.

Rahman, M. A. (1974) 'Reaction Effect of Eddy Currents on Open Circuit Tooth Ripple Loss in Smooth Laminated Poles', *IEEE Transactions on Power Apparatus and Systems,* vol. PAS-93, no. 5, pp. 1478-1487.

Robinson, R. B. (1962) 'Harmonics in a.c. rotating machines', *Proceedings of the IEE - Part C: Monographs,* vol. 109, no. 16, pp. 380-387.

Saban, D. M. and Lipo, T. A. (2007) 'Hybrid Approach for Determining Eddy-Current Losses in High-Speed PM Rotors*',IEEE International Conference on Electric Machines & Drives (IEMDC), 07',* vol.1, pp. 658-661.

Sadiku, M.N, (2001) 'Numerical Techniques in Electromagnetics', *2nd Edition, CRC Press LLC,* ISBN-142006309X

Schofield, N., Ng, K., Zhu, Z. Q. and Howe, D. (1997) 'Parasitic rotor losses in a brushless permanent magnet traction machine*', 8th International Conference on Electrical Machines and Drives,* vol. 444, pp. 200-204.

Seok-Myeong Jang, H.-W. C., and Yeaon-Ho Jeong (2006) 'Influence on the rectifier of rotor losses in high-speed permanent magnet synchronous alternator', *Journal of Applied Physics,* vol. 99, no. 8, pp. 3.

Sharkh, N. T. Irenji and Harris., M. (1999) 'Effect of power factor on rotor loss in high-speed PM alternators', *9th International Conference on Electrical Machines and Drives,* no. 468. pp. 346-350.

Sharkh, S. M., Qazalbash, A. A., Irenji, N. T. and R.G.Wills (2011) 'Effect of Slot Configuration and Airgap and Magnet thicknesses on Rotor Electromagnetic Loss in Surface PM Synchronous Machines', *International Conference on Electrical Machines and Syxtems, (ICEMS),* pp. 1-6.

Sharkh, S. M. A., Harris, M. R. and Irenji, N. T. (1997) 'Calculation of Rotor Eddy-Current Loss in High-Speed PM Alternators', *8th International Conference on Electric Machines and Drives (IEMDC).*

Shephard W, Hulley LN and DTW, L. (1995) 'Power Electronics and motor control', Cambridge University Press; 2nd edition, ISBN-0521478138

Stoll, R. L. and Sykulski, J. K. (1992) 'Modelling Tooth Ripple Losses In The Solid Pole Faces Of Synchronous Machines', *COMPEL-The International Journal for Computation and Mathematics in Electrical and Electronic Engineering,* vol. 11, no. 1, pp. 105-108.

Toda, H., Zhenping, X., Jiabin, W., Atallah, K. and Howe, D. (2004) 'Rotor eddy-current loss in permanent magnet brushless machines', *IEEE Transactions on Magnetics,* vol. 40, no. 4, pp. 2104-2106.

Vadher, V. V., Smith, I. R. and Fanthome, B. A. (1986) 'Simulation of Permanent Magnet Generator/Rectifier Combination', *IEEE Transactions on Aerospace and Electronic Systems,* vol. AES-22, no. 1, pp. 64-70.

Van der Veen, J. L. F., Offringa, L. J. J. and Vandenput, A. J. A. (1997) 'Minimising rotor losses in high-speed high-power permanent magnet synchronous generators with rectifier load', *IEE Proceedings on Electric Power Applications,* vol. 144, no. 5, pp. 331-337.

Weber, W. (1928) 'Der Nutungsfaktor in electrischen Maschinen', *ETZ,* pp. 4.

Wills, D. A. and Kamper, M. J. (2010a) 'Analytical prediction of rotor eddy current loss due to stator slotting in PM machines', *IEEE Energy Conversion Congress and Exposition (ECCE),* pp. 992-995.

Wills, D. A. and Kamper, M. J. (2010b) 'Reducing PM eddy current rotor losses by partial magnet and rotor yoke segmentation', *International Conference on Electric Machines (ICEM),* pp. 1-6.

Wu, L. J., Zhu, Z. Q., Staton, D., Popescu, M. and Hawkins, D. (2011a) 'An Improved Subdomain Model for Predicting Magnetic Field of Surface-Mounted Permanent Magnet Machines Accounting for Tooth-Tips', *IEEE Transactions on Magnetics,* vol. 47, no. 6, pp. 1693-1704.

Wu, L. J., Zhu, Z. Q., Staton, D., Popescu, M. and Hawkins, D. (2011b) 'Analytical prediction of electromagnetic performance of surface-mounted PM machines based on subdomain model accounting for tooth-tips', *Electric Power Applications, IET,* vol. 5, no. 7, pp. 597-609.

Wu, L. J., Zhu, Z. Q., Staton, D. A., Popescu, M. and Hawkins, D. (2012) 'Comparison of Analytical Models of Cogging Torque in Surface-Mounted PM Machines', *Industrial Electronics, IEEE Transactions on,* vol. 59, no. 6, pp. 2414-2425.

Wu, L. J., Zhu, Z. Q., Staton, D., Popescu, M. and Hawkins, D. (2012a) 'Analytical Model for Predicting Magnet Loss of Surface-Mounted Permanent Magnet Machines Accounting for Slotting Effect and Load', *IEEE Transactions on Magnetics,* vol. 48, no. 1, pp. 107-117.

Wu, L. J., Zhu, Z. Q., Staton, D., Popescu, M. and Hawkins, D. (2012b) 'Analytical Modeling and Analysis of Open-Circuit Magnet Loss in Surface-Mounted Permanent-Magnet Machines', *IEEE Transactions on Magnetics,* vol. 48, no. 3, pp. 1234-1247.

Xinghua, W., Qingfu, L., Shuhong, W. and Qunfeng, L. (2003) 'Analytical calculation of air-gap magnetic field distribution and instantaneous characteristics of brushless DC motors', *IEEE Transactions on Energy Conversion,* vol. 18, no. 3, pp. 424-432.

Yamazaki, K. and Fukushima, Y. (2011) 'Effect of Eddy-Current Loss Reduction by Magnet Segmentation in Synchronous Motors With Concentrated Windings', *IEEE Transactions on Industry Applications,* vol. 47, no. 2, pp. 779-788.

Yamazaki, K. and Watari, S. (2005) 'Loss analysis of permanent-magnet motor considering carrier harmonics of PWM inverter using combination of 2-D and 3-D finite-element method', *IEEE Transactions on Magnetics,* vol. 41, no. 5, pp. 1980-1983.

Yunkai, H., Jianning, D., Long, J., Jianguo, Z. and Youguang, G. (2011) 'Eddy-Current Loss Prediction in the Rotor Magnets of a Permanent Magnet Synchronous Generator With Modular Winding Feeding a Rectifier Load', *IEEE Transactions on Magnetics,* vol. 47, no. 10, pp. 4203-4206.

Žarko, D., Ban, D. and Lipo, T. A. (2006) 'Analytical calculation of magnetic field distribution in the slotted air gap of a surface permanent-magnet motor using complex relative air-gap permeance', *IEEE Transactions on Magnetics*, vol. 42, no. 7, pp. 1828-1837.

Žarko, D., Ban, D. and Lipo, T. A. (2008) 'Analytical Solution for Cogging Torque in Surface Permanent-Magnet Motors Using Conformal Mapping', *IEEE Transactions on Magnetics*, vol. 44, no. 1, pp. 52-65.

Zhu, Z. Q. and Howe, D. (1993) 'Instantaneous magnetic field distribution in brushless permanent magnet DC motors. III. Effect of stator slotting', *IEEE Transactions on Magnetics*, vol. 29, no. 1, pp. 143-151.

Zhu, Z. Q., Howe, D., Bolte, E. and Ackermann, B. (1993) 'Instantaneous magnetic field distribution in brushless permanent magnet DC motors. I. Open-circuit field', *IEEE Transactions on Magnetics*, vol. 29, no. 1, pp. 124-135.

Zhu, Z. Q., Howe, D. and Chan, C. C. (2002) 'Improved analytical model for predicting the magnetic field distribution in brushless permanent-magnet machines', *IEEE Transactions on Magnetics*, vol. 38, no. 1, pp. 229-238.

Zhu, Z. Q., K. Ng, N. S. and D. Howe (2001a) 'Analytical prediction of rotor eddy current loss in brushless machines equipped with surface-mounted permanent magnets. II. Accounting for eddy current reaction field', *Proceedings of the Fifth International Conference on Electrical Machines and Systems, ICEMS*, vol. 2, pp. 810-813.

Zhu, Z. Q., K. Ng, N. S. and Howe, D. (2001b) 'Analytical prediction of rotor eddy current loss in brushless machines equipped with surface-mounted permanent magnets. II. Accounting for eddy current reaction field', *5th International Conference on Electric Machines and Systems, ICEMS*, 810-813.

Zhu, Z. Q., Ng, K., Schofield, N. and Howe, D. (2001c) 'Analytical prediction of rotor eddy current loss in brushless machines equipped with surface-mounted permanent magnets. I. Magnetostatic field model', *5th IEEE Conference on Electric Machines and Sysytems (ICEMS)*, vol.2. pp. 806-809.

Zhu, Z. Q., Ng, K., Schofield, N. and Howe, D. (2004) 'Improved analytical modelling of rotor eddy current loss in brushless machines equipped with surface-mounted permanent magnets', *IEE Proceedings on Electric Power Applications*, vol. 151, no. 6, pp. 641-650.

Zhu, Z. Q., Wu, L. J. and Xia, Z. P. (2010) 'An Accurate Subdomain Model for Magnetic Field Computation in Slotted Surface-Mounted Permanent-Magnet Machines', *IEEE Transactions on Magnetics*, vol. 46, no. 4, pp. 1100-1115.